Tiberio A. Ezquerra
Aurora Nogales   *Editors*

Crystallization as Studied by Broadband Dielectric Spectroscopy

Springer

Advances in Dielectrics

Series Editor

Friedrich Kremer, Fakultät für Physik und Geowissenschaften, Peter-Debye-Institut für Physik der weichen Materie, Universität Leipzig, Leipzig, Germany

Aims and Scope

Broadband Dielectric Spectroscopy (BDS) has developed tremendously in the last decade. For dielectric measurements it is now state of the art to cover typically 8–10 decades in frequency and to carry out the experiments in a wide temperature and pressure range. In this way a wealth of fundamental studies in molecular physics became possible, e.g. the scaling of relaxation processes, the interplay between rotational and translational diffusion, charge transport in disordered systems, and molecular dynamics in the geometrical confinement of different dimensionality—to name but a few. BDS has also proven to be an indispensable tool in modern material science; it plays e.g. an essential role in the characterization of Liquid Crystals or Ionic Liquids and the design of low-loss dielectric materials.

It is the aim of "Advances in Dielectrics" to reflect this rapid progress with a series of monographs devoted to specialized topics.

Target Group

Solid state physicists, molecular physicists, material scientists, ferroelectric scientists, soft matter scientists, polymer scientists, electronic and electrical engineers.

More information about this series at http://www.springer.com/series/8283

Tiberio A. Ezquerra · Aurora Nogales
Editors

Crystallization as Studied by Broadband Dielectric Spectroscopy

Springer

Editors
Tiberio A. Ezquerra
Departamento de Física Macromolecular,
Instituto de Estructura de la Materia (IEM)
Consejo Superior de Investigaciones
Científicas (CSIC)
Madrid, Spain

Aurora Nogales
Departamento de Física Macromolecular,
Instituto de Estructura de la Materia (IEM)
Consejo Superior de Investigaciones
Científicas (CSIC)
Madrid, Spain

Preface

When a material is cooled down below the melting temperature, it either remains in the amorphous state or it may (at least partially) crystallize. In both cases, the molecular dynamics is dramatically modified. For glassy systems, the primary relaxation (dynamic glass transition) slows down by typically 12 orders of magnitude. In contrast, if crystallization takes place, the relaxation strength shows a sudden reduction and often an additional process is observed reflecting the constrained dynamics of the molecules or polymer segments at the surface of the crystallites. It is evident that broadband dielectric spectroscopy is a versatile tool to study such systems if polar moieties are involved.

With the present volume of *Advances in Dielectrics*, the editors aim to demonstrate the potential of broadband dielectric spectroscopy in both fundamental and applied researches on crystallization.

The editors are thankful to all contributors to this volume for the pleasant and effective collaboration. Support from Springer Company and Series Editor, F. Kremer, is gratefully acknowledged.

Madrid, Spain   Tiberio A. Ezquerra
February 2020   Aurora Nogales

Contents

General Concepts of Crystallization: Some Recent Results and Possible Future Developments

Jürn W. P. Schmelzer and Christoph Schick

Abstract Classical nucleation theory is till now the major tool in the interpretation of crystal nucleation and growth processes in a variety of liquids. For its application, the knowledge of the thermodynamic driving force and the dependence of the surface tension on pressure and temperature, respectively, the knowledge of relations describing the curvature dependence of the surface tension is required. New developments in this direction are summarized in the first part of the present chapter. Based on these results, in a second part, the interplay of stress evolution and stress relaxation and its effect on nucleation and growth are analyzed. It is shown then in a third part, in which directions classical nucleation theory has to be extended possibly in the future development in order to arrive at a satisfactory description of experimental data in the whole range of temperature and/or pressure. Particular attention is directed here, in this respect, to deviations of the properties of critical clusters as compared to the properties of the evolving macroscopic phases and different aspects of the interplay of glass transition and crystallization. These general considerations are supplemented by an analysis of some specific features of polymer crystallization completing the present chapter.

Keywords Glass · Crystal nucleation · Crystal growth · Diffusion · Viscosity · Decoupling · Fragility

J. W. P. Schmelzer (✉) · C. Schick
Institute of Physics, University of Rostock, Albert-Einstein-Strasse 23-25, 18059 Rostock, Germany
e-mail: juern-w.schmelzer@uni-rostock.de

C. Schick
e-mail: christoph.schick@uni-rostock.de

C. Schick
Kazan Federal University, Kremlyovskaya str. 18, Kazan 420008, Russian Federation

Abbreviations

k_B	Boltzmann constant
$\Delta g(T, p)$	Change of the Gibbs free energy in crystallization per unit volume of the newly evolving crystalline phase
μ_i	Chemical potential of the $i = 1, 2, \ldots, k$ components
Δv	Differences of the volumes between liquid and crystal phases per unit volume of the crystal phase
D	Diffusion coefficient
$\Phi(\varepsilon)$	Energy of elastic deformation caused by the formation of a crystallite of volume V in a liquid
α_p	Isobaric thermal expansion coefficient
κ_T	Isothermal compressibility
τ_R	Maxwell's relaxation time
$\Delta s_m, \Delta h_m$	Melting entropy and melting enthalpy per unit volume of the crystal phase
x_i	Molar fraction of the $i = 1, 2, \ldots, k$ components
η	Newtonian viscosity
c	Number of nucleation centers per unit volume of the liquid
n_c, V_c	Number of particles and volume of a critical crystal cluster
$\varepsilon, \varepsilon_0$	Parameters determining the elastic effects caused by crystal evolution in the liquid (ε) and in a Hookean solid (ε_0)
J_0	Pre-factor in the expression for the steady-steady-state nucleation rate determined by the kinetics of crystal evolution
p, p_m	Pressure, melting pressure
R, A, V	Radius, volume, and surface area of a crystal cluster
d_0	Size parameter of the particles of the liquid
c_p	Specific heat per unit volume of the crystal phase
J	Steady-state nucleation rate
σ	Surface tension referred to the surface of tension
T, T_m	Temperature, melting temperature
t	Time
τ_{ns}	Time-lag in nucleation
δ	Tolman parameter
W_c	Work of critical cluster formation

1 Introduction

Classical nucleation theory (CNT) is till now the major tool for the interpretation of experimental data on nucleation in a wide spectrum of phase transformation processes like condensation and boiling, segregation in solid and liquid solutions, melting or crystallization [1–6]. In a variety of applications, it allows one not only a qualitative

treatment of experimental data of nucleation and growth kinetics but even a quantitatively correct description, in other cases, it may fail even dramatically. Consequently, the question arises on how these problems can be explained and overcome, what the origin is for the success of CNT in some and its failure in other cases. These problems are considered here in detail starting with some recently obtained results and directing then the attention to problems we consider as highly perspective in the further development of theoretical and experimental analysis of crystal nucleation and growth. The general considerations are supplemented by a section dealing with selected specific features of polymer crystallization.

2   Classical Nucleation Theory

2.1   *Thermodynamic Driving Force of Crystallization in Dependence on Temperature and Pressure*

One of the basic ingredients in the application of classical nucleation theory to the description of experimental data consists of the appropriate specification of the work, W_c, of critical cluster formation in nucleation:

$$W_c = \frac{1}{3}\, \sigma A, \, A = 4\pi R^2, \, \left(p_\beta - p_\alpha\right) + \sigma \frac{\mathrm{d}A}{\mathrm{d}V} = 0 \tag{1}$$

where σ is the surface tension, A is the surface area of a critical cluster supposed to be of spherical shape with a radius R corresponding to the surface of tension, p is the pressure and V is the volume, the indices α and β specify the parameters of the critical crystal clusters (α), respectively, the parameters of the ambient phase (β) where the aggregates of the new phase are formed. W_c determines widely the probability of formation of a supercritical cluster of the newly evolving phase capable to a further deterministic growth, respectively, the steady-state nucleation rate, J:

$$J = J_0 \exp\left[-\frac{W_c}{k_B T}\right] \tag{2}$$

The steady-state nucleation rate is equal to the number of critical clusters formed per unit time in a unit volume of the ambient phase. Here k_B is the Boltzmann constant, T is the absolute temperature.

Critical crystallites are, in general, not of spherical but of different shapes, anyway, also crystallization can be described in terms of the above given simplified model as explained in detail in [7]. In brief, for any state of the ambient phase the pressure in the critical cluster is determined by the equilibrium conditions. It follows that for any value of the work of critical cluster formation, it is always possible to determine

via Eq. 1 the value of the surface tension and the radius of the critical model cluster leading to this particular value of W_c. We will utilize this simplified model here.

The pre-factor, J_0, in the expression for the steady-state nucleation rate, Eq. 2, is determined by the kinetic mechanism of aggregation. For one-component systems, it can be expressed via the diffusion coefficients, D, of the particles in the melt or—employing the Stokes–Einstein–Eyring relation connecting diffusion coefficient and the inverse of the viscosity—via the Newtonian viscosity, η. One of the standard expressions for this kinetic pre-factor widely equivalent to other formulations is [6]:

$$J_0 = c \sqrt{\frac{\sigma}{k_B T}} \left(\frac{D}{d_0} \right) \cong c \frac{\sqrt{\sigma k_B T}}{\eta d_0^2} \tag{3}$$

where d_0 is a parameter specifying the size of the particles and c is the number of centers of nucleation per unit volume or the particle number density in the liquid. In the application of above relations to crystallization in multi-component systems, these kinetic parameters have to be replaced by effective diffusion coefficients, respectively, effective size parameters [6, 10]. Similarly to nucleation rates, also the growth rates are determined via the thermodynamic driving force and the kinetic parameters as discussed above. To some extent, the description of growth processes is easier since size effects in the bulk properties can be frequently neglected and also the surface tension plays, at least, in a variety of cases a minor role.

Here, we concentrate the attention to thermodynamic aspects of nucleation theory connected with the determination of the work of critical cluster formation. According to Eq. 1, we have to have at our disposal the thermodynamic driving force of crystallization, expressed by the difference of pressures, $p_\alpha - p_\beta$, in the critical cluster and the ambient phase (or widely equivalent to it and more easily accessible expressions) and the surface tension, σ. Employing the basic assumptions of CNT, we will formulate below first the dependencies for both quantities on external pressure and temperature.

Equation 1 is a consequence of Gibbs classical thermodynamic theory of surface phenomena [8]. In line with his approach, it is supposed in CNT that the bulk properties of the critical clusters are widely identical to the properties of the newly evolving macroscopic phases [5, 6, 9]. This statement is a conclusion from the analysis of consequences of a subset of Gibbs' equilibrium conditions (equality of chemical potentials, μ_i, of the different components and temperature, T):

$$\mu_{i\alpha}\left(T_\alpha, p_\alpha, \{x_{j\alpha}\}\right) = \mu_{i\beta}\left(T_\beta, p_\alpha, \{x_{j\beta}\}\right), \quad i = 1, 2, \ldots, k$$
$$T_\alpha = T_\beta \tag{4}$$

In such treatment, the thermodynamic driving force of crystallization can be expressed via the change of the Gibbs free energy per unit volume of the newly evolving crystalline phase as:

$$p_\alpha - p_\beta \cong \Delta g(T, p)$$

$$\Delta g(T, p) = \sum_{i=1}^{k} \rho_{i\alpha} \left(\mu_{i\beta}(T, p, \{x_{i\beta}\}) - \mu_{i\alpha}(T, p, \{x_{i\alpha}\}) \right) \tag{5}$$

Accounting in addition to the assumed independence of the properties of the critical clusters on pressure and temperature, for both stoichiometric and non-stoichiometric crystallization, the thermodynamic driving force can be written then as:

$$\Delta g(T, p) \cong \Delta h_m \left(\frac{T_m - T}{T_m} \right) \left[1 - \gamma_T(T_m, p_m) \frac{(T_m - T)}{2 T_m} \right]$$
$$+ p_m \Delta v_m \left(\frac{p - p_m}{p_m} \right) \left[1 - \gamma_p(T_m, p_m) \frac{(p_m - p)}{2 p_m} \right] \tag{6}$$

Here (T_m, p_m) are temperature and pressure at a particular equilibrium state along the melting curve. Specific properties of the system under consideration are reflected here by the melting entropy, Δs_m, or the melting enthalpy, Δh_m, and the differences of the volumes between liquid and crystal phases per unit volume of the crystal phase:

$$\Delta s(T, p) = \frac{S_{\text{liquid}}(T, p, \{x_{i\beta}\}) - S_{\text{crystal}}(T, p, \{x_{i\alpha}\})}{V_{\text{crystal}}(T, p, \{x_{i\alpha}\})}$$

$$\Delta v(T, p) = \frac{V_{\text{liquid}}(T, p, \{x_{i\beta}\}) - V_{\text{crystal}}(T, p, \{x_{i\alpha}\})}{V_{\text{crystal}}(T, p, \{x_{i\alpha}\})} \tag{7}$$

The parameters γ_T, and γ_p are defined via:

$$\gamma_T(T_m, p_m) = \frac{\Delta c_p(T_m, p_m)}{\Delta s_m}, \quad \gamma_{Tp}(T_m, p_m) = \frac{p_m \Delta \kappa_T(T_m, p_m)}{\Delta v_m} \tag{8}$$

Here c_p is the specific heat per unit volume and κ_T is the isothermal compressibility, given by:

$$c_p = T \left(\frac{ds}{dT} \right)_p, \quad \Delta c_p(T_m, p_m) = c_p^{(\text{liquid})}(T_m, p_m) - c_p^{(\text{crystal})}(T_m, p_m)$$

$$\kappa_T = -\frac{1}{V} \left(\frac{dV}{dp} \right)_T, \quad \Delta \kappa_T(T_m, p_m) = \kappa_T^{(\text{liquid})}(T_m, p_m) - \kappa_T^{(\text{crystal})}(T_m, p_m) \tag{9}$$

Employing these results and the basic relations utilized in their derivation, it has been shown by us that at the Kauzmann temperature [11], corresponding to states where the specific entropies of glass-forming melt and crystal coincide, the thermodynamic driving force has a maximum in dependence on temperature. In addition, similarly to the mentioned well-known notation of a Kauzmann temperature, the

concept of a Kauzmann pressure [12] can be introduced for crystallization induced by variations of pressure. It is shown that the thermodynamic driving force of crystal nucleation has similarly maxima also at the Kauzmann pressure. Further, it is demonstrated that—as far as mentioned basic assumptions of CNT are fulfilled—in melt crystallization, a spinodal curve does not exist. In addition, it is shown that—in contrast to some recent statements—Kauzmann's suggestion of a pseudo-spinodal in melt crystallization characterized by intensive nucleation has no foundation [13–15]. Finally, setting in Eq. 6 the thermodynamic driving force equal to zero, we obtain an analytic expressions for the dependence of pressure on temperature or vice versa along the melting curve.

2.2 Surface Tension in Dependence on Temperature and Pressure

In the application of CNT to melt crystallization one very serious problem consists in the limitations caused by the fact that the surface tension melt-crystal cannot be determined directly experimentally with the accuracy required in nucleation theory. By this reason, in applications of CNT frequently the Stefan-Skapski-Turnbull relation is employed for its determination [5, 6]. In its standard so far application, it involves the assumption of the capillarity approximation, i.e., that the surface tension of critical clusters is equal to the respective value of equilibrium coexistence of both phases at a planar interface. However, the application of the capillarity approximation leads to serious problems in CNT [16]. They can be overcome by introducing a curvature dependence of the surface tension as suggested already by Gibbs [8] and widely employed in CNT. Based on a generalization of the Stefan–Skapski–Turnbull equation, a relation for the dependence of the surface tension on pressure and temperature has been derived by us [12, 17, 18]. Here we reproduce the basic results.

According to cited analysis, the dependence of the surface tension on temperature and pressure can be expressed as:

$$\frac{\sigma(T, p)}{\sigma(T_m, p_m)} \cong \frac{T}{T_m}\left(1 - \gamma_T(T_m, p_m)\frac{T_m - T}{T_m} - \frac{\Delta\alpha_p(T_m, p_m)}{\Delta s_m}(p - p_m)\right) \quad (10)$$

where α_p is the isobaric thermal expansion coefficient:

$$\alpha_p = \frac{1}{V}\left(\frac{dV}{dT}\right)_p, \quad \Delta\alpha_p(T_m, p_m) = \alpha_T^{(\text{liquid})}(T_m, p_m) - \alpha_T^{(\text{crystal})}(T_m, p_m) \quad (11)$$

It follows that in crystallization caused by variation of temperature, the surface tension decreases with decreasing temperature. A similar behavior is found for crystallization caused by variations of pressure. These theoretical predictions are in excellent agreement with a variety of experimental investigations and molecular dynamics

studies as discussed in detail in [7, 12, 17–19]. Again, employing the relation for the dependence of pressure on temperature along the melting curve obtained as described above based on Eq. 6, Eq. 10 results in an expression for the determination of the surface tension along the melting curve.

Quite frequently, the dependence of the surface tension of critical clusters is treated not in terms of its dependence on pressure and temperature as expressed by above given relation but in dependence on the size of the critical clusters or its curvature. A first relation in this respect has been derived already by Gibbs [8] in application to condensation. It was advanced later by Tolman [20] resulting in an equation of the form:

$$\sigma(R) = \frac{\sigma_\infty}{1 + \frac{2\delta}{R}}, \quad \sigma_\infty = \sigma_\infty(T_m, p_m), \quad \delta = \delta_\infty(T_m, p_m) \tag{12}$$

Here δ is the Tolman parameter. In accordance with its original definition by Tolman, it has to be considered as a property of the interface liquid-solid for an equilibrium coexistence of both phases at a planar interface, i.e., $\delta = \delta_\infty(T_m, p_m)$ is a function of melting pressure and temperature, $\sigma = \sigma_\infty(T_m, p_m)$ is the value of the surface tension for the respective state. However, both Gibbs [8] and Tolman [20] did not consider phase formation caused by variation of temperature but by variation of pressure. As mentioned by Tolman: "*We shall be concerned with the effect of changes in radius on surface tension in the case of droplets and vapor composed of a single substance maintained at some given constant temperature.*" Consequently, strictly speaking, it was not clear so far whether the Tolman equation can be really utilized at all for the description of melt crystallization if the process is caused by variations of temperature. This open problem was resolved by us in two recent publications [7, 19].

It was shown that the Tolman equation can be employed for the description of the curvature dependence of the surface tension of critical crystallites in one-component systems if either pressure or temperature is varied. This relation holds also for crystallization in multi-component systems provided the composition and shape of the critical crystal clusters do not change in dependence on pressure and temperature. As discussed here earlier this independence of the properties of critical clusters on pressure and temperature is a basic assumption of CNT. Consequently, employing basic ideas of CNT, the Tolman equation is a quite appropriate tool for the description of the curvature dependence of the surface tension of critical crystallites if either pressure or temperature is changed. However, the values of the Tolman parameter differ for both cases and are given by:

$$\delta_\infty^{(T)} \cong \sigma_\infty \left\{ \frac{1 + \gamma_T(T_m, p_m)}{\Delta h_m} \right\} \quad \text{at} \quad p = p_m \tag{13}$$

respectively:

$$\delta_\infty^{(p)} \cong \sigma_\infty \left\{ \frac{T_m \Delta \alpha_p(T_m, p_m)}{\Delta v_m \Delta h_m} \right\} \quad \text{at} \quad T = T_m \tag{14}$$

As shown in [7, 19], these estimates are in good quantitative agreement with data obtained via a fit of experimental results on steady-state nucleation rates for a variety of systems. However, as demonstrated there as well, if both temperature and pressure are varied, then the Tolman equation cannot be employed for the description of the curvature dependence of the surface tension.

Above relations for the thermodynamic driving force and the surface tension are formulated here for multi-component systems. For one-component systems, similar but slightly more precise relations can be derived avoiding one assumption required in the analysis of multi-component systems (for the details see [19]).

The application of CNT to the description of crystal nucleation shows that the classical concepts as described above and supplemented by the account of a curvature dependence of the surface tension allow one an accurate description of nucleation rates down to temperatures corresponding to the maximum of the steady-state nucleation rates. However, they fail at temperatures lower this maximum. In the next subsection, we will discuss another topic where a quite similar situation is observed.

2.3 Stress Evolution and Stress Relaxation and the Crystallization of Glass-Forming Melts

In cooling and/or at variation of pressure, liquids may undergo a glass transition, i.e., go over from a liquid to a solid state. This transformation can be expected to have also a significant effect both on crystal nucleation and growth.

One of the factors affecting crystallization and varying in the course of the glass transition is connected with the evolution of elastic stresses. This effect of elastic stresses in crystallization is caused frequently by differences of the specific volumes in the crystal and liquid phases. While in liquids elastic stresses cannot have any effect on nucleation due to its fast relaxation, they are expected to occur in the glass transition region and, in particular, below the glass transition temperature with magnitudes corresponding to the respective values for phase formation in Hookean solids. In [21, 22], it was shown for a variety of glass-forming melts that in latter case elastic stresses may considerably reduce the thermodynamic driving force of crystallization and even prevent crystallization at all. It was demonstrated, in addition, that such inhibiting nucleation elastic stress effects are considerably smaller near interfaces giving immediately a new general key to the understanding of the observed often preferential surface crystallization of glasses.

Elastic stresses evolving as the result of crystal nucleation and growth are reduced by relaxation processes. Consequently, the proper description of the interplay of stress evolution and stress relaxation is of outstanding significance for the understanding of crystal nucleation and growth. An overview of different results in this respect is given in [6]. Here we concentrate on the effect of the interplay of stress evolution and stress relaxation in crystal nucleation in the form as advanced first in [23, 24]. Below we present the basic ideas of this approach.

Accounting for the evolution of elastic stresses in crystallization, the change of the Gibbs free energy is given approximately by:

$$\Delta G \cong -V\Delta g + \sigma A + \Phi^{(\varepsilon)}, \quad \Phi^{(\varepsilon)} = \varepsilon V \tag{15}$$

The radius of the critical crystal cluster and the work of critical cluster formation have then the form:

$$R = \frac{2\sigma}{\Delta g - \varepsilon}, \quad W_c = \frac{16\pi}{3}\frac{\sigma^3}{(\Delta g - \varepsilon)^2} \tag{16}$$

Accounting in the simplest approach for relaxation via Maxwell's law (generalizations are studied in cited papers) with a relaxation time, τ_R, the change of the total energy of elastic deformation connected with the formation of a crystal of volume V in the liquid is given by:

$$\frac{d\Phi^{(\varepsilon)}}{dt} = -\frac{1}{\tau_R}\Phi^{(\varepsilon)} + \varepsilon_0\frac{dV}{dt} \tag{17}$$

Here ε_0 describes the parameters for stress evolution in a Hookean solid neglecting stress relaxation. Supplementing this relation by an appropriate expression for the crystal growth rate, one can then immediately analyze the effect of the interplay of evolution of elastic stresses and stress relaxation on this process.

However, in application of these ideas to nucleation, an additional question arises: How can one express the rate of growth of a cluster in its approach to the critical cluster size taking into account that this type of evolution is a stochastic process proceeding against macroscopic thermodynamic evolution laws. In [23, 24], we suggested to replace the growth rate via the relation $(dV/dt) \approx (V_c/\tau_{ns})$ resulting in:

$$\frac{dV}{dt} \cong \frac{V_c}{\tau_{ns}} \Rightarrow \frac{d\Phi^{(\varepsilon)}}{dt} \cong -\frac{1}{\tau_R}\Phi^{(\varepsilon)} + \varepsilon\frac{V_c}{\tau_{ns}} \tag{18}$$

Here τ_{ns} is the so-called time-lag in nucleation [6]. It is a measure of the time required to establish steady-state nucleation in a system consisting originally only of monomers. This quantity was introduced by Zeldovich [25] expressing the nucleation rate in the form:

$$J = J_0 \exp\left(-\frac{\tau_{ns}}{t}\right) \exp\left(-\frac{W_c}{k_B T}\right) \qquad (19)$$

The solution of Eq. 18 leads the following relation for the parameter $\varepsilon(n_c)$ being the result of the interplay of stress evolution and stress relaxation:

$$\frac{\varepsilon(n_c)}{\varepsilon_0} \cong \frac{\tau_R}{\tau_{ns}}\left(1 - \exp\left(\frac{\tau_{ns}}{\tau_R}\right)\right) \qquad (20)$$

Here n_c is the number of particles in a critical crystallite. Consequently, the effect of elastic stresses on crystal nucleation is essentially determined by the parameter $\theta = (\tau_{ns}/\tau_R)$.

Employing the standard model of aggregation kinetics resulting in Eq. 3, we arrive at the following relation for the time-lag and the Maxwellian relaxation time:

$$\tau_{ns} \cong \omega \frac{k_B T}{\sigma D} n_c^{2/3} \cong \omega \frac{\eta d_0}{\sigma} n_c^{2/3}, \quad \tau_R \cong \frac{\eta d_0^3}{k_B T} \qquad (21)$$

Here ω is a parameter of the order $\omega \approx 1$–4 in dependence on the assumptions made in the derivation of Eq. 21. Equation 21 yields:

$$\theta = \frac{\tau_{ns}}{\tau_R} \cong \omega \frac{k_B T}{\sigma d_0^2} n_c^{2/3} \qquad (22)$$

Utilizing the capillarity approximation in the interpretation of experimental data on crystal nucleation, i.e., assuming that the surface tension is equal to its value for a planar interface melt-crystal, it turns out that this ratio is of the order $\theta = (10^2$–$10^3)n_c^{2/3}$ [6, 26]. Provided this result would be true, then the relaxation time would be always much smaller as compared with the time-lag in nucleation and elastic stress effects would be always eliminated by relaxation. Such kind of behavior is in conflict with the general considerations on stress effects in glass transition formulated above. Moreover, as also already noted, the capillarity approximation leads to severe problems in application of CNT to crystallization, consequently, it has to be modified by a more correct approach involving a curvature dependence of the surface tension.

A detailed analysis shows [13–15] that, accounting for the curvature dependence of the surface tension, (i) in the range, where elastic stresses may affect nucleation, the average time of formation of a crystallite is determined by the time-lag, τ_{ns}. Near to the maximum of the steady-state nucleation rate (correlating widely with the standard glass transition temperature as defined by Tammann), the ratio $\theta = (\tau_{ns}/\tau_R)$ approaches typically values of the order of one. Consequently, elastic stresses may have an effect on crystal nucleation in highly viscous glass-forming melts.

However, extending the computations to temperatures considerably below the maximum of the steady-state nucleation rate, the parameter $\theta = (\tau_{ns}/\tau_R)$ does not tend to zero. Consequently, utilizing CNT and even accounting for a curvature dependence of the surface tension, we do not arrive at low temperatures in the interplay of stress

evolution and relaxation at the limiting case of Hookean solids as we did expect it from above mentioned general considerations. Obviously, some other factors have to be accounted for if one would like to obtain the correct limiting behavior. We will return to this problem here somewhat later.

3   Some Other Topics of Current Interest

Utilizing CNT and the described above methods, several other topics have been addressed in recent years, in particular, (i) the specification of the location of the maxima of nucleation and growth rates and the rates of overall crystallization both for temperature and pressure-induced phase formation [27, 28], (ii) the relevance of fragility concepts and the glass transition temperature for the understanding of crystallization in glass-forming melts [29], (iii) the effects of decoupling of diffusion and viscosity on crystallization, in general, and crystal growth, in particular [30], (iv) the analysis of the relation between the average time of formation of the first supercritical nucleus, the time-lag in nucleation, and the steady-state nucleation rate [31]. In [27, 28], a set of equations for determining temperature or pressure of the maximum nucleation, growth, and overall crystallization rates of glass-forming liquids is derived and analyzed. In [29], it is shown that the classical fragility concepts can be of relevance for the understanding of crystallization only if several severe conditions are fulfilled which are rarely met. However, a modification of the classical definition of fragility is shown to turn out to be highly useful in application to crystallization. In addition, general relations are derived correlating the maximum of the crystal nucleation rate and the glass transition temperature in its conventional definition as proposed long ago by Tammann (T_g corresponding to a viscosity 10^{12} Pa s). In [30], a relation is derived allowing one to correlate the decoupling temperature with the glass transition temperature and the fragility of the liquid. All results are confirmed by experimental data. In [31], general expressions are derived for the description of the correlations between average time of formation of the first supercritical nucleus, time-lag in nucleation, and the steady-state nucleation rate. The results have been employed by us in the proof of the absence of a pseudo-spinodal in melt crystallization performed in [13–15]. The existence of a pseudo-spinodal in melt crystallization characterized by intensive nucleation processes was suggested by Kauzmann [11] as a possible way of resolution of the Kauzmann paradox. It is discussed widely up to now and was recently even denoted as "*another vital concept related to supercooled liquids, which is not known within the glass research community*" [32]. Consequently, the analysis of this topic and the proof of the absence of such pseudo-spinodal curve with the properties assigned to it by Kauzmann are not merely of historical interest. The results obtained in [31] have been employed also in the analysis of the interplay between stress development and stress relaxation in crystallization of highly viscous glass-forming melts. In particular, it gives a confirmation of the basic assumption, Eq. 18, utilized in the analysis of the interplay of stress evolution and stress relaxation.

The present subsection we would like to complete with the brief analysis of another question posed by Adrjanowicz et al. [33, 34] and, as far as we know, not having found a definite answer so far. Adrjanowicz et al. [33, 34] made a variety of efforts to study so-called by them isochronal crystallization. By definition, this notation describes the procedure of varying pressure and temperature in such a way that the viscosity remains constant. This approach is a modification of a method used widely in the analysis of crystal nucleation where by measuring both steady-state nucleation rates and the time-lag, kinetic coefficients can be eliminated in the theoretical analysis of nucleation processes (see, e.g., [16]). In the analysis, it has been found by mentioned authors that for such type of variation of the external control parameters (temperature and pressure) the thermodynamic driving force remains nearly constant. We would like to sketch here how this problem can be understood in terms of CNT.

Indeed, in accordance with the definition of isochronal crystallization, the variation of viscosity caused by the change of temperature and pressure in such process is equal to zero, i.e.:

$$d\eta = \left(\frac{d\eta}{dT}\right)_p dT + \left(\frac{d\eta}{dp}\right)_T dp = 0 \tag{23}$$

It follows that any change of temperature is accompanied by a change of pressure given by:

$$\left.\frac{dp}{dT}\right|_{\text{isochronal}} = -\frac{\left(\frac{d\eta}{dT}\right)_p}{\left(\frac{d\eta}{dp}\right)_T} \tag{24}$$

The change of the thermodynamic driving force of crystallization in such isochronal processes is given then by:

$$\left.\frac{d\Delta g}{dT}\right|_{\text{isochronal}} = \left(\frac{d\Delta g}{dT}\right)_p + \left(\frac{d\Delta g}{dp}\right)_T \left.\frac{dp}{dT}\right|_{\text{isochronal}} \tag{25}$$

With Eq. 24, we obtain:

$$\left.\frac{d\Delta g}{dT}\right|_{\text{isochronal}} = \left(\frac{d\Delta g}{dT}\right)_p - \left(\frac{d\Delta g}{dp}\right)_T \frac{\left(\frac{d\eta}{dT}\right)_p}{\left(\frac{d\eta}{dp}\right)_T} \tag{26}$$

As the rule, the following inequalities hold [35]:

$$\left(\frac{d\Delta g}{dT}\right)_p < 0, \left(\frac{d\eta}{dT}\right)_p < 0, \left(\frac{d\Delta g}{dp}\right)_T > 0, \left(\frac{d\eta}{dp}\right)_T > 0 \tag{27}$$

It follows that the two terms in the right-hand side of Eq. 26 are of different signs. Utilizing in addition the relation [36]:

$$\left(\frac{d\eta}{dp}\right)_T = -\frac{\kappa_T(T, p)}{\alpha_T(T, p)}\left(\frac{d\eta}{dT}\right)_p \tag{28}$$

we obtain with Eq. 6:

$$\left.\frac{d\Delta g}{dT}\right|_{isochronal} = -\frac{\Delta h_m}{T_m} + \Delta v_m \frac{\kappa_T(T, p)}{\alpha_{Tp}(T, p)} \tag{29}$$

Consequently, if for the systems under consideration Eq. 29 yields values of the derivative nearly equal to zero, the mentioned result posed by Adrjanowicz et al. [33, 34] is easily understandable in terms of CNT and does not require any assumptions going beyond it. A detailed analysis of this topic in application to the systems studied by mentioned authors we consider as highly interesting.

4 Beyond Classical Nucleation Theory: Some Possible Directions of Its Further Development

In order to describe quantitatively correctly experimental data in the whole range of pressure and temperature, several generalizations of classical concepts have been advanced like the decoupling of diffusion and viscosity (or relaxation), the effect of the size of the "structural units" on crystallization, the possible effect of heterogeneous structure of glass-forming liquids on crystal nucleation, the account of deviations of the properties of critical clusters from the properties of the newly evolving stable or metastable macroscopic phases, the account of deviations of the state of the glass-forming melt from metastable equilibrium states. In the present section, we will discuss some of them in more detail.

4.1 Properties of Critical Clusters Versus Properties of the Newly Evolving Macroscopic Phases

One of the basic assumptions of CNT supported by Gibbs' theory consists of the assumed independence of the properties of critical clusters on the degree of deviation from equilibrium. This assumption is in a variety of cases in conflict with alternative theoretical approaches like density functional computations, computer simulations, and experimental data [37, 38]. It has been questioned immediately after the formulation of CNT and attempted to be overcome inside the framework of Gibbs theory (Scheil, Hobstetter, see [6, 39, 40]). This critique finally led then to the rediscovery of

density functional approaches of determination of the properties of critical clusters by methods originally developed by van der Waals. As it turned out, the properties of critical clusters and the size of the critical clusters as determined via density functional computations first by Hillert, Cahn, and Hilliard are quite different as compared to the results obtained via the classical Gibbs method. Consequently, the problem arises which of the theories is correct and which one has to be abandoned, respectively, generalized.

This problem in the theoretical description can be overcome by generalizing the classical Gibbs' approach as performed by us in the last two decades [6, 18, 41, 42]. Utilizing the generalized Gibbs approach the thermodynamic driving force of crystallization is given instead of Eq. 5 by:

$$p_\alpha - p_\beta = \Delta g\big(T_\alpha, p_\alpha, \{x_{i\alpha}\}; T_\beta, p_\beta, \{x_{i\beta}\}\big) \tag{30}$$

The properties of the critical clusters can be determined in this approach by relations similar to Eq. 4, however, being of much more complex form. It requires, in addition to Eq. 3, expressions for the dependence of the surface tension on the state parameters of both coexisting phases. By this reason, the possibility of application of the generalized Gibbs approach to a detailed quantitative description of crystallization has been opened only recently with the development of expressions for the surface tension utilizing the Stefan-Skapski-Turnbull as formulated first in [17]. However, already the assumption that the critical crystallites have different as compared to the macroscopic phases bulk properties allowed us to resolve a number of problems in the interpretation of experimental which were not possible to understand in terms of CNT [8, 37, 38].

The generalized Gibbs approach has been employed widely so far by us to the interpretation of nucleation and growth processes in condensation and boiling and of segregation in multi-components solutions. It demonstrates that composition and (in application to crystal nucleation) the shape of the critical crystal clusters may depend significantly on the degree of metastability caused by variations of pressure and/or temperature. As shown the results obtained via the generalized Gibbs approach are in full agreement with predictions of density functional computations. In particular, it is shown that nucleation for segregation in solutions does not proceed via the classical scenario but via a scenario resembling widely spinodal decomposition processes. In addition, it has been proven that the classical Gibbs method involving the capillarity approximation overestimates the work of critical cluster formation and underestimates the values of the steady-state nucleation rate [41]. Indeed, once there is an additional freedom in the choice of the bulk properties of critical crystallites, they will be selected in such a way as to result in the lowest possible values of the work of critical cluster formation. This idea was the starting point in the development of the generalized Gibbs approach [6]. Consequently, the proper account of such dependence of the critical cluster properties on the degree of metastability of the liquid can be considered as one perspective direction of future development of the theory of crystallization [18, 43, 44]. In advance to such development, we could recommend always to check whether different models of crystal nucleation really refer to

properties of critical clusters as described in terms of Gibbs theory, Eq. 4, or are governed by more advanced relations. Such analysis could supply us possibly with additional suggestions concerning the applicability of CNT, respectively, its limits in application to crystal nucleation.

4.2 Interplay of Crystallization and Glass Transition

Deviations of the properties of critical clusters as compared with the properties of the evolving macroscopic phases can be found frequently in different types of phase transformation processes. Going beyond such general type of behavior, crystallization is characterized by an additional particular feature which may be denoted as interplay of crystallization and glass transition. Here a variety of problems can be distinguished [45], we will concentrate on only some of them. As the starting point, we take an experimental fact observed first around 1980 [46] which turned out in the course of subsequent studies to be a very general phenomenon, an unexpected type of dependence of the work of critical cluster formation on temperature [16, 18, 44].

Mentioned result is found based on measurements of both steady-state nucleation rate and time-lag in nucleation. The time-lag can be described theoretically in terms of CNT by Eq. 21. Utilizing this relation, one can replace it in the pre-exponential term in Eq. 3 diffusion coefficient or viscosity by the time-lag. Having at one's disposal both parameters, steady-state nucleation rate, and time-lag data, one can then determine via Eq. 2 how the work of critical cluster formation depends on temperature (or pressure if the respective measurements will be performed). In line with CNT, it decreases with decreasing temperature starting at the melting or liquidus temperature but this decrease is observed only down to temperatures corresponding to the maximum of the steady-state nucleation rate (or the conventional glass transition temperature). With a further decrease of temperature, the work of critical cluster formation increases then again in contradiction to expectations based on CNT.

In [46], such behavior was interpreted originally as a consequence of a similar temperature dependence of the surface tension. This interpretation is followed by some authors till now but can be hardly given a foundation in terms of Gibbs' classical theory of capillarity [16–18]. In addition, it contradicts a variety of measurements showing a decrease of the latent heat of melting with the size of the crystallites and general rules like the principle of le Chatelier-Braun: With an increase of the degree of metastability, the surface tension is expected to decrease to favor nucleation processes counteracting the mentioned increase of the level of deviation from equilibrium.

For this reason, other factors have been analyzed with respect to the question whether they allow one to interpret the described above behavior. In a first such attempt [16], it was checked whether elastic stresses evolving as the result of critical cluster formation may be responsible for the observed increase of the work of critical cluster formation. Utilizing the theoretical concepts derived in terms of CNT sketched briefly here earlier it turns out that stresses do have an effect but it is not sufficient for an explanation of the experimental data. In a next study [47], in order to reconcile

experimental data and CNT, we assumed an increase of the size, d_0, of the structural units that control nucleation with decreasing temperature for temperatures below the nucleation rate maximum, $T < T_{max}$. This hypothesis was tested for several glass-forming liquids, where crystal formation proceeds by bulk homogeneous nucleation. It can explain also the temperature dependence of the nucleation rate in the range $T < T_{max}$, where the description of nucleation rate by CNT drastically fails. The size of the structural units can be correlated either with the size of the cooperatively rearranging regions (CRR) or connected with an effective size parameter, accounting for corrections in the theoretical treatment of the kinetics of aggregation in multi-component systems via a quasi-one-dimensional description.

In a third approach [48], a model for the description of crystal nucleation is proposed incorporating into classical nucleation theory concepts of spatial hetero-geneity of glass-forming liquids. It is assumed that nucleation processes may proceed with detectable rates only in liquid-like (soft) regions and are suppressed in solid-like (rigid) parts. Determining appropriately the fraction of liquid-like, respectively, solid-like regions in dependence on temperature, this approach allows one to achieve a satisfactory agreement between classical nucleation theory and experiment not only at relatively high temperatures but also at temperatures lower than that of the nucleation rate maximum. The model was tested successfully on several silicate and polymer glasses revealing homogeneous volume nucleation. Some other phenomena in the interplay of crystallization and glass transition are also discussed in this analysis giving an independent verification of the validity of our basic assumption.

But there exists also another feature, we consider as so far not appropriately incor-porated into the theoretical description of crystallization if one would like to account appropriately for the interplay of crystal phase formation and glass transition. In the analysis of the theoretical description of stress development and stress relaxation it has been shown by us that the effect of elastic stresses on crystal nucleation depends basically on the ratio of the time-lag, the time to establish steady-state conditions in nucleation, and the Maxwellian relaxation time. For liquids, this ratio has to be consequently large to prevent the effect of elastic stresses. For glasses as frozen-in liquids, the opposite situation should be fulfilled, i.e., this ratio should tend to zero in order to obtain in the theory the limiting cases of a Hookean solid as a special limiting case. Accounting for a curvature dependence of the surface tension we arrived at the conclusion that near to the conventional glass transition temperature (corresponding to a viscosity 10^{12} Pa s) this ratio is of the order of one and has to tend to zero below the glass transition temperature.

However, once this is the case, another problem arises. In CNT, the thermodynamic driving force is computed as the difference between the bulk states of the system both in the crystalline states and the metastable liquid. As already mentioned, the critical crystal cluster may have, however, different properties as compared to the respective macroscopic crystal phase. But, in addition, once the mentioned ratio tends to zero, the initial state of the liquid will not refer to the metastable equilibrium state but to a particular non-equilibrium state realized in the course of cooling. Both the ther-modynamic driving force for crystal nucleation and the surface tension will depend

on such cases also on the degree of deviation of the liquid state from the respective metastable equilibrium state. The principal features how such dependence can be incorporated into the theory have been described in [49–51]. However, its implementation as a regular tool into the theory of crystal nucleation and growth is very far from a comprehensive realization. Accounting for the dependence of the relaxation time on the structural order parameter, in [50, 51] a possible origin of stretched exponential relaxation was described. In addition, it is shown that particular relaxation mechanisms distinguished already by Kauzmann [11] and recently reconfirmed to be of particular significance for dielectric relaxation can be explained in such model terms. Some more information and the discussion of some other topics related to crystallization of oxide glasses can be found in monographs [5, 6] and reviews [40, 52]. A detailed theoretical analysis of the effects of interplay of deviations of the liquid from metastable equilibrium and stress development and stress relaxation in crystal nucleation is presently in preparation.

5 Polymer Crystallization: Some Specific Features

Above described spectrum of achievements and problems is of interest independently on the particular system where crystallization is studied. Some specific problems of polymer crystallization will be described below. Generally, also polymer crystallization can be subdivided in primary nucleation and growth, similar to the systems described above. But due to the chain structure of the polymer molecules, particular situations exist for nucleation, growth, and for the crystalline morphologies developing.

From a thermodynamic point of view, the equilibrium configuration of a polymer chain in the crystalline state should be the extended chain. Commonly, this configuration is not realized for long-chain polymers because of entropic penalties. Polymer crystals generally represent non-equilibrium states usually referred to as folded chain crystals [53–56]. Only crystals containing fully stretched chains can be regarded as an equilibrium thermodynamic state. The occurrence of non-equilibrium folded states has its origin in the high internal conformational entropy of individual chains in the melt. Sommer et al. [57] made an estimate for the time needed to create a fully stretched chain made of 100 monomers by spontaneous fluctuations. The required time of 10^{58} s is obviously behind any practical relevance. As a consequence of chain folding lamellar, plate-like crystals with thickness of the order of 10 nm and lateral dimensions up to several ten μm are often formed. The lamellae are further arranged in lamellae stacks where the crystals are separated by amorphous layers of a few nm thickness and the stacks may form 100 μm sized spherulites.

Regarding the dielectric relaxation behavior, the lamellae stack morphology is of particular interest. Lamellae stacks comprise crystalline lamellae and amorphous layers in between [58]. The amorphous layer is often subdivided into a fraction participating in the segmental relaxation (glass transition) and another fraction not

participating in segmental relaxation even if is non-crystalline. The latter is called rigid amorphous fraction (RAF) [59, 60]. The RAF does not contribute to the glass transition (segmental relaxation) but to the secondary relaxations like the β-relaxation in polyethylene terephthalate [61].

Primary crystal nucleation in polymers shows some peculiarities as described, e.g., by Muthukumar [62]. Along one polymer chain (one molecule) several crystal nuclei may evolve. Due to their coupling through the polymer chain, these nuclei are not independent and there will be some competition between them. With the introduction of fast scanning calorimetry (FSC) [63] detailed kinetic studies of homogeneous nucleation in many polymers became feasible [38] and the often resulting nodular morphology (crystal size in the order of 10 nm) became accessible for relaxation studies [64].

Until now, there is a strong controversy regarding the question on how a polymer crystal lamella is growing. Several models were proposed. An early, widely applied model is the Hoffman-Lauritzen theory of polymer crystallization [65]. Nevertheless, the Hoffman-Lauritzen approach was frequently challenged and several competing theories were developed (for recent reviews see references [55–57, 66–70]). Consequently, also in this respect a broad spectrum of problems remains not finally settled.

6 Concluding Remarks

Once one is dealing with the theory of different phenomena in nature, one has also to realize for which purposes the respective analysis is made. The basic desire of experimenters attempting to apply the theory is that the theory should be as simple as possible. In contrast, theoreticians always recognize a variety of effects which may also be of importance tending to advance the theory making it more and more complex and, consequently, harder to apply. Albert Einstein suggested to make a compromise in this connection proposing that "*everything should be done as simple as possible but not simpler*". A foundation of the possibility to proceed in such way was also given by him stating "*subtle is the Lord but malicious he is not*". With respect to the description of crystallization, CNT with its basic assumptions and its development in different directions can be considered possibly as a realization of such compromise. However, thinking once again about these problems Einstein revised his opinion: "*I have thought about once again. Quite it could be that God is malicious*". Consequently, not the theoreticians are responsible for the trouble they sometimes cause the experimenters demanding and trying to advance a variety of partly principal improvements of CNT. Hopefully, these developments can be brought into a form similarly tractable in application to experiment as CNT provides it now but at a higher level.

References

1. Skripov VP, Metastable liquids, Nauka, Moscow, 1973; Wiley, New York, 1974
2. Baidakov VG (2007) Explosive boiling of superheated cryogenic liquids. Wiley-VCH, Berlin-Weinheim
3. Slezov VV (2009) Kinetics of first-order phase transitions. Wiley-VCH, Berlin-Weinheim
4. Gusak AM (2010) Diffusion-controlled solid-state reactions. WILEY-VCH, Berlin-Weinheim
5. Kelton KF, Greer AL (2010) Nucleation in condensed matter: applications in materials and biology. Pergamon, Amsterdam
6. Gutzow IS, Schmelzer JWP (2013) The vitreous state: thermodynamics, structure, rheology, and crystallization, First edn, Springer, Berlin, 1995; Second enlarged edn, Springer, Heidelberg
7. Schmelzer JWP, Abyzov AS, Ferreira EB, Fokin VM (2019) Curvature dependence of the surface tension and crystal nucleation in liquids. Int J Appl Glass Sci 10:57–60
8. Gibbs JW (1928) Collected works. Thermodynamics, vol 1. Longmans & Green, New York, London, Toronto
9. Schmelzer JWP, Abyzov AS (2016) Crystallization of glass-forming liquids: thermodynamic driving force. J Non-Cryst Solids 449:41–49
10. Schmelzer JWP (2010) On the determination of the kinetic pre-factor in classical nucleation theory. J Non-Cryst Solids 356:2901–2907
11. Kauzmann W (1948) The nature of the glassy state and the behavior of liquids at low temperatures. Chem Rev 43:219–256
12. Schmelzer JWP, Abyzov AS, Fokin VM (2016) Thermodynamic aspects of pressure induced nucleation: Kauzmann pressure. Int J Appl Glass Sci 7:474–485
13. Schmelzer JWP, Abyzov AS, Fokin VM, Schick C (2018) Kauzmann paradox and the crystallization of glass-forming melts. J Non-Cryst Solids 501:21–35
14. Schmelzer JWP, Tropin TV (2018) Glass transition, crystallization of glass-forming melts, and entropy. Entropy 20(1–32):103
15. Schmelzer JWP, Tropin TV (2018) Reply to "Comment on 'Glass transition, crystallization of glass-forming melts, and entropy' by Zanotto and Mauro." Entropy 20:704. https://doi.org/10.3390/e20090704
16. Abyzov AS, Fokin VM, Rodrigues AM, Zanotto ED, Schmelzer JWP (2016) The effect of elastic stresses on the thermodynamic barrier for crystal nucleation. J Non-Cryst Solids 432:325–333
17. Schmelzer JWP, Abyzov AS (2016) Crystallization of glass-forming liquids: specific surface energy. J Chem Phys 145(1–11):064512
18. Schmelzer JWP, Abyzov AS (2018a) Crystallization of glass-forming melts: new answers to old questions. J Non-Cryst Solids 501:11–20
19. Schmelzer JWP, Abyzov AS, Baidakov VG (2019) Entropy and the Tolman parameter in Nucleation theory. Entropy 21:670. https://doi.org/10.3390/e21070670
20. Tolman R (1949) The effect of droplet size on surface tension. J Chem Phys 17:333–337
21. Schmelzer JWP, Pascova R, Möller J, Gutzow I (1993) Surface-induced devitrification of glasses: the influence of elastic strains. J Non-Cryst Solids 162:26–39
22. Schmelzer JWP, Möller J, Gutzow I, Pascova R, Müller R, Pannhorst W (1995) Surface energy and structure effect on surface crystallization. J Non-Cryst Solids 183:215–233
23. Schmelzer JWP, Müller R, Möller J, Gutzow IS (2002) Elastic stresses, stress relaxation, and crystallization: theory. Phys Chem Glasses 43(C):291–300
24. Schmelzer JWP, Müller R, Möller J, Gutzow IS (2003) Theory of Nucleation in viscoelastic media: application to phase formation in glass-forming melts. J Non-Cryst Solids 315:144–160
25. Zeldovich YB, On the theory of new phase formation: cavitation. Sov Phys JETP 12:525–538 (1942); Acta Physicochimia USSR 18(1) (1943)
26. Angell CA, MacFarlane DR, Oguni M (1986) The Kauzmann paradox, metastable liquids, and glasses: a summary. In: Angell CA, Goldstein M (eds) Dynamic aspects of structural change in liquids and glasses. Ann N Y Acad Sci 484:241–247

27. Schmelzer JWP, Abyzov AS, Fokin VM, Schick C, Zanotto ED (2015a) Crystallization in glass-forming liquids: maxima of nucleation, growth, and overall crystallization rates. J Non-Cryst Solids 429:24–32

28. Schmelzer JWP, Abyzov AS (2018b) Pressure-induced crystallization of liquids: maxima of nucleation, growth, and overall crystallization rates. Int J Appl Glass Sci 9:198–207

29. Schmelzer JWP, Abyzov AS, Fokin VM, Schick C, Zanotto ED (2015b) Crystallization in glass-forming liquids: effects of fragility and glass transition temperature. J Non-Cryst Solids 428:68–74

30. Schmelzer JWP, Abyzov AS, Fokin VM, Schick C, Zanotto ED (2015c) Crystallization in glass-forming liquids: effects of decoupling of diffusion and viscosity on crystal growth. J Non-Cryst Solids 429:45–53

31. Schmelzer JWP, Abyzov AS, Baidakov VG (2017) Time of formation of the first supercritical nucleus, time-lag, and the steady-state nucleation rate. Int J Appl Glass Sci 8:48–60

32. Zanotto ED, Mauro JC (2017) The glassy state of matter: its definition and ultimate fate. J Non-Cryst Solids 471:490–495

33. Adrjanowicz K, Grzybowski A, Grzybowska K, Pionteck J, Paluch M (2013) Towards better understanding crystallization of supercooled liquids under compression: isochronal crystallization kinetics approach. Cryst Growth Des 13:4648–4654

34. Adrjanowicz K, Grzybowski A, Grzybowska K, Pionteck J, Paluch M (2014) Effect of high pressure on crystallization kinetics of van der Waals liquid: an experimental and theoretical study. Cryst Growth Des 14:2097–2104

35. Skripov VP, Faizullin MZ (2005) Crystal-liquid-gas phase transitions and thermodynamic similarity. WILEY-VCH, Berlin-Weinheim

36. Schmelzer JWP, Zanotto ED, Fokin VM (2005) Pressure dependence of the viscosity. J Chem Phys 122(1–10):074511

37. Fokin VM, Zanotto ED, Yuritsyn NS, Schmelzer JWP (2006) Homogeneous crystal nucleation in silicate glasses: a 40 years perspective. J Non-Cryst Solids 352:2681–2714

38. Schick C, Androsch R, Schmelzer JWP (2017) Homogeneous crystal nucleation in polymers. J Phys Condens Matter 29(1–35):453002

39. Cahn JW (1998) Reflections on diffusive interfaces and spinodal decomposition. In: Carter WC, Johnson WC (eds) The selected works of J. W. Cahn. The Minerals, Metals, and Materials Society, pp 1–8

40. Schmelzer JWP, Abyzov AS (2017) How do crystals nucleate and grow: Ostwald's rule of stages and beyond. In: Sestak J, Hubik P, Mares JJ (eds) Thermal physics and thermal analysis: from macro to micro highlighting thermodynamics, kinetics, and nano-materials. Springer, Cham, Switzerland, pp 195–211. ISBN 9789048131495

41. Schmelzer JWP, Boltachev GS, Baidakov VG (2006) Classical and generalized Gibbs approaches and the properties of critical clusters in nucleation theory. J Chem Phys 124(1–17):194503

42. Schmelzer JWP (2009) Generalized Gibbs thermodynamics and nucleation-growth phenomena. In: Rzoska S, Drozd-Rzoska A, Mazur V (eds) Proceedings of the NATO advanced research workshop metastable systems under pressure, Odessa, Ukraine, 4–8 October 2008. Springer, pp 389–402

43. Johari GP, Schmelzer JWP (2014) Crystal nucleation and growth in glass-forming systems: some new results and open problems. In: Schmelzer JWP (ed) Glass: selected properties and crystallization. de Gruyter, Berlin, pp 521–585

44. Schmelzer JWP, Fokin VM, Abyzov AS (2016) Crystallization of glass: what we know, what we need to know. Int J Appl Glass Sci 7:253–261

45. Schick C, Höhne GWH (eds) (2011) Interplay between nucleation, crystallization, and the glass transition. Thermochim Acta 522(Special Issue):1–220

46. Fokin VM, Kalinina AM, Filipovich VN (1981) Nucleation in silicate glasses and effect of preliminary heat treatment on it. J Crystal Growth 52:115–121

47. Fokin VM, Abyzov AS, Zanotto ED, Cassar DR, Rodrigues AM, Schmelzer JWP (2016) Crystal nucleation in glass-forming liquids: effect of the size of the "structural units." J Non-Cryst Solids 447:35–44

48. Abyzov AS, Fokin VM, Yuritsyn NS, Rodrigues AM, Schmelzer JWP (2017) The effect of heterogeneous structure of glass-forming liquids on crystal nucleation. J Non-Cryst Solids 462:32–40
49. Davies MJ, Ihinger PD (2002) Effects of thermal history on crystal nucleation in silicate melts: numerical simulations. J Geophys Res 107(B11/1–20):2284
50. Schmelzer JWP, Gutzow IS (2011) Glasses and the glass transition. Wiley, Berlin
51. Schmelzer JWP, Schick C (2012) Dependence of crystallization processes of glass-forming melts on prehistory: a theoretical approach to a quantitative treatment. Phys Chem Glasses, Eur J Glass Sci Technol B 53:99–106
52. Komatsu T (2015) Design and control of crystallization in oxide glasses. J Non-Cryst Solids 428:156–175
53. Keller A (1957) A note on single crystals in polymers: evidence for a folded chain configuration. Phil Mag 2:1171–1175
54. Fischer EW, Goddar H, Schmidt GF (1968) Über Zusammenhänge zwischen der Röntgen-kleinwinkelstreuung und der morphologischen Struktur verstreckter Hochpolymere. Kolloid Zeitschrift und Zeitschrift für Polymere 226:30–40
55. Armistead K, Goldbeck-Wood G, Keller A (1992) Polymer crystallization theories. Adv Polym Sci 100:219–312
56. Zhang M, Guo B-H, Xu J (2017) A review on polymer crystallization theories. Crystals 7(1–37):4
57. Sommer JU, Reiter G (2003) Polymer crystallization—observations, concepts and interpretations. Springer-Verlag, Berlin, Heidelberg, New-York, Barcelona, Hong-Kong, London, Milan Paris, Singapore, Tokyo
58. Keller A (1968) Polymer crystals. Rep Progr Phys 31:623
59. Ishida Y, Yamafuji K, Ito H, Takayanagi M (1962) Effects of degree of crystallinity upon dielectric behaviors in some aromatic polyesters. Kolloid-Zeitschrift und Zeitschrift für Polymere 184:97–108
60. Suzuki H, Grebowicz J, Wunderlich B (1985) Glass transition of poly(oxymethylene). Br Polym J 17:1–3
61. Dobbertin J, Hensel A, Schick C (1996) Dielectric spectroscopy and calorimetry in the glass transition region of semicrystalline poly(ethylene terephthalate). J Therm Anal 47:1027–1040
62. Muthukumar M (2003) Molecular modelling of nucleation in polymers. Phil Trans R Soc Lond A 361:539–556
63. Schick C, Mathot V (eds) (2016) Fast scanning calorimetry (Springer)
64. Zhuravlev E, Schmelzer JWP, Wunderlich B, Schick C (2011) Kinetics of nucleation and crystallization in poly(epsilon caprolactone) (PCL). Polymer 52:1983–1997
65. Lauritzen JI Jr, Hoffman JD (1960) Theory of formation of polymer crystals with folded chains in dilute solution. J Res Natl Bur Stan 64:73–102
66. Hoffman JD, Miller RL (1997) Kinetics of crystallization from the melt and chain folding in polyethylene fractions revisited: theory and experiment. Polymer 38:3151–3212
67. Reiter G, Strobl G (2006) Progress in understanding of polymer crystallization. Springer-Verlag, Mulhouse, Freiburg
68. Strobl G (2009) Colloquium: laws controlling crystallization and melting in bulk polymers. Rev Mod Phys 81:1287–1300
69. Piorkowska E, Rutledge GC (2013) Handbook of polymer crystallization. Wiley
70. Hu W (2018) The physics of polymer chain-folding. Phys Rep 747:1–81

High-Pressure Crystallization of Glass-Forming Liquids at Varying Thermodynamic Conditions

Karolina Adrjanowicz

Abstract A liquid is called "glass-forming" when it can avoid crystallization on cooling and become a disordered solid called a glass. Glasses have unique properties and highly promising applications. However, it is a longstanding open scientific question what makes a liquid crystallize easily in one case, and form a stable glass in another. This research focuses on the crystallization tendency of glass-forming liquids and effective ways of tuning it. To provide a new insight into the crystallization phenomenon, we have taken full advantage of the fact that a phase space for every system is not one- but two-dimensional. Therefore, temperature T and pressure p are used as two independent thermodynamic variables to control and affect the crystallization outcome. The scientific target was to give an insight into the crystallization phenomenon at a fundamental level. To do so, experimental studies at varying thermodynamic conditions were carried out with the use of dielectric spectroscopy. This includes (i) a pioneering approach which allows to separately control molecular mobility and thermodynamic driving force towards crystallization, (ii) development of the time-pressure-transformation (TPT) and continuous-decompression-transformation (CDT) diagrams as the pressure analogs for time-temperature-transformation (TTT) and continuous-heating-transformation (CHT) diagrams which can be used to describe crystallization/vitrification tendencies of the molecular systems under non-isothermal or non-isobaric conditions, (iii) investigation on the effect of path dependence and (iv) enantiomeric composition on the crystallization tendency of the glass-forming liquids. The results gained from this study are of great scientific and practical importance. First, they improve our knowledge on the crystallization behavior of molecular glass-forming systems under varying thermodynamic conditions and second, demonstrate effective strategies which can be used to control/modify the crystallization outcome by ably control of T and p when moving through the phase diagram.

K. Adrjanowicz (✉)
Institute of Physics, University of Silesia, 75 Pulku Piechoty 1, 41-500 Chorzow, Poland
e-mail: karolina.adrjanowicz@us.edu.pl

SMEBI, 75 Pulku Piechoty 1a, 41-500 Chorzow, Poland

Abbreviations

τ_α	α-Relaxation time
n	Avrami parameter
CNT	Classical nucleation theory
$t_{1/2}$	Crystallization half-time
k	Crystallization rate constant
CDT diagram	Continuous-decompression-transformation diagram
CHT diagram	Continuous-heating-transformation diagram
ΔT	Degree of undercooling ($T_m - T$)
DS	Dielectric spectroscopy
T_g	Glass transition temperature
U	Growth rate
t_{ind}	Induction time
σ	Liquid/crystal interface energy
T_m	Melting temperature
$\varepsilon'N$	Normalized dielectric permittivity
I	Nucleation rate
p	Pressure
PC	Propylene carbonate
T	Temperature
$\tau_\#$	The nucleation time lag
$\Delta\mu$	Thermodynamic driving force towards crystallization
TPT diagram	Time-pressure-transformation diagram
TTT diagram	Time-temperature-transformation diagram

1 Introduction

When a liquid is cooled below the melting temperature, it will solidify and form a
crystal of a regular, well-defined array of atoms/molecules. However, sometimes it
can be also supercooled and with lowering temperature further it enters the glassy
state. The liquid is metastable in the supercooled regime and tends to crystallize. This
is a fundamental problem which scientists have to deal with for decades, particularly
if they want to focus on the glass transition phenomenon or the practical advantages
given by the glassy state [1–3]. Since crystallization and glass-formation are two
sides of the same coin, by understanding what governs crystallization in supercooled
liquids, we can learn how to make good glass-formers.

Formation of the crystalline phase is of great interest from both, scientific point of view and technological applications. Crystallization underlies natural phenomena such as biomineralization, honey granulation, natural rocks, and cave calcites creation. On the other hand, artificial crystallization has been applied in various areas of science and industrial processing for chemical synthesis, purification, and selective fabrication of organic as well as inorganic materials with preferable physicochemical features. Because of the fundamental significance, the interest in the crystallization last endlessly for decades and continues to excite a large spectrum of research activities [4–7].

Crystallization is essentially well studied, but not necessarily well-understood phenomenon. Surprisingly, despite years of intensive studies, there are numerous aspects related to the crystallization process which are being poorly recognized or still intriguing in their nature. For example, it is by no means easy to understand why some of the liquids are not prone to crystallize on cooling (even if a very slow cooling rate is applied), whereas undercooling of the other ones require a tremendous effort [8, 9]. Some of the glassy materials can be physically stable for years, while the other ones recrystallize within a few minutes or hours. A complete and consistent description of the glass transition and crystallization phenomena constitute an enormous challenge in the field of modern condensed matter physics. This includes for example explanation why on approaching the glass transition relatively small changes in temperature affect the dynamic features of supercooled liquids (viscosity, relaxation time or diffusion coefficient) by several orders of magnitude [10–12]. There have been efforts in both, theory and experiment to provide a physical understanding of the vitrification process which is predominantly discussed in the context of its intimate link to crystallization [13]. Recent studies have also revealed that the formation of the nuclei might follow a two-step mechanism, which in many cases accounts better for the experimentally determined kinetic dependencies than the predictions of the classical theory [14, 15].

There is a tremendous interest in manipulating and controlling crystallization behavior of complex systems (i.e., supercooled liquids, polymer melts, liquid crystals or bio-fluids) which is an important aspect in the field of material physics, chemical engineering, food, and pharmaceutical developments. For example, in the pharmaceutical formulation, the disordered phase is usually more preferable than crystalline one because of improved solubility and bioavailability [16]. However, this can be difficult to achieve as thermodynamic instability prompt the amorphous system to spontaneous recrystallization beginning just after a few hours, days, or months after preparation. In some other cases, it is highly desirable to control in a selective way formation of different polymorphic forms of the same compound as to be able to affect its solid-state features (stability, dissolution rate, biological activity, optical, and mechanical properties) [17, 18]. Because of that reason identification and understanding, the critical factors that can influence the crystallization progress are of great practical importance.

One of the most interesting strategies that can be employed to modify the crystallization behavior of glass-forming liquids is compression. Experimental studies

carried out on increased pressure have revealed that the physical and chemical properties of matter may drastically change when subjected to increased pressure. At high pressure, it is possible to achieve organic and inorganic materials with interesting physicochemical properties, sometimes not attainable by any other experimental attempt performed at atmospheric pressure [19–26]. For example, except the pressure-induced polymorphic transformation [27], one of the most thrilling theoretically predicted applications of hydrostatic pressure is spontaneous enantiomers separation from the racemic crystal above certain pressure [28]. For that reason, high-pressure studies are the source of unique information about different phenomena or processes of fundamental importance in science and technology. On increased pressure, we can expect spectacular changes in the molecular packing and the character of the intermolecular interactions. This has a critical effect on the dynamic and thermodynamic properties, as well as the physicochemical stability of glass-forming materials. Thus, it has been suggested to be a very promising parameter that controls the crystallization tendency of glass-forming liquids [29]. On the other hand, we all know that crystallization is a very complex phenomenon influenced by many factors at the same time. Control over all of them is difficult, if not impossible. Therefore, introducing pressure as another thermodynamic variable to control brings up an additional parameter that potentially makes an in-depth understanding of the principle aspects related to crystallization mechanism and its characteristics far more challenging.

In the field of crystallization carried out under high-pressure conditions, a lot of work has been already reported for inorganic materials [20, 27, 30–33]. Most of them have been carried out to understand changes in the morphology, crystalline structure, and the phase diagram rather than the crystallization kinetics. On the other hand, the importance of such information is critical to control the properties of the newly evolving phases, especially in industrial processing when most of the processes are carried out under varying temperature and pressure conditions.

Study the effect of pressure on crystallization propensity or structural transformation of minerals or silica glasses has attracted considerable attention because of its importance in material science and geophysics [34–36]. Compression has been also used to induce crystallization of molecular liquids or polymers, especially reaching very high degrees of crystallinity [19], obtaining crystal morphology of desired features [37] or accelerating the crystallization rate [38, 39]. However, the exact effect of pressure on the crystallization of glass-forming materials is somewhat unclear. For example, for the low-molecular-weight glass-forming liquid triphenyl phosphite (TPP) it has been observed that compression inhibit crystallization [40]. Likewise, increased pressure was found to retard crystal growth of cordierite glass and increase the nucleation time [41]. In contrast, some other reports demonstrate that compression induces crystallization and facilitates its progress. Just to mention that crystallization rate of amorphous Si at pressures up to few GPa can be enhanced by a factor of 10 over that at atmospheric pressure [31, 42]. These contrasting examples point out that our knowledge about the effect of pressure on the crystallization of glass-forming materials is still very incomplete. This can be related to the fact that most of the high-pressure research devoted to crystallization is performed at randomly

selected combinations of temperature and pressure without taking into account the relative impact of the fundamental factors governing its progress (molecular mobility and thermodynamic) at any given (T, p) conditions. On the other hand, one should also remember that in experimental reality it is not so easy to explore the T-p (T-ρ) phase diagram. This, in turn, is a major impediment in the case of many commercially available high-pressure setups.

1.1 General Information About the Crystallization

The crystallization process itself involves two steps: nucleation, i.e., the formation of a crystal nucleus big enough to grow, and the subsequent growth of the nucleus into a proper crystal phase. According to the classical theory [43–45] to provide complete information about the overall crystallization progress of a glass-forming liquid at any given (T, p) condition it is necessary to describe three basic parameters: nucleation rate I, crystal growth rate U and the nucleation time lag, $\tau_\#$. The first attempt to describe changes in the rates of nucleation and crystal growth caused by pressure variations were carried out by Turnbull and coworkers [30, 32, 46]. However, that time as due to a limited number of the experimental results a more elaborate characteristics of the crystallization processes in dependence on pressure was not possible. Later, as more experimental data showed up, an attempt to provide a generalized theoretical description of the crystallization process carried out in the presence of increased pressure was developed by Gutzow et al. [36] and Schmelzer et al. [33, 34, 47, 48].

The general expression for the nucleation rate I, defined as the number of nuclei formed per volume unit per unit of time, is [36, 49, 50, 51]:

$$I(T, p) = C_1 \exp\left(-\frac{W^*(T, p)}{k_B T}\right) \exp\left(-\frac{\Delta G_D(T, p)}{k_B T}\right) \tag{1}$$

where W^* and ΔG_D define thermodynamic and kinetic barriers to nucleation, respectively. W^* is the work required to form critical nuclei, whereas ΔG_D is often discussed in terms of an effective diffusion coefficient (D), related to the viscosity (η) via the Stokes–Einstein relation ($D = k_B T/6\pi r\eta$) or then α-relaxation time via Debye–Stokes–Einstein relation ($\tau_\alpha^{-1} = k_B T/8\pi r^3 \eta$). Of course, this requires to assume that the relationship between D-η (and D-τ_α) remains unchanged by temperature and pressure.

The growth rate U describes the increase of the characteristic crystal size per unit of time and can be expressed as:

$$U(T, p) = C_2 \left[1 - \exp\left(-\frac{\Delta G(T, p)}{k_B T}\right)\right] \exp\left(-\frac{\Delta E(T, p)}{k_B T}\right) \tag{2}$$

where ΔE and ΔG are kinetic and thermodynamic barriers to crystal growth, respectively. Same like ΔG_D, ΔE is also related to the diffusion coefficient or the viscosity. The value of the thermodynamic driving force for the growth of crystals ΔG can be replaced by $\Delta \mu$, i.e., the difference between chemical potentials of liquid and crystalline phases [52]. C_1, C_2 and C_3 are constants.

The nucleation time lag is defined as:

$$\tau_{\#}(T, p) = \left(C_3 \frac{\sigma(T, p)}{\Delta \mu^2(T, p)} \right) \left[\exp\left(-\frac{\Delta G_D(T, p)}{k_B T} \right) \right] \tag{3}$$

where σ is the liquid/crystal interface energy.

Without going much into the details, we draw the reader's attention to the fact that abovementioned equations are both composed of the two parts. In each of them, the first term refers to the thermodynamic factor of crystallization, whereas the second one to the kinetic factor. Broadly speaking one distinguishes between two effects governing crystallization: (1) the thermodynamic driving force, "*how much the materials want to crystallize*"; this depends among other things, on how far the system below the melting point is, and (2) the kinetic factor: "*how quickly can molecules move/rearrange into the right position to form a critical nucleus and make it grow*". Both factors have, in fact, the opposite effect on the crystallization kinetics. At p = const., the exponential terms related to the thermodynamic factor act in such a way that on decreasing temperature of the melt they are responsible for increasing nucleation and growth rates (Eqs. 1 and 2). At the same time, the exponential terms describing the kinetic factor are responsible for slowing down the molecular movements which can result in halting down the crystallization progress. In Fig. 1 we demonstrate the typical behavior of thermodynamic driving force towards crystallization $\Delta \mu$ and characteristic α-relaxation time when lowering the temperature. As can be seen, with increasing the degree of undercooling (i.e., the distance from the melting temperature T_m) $\Delta \mu$ increases, while the molecular movements slow down (τ_α increases). Thus, the overall crystallization outcome depends on the interplay between kinetic and thermodynamic and can be entirely modified if one term gets dominance over another one. As a result, crystallization of supercooled liquid will

Fig. 1 Schematic evolution of the thermodynamic driving force towards crystallization $\Delta \mu$ and characteristic α-relaxation time when lowering the temperature of the melt
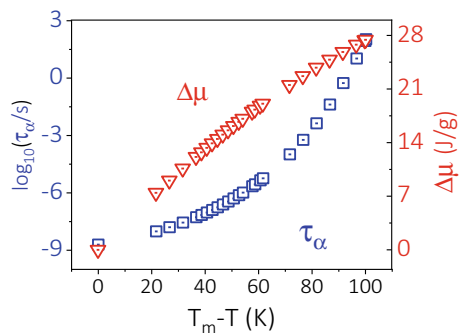
slow down or accelerate. Regrettably, in experimental studies, it is extremely difficult, if not impossible, to control and separate the individual contributions coming from the kinetic and thermodynamic factors. Therefore, we are still missing some key information related to the crystal formation allowing us to make use of it in a fully aware manner.

In contrast to α-relaxation time, $\Delta\mu$ cannot be measured directly. At most, it can be calculated from volumetric and calorimetric data with the use of the following expression:

$$\Delta\mu(T, p) = -\int_{T_m(0)}^{T} \Delta S(T, p)\mathrm{d}T + \int_{p_0}^{p} \Delta V(T_m(0), p)\mathrm{d}p \qquad (4)$$

where $\Delta V = V_{\text{liq}} - V_{\text{cry}}$ (in cm³/g) and $\Delta S = S_{\text{liq}} - S_{\text{cry}}$ [in J/(K g)] are the differences in the specific volumes and entropies of the liquid and crystalline states, respectively. Thus, calorimetric and volumetric data are required to determine the T-p evolution of the thermodynamic driving force towards a crystallization. Values of $\Delta S(T, P)$ can be estimated with the use of the following formula:

$$\Delta S(T, P) = \int_{T_K(P)}^{T} \frac{\Delta C_p(T, P)}{T}\mathrm{d}T \qquad (5)$$

where ΔC_p is the difference in the specific heat between liquid and crystalline phases (or the glassy state, if needed). The temperature T_K in the integration limit is Kauzmann temperature. It can be estimated on the basis of Vogel temperature T_0, obtained from the fitting of the isobaric $\tau_\alpha(T)$ dependences with the use of Vogel–Fulcher–Tammann equation (VFT). Since high-pressure calorimetric data are not available in many cases, $\Delta C_p(T, p)$ values can be estimated from the heat capacity measurements at ambient pressure $\Delta C_p(T, p_0)$ and pressure–volume–temperature (PVT) data by using Maxwell's thermodynamic relations:

$$\Delta c_p(T, p) = \Delta c_p(T, p_0) - T\int_{p_0}^{p}\left(\frac{\partial^2 V}{\partial T^2}\right)\mathrm{d}p \qquad (6)$$

where $\Delta c_p(T, p_0) = a * T + b$.

The rates of nucleation and crystal growth form characteristic bell-shaped curves with the maxima located within the melting temperature T_m and the glass transition temperature T_g, see Fig. 2. Depending on the intensity and the extent of overlap of both curves we can determine good or bad glass-forming ability on cooling from the melt so as when reheating the material from the glassy state. For example, when nucleation and growth maxima are well-separated from each other crystallization can be omitted on cooling. However, on subsequent heating from the glassy state

Fig. 2 Schematic evolution of the temperature dependences of the nucleation and crystal growth rates
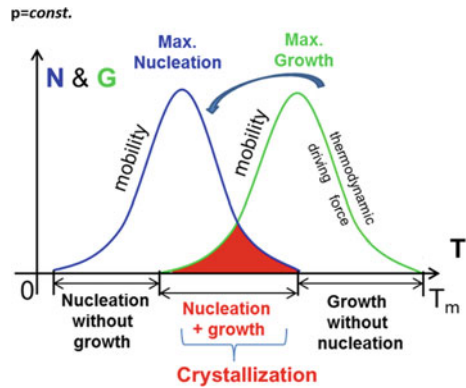
recrystallization takes place in many cases, as the nucleation process is more effective near T_g.

The classical theory of nucleation (CNT) and crystal growth models are often criticized for numerous approximations and large discrepancies between the rates obtained from the experimental study and that predicted theoretically. The most important simplification is assuming that the crystal nuclei retain the same properties as the macroscopic crystal, so follows the same description in terms of the thermodynamics. For deeply supercooled liquids, it has been also observed that in contrast to the classical description the kinetic barrier for crystallization is not similar to that for the diffusion process. Hence, crystallization can take place in "diffusion-less" controlled manner [53, 54]. Despite some of these limitations, the classical description of the nucleation and crystal growth still serves as a guiding picture of the crystal formation, and a good starting point to understand and analyze the effect of high-pressure on crystallization tendency of glass-forming liquids.

1.2 Experimental Methods to Study Crystallization on Increased Pressure

To study crystallization, a variety of different experimental techniques can be used. If the structural properties of the crystalline materials are of prime importance, diffraction techniques (X-ray or neutron) are irreplaceable. On the other hand, when the research interest is on the analysis of the crystallization kinetics, detecting phase transformation or glass transition event a more useful and convenient technique is differential scanning calorimetry. Due to its simplicity and high sensitivity in detecting numerous phase transformations, it is widely used for scientific, technical, and industrial purposes. However, among other methods which are very effective

to characterize especially dynamics aspects related to the glass-formation and crystallization, dielectric spectroscopy emerges as a highly promising experimental tool [44].

The principle idea of the dielectric relaxation relies on the interactions of the molecules possessing a permanent dipole moment with an external electric field. When a time-dependent electric field is applied it causes polarization of the dielectric material and by following time-dependent changes in the relaxation function one gets information on certain molecular movements in the sample. Dielectric spectroscopy is a very powerful tool to study the molecular dynamics of supercooled liquids and glasses in the broad range of characteristic relaxation times and temperature. It can also be used to detect phase transitions (e.g., in liquid crystals) and follow the kinetics of the different processes (e.g., crystallization, polymerization, mutarotation, isomerization, physical aging, etc.). In this chapter, dielectric studies of crystallization are of primary importance. Therefore, we will limit further discussion only to those aspects of the dielectric response in glass-forming systems that are related only to the crystallization event. For more detailed information on the dielectric spectroscopy and its applicability in diverse fields of science and industry the readers are referred to more specialized literature, e.g., [55–59].

In Fig. 3, we demonstrate typical dielectric response recorded for a glass-forming liquid at some certain, fixed, temperature and pressure conditions. Panel (a) refers to the real part while (b) to the imaginary part of the dielectric permittivity. The presence of the α-relaxation process—associated with cooperative movements of the molecules—is signified in the dielectric spectra as a characteristic step in frequency
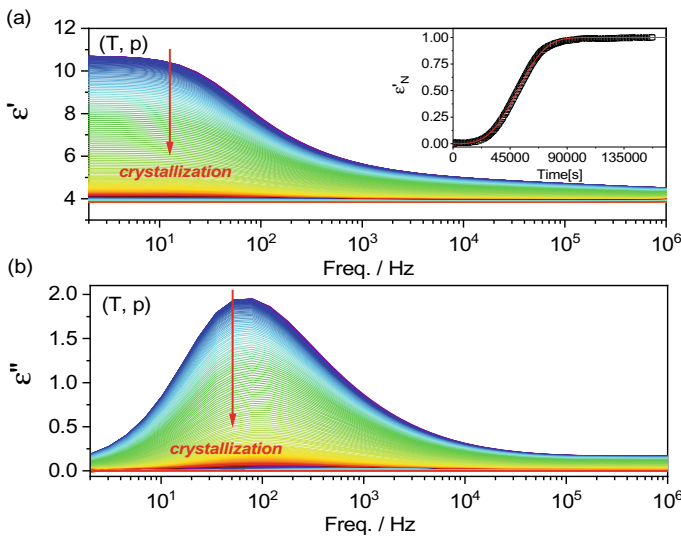
Fig. 3 Time evolution of the real **a** and imaginary **b** parts of the dielectric permittivity for a typical glass-forming liquid at a given (T, p) conditions as due to crystallization. The inset shows normalized dielectric constant $\varepsilon_N{'}$ as a function of crystallization time

dispersion (ε') and the loss peak (ε''). When crystallization takes place, the dielectric response of glass-forming liquids changes with time. As can be seen, in the real part of the dielectric permittivity we observe a decrease of the static permittivity increment, while in the imaginary part the same situation is reflected by a gradual drop of the α-peak intensity. The decrease of the dielectric strength with time indicates that the number of reorientating dipoles is drastically reduced as crystallization proceeds. In the liquid phase, reorientational movements of the molecules are freed, while in the crystalline phase restricted. Thus, we can use this very useful feature to follow the crystallization kinetics of the glass-forming systems with the use of dielectric spectroscopy. The idea relies, however, on the assumption that the total dipole moment is associated with a molecule as a whole. In such a case, changes recorded in the loss spectra during crystallization can be assumed to give equivalent information about the kinetics of the transformation as that obtained from the diffraction measurements. This might not be essentially true for more complex systems like polymers for which the dipole moment might be attached to the skeletal bonds or located only in some flexible side groups.

Changes occurring in the static permittivity can be used to follow crystallization kinetics after normalization according to the following formula:

$$\varepsilon'_N(t) = \frac{\left(\varepsilon'_{\text{initial}} - \varepsilon'(t)\right)}{\left(\varepsilon'_{\text{initial}} - \varepsilon'_{\text{final}}\right)} \tag{7}$$

where $\varepsilon'_{\text{initial}}$ and $\varepsilon'_{\text{final}}$ are the initial and final values of the real part of dielectric permittivity at selected frequency taken from the low-frequency (static) regime. For imaginary part of the dielectric permittivity, the ongoing changes as due to crystallization can be followed by analyzing the intensity of the α-relaxation peak. Its complete disappearance and a flat signal, as demonstrated in Fig. 3b, points out for complete crystallization of the sample (as reorientational movements in crystals are not possible anymore). The exemplary of the normalized curve plotted versus time is shown in the inset of Fig. 3. In such a case, the two limiting values –0 and 1—refers to 0 and 100% crystallinity. To determine the rate of crystallization the normalized dielectric data are fitted using Avrami equation [60]:

$$\varepsilon'_N(t) = 1 - \exp\left(-kt^n\right) \tag{8}$$

where n is the Avrami exponent, and k is the crystallization constant rate related to nucleation I and growth U rates via the relation $k = IU^{n-1}$. In turn, the Avrami parameter depends on the growth mechanisms and crystal shape. It typically varies within 1–4. Solid red lines presented in the insets of Fig. 3b are the best fits of the experimental data to the Avrami equation. It should be noted that the values of k calculated using Eq. 8 are given as seconds to the power of $(-n)$. Therefore, to have the crystallization rates presented in more practically meaningful units, i.e., s^{-1}, the values obtained from Eq. 8 should be corrected by the value of the Avrami parameter.

Fig. 4 Evolution of the crystallization rate k as a function of temperature for different glass-forming liquids, determined based on dielectric studies carried out at atmospheric pressure
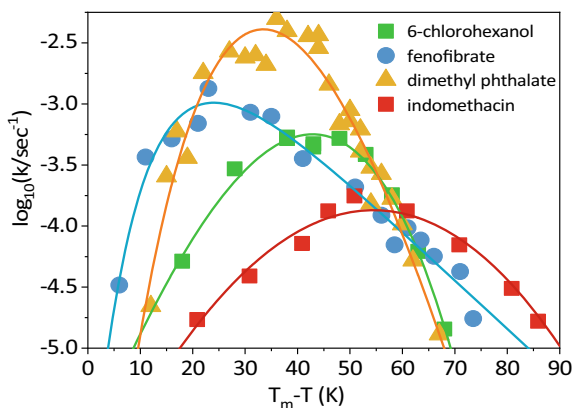
If the same procedure, like that described above, is then used to analyze crystallization kinetics at a different temperature or pressure conditions. Once can get information on the intensity and location of the maximum crystallization rate with respect to the melting or glass transition temperatures for a given compound. Then, obtained crystallization rate curves can be used to compare crystallization tendencies within different groups of glass-forming liquids, as presented in Fig. 4.

The advantage of the dielectric spectroscopy in comparison to other experimental techniques used to follow crystallization is relative ease to adapt to various thermodynamic conditions, in particular, high pressures. The experimental setups which were used in this study are mostly based on Unipress systems (Institute of High-Pressure Physics, Warsaw, Poland). In such systems, the pressure is generated by a manual (or either automatic) pump and transmitted with the use of nonpolar silicon oil via systems of capillaries (Nova Swiss) to high-pressure vessels. The high-pressure cell with a homemade capacitor is connected to an impedance analyzer (Novocontrol GmbH). The speed of compression/decompression can be regulated via the control unit, i.e., by changing the frequency of the motor movements (and therefore also the piston position). For temperature stabilization, we use either a thermal bath (Julabo) connected to a heating jacket located on the pressure chamber or the environmental chamber (Weiss Umwelttechnik GmbH). More details regarding experimental setups used for high-pressure dielectric studies can be found in the literature [55, 61–67].

2 Results and Discussion

2.1 The Effect of Cooling Rate versus Compression Rate on the Crystallization Tendency of the Glass-forming Liquids

When decreasing the temperature at constant pressure a liquid can either crystallize or form a glass, depending on the applied cooling rate. Generally, crystallization takes place when the rate of cooling is slow enough so that there is enough time for the stable nuclei to form and grow into the macroscopic dimensions. On the other hand, when the cooling rate surpasses the rates of nucleation and crystal growth, crystallization is avoided. In such a case, a liquid can be supercooled and reach the glassy state. The critical cooling rate needed to bypass crystallization is an individual property of each system, meaning that 50 K/min might be far enough for a one glass-former, while not necessarily for the other one. For example, the critical rate needed to vitrify metallic alloys can reach even 1000 K per 1 ms, while for some silica glasses 1–10 K/h is still relatively "fast" to form a glass, or ironically not slow enough to form the crystal [68]. As a rule, the critical cooling rate necessary to inhibit the crystallization depends on the location of the nucleation and growth rates maxima, their intensity and the extent of overlap, as illustrated in Fig. 2.

For practical reasons, the crystallization/vitrification tendency of various systems on cooling is often visualized in terms of the time-temperature-transformation (TTT) diagram (see Fig. 5). TTT demonstrates the location of the crystallization zone with respect to the temperature and the processing time. From the analysis of the TTT curve, it is possible to determine the critical cooling rate necessary to avoid crystallization when lowering the temperature of the melt. As demonstrated in Fig. 5, crossing the 'nose' area implies that a particular cooling rate may not be fast enough to completely suppress the crystallization. In such a case, for the slowest processing times, one may expect the extent of the crystalline fraction in the final product.

Compression of liquid at a fixed temperature, just like lowering the temperature under isobaric condition, can be used to promote either crystallization or vitrification. Therefore, in analogy to temperature evolution of the nucleation and growth rates curves, we can draw a very similar crystallization profile for a pressure case. When pressurization starts above the melting point, a liquid overpass first via the crystal growth region located at lower pressures. Then, with increasing the pressure the nucleation process becomes more favorable. Such evolution of the nucleation and crystal growth rates as a function of pressure is schematically presented in Fig. 6. From the above scheme, one can get an impression that irrespectively of the chosen thermodynamic variables, T or p, we end up with the same qualitative picture. However, then the question arises: *can we use temperature and pressure interchangeably to tune the vitrification/crystallization ability of the molecular systems?*
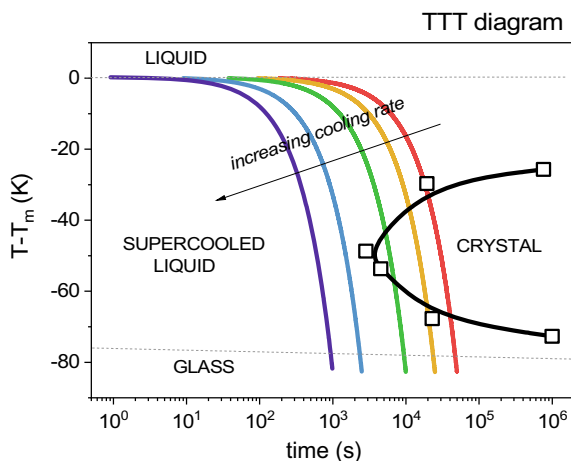
Fig. 5 Schematic representation of TTT diagram for a typical glass-forming liquid. The temperature changes are presented with respect to the melting point. The arrow points out towards the direction of the increased cooling rate. Dashed lines separate from each other the liquid/supercooling liquid and glassy state regions. Note that the glass transition temperature depends slightly on the cooling rate. The minimal cooling rate necessary to completely avoid crystallization is depicted by the blue line. When cooling line intersects with the TTT 'nose' crystallization takes place
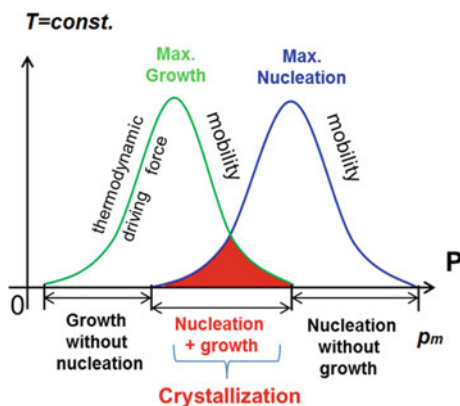
Fig. 6 Schematic evolution of the nucleation rate and the crystal growth rate as a function of pressure. In analogy to temperature dependences of I and U, the overlap zone signifies the optimal pressure region for crystallization. However, it is not clear yet, if both thermodynamic variables, T and p, affect the magnitude, the location, and the extent of overlap of both maxima in the same way. Re-adapted with permission from [61]. Copyright (2018) American Chemical Society

Since a number of natural phenomena and industrial processes require fast processing or take place under non-isothermal or non-isobaric conditions, understanding the accompanying phase transformation phenomena is critical to obtain materials with desired physicochemical features. Therefore, the idea of this study was to qualitatively compare the effect of temperature and pressure on the crystallization tendency of glass-forming liquid. Studied sample is propylene carbonate (PC) often termed in the literature as a canonical glass-former with $T_g = 159$ K and $T_m = 218$ K. Both values refer to atmospheric pressure conditions [61, 69]. The chemical structure of PC is presented in the inset of Fig. 7a. To affect the crystallization behavior of PC, we have varied with (i) the cooling/heating rate at ambient pressure as well as (ii) compression/decompression rate under isothermal conditions. Changes in the crystallization tendency of the sample were followed by using dielectric spectroscopy. Obtained results are discussed below in terms of the transformation diagrams presented either in temperature or pressure coordinates.

Figure 7a, b illustrate changes in the crystallization behavior of PC at 0.1 MPa as a function varying cooling and heating rates, respectively. A characteristic step of ε' (at 1 MHz) recorded when lowering the temperature (Fig. 7a) is due to dielectric dispersion. For supercooled liquids, it signifies the presence of the α-relaxation—which originates from cooperative movements of the molecules—that systematically
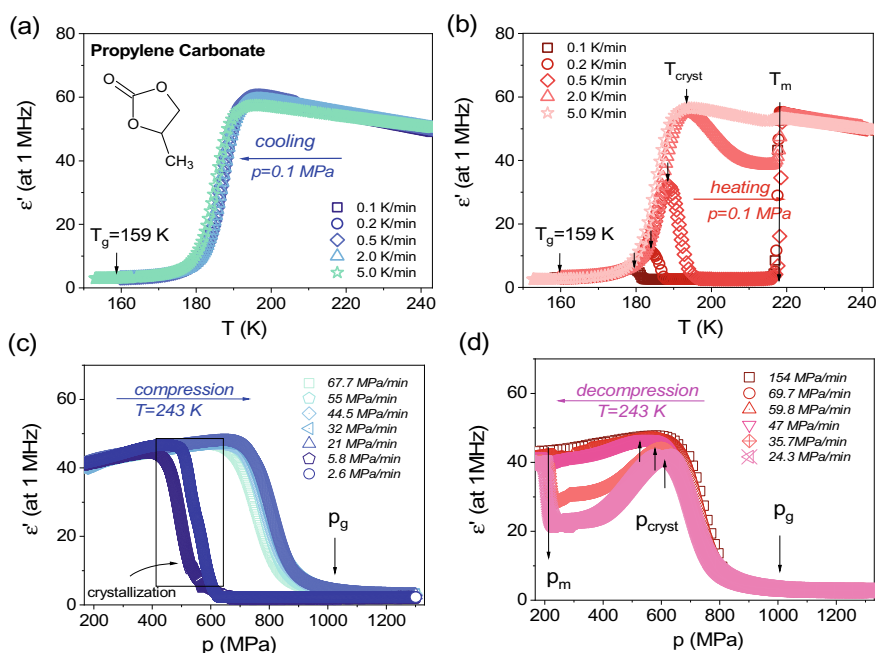
Fig. 7 Evolution of the dielectric permittivity at 1 MHz as measured for PC upon **a** cooling and **b** heating at 0.1 MPa, **c** compression and **d** decompression at 243 K with different scanning rates. Adapted with permission from [61]. Copyright (2018) American Chemical Society

slows down and moves out of the experimental window as the glass transition is approached. Since $\varepsilon'(T)$ dependences collected with the cooling rates from 0.1 K/min up to 5 K/min are almost identical, one can suppose that PC indeed easily reach the glassy state. On the other hand, it should be also remembered that the presence of only a small crystalline fraction might be hardly detectable in the dielectric response of the bulk material.

Subsequent heating starting from the glassy state (Fig. 7b) reveals dramatic changes in the crystallization behavior of PC. In this case, recrystallization event is detected as a sudden drop of the dielectric permittivity, with the onset that shifts towards higher temperatures with increasing the heating rate. We associate such a sudden drop in the dielectric permittivity with reducing the number of the reorientating dipoles as the liquid volume fraction decrease. In each case, the crystal melts at the same temperature, $T_m = 218$ K, indicating for the presence of only one polymorphic form. From the results presented above, it becomes evident that preventing crystallization of PC upon heating from the glassy state is far more complicated than on cooling a liquid from the melt. This type of behavior is very typical for numerous molecular liquids and agree with the schematic picture of the nucleation and growth rates maxima located at different temperature regions, as presented in Fig. 2.

Similarly, we have performed compression/decompression rate-dependent studies carried out for PC under isothermal conditions, $T = 243$ K. The results of these experiments are collected in Fig. 7c, d, respectively. In analogy to cooling rate dependent scans, we have also observed a characteristic dispersion curve in the dielectric response of the pressurized sample, indicating slowing down of the molecular movements and approaching the glassy state. For the two slowest compression rates (2.6 and 5.8 MPa/min) at least partial crystallization of PC was observed, as both curves deviate from all the others. This was additionally certified by comparing the values of the dielectric permittivity for the glassy and crystalline materials obtained on increased pressure [61]. Upon decompression from the glassy state, just like when heating the glassy sample, crystallization is far more difficult to avoid and this requires higher scanning rates (see Fig. 7d). Nevertheless, the values of ε' do not drop down completely to that characteristic for the crystalline material (~2.55), meaning that there is still some substantial amount of the liquid volume fraction in the depressurized material. Using decompression rate of 154 MPa/min, we have not observed any traces of the PC crystallization which indicates that at such high-compression rates there is not enough time for the nuclei to grow. Therefore, we conclude that by varying with compression/decompression rate it is possible to affect crystallization/vitrification tendency of the molecular liquids, same as when using the temperature. The results presented in Fig. 7d also reveal only one melting event ($p_m = 200$ MPa at 243 K), which is again consistent with the heating rate dependent studies carried out at ambient pressure. However, it has been also observed—especially for ice phases—that different compression/decompression rates might induce elusive polymorphic transformations [70, 71]. The increased tendency of the depressurized PC to crystallization conform the schematic picture of the nucleation and growth rates maxima located at slightly different pressure regions, as introduced in Fig. 6.

To describe the crystallization kinetics of PC at atmospheric pressure we have also performed time-dependent studies carried out at few temperatures located within T_g and T_m. Obtained temperature evolution of the overall crystallization time is presented in Fig. 8a. Its maximum forms a characteristic 'nose' on the TTT diagram. When decreasing the temperature of the melt, crystallization can be avoided when the cooling line does not intersect with the crystallization zone. For PC, such a critical cooling rate is 1 K/min.

In analogy to TTT diagram, crystallization tendency of glass-forming systems can be also analyzed in terms of Continuous-Heating-Transformation diagrams (CHT)
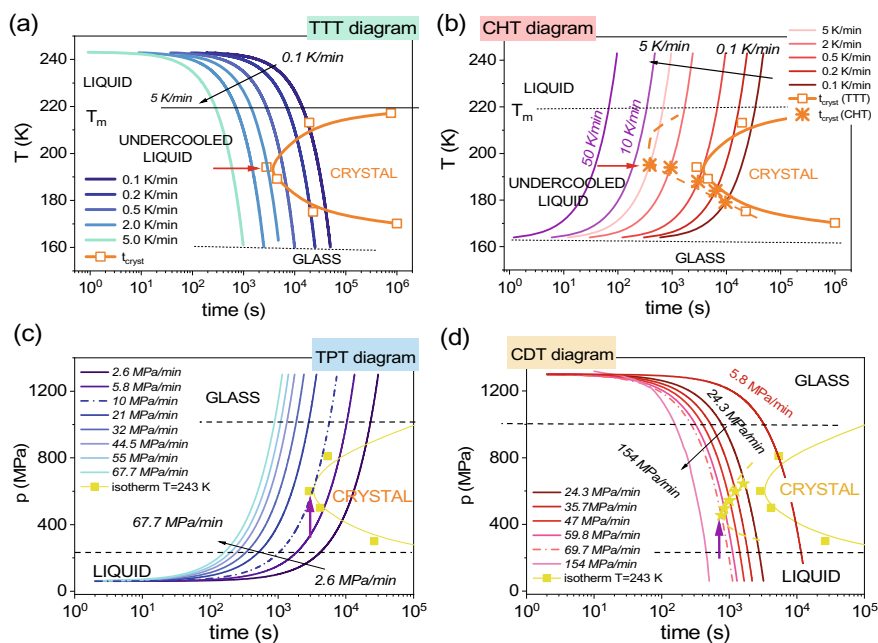
Fig. 8 **a** TTT diagram demonstrating crystallization tendency of PC at atmospheric pressure upon lowering the temperature with different cooling rates. The crystallization data were collected upon time-dependent studies carried out at a few different temperatures. In each case, the experimental protocol involved cooling the liquid from $T > T_m$ to the desired crystallization temperature ($T < T_m$); **b** CHT diagram demonstrating crystallization tendency of PC at 0.1 MPa upon reheating of the glassy sample with different heating rates. The maxima of the overall crystallization determined based on experimental data for cooling and heating scenarios are presented as orange square and star symbols, respectively; **c** TPT diagram demonstrating crystallization tendency of PC upon compression at 243 K with different scanning rates. The crystallization data were collected upon time-dependent studies carried out at few different pressures along isotherm $T = 243$ K. In each case the experimental protocol involved compression of the liquid at 243 K from atmospheric pressure to a desired crystallization pressure; **d** CDT diagram demonstrating crystallization tendency of PC at 243 K upon decompression carried out with different rates. Star symbols demonstrate the nose of the crystallization curve constructed using dielectric results collected upon decompression experiments, while solid symbols refer to crystallization data collected for the pressured sample. Adapted with permission from [61]. Copyright (2018) American Chemical Society

which provide a similar type of information but considering only the course of continuous heating with a constant rate. The example of CHT diagram is given in Fig. 8b. Since the crystallization tendency of PC is greatly increased when heating from the glassy state, only a low-temperature side of the crystallization curve was possible to be determined from the experimental studies. Nevertheless, by comparing the crystallization times recorded for the same temperature range on either cooling a liquid or heating a glass we found that they can be much different. This leads to a very important finding that the critical scanning rate necessary to avoid crystallization on cooling might be not enough to prevent recrystallization of glass upon heating.

In the next step, we have constructed time-pressure-transformation (TPT) and continuous-decompression-transformation (CDT) diagrams as the pressure analogs for TTT and CHT diagrams. For PC, they are shown in Fig. 8c, d, respectively. The maximum of the crystallization rate along isotherm 243 K is located at ~600 MPa and forms a characteristic nose on the TPT diagram. Compression rates which do not intersect the crystallization curve lead to vitrification. From the results presented in Fig. 8c, it is an event that more than 10 MPa/min is needed to avoid crystallization of PC upon pressurization. Thus, TPT diagram explains why the compression rates of 2.6 and 5.8 MPa/min were found in the dielectric studies too slow to form the glassy state. On the other hand, CDT diagrams show increased by almost one-decade crystallization times for decompressed PC and thus rationalize faster processing times needed to inhibit crystallization, as also observed in the dielectric study.

As a final point, the temperature and pressure evolution of the crystallization time ($t_{cryst} = 1/k$, where k is crystallization rate constant) measured along isobar 0.1 MPa and isotherm 243 K were plotted together, as illustrated in Fig. 9. Interestingly,
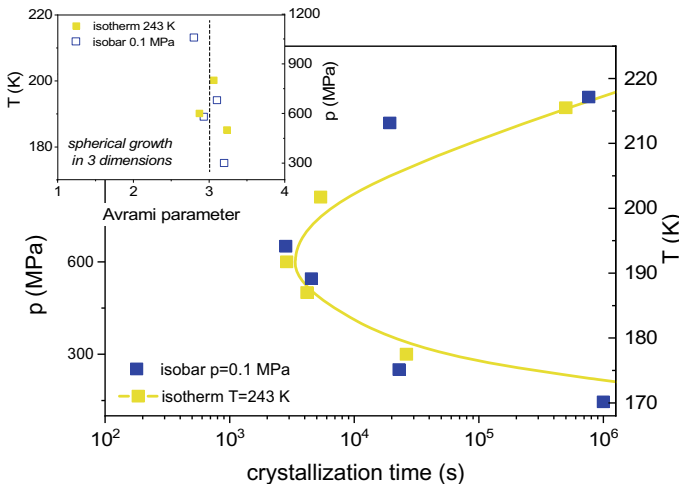
Fig. 9 Changes in the crystallization time versus temperature and pressure for PC as measured along isobar 0.1 MPa and isotherm 243 K, respectively. Re-adapted with permission from [61]. Copyright (2018) American Chemical Society

obtained dependences look very much the same. Moreover, it was found that the value of the Avrami parameter—providing information on the dimensionality of the growing crystals—shows very weak variation with temperature and pressure. In the considered *T-p* range, which covers a change of temperature by more than 50 K and 1 GPa in pressure, it varies around 3. From that, it can be concluded that the changes in the density of the supercooled PC do not affect in any way the morphology of the growing crystalline phase.

Summarizing, we have demonstrated that the glass-forming/crystallization tendency of the molecular liquids can be controlled not only by changing the rate of cooling/heating at constant pressure but also compression/decompression rate under isothermal conditions. The results also suggest that when it comes to crystallization increasing pressure, to some extent, produces a similar effect as lowering the temperature. Interestingly, within studied *T-p* range crystallization time and the dimensionality of growing crystals do no depend significantly on whether temperature or pressure is used as the control thermodynamic variable. Thus, we can transfer to high-pressure research the formalism used so far to describe the overall crystallization behavior of the glass-forming systems as a function of temperature. In line with this, we constructed TPT/CDT diagrams as the pressure analogs of TTT/CHT diagrams. The applicability of such diagrams to describe crystallization/vitrification tendencies of the molecular systems upon non-isothermal or non-isobaric conditions covers not only numerous research investigations but also industrial processing.

2.2 The Effect of Path Dependence on the Crystallization Tendency of Glass-forming Liquids

The motivation for this research was to examine the effect of path dependence on the crystallization of the molecular glass-formers [72]. Because of the experimental difficulties arising when using high-pressure, it is typically more important to focus on a particular feature of the studied material at a given (T, p) conditions rather than analyze in detail the way how new thermodynamic state was approached. Compression at a fixed temperature is more convenient because the stabilization of pressure usually takes less time than the temperature. This is not a big issue when considering dynamics of liquids far above the glass transition temperature, because molecular motions in the liquid state are always much faster the time needed for adjusting new (T, p) conditions. On the other hand, when the liquid becomes more viscous and reaches the glassy state molecular movements drastically slow down and the thermal history aspect becomes extremely important. In such a case, the choice of the thermodynamic path to attain the same final state point results in obtaining glassy materials of different density and local relaxation dynamics [73, 74].

Intuitively, we can expect that the effect of path dependence is important not only in the context of the glass transition but also such multivariable-dependent process
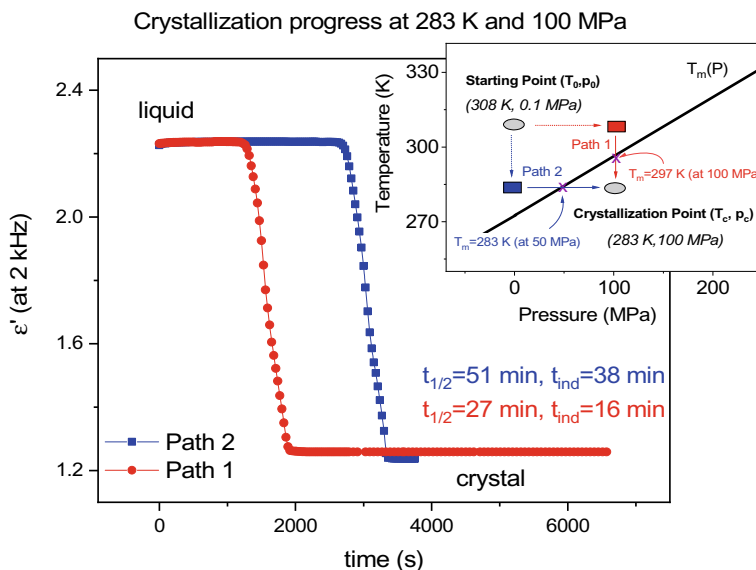
Fig. 10 Changes in the real part of the dielectric permittivity (at 2 kHz) as a function of crystallization time recorded at 283 K and 100 MPa for dimethyl phthalate. Red circles and blue squares refer to dielectric data collected after reaching the same (T_c, p_c) conditions by using two different pathways. The inset shows the schematic T-p phase diagram for dimethyl phthalate with the location of the initial and final state points. Adapted with permission from [72]. Copyright (2017) American Chemical Society

like crystallization. Therefore, to verify this supposition, we have investigated crystallization kinetics of a van der Waals liquid, dimethyl phthalate, at selected (T_c, p_c) conditions approached via two alternative routes. The inset in Fig. 10 demonstrates the general idea of this study. When both thermodynamic variables, temperature, and pressure, are available to control, we can move from the starting conditions (T_0, p_0) to final (T_c, p_c) point located in the metastable supercooled liquid regime via two different pathways. The first one involves isothermal compression to p_c, then isobaric cooling to T_c, and the second, isobaric cooling to T_c followed by isothermal compression to p_c. Since crystallization is thermodynamically favored only below $T_m(p)$ line, we can limit this consideration only to those stages which take place in the supercooled liquid regime, namely, lowering the temperature at constant pressure (for path 1) and increasing the pressure at a fixed temperature (for path 2). Please note that in the first case, the melting point is always approached from the higher temperature and higher pressure than for path 2. The time needed to reach the final (T_c, p_c) point must be comparable for both pathways, otherwise, it won't be possible to ascribe changes in the crystallization rate as due to a choice of a particular method of moving in the T-p phase diagram. This is the most important challenge in such a study.

For dimethyl phthalate, the initial and final state points are, ($T_0 = 308$ K, $p_0 = 0.1$ MPa) and ($T_c = 283$ K, $p_c = 100$ MPa), respectively. As can be seen, the latter one is located in the undercooled liquid state, but far above the glassy state. Crystallization progress at a given (T_c, p_c) conditions were followed with the use of the dielectric spectroscopy. The results presented in Fig. 10 demonstrate changes in the real part of complex dielectric permittivity at 2 kHz that accompanies crystallization progress for the investigated sample at (T_c, p_c) approached either via pathway 1 or 2. As can be seen, at the initial stages no changes in the value of ε' as a function of time is observed in both cases. Then, after some time, ε' starts to decrease. This effect is as due to a reduction in the number of actively reorientating dipoles as crystallization proceeds. Interestingly, we found that the crystallization behavior of dimethyl phthalate at (T_c, p_c) depends strongly on the chosen path. Firstly, we note that the crystallization half-time, $t_{1/2}$, defined as a time when changes in crystallinity reach 50% is much shorter for pathway 1. As we get $t_{1/2} \cong 27$ min for path 1, and $t_{1/2} \cong 51$ min for path 2. A clear difference is also observed in the induction period, t_{ind}, which is related to the nucleation process. Formally, t_{ind} is composed of three parts: the relaxation time required for a system to achieve quasi-steady-state conditions, the time needed to form stable nuclei and the time for nuclei to grow to detectable size [75]. In our case, the first and third components remain exactly the same. Therefore, the differences in the induction time at (T_c, p_c) conditions, as due to the choice of the different thermodynamic path, must be related to the nucleation time.

Lastly, we also note differences in the value of the dielectric permittivity for the fully crystallized sample. The sample which approaches crystallization conditions via pathway 1 has a slightly higher value of the dielectric constant than for path 2. This suggests that in the first case there should be a more irregular alignment of the molecules within the crystalline structure which changes polarization and affect the dielectric response of the material. This supposition was also verified with the use of molecular dynamics simulations for a Lennard-Jones system (the results are presented in Fig. 11) and demonstrates that it is statistically more probable to get uniformly formed crystalline material with denser structure when isothermal compression (80%) is chosen rather than isobaric cooling (65%).

To conclude, crystallization is *T-p* path-dependent meaning that the way of moving in the phase diagram to reach the final state point might itself affect the overall crystallization behavior of the glass-forming liquid at a selected (T_c, p_c) point. The results of this study indicate also that the path-dependent effect arises mostly from the changes at the very early stages of the crystallization process (the number and size of the initial clusters). Moreover, it was found that the choice of a particular thermodynamic pathway to reach the final (T_c, p_c) point might affect also the crystalline structured of obtained material, leading to denser and ordered structure or either less dense with a more random arrangement. Thus, the crystallization tendency of various materials on increased pressure can be tuned depending on the chosen path. Although demonstrated here differences in the overall crystallization times for isobaric cooling and isothermal compression takes only minutes, we suppose that more pronounced effects should be observed at a higher temperature and in the gigapascal regime where the changes in the density of the liquid will be more pronounced. The results presented
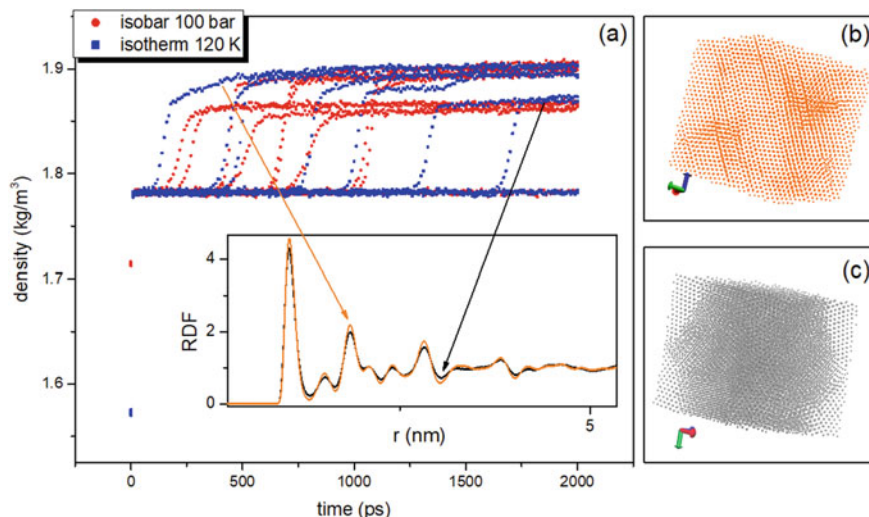
Fig. 11 a Changes in the density for a LJ system as a function of time as obtained from MD simulations carried out at 120 K and 100 bars. The desired conditions were reached either via isobaric cooling at 100 bar or isothermal compression at 120 K. Panels **b** and **c** show the differences in the final configuration of the crystallized system when reached by using two different thermodynamic pathways. Adapted with permission from [72]. Copyright (2017) American Chemical Society

above improve our understanding of the high-pressure crystallization which is also important in the different fields of science. For example, the exact knowledge of the thermodynamic path selected to approach crystallization conditions might be essential to estimate or reconstruct the transformation kinetics of some natural minerals in the deep interior of the Earth or other planets.

2.3 Isochronal Crystallization

As already noted crystallization process is governed by two factors—thermodynamic and kinetic—which makes it highly variable and difficult to control. On lowering the temperature, thermodynamic driving force favors the crystal formation, but at the same time slowing down of the molecular movements retards it. Controlling or separating the individual contribution coming from both factors seems to be extremely difficult, if not impossible. However, when operating with temperature and pressure, we can move in *T-p* space in such a way that the time scale of the global molecular motion remains unchanged (isochrone, $\tau_\alpha = $ const.). The invaluable asset of such approach is that it provides a unique opportunity to disentangle thermodynamic effects on crystallization from kinetic ones. When studying crystallization along isochronal conditions, all the changes in the overall crystallization rate are expected to originate exclusively from the variation of the thermodynamic factor, i.e., the

increase in the thermodynamic driving force of crystallization $\Delta\mu$ and the decrease in the melt/crystal interface energy σ.

Isochrones are characteristic curves on the phase diagram of a liquid along which the time scale of global/cooperative mobility remains constant. To determine isochrone, one needs to perform first dielectric relaxation studies to find the various temperature and pressure conditions at which the position of the α-loss peak is the same. For investigated sample which was pharmaceutical glass-formers—indomethacin—three different combinations of temperature and pressure conditions were considered to maintain approximately the same α-relaxation time, $\log_{10}(\tau_\alpha/s) \cong -3.13$; (343 K, 10 MPa), (368 K, 100 MPa) and (391 K, 220 MPa). When crystallization studies were carried out along selected isochrone, it has been observed that crystallization rate speeds up with increasing pressure, see results presented in Fig. 12.

To understand in details our finding we have analyzed thermodynamic aspects related with crystallization. In Fig. 13 we have plotted estimated pressure dependences of $\Delta\mu$ and σ for indomethacin crystallized at three different combinations of temperature and pressure located on the considered isochrone, $\log_{10}(\tau_\alpha/s) \cong -3.13$.

To estimate pressure evolution of $\Delta\mu$ one can use Eq. 4 with $\Delta S(T, p_0)$. Under the assumption of temperature and pressure independent values of ΔV and ΔS it can be simplified as:

$$\Delta\mu(T, p) \cong \Delta S[T_m(p) - T] \tag{9}$$
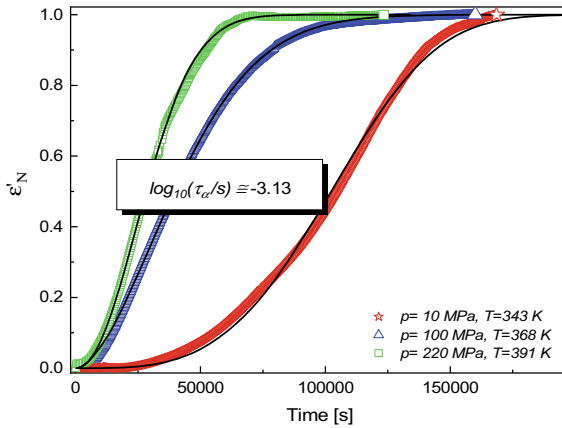
Fig. 12 Normalized dielectric constant as a function of time for crystallization carried out at three different T, p combinations at the same τ_α. The solid lines represent Avrami fits. Re-adapted with permission from [64]. Copyright (2013) American Chemical Society
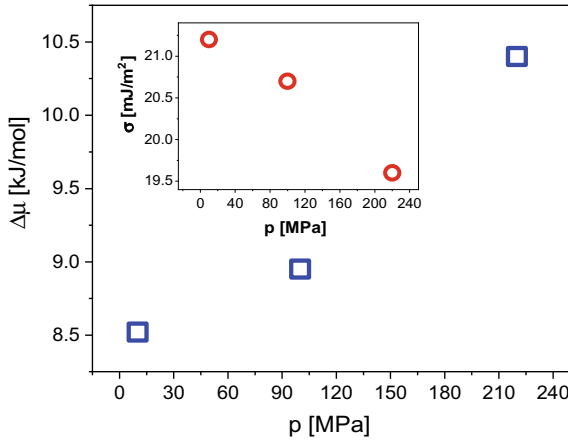
Fig. 13 Estimated changes in $\Delta\mu$ and σ (Inset) an isochrone $\log_{10}(\tau_\alpha/\text{s}) \cong -3.13$ for indomethacin. Re-adapted with permission from [64]. Copyright (2013) American Chemical Society

For that, however, we have to also make use of the Clausisus–Clapeyron relation:

$$T_m(p) - T_m(p_0) \cong \left(\frac{\Delta V}{\Delta S}\right)(p - p_0) \tag{10}$$

To estimate the pressure evolution of σ we have employed the formula introduced by Gutzow and coworkers [36]:

$$\sigma(T, p) \approx \sigma(T, p_0)\left[1 - (K_0/\gamma_0)T_m(p)\right] \tag{11}$$

where $\sigma(T, p_0)$ is the liquid/crystal interface energy at ambient pressure, K_0 (≈ 0.55) and γ_0 (≈ 0.4) are parameters introduced by the Gutzow formalism.

As can be seen, within the studied pressure range there is an increase in $\Delta\mu$ (approximately 20%) and a decrease in the melt/crystal interface energy (10% drop). Since $\Delta\mu$ and σ are directly involved in equations defining thermodynamic barriers to nucleation and crystal growth, we can expect that their changes with compression reflect also changes in the thermodynamic factor governing the crystallization process along an isochrone. This explains why crystallization of the molecular liquids speeds up with pressure, as also observed for indomethacin. Hence, the isochronal approach enables to clarify to what extent thermodynamics and molecular mobility influence the crystallization behavior of the investigated materials.

2.4 Changing Crystallization Behavior of Glass-Forming Liquids by Moving Along Different Iso-Lines

As already demonstrated, in T-p space of glass-forming liquid, we can find state points along which the time scale of the cooperative molecular movements remains the same. In practice, this implies that the changes in the crystallization behavior of investigated materials comes exclusively due to the variation of the thermodynamic factor. However, one can also look at this aspect from a much broader perspective and investigate the crystallization tendency of glass-forming liquids along different iso-lines among which isobars and isotherms are the easiest to approach from the experimental point of view (e.g., no need to perform prior high-pressure dielectric studies).

Figure 14a presents changes in the crystallization rate as a function of pressure or either density for racemic ketoprofen and its methylated derivative (no possibility of h-bonding). It can be seen that each crystallization line (i.e., isobar, isochrone, isotherm) spans in the two-dimensional T-p space differently, signifying that the crystallization tendency of the studied liquids can be modified by choosing an adequate
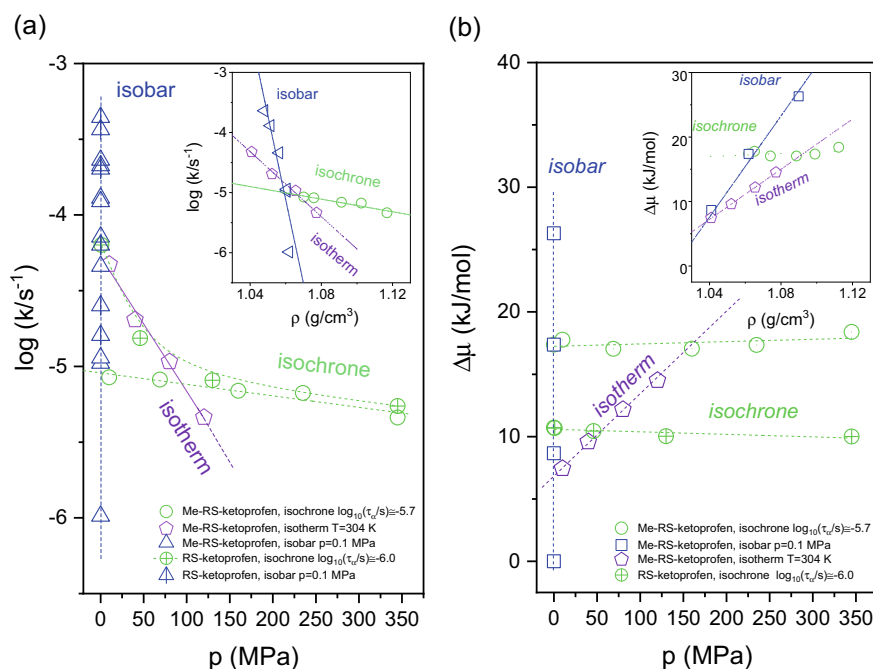
Fig. 14 Changes in the crystallization rate constant k **a** and a thermodynamic driving force towards crystallization $\Delta\mu$ **b** as a function of pressure and density (insets) along different iso-lines for ketoprofen and methyl ketoprofen (in the form of racemic mixtures). Re-adapted with permission from [66]. Copyright (2016) American Chemical Society

thermodynamic pathway. For example, a systematic slowing down of the crystallization rate is observed when lowering the temperature at a fixed pressure, or increasing pressure at a fixed temperature (Fig. 14a). Interestingly, considering changes of the liquid's density ρ along different iso-lines, it turns out that when keeping the same time scale of the molecular movements (isochrone) changes in the crystallization rate are relatively very small.

Intuitively, the thermodynamic driving force is expected to vary freely along isochrone. However, it is remarkable that $\Delta\mu$ (calculated using Eq. 4) changes only very little when increasing temperature and pressure while controlling the time scale of the molecular motions (see Fig. 14b). This surprising finding indicates that both fundamental factors governing the crystallization progress are in some way connected (or sense each other) even though only one of them is being explicitly controlled.

Same like with isochrones, we can also look in the T-p (T-ρ) space for iso-$\Delta\mu$ lines. While moving along such lines the contribution coming from the thermodynamic driving forces towards crystallization should be under control. Along iso-($\Delta\mu$) lines, the crystallization behavior of the supercooled liquid is expected to be driven primarily by the molecular mobility factor, while under isochronal conditions by the thermodynamic factor. Such experiments were performed for indomethacin (see Fig. 15). The results of the crystallization kinetic studies have led to a quite interesting
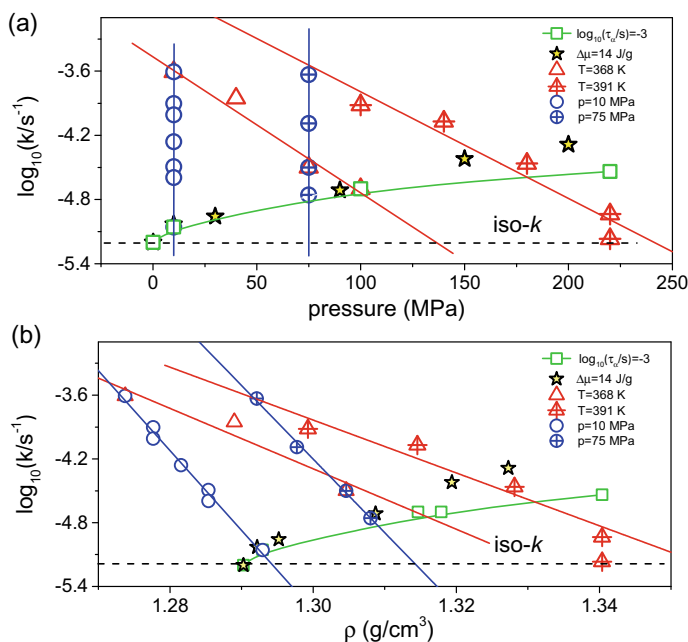
Fig. 15 Changes of the crystallization rate k as a function of **a** pressure and **b** density along different iso-lines for indomethacin. Adapted with permission from [62]. Copyright (2016) American Chemical Society

finding. When controlling exclusively the time scale of the molecular mobility (as reflected by α-relaxation) or the thermodynamic driving force, this leads to almost the same crystallization rate of indomethacin in the *T-p* plane. The very similar behavior of the crystallization rate along iso-τ_α and iso-$\Delta\mu$ lines indicate that there must be some hidden link between the kinetic and thermodynamic factors. This explains why keeping one factor to remain constant upon crystallization progress is immediately sensed by the other one, and why controlling thermodynamics and dynamics independently eventually leads to the same crystallization rate. Regrettably, it also demonstrates that with the use of pressure it is impossible to separate thermodynamics from dynamics. Lastly, by looking at the results presented in Fig. 15 it should be noted that in the *T-p* phase space it is also possible to find such iso-invariant points along which it will be possible to keep under control the crystallization rate (iso-*k*). Hence, by ably control of the temperature and pressure conditions, it is possible to control in a fully aware manner the crystallization behavior of the glass-forming liquids.

2.5 Crystallization of Single Enantiomers and Racemic Mixtures on Increased Pressure

Enantiomers are the pair of stereoisomers which are non-superimposable mirror images of each other. Although they are defined to be the optical isomers with no difference in the chemical and physical properties, numerous evidences demonstrate that they can differ in many different features (e.g., flavor or biological activity). This, potentially, might include also the differences in crystallization tendencies. Therefore, this study aimed to compare the crystallization tendency of pure enantiomers and their equimolar mixtures at ambient and elevated pressure. The sample under investigation is a chiral compound, ketoprofen, which belongs to a class of non-steroidal anti-inflammatory drugs. It is available on the market in the form of a racemic (1:1) mixture, although its biological activity results only from S-enantiomer (*R* is inactive) [76]. The worst scenario is however when one of the enantiomers has a therapeutic effect, while the other one is toxic (e.g., *thalidomide*).

Crystallization studies were carried out in the supercooled liquid state of racemic and enantiopure S-isomer. Both starting materials were completely crystalline with melting points at around 93.5 and 75 °C, respectively. The idea to compare the crystallization tendency of single enantiomer and the racemic mixture was based on the isochronal approach, i.e., following crystallization kinetics at various combinations of (T, p) but approximately the same τ_α. Although both materials differ significantly in the value of the melting temperature, their dynamics in the supercooled liquid state diverge only slightly [65]. Therefore, to match selected isochrone, $\log_{10}(\tau_\alpha/\text{s}) \cong -6$, a slightly different choice of (T, p) points were needed. For racemic ketoprofen this has included (314 K, 1 MPa), (323 K, 46 MPa), (343 K, 130 MPa), (383 K, 345 MPa)
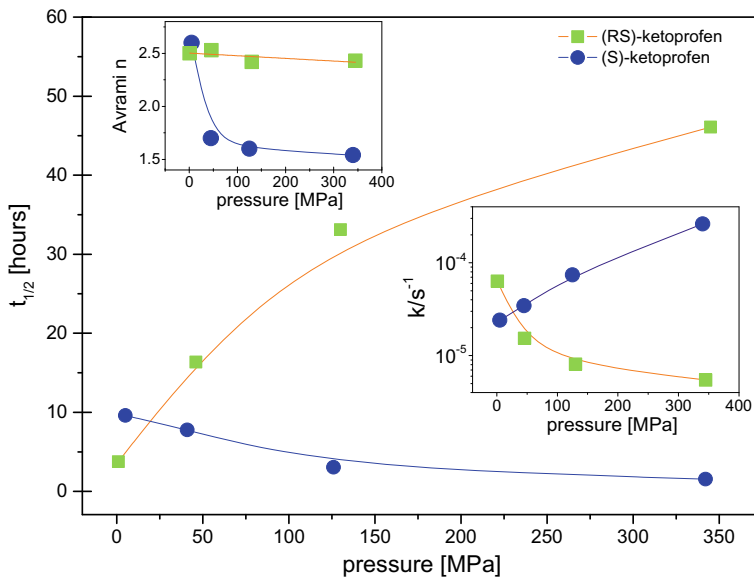
Fig. 16 Pressure evolution of the crystallization half-time (main panel), overall crystallization rate (lower inset), and Avrami parameter (upper inset) for S-ketoprofen and RS-ketoprofen crystallized along the same isochrone. Adapted with permission from [65]. Copyright (2015) American Chemical Society

while for S-ketoprofen (314 K, 5 MPa), (324 K, 41 MPa), (343 K, 126 MPa), (384 K, 342 MPa).

Changes in the overall crystallization rate and Avrami parameter for all studied (T, p) points located on the same isochrone are shown in the insets of Fig. 16. The former one provides information about the rate of transformation, while the latter one depends on the growth mechanisms and crystal shape. It is evident that when moving along an isochrone toward higher pressures, the crystallization of RS-ketoprofen slows down with increasing compression, while for S-ibuprofen it speeds up. These differences are even more straightforward when the crystallization half-time (i.e., time after which changes in the crystallinity of the sample reaches 50%) is considered. For example, for the racemic sample kept at 345 MPa and 384 K $t_{1/2}$ is almost 5 times longer when compared to its ambient pressure value. Meanwhile, the evolution of the Avrami exponent for racemic sample seems to be almost temperature and pressure invariant. In contrast, for S-enantiomer crystallization along the same isochrone speeds up with increasing pressure and half-time decreases. We found it very surprising that the crystallization tendencies of the racemic mixture and pure isomer are much different already at low pressure. For RS-ketoprofen, it proceeds faster ($t_{1/2} \cong 4$ h) than for its pure enantiomer ($t_{1/2} \cong 10$ h). This trend, however, changes completely on increased pressure. At around 345 MPa $t_{1/2} \cong 46$ h for RS while for the pure S form $t_{1/2} \cong 1.5$ h. As we suppose, at much higher pressure this may result in complete inhibition of the crystallization progress for the racemic

sample. Slowing down of the crystallization tendencies for racemic ketoprofen with increasing pressure and no evident changes in the value of the Avrami parameter is consistent with the results reported previously for RS-ibuprofen [77]. On the other hand, changes in the crystal morphology or growth process are expected for the single enantiomer sample, as indicated by the decrease of the Avrami parameter with pressure.

In agreement with the classical theory of nucleation and growth, when the kinetic factor is under control, changes in the crystallization rate can be ascribed solely due to thermodynamic force. Indeed, this is what we have observed for other molecular liquids, like describe above indomethacin. This argumentation can be also used to explain the ease of crystal formation with increasing pressure for S-ketoprofen. However, it fails for the racemic system under pressure. Note that similar slowing down of the crystallization progress was also reported for the racemic methylated derivative of ketoprofen in which we can exclude the hydrogen bonding contribution (see results in Fig. 14). As we presume, the peculiar behavior of racemic compounds must be related to the fact that it is a mixture of two "kinds" of molecules, not a single one. It is known from experimental studies that increasing the number of components in the mixture tends to suppress nucleation, as the chances that a critical nucleus of one particular kind is formed are reduced. However, in this case, another possible explanation should be also considered. As speculated by Jacques et al. [28] at certain conditions the Wallach rule can be invalidated and more densely packed structure of single enantiomers become suddenly more preferable under pressure, than their racemic mixture. As a result, by the application of pressure, spontaneous enantiomers resolution might be possible.

In the past few years, several experimental attempts (but without a success) have been carried out to prove that by crystallizing racemic compounds from various solvents under pressure or by squeezing racemic crystals it is possible to resolve optical isomers [78, 79]. Intriguingly, this remains still one of the most puzzling subjects within that field with no convincing experimental data provided so far. On the other hand, it is important to mention that Gonnade et al. demonstrated the occurrence of spontaneous resolution of racemates or even chiral symmetry breaking for crystallization carried out under various nonequilibrium conditions at ambient pressure [80]. Nevertheless, it remains rather an open question if the same effect can be obtained by high-pressure crystallization from the metastable supercooled liquid state, and whether the eutectic equilibrium between the racemate and single enantiomer follows the same lines as their melting transitions.

To summarize, the problem of physicochemical stability of racemic compounds on increased pressure is certainly an intriguing topic to study in the future, especially how pressure affects the affinity of enantiomers to each other. This study emphasizes the difference between the crystallization behavior of single enantiomers and their racemic mixture and demonstrates that in case of chiral compounds/or probably in more general sense eutectic compositions other factors should be also considered to gain some elementary understanding of their high-pressure crystallization behavior.

3 Summary and Conclusion

Controlling crystallization and glass-formation is important from both fundamental and practical application points of view. Crystallization is commonly discussed in many different fields of science, e.g., physics, chemistry, pharmacy, or material engineering. Irrespectively of that, there are still many numerous unclear aspects related to the crystallization process. Here, we demonstrate that some of them cannot be simply addressed by operating only with one thermodynamic variable, temperature, or either pressure. We need both, inasmuch the phase diagram for each substance is two, not one dimensional. Therefore, by ably control temperature and pressure conditions or moving in *T-p* phase space along certain iso-lines it is possible to affect the crystallization outcome in a fully aware manner. This has allowed us to perform first experimental attempts aimed at controlling the kinetic and thermodynamic factors responsible for crystallization progress, and demonstrate that the crystallization tendency of the glass-forming liquids is a path-dependent, and can be tuned—just like with the temperature—by changing the rate of compression/decompression. Another interesting aspect gained from this study is the peculiar behavior of racemic compounds, which in contrast to other systems shows spectacular slowing down of the crystallization progress on increased pressure. This raises the question of the possibility of spontaneous separation of enantiomers/or changes in the enantiomeric concentration as the effect of high-pressure crystallization. More research on high-pressure crystallization of glass-formers with different structures and intermolecular interactions; particularly liquids with competing interactions and strong directional bonding (e.g., hydrogen bonds and ionic liquids) should elucidate whether our observation regarding crystallization behavior of glass-forming liquids along different iso-lines can be treated as more general. This should benefit in the future to more ably control crystallization propensity of glass-forming liquids under various thermodynamic conditions.

References

1. Ediger MD, Harrowell P (2012) Perspective: supercooled liquids and glasses. J Chem Phys 137:080901
2. Kawasaki T, Tanaka H (2010) Formation of a crystal nucleus from liquid. PNAS 107(32):14036–14041
3. Tammann G (1925) Glasses as supercooled Liquids. J Soc Glas Technol 9:166–185
4. Pukánszky B, Mudra I, Staniek P (2004) Relation of crystalline structure and mechanical properties of nucleated polypropylene. J Vinyl Addit Technol 3(1):53–57
5. Myerson A (2001) Handbook of industrial crystallization, 2nd edn. Butterworth-Heinemann
6. Wunderlich B (1973) Macromolecular physics. Volume 1: Crystal structure, morphology, defects. Academic Press

7. Fredriksson H, Åkerlind U (2012) Solidification and crystallization processing in metals and alloys. Wiley
8. Kauzmann W (1948) The nature of the glassy state and the behavior of liquids at low temperatures. Chem Rev 43(2):219–256
9. Turnbull D (1969) Under what conditions can a glass be formed? Contemp Phys 10(5):473–488
10. Anderson PW (1995) Through the glass lightly. Science 267(5204):1615–1616
11. Chang K (2017) The nature of glass remains anything but clear. Physics Today
12. Seife C (2005) So much more to know. Science 309(5731):78–102
13. Shintani H, Tanaka H (2006) Frustration on the way to crystallization in glass. Nat Phys 2:200–206
14. Vekilov PG (2010) The two-step mechanism of nucleation of crystals in solution. Nanoscale 2:2346–2357
15. Erdemir D, Lee YA, Meyerson AS (2008) Nucleation of crystals from solution: classical and two-step models. Acc Chem Res 42:621
16. Hancock BC, Zografi G (1997) Characteristics and significance of the amorphous state in pharmaceutical systems. J Pharm Sci 86(1):1–12
17. Bernstein J (2002) Polymorphism in molecular crystals. Oxford Science Publications
18. Shekunov BY, York P (2000) Crystallization processes in pharmaceutical technology and drug delivery design. J Cryst Growth 211:122–136
19. Zhang J, Yan D-X, Xu J-Z, Huang H-D, Lei J, Li Z-M (2012) Highly crystallized poly(lactic acid) under high pressure. AIP Adv 1:042159
20. Bridgman PW (1964) General survey of certain results in the field of high-pressure physics. Nobel Lectures, Bridgman PW (ed). Elsevier Publishing Company, Amsterdam
21. Yuan Y, Bi Y, Huang J (2011) Achieving high efficiency laminated polymer solar cell with interfacial modified metallic electrode and pressure induced crystallization. J Appl Phys Lett 98:063306
22. Sauer JA, Pae KD (1968) Structure and thermal behavior of pressure crystallized polypropylene. J Appl Phys 39:4959
23. Neumann MA, van de Streek J, Fabbiani FPA, Hidber P, Grassmann O (2015) Combined crystal structure prediction and high-pressure crystallization in rational pharmaceutical polymorph screening. Nat Commun 6:7793
24. Visuri K, Kaipainen E, Kivimaki J, Niemi H, Leisola M, Palosaari S (1990) A new method for protein crystallization using high pressure. Bio/Technol 8:547–549
25. McMillan PF (2002) New materials from high-pressure experiments. Nature 1(19):19–25
26. Torikachvili MS, Bud'ko SL, Ni N, Canfield PC (2008) Pressure induced superconductivity in $CaFe_2As_2$. Phys Rev Lett 101:057006
27. Sato T, Funamori N (2010) High-pressure structural transformation of SiO_2 glass up to 100 GPa. Phys Rev B 82:184102
28. Jacques J, Collet A, Wilen SH (1994) Enantiomers, racemates, and resolutions. Krieger Publishing Company
29. Tanaka H (2011) Roles of bond orientational ordering in glass transition and crystallization. J Phys Condens Matter 23:284115
30. Aziz MJ, Nygren E, Hays JF, Turnbull D (1985) Crystal growth kinetics of boron oxide under pressure. J Appl Phys 57(6):2233–2242
31. Lu G-Q, Nygren E, Aziz MJ, Turnbull D, White CW (1989) Interferrometric measurement of the pressure-enhanced crystallization rate of amorphous Si. Appl Phys Lett 54:2583–2585
32. Uhlmann DR, Hays JF, Turnbull D (1966) The effect of high pressure on crystallization kinetics with special reference to fused silica. Phys Chem Glas 7(5):159–168
33. Lu GQ, Nygren E, Aziz MJ, Turnbull D, White CW (1989) Pressure-enhanced crystallization kinetics of amorphous Si and Ge: implications for point-defect mechanisms. Appl Phys Lett 54:2583–2585
34. Ohtani E (ed) (2007) Advances in high-pressure mineralogy. Geological Society of America Special Papers. No. 421. Geological Society of America

35. Syono Y, Manghnani MH (eds) (1992) High-pressure research: application to earth and planetary sciences, geophysical. Terra Scientific Publishing Company
36. Gutzow I, Durschang D, Russel CJ (1997) Crystallization of glassforming melts under hydrostatic pressure and shear stress. Part 1. Crystallization catalysis under hydrostatic pressure: possibilitites and limitations. J Mater Sci 32:5389−5403
37. Hikosaka M, Rastogi S, Keller A, Kawabata H (1992) Investigations on the crystallization of polyethylene under high pressure: role of mobile phases, lamellar thickening growth, phase transformations, and morphology. J Macromol Sci Part B Phys 32(1):87–131
38. Munehisa Y, Chitoshi N, Tetuo T (1973) Melting and crystallization process of polyethylene under high pressure. Polym J 4(5):526–533
39. Phillips PJ, Tseng HT (1989) Influence of pressure on crystallization in poly(ethylene terephthalate). Macromolecules 22(4):1649–1655
40. Mierzwa M, Paluch M, Rzoska SJ, Ziolo J (2008) The liquid—glass and liquid—liquid transitions of TPP at elevated pressure. J Phys Chem B 112:10383–10385
41. Chason E, Aziz MJ (1991) Effect of pressure on crystallization kinetics of cordierite glass. J Non-Cryst Solids 130:204–210
42. Lu G-Q, Nygren E, Aziz MJ, Turnbull D, White CW (1988) Time-resolved reflectivity measurement of the pressure-enhanced crystallization rate of amorphous Si in a diamond anvil cell. Mater Res Soc Symp Proc 100:435–440
43. Becker R, Döring W (1935) Kinetische Behandlung Der Keimbildung in Übersättigten Dämpfen. Ann Phys 24:719–752
44. Farkas LZ (1927) Keimbildungsgeschwindigkeit in übersättigten Dämpfen. Phys Chem A 125:236–242
45. Turnbull D, Fisher JC (1949) Rate of nucleation in condensed systems. J Chem Phys 17(1):71–73
46. Devaud G, Aziz MJ, Turnbull D (1989) High pressure crystallization of As_2S_3. J Non-Cryst Solids 109:121–128
47. Schmelzer JWP, Abyzov AS, Fokin VM (2016) Thermodynamic aspects of pressure-induced crystallization: Kauzmann pressure. Int J Appl Glas Sci 7:474–485
48. Schmelzer JWP, Abyzov AS (2018) Pressure-induced crystallization of liquids: maxima of nucleation, growth, and overall crystallization rates. Int J Appl Glas Sci 9:198–207
49. Schmelzer JWP (2005) Nucleation theory and applications. Wiley-VCH
50. Shelby JE (1997) Introduction to glass science and technology. Royal Society of Chemistry
51. Zanotto ED (1992) Crystallization of liquids and glasses. Bras J Phys 22:77–84
52. Schmelzer JWP, Zanotto ED, Avramov I, Fokin VMJ (2006) Stress development and relaxation during crystal growth in glass-forming liquids. J Non-Cryst Solids 352:434−443
53. Hatase M, Hanaya M, Hikima T, Oguni M (2002) Discovery of homogeneous-nucleation-based crystallization in simple glass-forming liquid of toluene below its glass-transition temperature. J Non-Cryst Solids 307:257–263
54. Konishi T, Tanaka H (2007) Possible origin of enhanced crystal growth in a glass. Phys Rev B 76:220201(R)
55. Floudas G, Paluch M, Grzybowski A, Ngai KL (2011) Molecular dynamics of glass-forming systems. Springer-Verlag Berlin and Heidelberg GmbH & Co. KG
56. Descamps M, Disordered pharmaceutical materials. Wiley-VCH Verlag GmbH & Co. KGaA
57. Richert R (ed) (2018) Nonlinear dielectric spectroscopy. Springer International Publishing
58. Volkov AA, Prokhorov AS (2003) Broadband dielectric spectroscopy of solids. Radiophys Quantum Electron 46(8–9):657–665
59. Kremer F, Schönhals A (2003) Broadband dielectric spectroscopy. Springer-Verlag Berlin Heidelberg
60. Avrami M (1940) Kinetics of phase change I General theory. J Chem Phys 8:212–224
61. Szklarz G, Adrjanowicz K, Paluch M (2018) Cooling-rate versus compression-rate dependence of the crystallization in the glass-forming liquid. Propylene Carbonate Cryst Growth Des 18(4):2538–2544

62. Adrjanowicz K, Koperwas K, Szklarz G, Tarnacka M, Paluch M (2016) Exploring the crystallization tendency of glass-forming liquid indomethacin in the T-p plane by finding different iso-invariant points. Cryst Growth Des 16(12):7000–7010

63. Adrjanowicz K, Grzybowski A, Grzybowska K, Pionteck J, Paluch M (2014) Effect of high pressure on crystallization kinetics of van der Waals liquid: an experimental and theoretical study. Cryst Growth Des 14(5):2097–2104

64. Adrjanowicz K, Grzybowski A, Grzybowska K, Pionteck J, Paluch M (2013) Toward better understanding crystallization of supercooled liquids under compression: isochronal crystallization kinetics approach. Cryst Growth Des 13(11):4648–4654

65. Adrjanowicz K, Kaminski K, Paluch M, Niss K (2015) Crystallization behavior and relaxation dynamics of supercooled S-ketoprofen and the racemic mixture along an isochrone. Cryst Growth Des 15(7):3257–3263

66. Adrjanowicz K, Koperwas K, Tarnacka M, Grzybowska K, Niss K, Pionteck J, Paluch M (2016) Changing the tendency of glass-forming liquid to crystallize by moving along different isolines in the T-p phase diagram. Cryst Growth Des 16(11):6263–6268

67. Paluch M (2016) Dielectric properties of ionic liquids. Springer International Publishing

68. Zallen R (2004) The physics of amorphous solids. Wiley-VCH Verlag GmbH & Co. KGaA

69. Koperwas K, Adrjanowicz K, Wojnarowska Z, Jedrzejowska A, Knapik J, Paluch M (2016) Glass-forming tendency of molecular liquids and the strength of the intermolecular attractions. Sci Rep 6:36934

70. Bauer M, Elsaesser MS, Winkel K, Mayer E, Loerting T (2008) Compression-rate dependence of the phase transition from hexagonal ice to ice II and/or ice III. Phys Rev B Condens Matter Mater 77:220105

71. Bauer M, Winkel K, Toebbens DM, Mayer E, Loerting T (2009) Hexagonal ice transforms at high pressures and compression rates directly into "doubly metastable" ice phases. J Chem Phys 131:224514

72. Adrjanowicz K, Koperwas K, Paluch M (2017) Isobaric cooling or isothermal compression? Unveiling the effect of path dependence on crystallization. Cryst Growth Des 17(6):2950–2954

73. Sharifi S, Prevosto D, Capaccioli S, Lucchesi M, Paluch M (2007) Effect of thermodynamic history on secondary relaxation in the glassy state. J Non-Cryst Solids 7(353): 4313–4317

74. Prevosto D, Capaccioli D, Lucchesi M, Rolla PA, Paluch M, Pawlus S (2006) On the relevance of the coupling model to experiments. Phys Rev B Condens Matter Mater Phys 73:104205

75. Mullin JW (2001) Crystallization, 4th edn. Butterworth-Heinemann

76. Jamali F, Brocks DR (1990) Clinical pharmacokinetics of ketoprofen and its enantiomers. Clin Pharmacokinet 19:197–217

77. Adrjanowicz K, Kaminski K, Wojnarowska Z, Dulski M, Hawelek L, Pawlus S, Paluch M, Sawicki W (2010) Dielectric relaxation and crystallization kinetics of ibuprofen at ambient and elevated pressure. J Phys Chem B 114(19):6579–6593

78. Marciniak J, Andrzejewski M, Cai W, Katrusiak A (2014) Wallach's rule enforced by pressure in mandelic acid. J Phys Chem C 118(8):4309–4313

79. Rietveld IB, Barrio M, Tamarit J-L, Do B, Ceolin R (2011) Enantiomer resolution by pressure increase: inferences from experimental and topological results for the binary enantiomer system (R)- and (S)-mandelic acid. J Phys Chem B 115:14698–14703

80. Gonnade RG, Iwama S, Sugiwake R, Manoj K, Takahashi H, Tsue H, Tamura R (2012) Occurrence of spontaneous resolution of ketoprofen with a racemic crystal structure by simple crystallization under nonequilibrium preferential enrichment conditions. Chem Commun 48:2791–2793

Crystallization of Amorphous Pharmaceuticals at Ambient and Elevated Pressure Conditions

Justyna Knapik-Kowalczuk, Krzysztof Chmiel, and Marian Paluch

Abstract Currently, the pharmaceutical industry is struggling with the problem of solubility-limited bioavailability of marketed and newly synthesized Active Pharmaceutical Ingredients (APIs). The conversion of these APIs into its amorphous form is, without a doubt, a solution for this serious problem. There is, however, one main limiting factor of widespread use of these drugs. Amorphous materials are thermodynamically unstable, and therefore, during the time of storage or manufacturing, they might revert to their crystalline form. In this chapter, we describe the main factors responsible for the re-crystallization of an amorphous APIs. Special attention is paid on differences between the physical stability of amorphous pharmaceuticals stored at standard and manufacturing storage conditions.

Keywords Broadband Dielectric Spectroscopy · Crystallization · Physical stability · Elevated pressure · Amorphous pharmaceutical · Solubility limit

Abbreviations

APIs	Active Pharmaceutical Ingredients
AG	Adam and Gibbs model
ASD	Amorphous Solid Dispersion
ARP	Aripiprazol
BIC	Bicalutamide
BCS	Biopharmaceutics Classification System

J. Knapik-Kowalczuk · K. Chmiel · M. Paluch (✉)
Faculty of Science and Technology, Institute of Physics, University of Silesia, SMCEBI, 75 Pułku Piechoty 1a, 41-500 Chorzow, Poland
e-mail: marian.paluch@us.edu.pl

J. Knapik-Kowalczuk
e-mail: justyna.knapik-kowalczuk@us.edu.pl

K. Chmiel
e-mail: krzysztof.chmiel@smcebi.edu.pl

BDS   Broadband Dielectric Spectroscopy
DSC   Differential Scanning Calorimetry
EZB   Ezetimibe
FLU   Flutamide
G-T   Gordon-Taylor
HN   Havriliak-Negami
HME   Hot Melt Extrusion
KVA   Kollidon VA64®
LDL   Low-density lipoprotein
NPC1L1   Niemann-Pick C1-Like1
NIM   Nimesulid
NSAID   Non-steroidal anti-inflammatory drug
NMR   Nuclear Magnetic Resonance
PCS   Photon Correlation Spectroscopy
PVAc   Poly vinylacetate
PVP   Poly vinylpyrrolidone
PALS   Positron Annihilation Lifetime Spectroscopy
PBC   Probucol
QENS   Quasielastic Neutron Scattering
R&D   Research and Development
SOP   Soluplus®
TMDSC   Temperature-Modulated Differential Scanning Calorimetry
THz   Terahertz spectroscopy
TSDC   Thermally Stimulated Depolarization Current
TTS   Time–Temperature Superposition
VFT   Vogel−Fulcher−Tammann equation
XRD   X-ray diffraction

1 Introduction

The Biopharmaceutics Classification System (BCS) categorizes Active Pharmaceutical Ingredients (APIs) based on their aqueous solubility and intestinal permeability into four groups [1]. Drugs belonging to BCS class I are characterized by high permeability and high solubility. Pharmaceuticals from II BCS class have also high permeability, but unfortunately, they reveal low solubility. The opposite situation, i.e. high solubility but low permeability, can be found in APIs from BCS class III, while the last—IV—BCS group consists of drugs revealing low solubility together with low permeability. The solubility in the BCS is defined in relation to the highest dose strength in an immediate-release product. An API is considered *highly soluble* when the highest dose strength is soluble in 250 mL or less of aqueous media over the pH range of 1–7.5 at 310 K. The permeability classification in the BCS is based directly on the extent of intestinal absorption of an API in humans or indirectly on the

Table 1 Solubility and permeability drugs in the market and in the development pipeline according to Biopharmaceutical Classification System

BCS class	Solubility	Permeability	% drugs on the market[a]	% drugs in the R&D pipeline[a]
I	High	High	35	5–10
II	Low	High	30	60–70
III	High	Low	25	5–10
IV	Low	Low	10	10–20

[a]Data are taken from [3, 4]

measurements of the rate of mass transfer across the human intestinal membrane [2]. A drug substance is considered *highly permeable* when the extent of absorption is determined to be equal or higher than 90% of an administered dose. Table 1 presents the percentage of drugs on the market and in research and development (R&D) pipeline in each of the aforementioned BCS classes.

The data presented in Table 1 indicate that the pharmaceutical industry is facing a serious problem connected with incising number of poorly soluble APIs. To the II and IV BCS classes, one can classify approximately 40% of all drugs currently available on the market. Interestingly, it has been estimated that nearly 90% of drugs in the R&D pipeline suffer from the same problem. Solubility-limited bioavailability of both current and novel APIs led to the exploration of innovative methods helping to overcome this issue [5]. Salt formation, cocrystallization, amorphization and transformation into metastable polymorphic forms are the best examples of these approaches [6]. Recent studies revealed that among all aforementioned methods the conversion of a crystalline drug into its amorphous form is the most promising approaches improving the water solubility of APIs [7–10].

Due to the lack of long-range three-dimensional molecular order, the amorphous state is the highest energy form of a solid material [11, 12]. As a result, the conversion to an amorphous form API is characterized by higher apparent solubility, faster dissolution rate as well as better bioavailability in comparison with its crystalline counterpart [13]. These benefits, however, come at a cost [14]. Foremost, amorphous pharmaceuticals are physically unstable systems [15]. Consequently, during manufacturing or storage, they might revert to their crystalline form, losing at the same time their superior properties [16–18]. Thus, to fully exploit the advantages given by APIs in the disordered state, it is important to characterize their tendency towards re-crystallization, and if necessary find the most effective method of their stabilization [19–21].

One of the approaches proposed to determine the physical stability of the amorphous pharmaceuticals was based on the analysis only the thermodynamic properties such as the configurational entropy (S_{conf}), the configurational enthalpy (H_{conf}), and the configurational Gibbs free energy (G_{conf}).[22–24]. According to the performed analysis, it has been suggested to correlate the physical stability of amorphous APIs and their tendency towards re-crystallization to S_{conf} or H_{conf}. However, throughout

the further investigations, it has been realized that solving the problem associated with physical instability of amorphous pharmaceuticals is impossible only on the basis of the thermodynamic factors [25]. It turns out that the investigated macroscopic thermodynamic quantities do not fully reflect the molecular mechanisms that govern the devitrification. Thus, the most relevant factor that is currently recommended to be studied to predict the tendency of amorphous pharmaceuticals toward re-crystallization is molecular mobility [1, 14, 26–29]. It has to be highlighted that the search for the proper correlation between physical stability of amorphous APIs and their molecular mobility is also not an easy task. It is mainly because pharmaceuticals usually exhibit complex molecular structures of different configurational topologies and a variety of intra- or intermolecular interactions such as hydrogen bonds of various strength and electrostatic forces. Consequently, amorphous pharmaceuticals usually reveal complex molecular mobility that is reflected in the multitude relaxation processes. Taking this fact into account, it is crucial to assess which molecular motion is responsible for the re-crystallization of the specific amorphous API. *Does the primary (global) relaxation, associated with the glass transition, control the devitrification process*? *Or maybe the secondary (local) relaxation plays here a crucial role*?

There is a number of experimental methods which can be employed to study molecular dynamics of amorphous pharmaceuticals. The following list includes some of them: mechanical spectroscopy, Broadband Dielectric Spectroscopy (BDS), Nuclear Magnetic Resonance (NMR), Temperature-Modulated Differential Scanning Calorimetry (TMDSC), Quasielastic Neutron Scattering (QENS), Photon Correlation Spectroscopy (PCS), Terahertz spectroscopy (THz) or Positron Annihilation Lifetime Spectroscopy (PALS) [12, 25, 30]. Taking into account that BDS, in comparison with the other techniques, allows to perform measurements in the widest range of frequency (i.e., 18 decades—from µHz to THz), temperatures (from 123 to 523 K) and even pressures (from 0.1 MPa to 1.8 GPa) it is considered the most powerful tool to study the molecular dynamics of disordered APIs (see Fig. 1). By employing this experimental method, it is possible to examine the molecular mobility of pharmaceuticals in both supercooled liquid and glassy states that enable to distinguish both global and local molecular motions.

In addition, it has been recently demonstrated that the BDS technique can be used to investigate the physical stability of amorphous APIs at conditions imitating drugs manufacturing, for example, short-term compression. Because in some cases it was established that such conditions might entirely modify the tendency of amorphous APIs toward devitrification, the imitating drug manufacturing dielectric studies become more and more important [16, 19, 31, 32]. Based on dielectric data, it is also possible to determine the solubility limit of the amorphous drug in stabilizer, e.g. polymeric matrix, what finally allows to create a saturated solution [33]. This is crucial considering the fact that supersaturated solution (e.g. of the API–polymer composition) is by definition thermodynamically unstable.

In this chapter, it will be described how to investigate the tendency of amorphous pharmaceuticals toward re-crystallization based only on the dielectric data. It will be shown how quickly, i.e., based on non-isothermal studies, determine which API
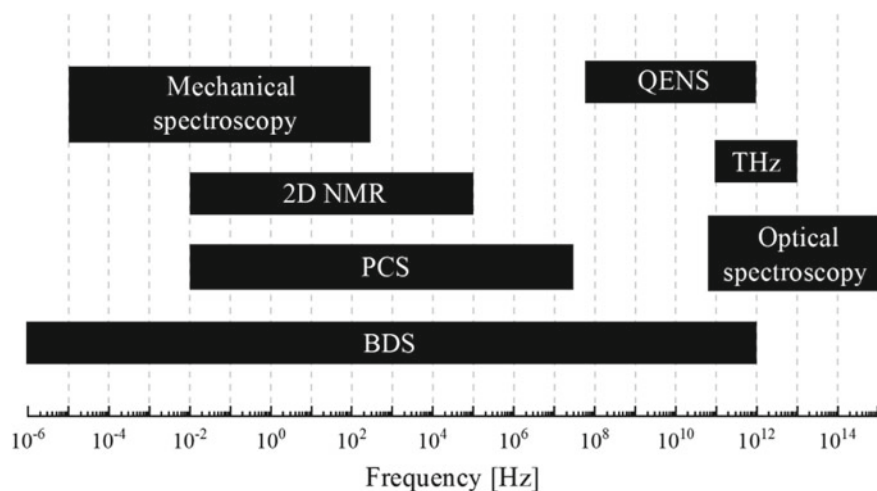
Fig. 1 The frequency range available for various experimental methods for the investigation of molecular

reveals the greatest tendency toward devitrification. On the example of isothermal dielectric experiments, it will be explained how to investigate and analyse the crystallization kinetics of amorphous APIs. Additionally, it will be shown how, based on the data obtained from BDS measurements, one can predict the physical stability of disordered drugs. The last two subsections will be devoted to (i) the dielectric experiments performed under conditions imitating drug's manufacturing as well as (ii) determination of the solubility limit in the drug-excipient compositions with the use of the dielectric spectroscopy.

2 Physical Stability Studies of Amorphous APIs Stored at Ambient Pressure Conditions

The limited physical stability of amorphous APIs is the main reason behind the lack of their widespread use in pharmaceutical industry. Therefore, it is very important to assess the re-crystallization tendency of disordered APIs as well as to determine the minimal time of their physical stability at both standard storage and elevated temperature conditions. Very sensitive experimental tool for detecting and quantifying recrystallization processes occurring in drugs is BDS [34]. This technique is very sensitive to the changes associated with a reduction of the number of relaxing dipoles. As the degree of drug's crystallinity increases, the number of relaxing dipoles decreases, because of their immobilization in crystal lattice. Reduction in the number of relaxing dipoles is observed as a drop in the dielectric strength $\Delta\varepsilon_\alpha$ of the structural α-process. The dielectric strength $\Delta\varepsilon_\alpha$ depends on the number N of relaxing

dipoles per unit of volume, which are characterized by the permanent dipole moment μ (e.g. $\Delta\varepsilon_\alpha \sim N\mu^2$ in the Onsager model). Thus, by employing the BDS, it is possible to investigate both the non-isothermal and isothermal crystallization of amorphous pharmaceuticals by analysing the changes in $\Delta\varepsilon_\alpha$ as a function of temperature or time.

In the following subsections, it will be presented how to quickly assess the tendency of amorphous APIs toward re-crystallization based on non-isothermal dielectric experiments. Additionally, it will be shown what information about the drug's physical stability can be obtained from the isothermal dielectric measurement and the appropriate way to analyse such data. Since pharmaceuticals for most of the time are stored at standard storage conditions, i.e. room temperature and atmospheric pressure, we will describe the methods that are usually employed to predict the physical stability of disordered pharmaceuticals stored at glassy state, based on the dielectric data registered at $T > T_g$.

2.1 Non-isothermal Crystallization Studies

To investigate the molecular mobility of amorphous APIs, and consequently to determine the temperature evolution of the measured relaxation processes, one needs to perform a non-isothermal BDS experiment. During this measurement, the dielectric spectra might be collected within a broad range of temperatures and frequencies. Therefore, it is possible to observe the relaxation processes occurring both below and above the glass transition temperature. In the supercooled liquid region i.e. above T_g (defined as the temperature at which the τ_α reaches 100 s), the dominant process is structural (α; global) relaxation, which originates from cooperative motion of many molecules. On the other hand, at $T < T_g$, the α-process becomes too slow to be experimentally observed, and only a secondary relaxation processes, which reflect fast local motions having an inter- or intramolecular origin, can be detected. The representative imaginary (ε'') and real (ε') parts of complex dielectric permittivity, of four different pharmaceuticals, which were investigated at $T > T_g$ are presented in Fig. 2. Panels a and b of this figure show the spectra of flutamide (FLU)—a non-steroidal antiandrogen, which is mainly used to treat prostate cancer. Dielectric dispersion spectra of nimesulid (NIM) are depicted respectively in panels c and d. This pharmaceutical is a non-steroidal anti-inflammatory drug (NSAID) with analgesic and antipyretic properties [35]. Third pharmaceutical, which spectra have been presented in Fig. 2 (panel e and f) is ezetimibe (EZB). This API is mainly used to lower plasma cholesterol levels. EZB is collected in the small intestinal brush border membrane, where it selectively inhibits the absorption of cholesterol by binding it to Niemann-Pick C1-Like1 (NPC1L1) proteins. Probucol (PBC), i.e. the last pharmaceutical of which dielectric spectra are presented in Fig. 2, has very similar to EZB pharmacological properties—it lowers cholesterol levels. This API, however, has completely different mechanism of action than EZB. Mainly, it eliminates cholesterol from the body by increasing the fractional rate of low-density lipoprotein (LDL) catabolism in the
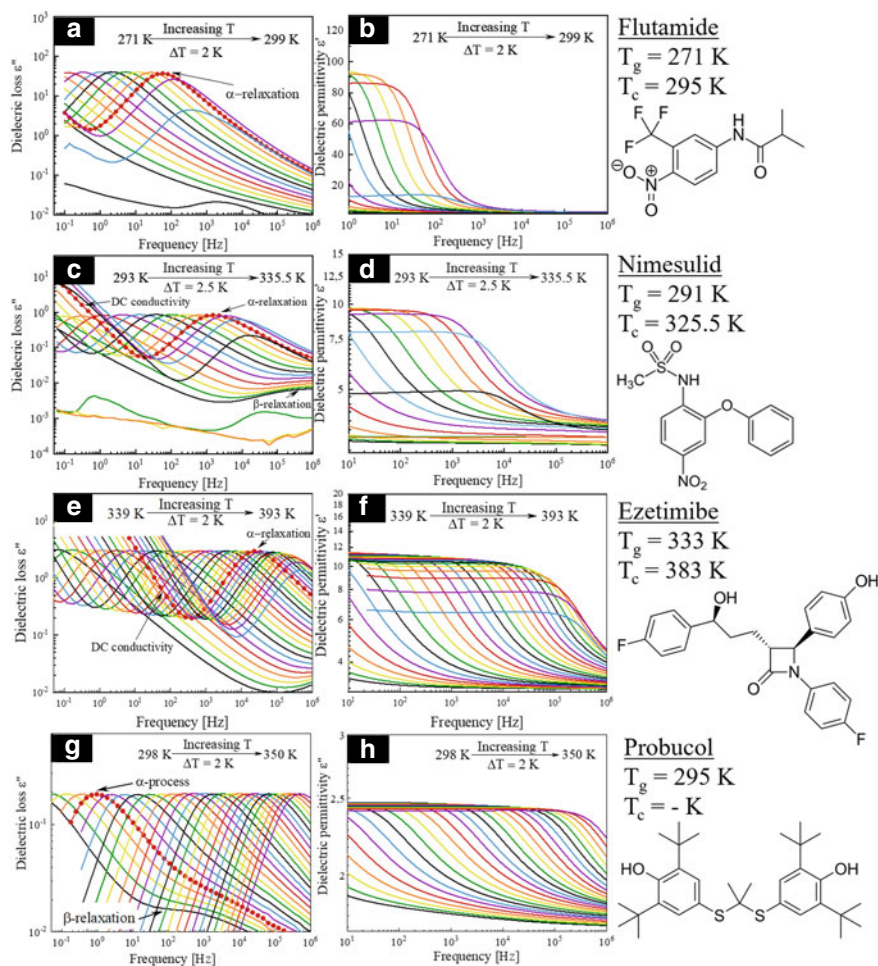
Fig. 2 Dielectric spectra of four selected APIs: **a** and **b** FLU, **c** and **d** NIM, **e** and **f** EZB and **g** and **h** PBC, measured at ambient pressure and at different temperatures above their T_g

final metabolic pathway. It also acts as an inhibitor of the initial stages of cholesterol synthesis, blocks the oxidation and tissue deposition of LDL cholesterol, thereby inhibiting atherogenesis.

As can be seen in Fig. 2 a, c, e, and f, on the dielectric loss spectra of amorphous pharmaceuticals, which were register at $T > T_g$, one might notice even three features. Beginning from the lowest frequencies: (i) the dc conductivity associated with translational motions of ions (see loss spectra of NIM and EZB); (ii) the well-resolved loss peak associated with the structural (α; global) relaxation process (visible in all presented cases); as well as (iii) the secondary (β; local) relaxation peak of much weaker than α-relaxation amplitude (see loss spectra of PBC and NIM).

It should be pointed out that the structural relaxation process moves toward higher frequencies during heating of the sample, indicating increased molecular mobility. For some pharmaceuticals, above a certain temperature, a rapid drop in the intensity of the α-relaxation peak (in the case of ε'') and a gradual decrease of the static permittivity (ε_s) (in this case of ε') can be observed. Discussed phenomenon was observed in case of the presented above FLU, NIM and EZB. The rapid drop in the intensity of the α-relaxation process begins at temperatures equal to 295, 325.5 and 385 K for FLU, NIM and EZB, respectively (see Fig. 2a–f). This, naturally, is a consequence of the reduction in the total number of actively reorienting dipoles, which contribute to the relaxation process while the fraction of amorphous phase decreases during the crystallization:

$$N\mu^2 \sim \varepsilon_s - \varepsilon_\infty = \Delta\varepsilon = \frac{2}{\pi}\int_0^\infty \varepsilon''(\omega)d\ln\omega \qquad (1)$$

The tendency of amorphous APIs toward non-isothermal re-crystallization can be evaluated in relation to either room temperature (T_{room}) or glass transition temperature (T_g). By comparing the temperature of the onset of the drug re-crystallization to the room temperature, one can assess which pharmaceutical has a greater potential to remain in an amorphous form at standard storage condition for required—shelf-life time—stability. On the basis of, presented in Fig. 3a, plot of $\Delta\varepsilon'_N(T)$ one can observe that FLU begins to re-crystallize during non-isothermal measurements at $T < T_{\mathrm{room}}$. This result clearly indicates that amorphous form of this pharmaceutical, among all investigated above APIs, reveals the lowest physical stability. The amorphous form of FLU, stored at room temperature, fully reverts to its crystalline form in less than half an hour [36]. Another examined pharmaceutical—NMS—has a slightly higher physical stability. It begins to re-crystallize during non-isothermal BDS experiment at temperature approximately 20 K higher than T_{room}. Interestingly, PBC having almost the same T_g value as NIM did not reveal any propensity to the re-crystallization during dielectric measurement, what suggest high stability of the amorphous form of this medication. EZB starts to devitrify over 80 K above room temperature indicating that this API should be definitely more stable, when stored at T_{room}, than NIM or FLU. Considering that NIM remains physically stable at $T = T_{\mathrm{room}}$ for a few hours, while the first sign of the EZB's crystallization, at the same temperature conditions, was observed after 21 days, one can conclude that the latter compound exhibits indeed greater physical stability than the former.

The physical stability of amorphous APIs can be also assessed by comparing the differences between the temperature at which the crystallization onset was registered (T_c) to the sample's T_g. This approach allows to evaluate the tendency of amorphous drugs toward re-crystallization at isochronal conditions ($\tau_\alpha = $ const.). Representative example of the discussed comparison, performed according to the aforementioned approach, is presented in Fig. 3b. This analysis was made on the same data sets of FLU, NIM, EZB and PBC. As can be seen in this representation the very high physical stability of PBC is greatly emphasized.
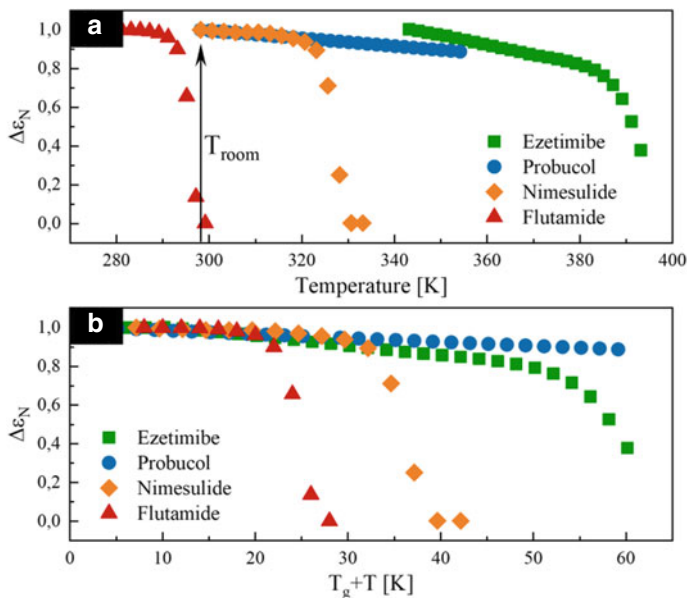
Fig. 3 Comparisons of temperature dependences of normalized dielectric strengths $\Delta\varepsilon'_N$ of four selected pharmaceuticals FLU (red triangles), NIM (orange diamonds), EZB (green squares) and PBC (blue circles). **a** Data as a function of temperature (T) and **b** as a function of $T_g + T$

2.2 Isothermal Crystallization Studies

Besides the non-isothermal studies, the crystallization of amorphous APIs can be monitored by BDS also at isothermal conditions. During such experiments the spectra of complex dielectric permittivity ($\varepsilon^*(\omega) = \varepsilon'(\omega) - i\varepsilon''(\omega)$) of the examined pharmaceutical are registered at a chosen temperature, in the supercooled liquid region, at the specified time intervals until the sample fully re-crystallize. Figure 4 shows the representative results from discussed measurements i.e. frequency dependencies of the real and the imaginary part of the complex dielectric permittivity of NIM panels a and b, respectively. During this experiment NIM was stored at $T = 328$ K, while the set time interwall was equal to 120 s. The total re-crystallization of the sample occurred after approximately 90 min.

It is clearly seen that after an induction time, during which no changes between the spectra were observed, both the amplitude of α-relaxation loss peak as well as a static dielectric permittivity begin to rapidly decrease with time. As it has been already mentioned, such a sudden drop in the $\Delta\varepsilon_\alpha$ is typical for the re-crystallization process during which a reduction in the number of reorienting dipoles, contributing to the structural relaxation, proceeds.

To properly analyse the kinetics of devitrification of amorphous pharmaceuticals, data corresponding to the real permittivity should be normalized (ε'_N) as follows:

Fig. 4 Dielectric spectra of the real (**a**) and imaginary (**b**) parts of the complex dielectric permittivity during an isothermal cold crystallization of NMS at fixed temperature equal to 238 K
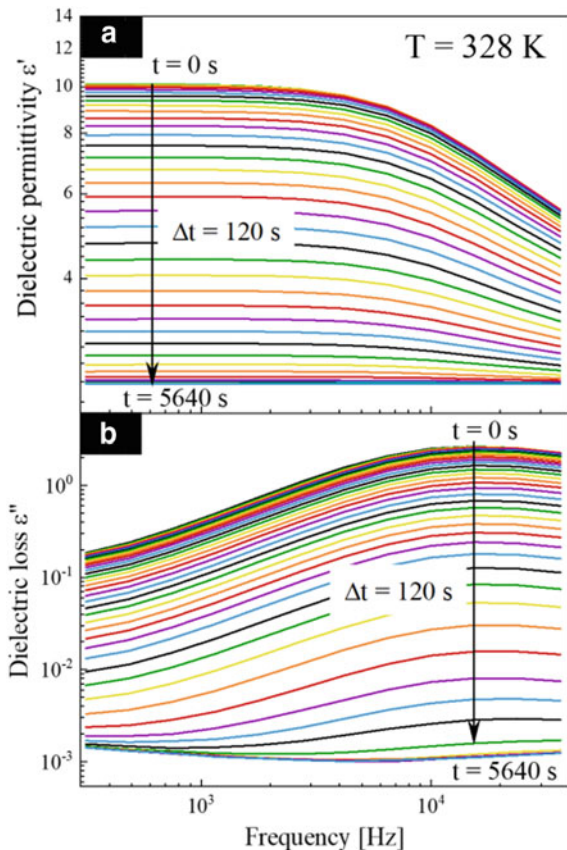
$$\varepsilon'_N(t) = \frac{\varepsilon'(0) - \varepsilon'(t)}{\varepsilon'(0) - \varepsilon'(\infty)} \tag{2}$$

where $\varepsilon'(0)$ is the initial static dielectric permittivity, $\varepsilon'(t)$ is the value at time t, and $\varepsilon'(\infty)$ is the long-time limiting value. Kinetic curves of NIM obtained from experiments performed at four different temperatures equal to 318, 323, 328 and 330.5 K were normalized according to the procedure described above and are presented in Fig. 5. As can be seen, with decreasing temperature, the re-crystallization processes of NIM slows down.

There are two key models that are usually employed to analyse the isothermal crystallization kinetics of amorphous pharmaceuticals investigated by means of BDS. First one was proposed by Avrami in 1940 [37, 38]. According to this approach the isothermal crystallization kinetics should be analysed by means of the following equation:

$$1 - \varphi_c = \exp(-Kt^n) \tag{3}$$

Fig. 5 Normalized dielectric constant ε'_N of NIM as a function of time from crystallization processes occurring at 318, 323, 328, and 330.5 K. The solid lines represent the fits of Eq. 4
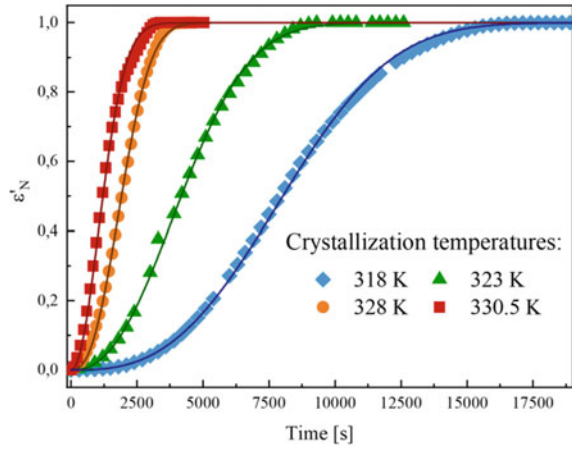
where φ_c is the crystalline volume fraction, $K = k^n$ is a rate constant, given by the temperature and the geometry of the sample, while n is the Avrami exponent. The value of the latter parameter is directly related to the nucleation dimensionality, thus usually n falls in the range of $2 - 3$ [39].

By combining Eqs. 2 and 3, one can obtain the modified Avrami equation which might be used to analyse data directly collected during the dielectric measurements:

$$\varepsilon'_N(t) = 1 - \exp(-Kt^n) \tag{4}$$

To determine values of both K and n, one might either fit the above equation to the $\varepsilon'_N(t)$ curves, which are presented in Fig. 5 or plotted so-called Avrami plot—see Fig. 6.

Fig. 6 The Avrami plots obtained from dielectric data of NIM measured at four temperatures equal to 330.5, 328, 323 and 318 K. The plots were performed in terms of Eq. 5 where the dependencies were linear
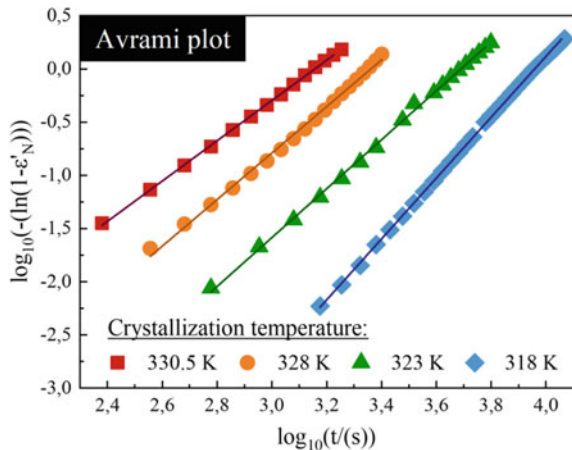
Table 2 Comparison of parameters estimated from Avrami and Avramov models for kinetics of isothermal crystallization of NIM obtained from dielectric experiments

T_c [K]	Avrami model		Avramov model		
	N	K	n^a	n^b	τ_{cr}^{-1}
318	2.86	1.09×10^{-4}	2.95	2.89	1.23×10^{-4}
323	2.30	2.04×10^{-4}	2.53	2.45	2.08×10^{-4}
328	2.18	4.21×10^{-4}	2.45	2.33	4.35×10^{-4}
330.5	1.89	6.85×10^{-4}	2.21	2.28	7.57×10^{-4}

[a]Calculated from Eq. 8; [b]Calculated from Eq. 9

The Avrami plot is based on the equation:

$$\log\left(-\ln\left(1 - \varepsilon_N'\right)t\right) = \log K + n \log(t) \tag{5}$$

As can be clearly seen, if the $\log\left(-\ln\left(1 - \varepsilon_N'\right)\right)$ versus $\log t$ is linear, the $\log K$ and n can be determined as the intercept and the slope of the obtained straight line, respectively. The values of the Avrami parameters, which were determined in both aforementioned ways are collected in Table 2. It can be noted that the value of Avrami exponent n changes in the standard way, i.e. decreases with temperature (from 2.9 to 1.8), indicating that the crystallization process of NIM, at isothermal conditions, is two dimensional at low and three dimensional at high temperatures. Considering that the parameter K decreases with decreasing the crystallization temperature, one can conclude that the dominant mechanism of NIM isothermal devitrification is the diffusion of molecules.

Second approach that is as often used to parametrize the time dependencies of the normalized real permittivity as Avrami model was proposed in 2005 by Avramov et al. [40]:

$$\varepsilon_N'(t) = 1 - \exp\left(-\left(\frac{t - t_0}{\tau_{cr}}\right)^n\right) \tag{6}$$

τ_{cr} in the above equation represents a characteristic time for the overall isothermal crystallization, t_0 is the induction time of crystallization, while the parameters n has the same meaning as it was in the Avrami model (see Eq. 4). It is worth to mention that τ_{cr} is related to the Avrami parameters as $\tau_{cr} = K^{-1/n}$.

In comparison with the Avrami model, the Avramov approach allows to: (i) estimate, more precisely, the crystallization induction time t_0 as well as (ii) eliminate errors caused by the thermal instability at the beginning of the experiment.

To determine the Avramov parameters, the Avrami—Avramov plot for each crystallization temperature, should be construct. In this plot the time dependence of ε_N' together with its first derivative is plotted versus $\ln t$. An example of the Avrami—Avramov plot, which were constructed based on NMS's data collected at 328 K are presented in Fig. 7.
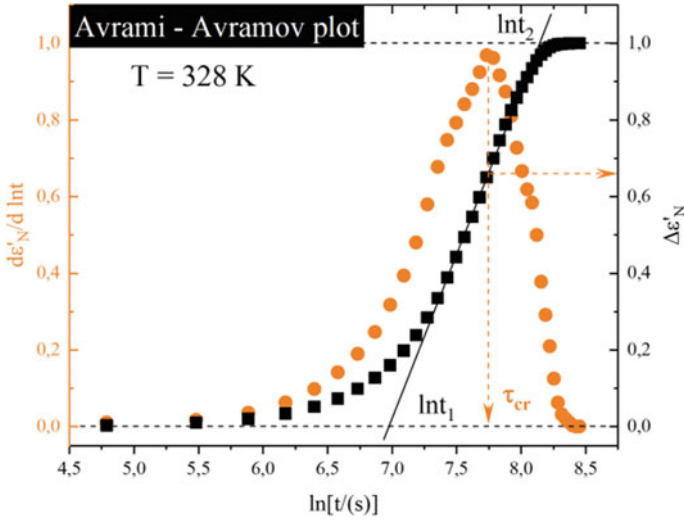
Fig. 7 Example of the Avrami–Avramov plot performed on the data for NIM collected at $T = 328$ K. The evolution of normalized real permittivity ε'_N (orange circles) and its first derivative versus the natural logarithm of the time (black squares)

It is worth noting that the derivative:

$$\frac{d\varepsilon'_N(t)}{d(\ln(t - t_0))} = n\left(\frac{t - t_0}{\tau_{cr}}\right)^n \exp\left(-\left(\frac{t - t_0}{\tau_{cr}}\right)^n\right) \tag{7}$$

reaches the maximum value of ε'_N $(d^2\varepsilon'_N/d(\ln(t - t_0))^2 = 0)$ at $t = \tau_{cr} + t_0$. Therefore, assuming that $t_0 = 0$ s, one can determine the value of characteristic time of the crystallization process (τ_{cr}) from the $d^2\varepsilon'_N/d(\ln t)^2$ peak maximum $((\varepsilon'_N)'_{max})$. In a similarly simple way it is possible to calculate also n i.e. the another Avramov parameter which is related to the nucleation dimensionality. This parameter can be calculated by employing the following equation:

$$n = \frac{\left(\varepsilon'_N\right)'_{max}}{0.368} \tag{8}$$

There is also an alternative method that can be used to evaluate the parameter n. This method is based on drawing a tangent to the experimentally determined sigmoidal curve ε'_N $(\ln t)$ (see dashed line in Fig. 7). By determining the values of $\ln t_1$ and $\ln t_2$, which corresponds to the points of intersection of the tangent line with the horizontal straight lines, constructed at the limit values of ε'_N i.e. at 0 and 1, it is possible to establish the n parameter from the following formula:

$$n = \frac{e}{\ln t_2 - \ln t_1} \tag{9}$$

Both τ_{cr} and n Avramov parameters of all investigated temperatures are collected together with the Avrami parameters in Table 2.

It should be noted that the $\varepsilon'_N(\tau_{cr}) = 1 - 1/e$, what approximately gives the value of 3.63. If the ε'_N at τ_{cr} will be lower than this value, it means that the induction time is different than 0. Since in the example presented in Fig. 7 the value of $\varepsilon'_N(\tau_{cr})$ is equal to 0.65, one can conclude that the $t\varepsilon'_N$, in this particular case, is equal to 0. However, at lower temperatures the induction time of crystallization of NIM is greater than zero since $\varepsilon'_N(\tau_{cr}) < 0.63$.

The parameters obtained from either Avrami or Avramov model can be further used to determine the activation energy for crystallization (E_a) by employing the Arrhenius law:

$$\log k = \log k_0 - \frac{E_a}{RT} \log e \tag{10}$$

The crystallization rate k presented in the above equation is related to (i) the Avrami parameters as follow: $k = K^{1/n}$ or (ii) the Avramov parameter τ_{cr} as $k = 1/\tau_{cr}$. R in above formula is the gas constant, while k_0 and E_a are fitting parameters. The plots constructed based on the values of the parameters k and τ_{cr} determined from the Avrami and the Avramov models are shown together in Fig. 8. The activation energies for overall crystallization of NIM are nearly the same and equal to: $E_a = 126 \pm 8$ and 125 ± 13 kJ/mol, when calculated by employing the parameters from Avrami and Avramov model, respectively.

At the end of this section, it is worth to mention that the activation energy for overall drug crystallization, which was determined by one of the described methods,
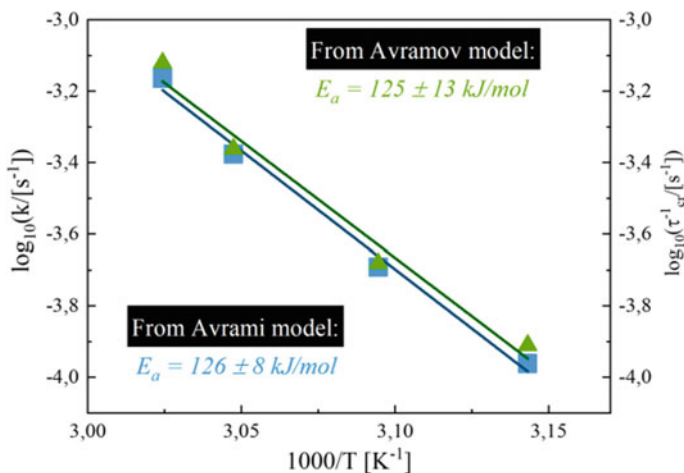
Fig. 8 The temperature dependence of the logarithm of: (left axis and blue data) the crystallization rate k parameter related to the Avrami parameters as $k = K^{1/n}$ and (right axis and green data) inverse crystallization time τ_{cr} from the Avramov model related to k as $k = 1/\tau_{cr}$ for NIM. The solid lines denote the linear fit
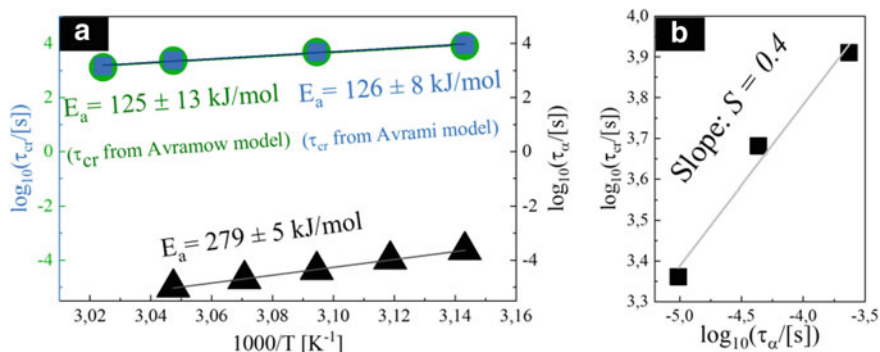
Fig. 9 a Comparison of temperature dependences of the characteristic isothermal crystallization times τ_{cr} found from the Avramov (green circles) and Avrami (blue squares) models, and structural relaxation times τ_α (black triangles) of NIM at the temperatures at which the isothermal crystallizations were performed by means of BDS. The solid lines indicate linear fits to the Arrhenius law. **b** Log − log plot of $\tau_{cr}(\tau_\alpha)$ within the crystallization temperatures range—the solid line denotes linear fits.

might be compared to the activation energy for the structural α-relaxation (see Fig. 9). This kind of analysis can help answer the question: *Can the time of the physical stability of amorphous drugs be estimated on the basis of the molecular mobility, reflected in the α-relaxation*? By analysing the slope (S) of the dependence log τ_{cr} (logτ_α) it is possible to determine the correlation coefficient of τ_{cr} with τ_α. When the slope, called also *coupling coefficient*, is equal 1, one can assume that the crystallization process is fully controlled by the structural relaxation. Otherwise, i.e. when the value of S lower than 1, the devitrification is not solely controlled by α-relaxation.

As can be seen in Fig. 9, the activation energy of NIM's isothermal crystallization ($E_a = 125$ kJ/mol) determined from the Arrhenius law is much lower than that of structural relaxation ($E_a = 279$ kJ/mol). The coupling coefficient is equal to 3.4. This result indicates that the α-relaxation is not a dominant factor which controls the re-crystallization in case of supercooled NIM. However, it should be emphasized that at $T < T_g$, the $\tau_\alpha(T)$ changes its character. Thus, lack of correlation between τ_α and τ_{cr} in supercooled liquid state does not exclude the possibility that the structural relaxation controls devitrification of glassy API.

2.3 Physical Stability Predictions

In the vast majority of cases pharmaceuticals are stored at standard storage conditions i.e. room temperature and atmospheric pressure. Therefore, a lot of efforts is paid to determine or predict the time of the physical stability of amorphous drugs stored at that specific conditions. The most commonly employed experimental tool

for investigating long-term physical stability of amorphous APIs is X-ray diffraction (XRD). However, it has to be pointed out that the long-term isothermal XRD studies performed at room temperature are very time consuming. Such experiments can take even several years prior the first sign of the sample re-crystallization will be registered. Therefore, scientists constantly try to find method that enables the prediction of the minimal time of amorphous APIs physical stability.

As it has been mentioned, in the above section, the re-crystallization of amorphous APIs can be controlled by the structural relaxation. Thus, by determining the time of the α-relaxation of these pharmaceuticals stored at room temperature, it is possible to estimate the time of their physical stability. Unfortunately, below T_g the structural α-relaxation becomes too slow to be experimentally observed. To overcome this problem, one can use a few methods, which were originally developed for estimation of the structural relaxation times of glasses. Application of these methods is based on the measurements of $\tau_\alpha(T)$ in the supercooled liquid region. In this section two of these methods will be thoroughly describe.

The first, commonly used, approach to predict temperature dependence of τ_α at $T < T_g$ is based on the modified Adam and Gibbs (AG) model proposed by Hodge:

$$\tau_\alpha\left(T, T_f\right) = \tau_\infty \exp\left(\frac{B}{T\left(1 - \frac{T_0}{T_f}\right)}\right) \tag{11}$$

where τ_∞, B, and T_0 are fitting parameters from the Vogel–Fulcher–Tammann (VFT) equation which describes $\tau_\alpha(T)$ at $T > T_g$ and is defined as follows:

$$\tau_\alpha(T) = \tau_\infty \exp\left(\frac{B}{T - T_0}\right) \tag{12}$$

T_f in the Eq. 11 is the so-called *fictive temperature* that is defined as:

$$\frac{1}{T_f} = \frac{\gamma_{C_p}}{T_g} + \frac{1 - \gamma_{C_p}}{T} \tag{13}$$

The fictive temperature defines the glass properties in terms of the equilibrium supercooled liquid which has the same configurational entropy, while γ_{Cp} is a thermodynamic parameter given as follows:

$$\gamma_{C_p} = \left.\frac{C_p^{\text{liq}} - C_p^{\text{glass}}}{C_p^{\text{liq}} - C_p^{\text{cryst}}}\right|_{T-T_g} \tag{14}$$

It is important to note that the values of the heat capacity for crystalline (C_p^{cryst}), liquid (C_p^{liq}), and glassy (C_p^{glass}) sample should be determined at T_g (see Fig. 10). In the case when $\gamma_{Cp} = 0$, i.e. $T_f = T$, the AG model corresponds to VFT equation. On the other hand, for $T_f = T_g$, i.e. $\gamma_{Cp} = 1$ the Eq. 11 represents Arrhenius law.
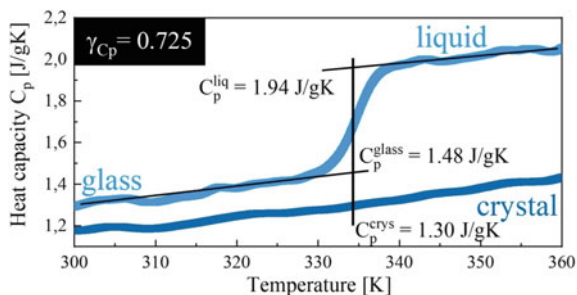
The second method, which also is used to estimate the time scale of structural relaxation in the glassy state, is much easier. In this method the dielectric spectrum collected above T_g (spectrum on which α-relaxation is well resolved) is horizontally shifted to match the one registered at $T < T_g$ in which only the high-frequency flank of α-process is present in the experimental frequency range (see Fig. 11a). The result of such shifting, so-called *master plot*, allows to predict the structural relaxation time of the material from the maximum of the reconstructed α-peak since: $\tau_\alpha = 1/2\pi f_{max}$.

It has to be noted that this approach is strictly limited to the samples in which the shape of the α-relaxation peak is temperature invariant i.e. TTS is valid. To check whether the temperature affects the shape of the α-relaxation, the dielectric loss spectra from the whole registered supercooled liquid region should be shifted to superimpose on the reference spectrum. Time–temperature superposition (TTS) plot, presented in Fig. 11b, shows that the temperature does not change the shape of the structural loss peak of a model API—EZB—measured at temperatures from the region 341–357 K. Thus, the procedure based on construction of master plot can be employed to predict its temperature dependence of τ_α at $T < T_g$.
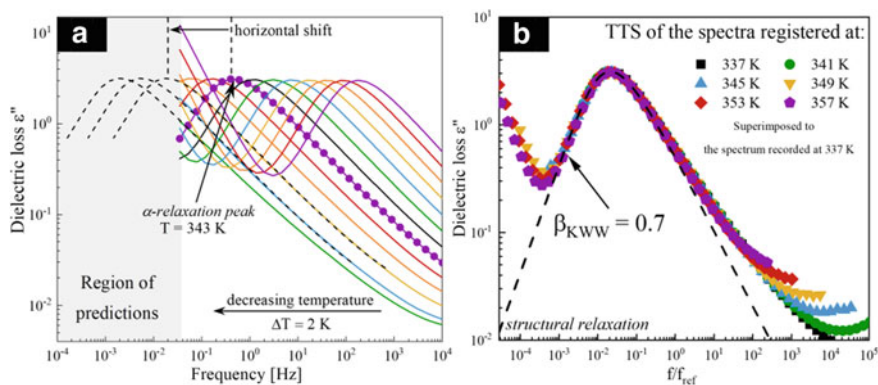
Fig. 11 **a** The procedure of master plot constriction involving shifting the α-relaxation peak to dielectric spectra registered in at $T < T_g$—on the basis data of EZB. **b** The master plot of EZB formed by horizontally shifting of spectra to overlap that at 337 K.
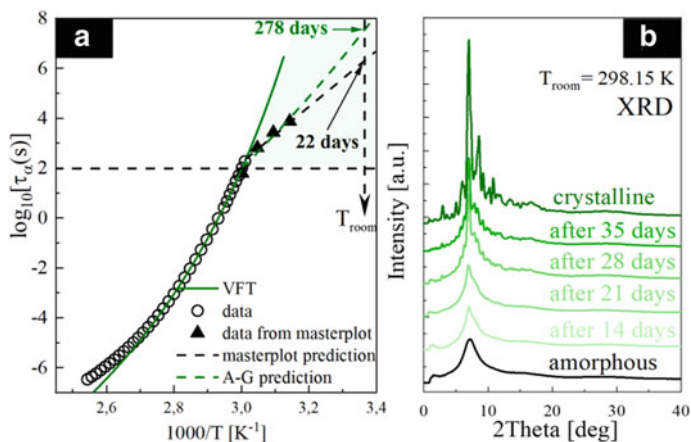
Fig. 12 a The relaxation map of EZB. Data obtained from BDS measurements (open circles) and from master plots (closed triangles). The solid line represents the VFT fit, while the dashed lines represent the predictions from the AG model (green) and from master plots (black). **b** Long-term isothermal XRD measurement of EZB carried out at $T = 298$ K and $p = 0.1$ MPa.

Figure 12a presents $\tau_\alpha(T)$ of glassy EZB, which were predicted by two described above—AG and *master plot*—strategies.

The structural relaxation time of EZB predicted from the AG model is shown in Fig. 12a as a red dashed line, while black dashed line represents the prediction obtained based on the master plot. According to the master plot method $\tau_\alpha \approx 10^{6.3}$ s (22 days) at room temperature (i.e. 298 K), whereas the time of α-relaxation determined from the AG approach is equal to $10^{7.38}$ s, which corresponds to 278 days. To check which of those methods gives more adequate results to the reality, the long-term isothermal XRD experiment of EZB was performed. The results obtained from this study are presented in panel b of Fig. 12. As can be seen the first sign of EZB's re-crystallization was observed after 21 days indicating that the master plot procedure predicts the physical stability of this particular amorphous pharmaceutical witch high accuracy.

At the end of this section, it is worth highlighting that the validity of the AG model as well as the master plot method, in prediction of the time-scale of the re-crystallization tendency, was confirmed for several amorphous APIs, excluding EZB (e.g. bicalutamide [41], celecoxib [42], sildenafil [43], azithromycin, clarithromycin, roxythomycin [44], Trehalose [18]). This fact indicates that the presented methods are trustworthy and can be widely used for the prediction of the physical stability of amorphous pharmaceuticals.

3 Physical Stability Studies of Amorphous APIs at Conditions Mimicking Their Manufacturing

The amorphous APIs and their molecular dispersions might be produced by either melting or solvent methods [45]. However, due to both economic and ecological limitations of solvent techniques, currently the most preferred production way of these systems is Hot Melt Extrusion (HME) [46–48]. A typical HME process includes heating and softening of a physical mixture of an API and a thermoplastic polymer inside the extruder, followed by pressurization of the molten mass through a die, to finally form the granules, cylinders or films [47, 49]. In this technological process the temperature plays undeniably a crucial role [50]. Therefore, it has to be carefully chosen to finally obtain an appropriate dosage form. The manufacturing temperature cannot be too high or too low. At too high temperature the sample might undergoes thermal degradation [51, 52]. If, however, the elevated temperature does not harm the extruded composition, it can still over-reduce the sample's viscosity, and consequently will make it impossible to form the filaments. At the same time, the manufacturing temperature should not be too low. Firstly, at insufficient temperature the dissolution of an API into the polymeric matrix or its melting (depending on the drug concentration) might not be possible. Secondly, at that conditions the material can be too viscous to be extrudable. Choosing appropriate processing temperature, one should also keep in mind that at this specific temperature an amorphous sample might undergoes re-crystallization [53–55]. Therefore, it is important to investigate the effect of elevated temperature on the physical stability of amorphous APIs. The studies of amorphous drugs re-crystallization performed at elevated temperature conditions were a subject of the above subsection. Another, very important, factor on which the drug is exposed to during its manufacturing process is elevated pressure. It can be exerted on a sample at both: (i) supercooled liquid state i.e. during pressurization of the molten mass through a die to form the filaments as well as (ii) glassy state i.e. during palletization, grinding and tableting (depending on the final dosage form: tablet or capsule). Thus, another important question which should be asked prior the production is: *whether the compression triggers the re-crystallization of the investigated API*?

It has been recently shown that the influence of the compression imitating conditions during manufacturing of amorphous APIs on their physical stability might be investigated by employing BDS equipped with the high-pressure setup. One of the best examples of pharmaceutical extremely sensitive to compression is PBC. As can be seen in Fig. 13a, the amorphous form of this API reveals incredibly high physical stability, when store at room temperature. According to long-term isothermal XRD studies, this material does not reveal any signs of re-crystallization even after 200 days of storage (T_{room} and $p = 0.1$ MPa). Interestingly, PBC is physically stable also at elevated temperature conditions (see panel b of Fig. 13). However, despite high physical stability observed at atmospheric pressure, a very gentle compression triggers PBC's re-crystallization (see Fig. 13c).
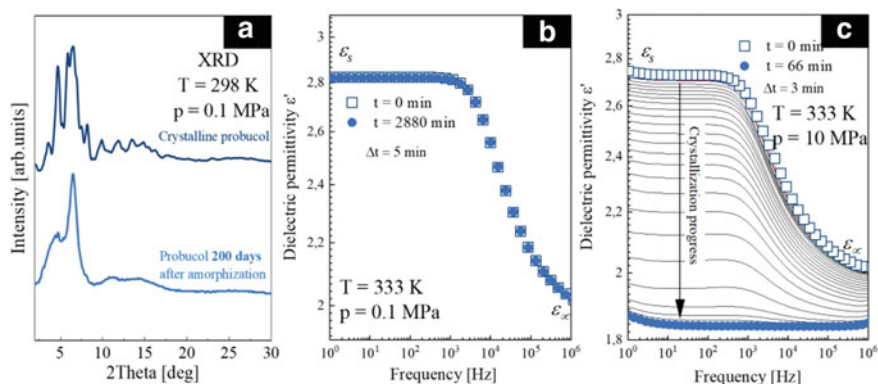
Fig. 13 **a** Long-term isothermal XRD measurement of PBC carried out at $T = 298$ K and $p = 0.1$ MPa; **b** dielectric spectra of the real part of the complex dielectric permittivity of PBC during isothermal dielectric experiment performed at $T = 333$ K and $p = 0.1$ MPa; **c** dielectric spectra of the real part of the complex dielectric permittivity of PBC during isothermal dielectric experiment performed at $T = 333$ K and $p = 10$ MPa.

Since the pressure is not applied throughout the whole manufacturing process, it has been proposed, to use BDS as a method monitoring drugs physical stability at imitating this short-time compression exposure conditions. By employing dielectric spectroscopy with a high-pressure setup, it is possible to quickly compress and decompress the sample at defined by the user temperature conditions. The available by this equipment pressure range starts from 0.1 MPa and going up to 1.8 GPa, what far exceeds the pharmacists' needs. It is because the usually used compression during the tabletting process ranges from 50 to 250 MPa, while pressures not higher than 20 MPa can be exerted on the sample during HME. It is also worth noting that by applying the high-pressure dielectric setup it is possible to monitor physical stability of amorphous drugs during all, imitating production steps (i.e. compression, decompression, storage time, second compression, temperature change). This option allows to assess in which particular part of production line the API is exposed to the most danger for stability conditions. In Fig. 14, the comparison of results obtained for PBC stored at: (i) ambient pressure; (ii) elevated pressure; and (iii) ambient pressure after the compression and decompression procedure are presented. It can be well seen that the elevated pressure triggers PBC's re-crystallization. Thus, even the slightest pressure exerted to the sample promotes the formation of crystallization nuclei, and consequently even after decompression PBC's crystal growth might be observed.

Fig. 14 Normalized dielectric constant ε'_N of PBC as a function of time calculated based on eq. (2) based on the three different dielectric experiments: (i) performed at $T = 333$ K and $p = 10$ MPa, (ii) performed at $T = 333$ K and $p = 0.1$ MPa and (iii) performed at $T = 333$ K after compression and decompression procedure
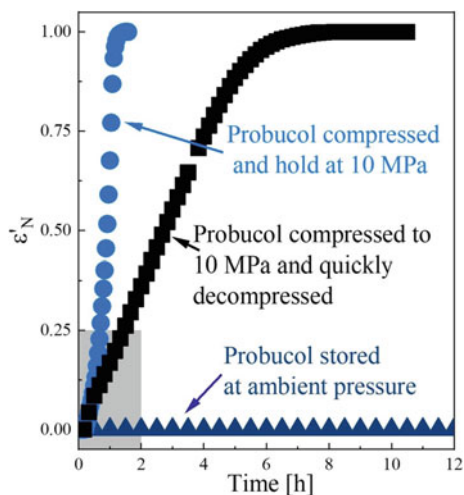
4 Dielectric Spectroscopy as a Method to Investigate drug's Solubility Limit in Polymer Matrix

As was already stated in this chapter: *the main flaw of the amorphous pharmaceuticals is their physical instability.* This is crucial since shelf-life requirements for most pharmaceutical systems are on the order of several years [27]. Due to the fact that in the required time most of the drugs in the amorphous form will return to a more stable crystalline form, the use of certain excipients (crystallization inhibitors) is inevitable. There is a variety of possibilities when it comes to choosing appropriate excipient. Successful stabilizer can be characterized by different molecular weights, including low molecular weight compounds such as acetylated sugars [56–59], organic acids [60–62] or even other drugs [16, 36, 63–65] or the opposite large molecular weight compounds like polymers [5, 25, 66–71]. It has to be pointed out, however, that the use of the latter, for the pharmaceutical purposes, is disproportionally larger. Furthermore, multi-functional use of polymers in the pharmaceutical industry as the way to improve: water solubility [53, 72–74] or processing conditions (e.g., during Hot Melt Extrusion (HME)) [75–77] made them the most commonly chosen excipients.

The apparent enhancement of the physical stability of the drug-polymer Amorphous Solid Dispersion (ASD), even if significant, might not ensure thermodynamic stability [78–80]. Therefore, to achieve needed stability of the ASD formulation, two main requirements must be met. The first and for most is the possibility to dissolve the drug within the polymer matrix (drug-polymer miscibility). The second is the need to preserve the concentration below the equilibrium solubility of the drug in the polymer (solubility limit) [81–86]. Thus, the determination of drug-polymer solubility is a critical parameter when preparing the ratio between drug and polymer in the formulation development of an amorphous solid dispersion.

Fig. 15 Time evolutions of
the glass transition
temperature of a
drug/polymer mixture when
reaching the equilibrated
state by either dissolution
(mixing) or re-crystallization
(demixing) process
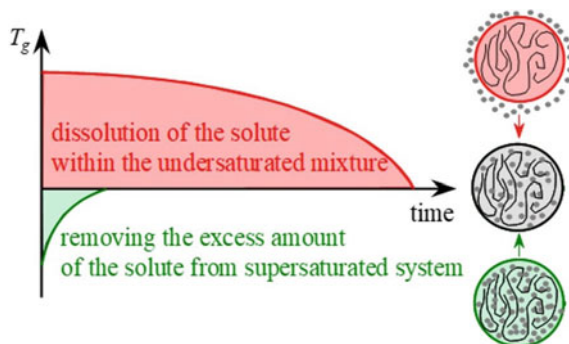
A number of the methods were introduced in order to experimentally determine
the API's solubility within the polymer matrix. Generally they are based on the
calorimetric measurements such as (i) melting point depression [87, 88]; (ii) re-
crystallization method [81] or (iii) various different annealing methods proposed
throughout the years [89–92]. These approaches provide the desired answer only at
the temperature well above the sample's T_g. This limitation comes from the fact that
at temperatures close to or below T_g viscosity of this composition becomes too high
to reach an equilibrium state, therefore, its determination is very-time consuming
[81, 90, 93, 94]. Mentioned equilibrium (saturated) state can be reached either by the
demixing or dissolution process [81]. Until 2013, when Mahieu et al. presented new
protocol allowing fast and relatively easy determination of the solubility of drugs
into a polymer matrix, most of the experimental determination was based on the
latter. From what has been presented by Mahieu et al. the time scales of these two
processes differ significantly (see Fig. 15) [81].

Discussed protocol is based on the following steps: i) scanning during heating
of the supersaturated sample to determine initial glass transition temperature; (ii)
annealing of the supersaturated sample at certain temperature (above the sample's
T_g); (iii) rescanning of the sample after annealing to determine the final glass
transition temperature, after the excess of the drug re-crystallize from the system,
followed by (iv) identification of newly obtained concentration by comparing its
glass transition to the Gordon-Taylor (G-T) prediction. However, method based on
the demixing (re-crystallization) process would have an obvious limitation. Namely,
a sample's tendency towards re-crystallization is crucial in the determination of
the solubility limits. Despite this restriction, Mahieu's approach is faster than the
preceding methods. Thus, in 2017 Chmiel et. al introduced the latest modification
of this approach. Proposing dielectric studies as an alternative to the calorimetric
measurements was one of the differences between those two approaches [33].

When using BDS instead of the Differential Scanning Calorimetry (DSC), one
should act accordingly to the procedure described below. The first step is the experi-
mental determination of the concentration dependence of the glass transition temper-
ature of the ASD systems. This will be used to identify the concentration obtained
after the re-crystallization of the excess amount of the drug from the supersaturated
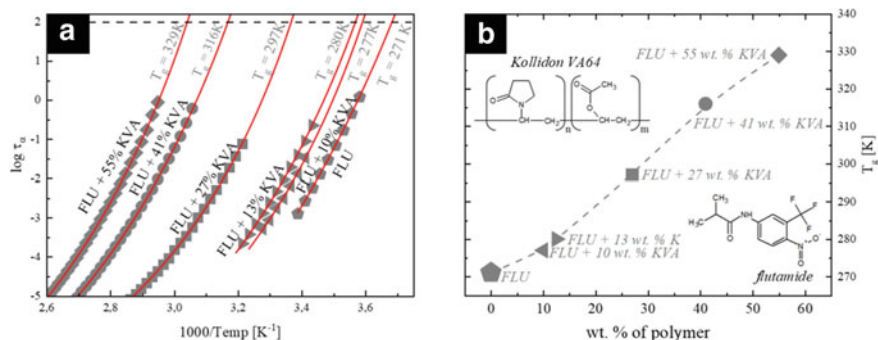
Fig. 16 Panel **a** shows relaxation map of the fully amorphous FLU, FLU + 10 wt.% of KVA, FLU + 13 wt.% of KVA, FLU + 27 wt.% of KVA, FLU + 41 wt.% of KVA and FLU + 55 wt.% of KVA as grey pentagons, triangles pointing left, triangles pointing right, squares, circles and diamonds respectively. Temperature dependence of τ_α in the supercooled liquid has been described by VFT equations (red solid lines). Panel **b** presents concentration dependence of the glass transition temperatures of FLU-KVA ASD systems, determined utilizing BDS. Grey pentagons, triangles pointing left, triangles pointing right, squares, circles and diamonds are assigned to the neat amorphous FLU, FLU + 10 wt.% of KVA, FLU + 13 wt.% of KVA, FLU + 27 wt.% of KVA, FLU + 41 wt.% of KVA and FLU + 55 wt.% of KVA respectively. Left and right molecular structure refer to KVA and FLU respectively

solution. Beginning with the analysis of the dielectric loss spectra recorded above the glass transition temperature, one is able to determine the temperature dependence of the α-relaxation time ($\tau_\alpha(T)$) of the examined sample (as presented in Fig. 16a).

To obtain the values of τ_α at various temperatures, the experimental data should be fitted using the Havriliak-Negami (HN) [95] function:

$$\varepsilon^*(\omega) = \varepsilon_\infty + \frac{\Delta\varepsilon}{\left[1 + (i\omega\tau_{HN})^a\right]^b} \tag{15}$$

where ε_∞ is high-frequency limit permittivity, ε_0 is the permittivity of vacuum, $\Delta\varepsilon$ is dielectric strength, ω is equal to $2\pi f$, τ_{HN} is the HN relaxation time, a and b represents symmetric and asymmetric broadening of relaxation peak. Using the fitting parameters determined above, one can calculate the values of τ_α by means of the following formula:

$$\tau_{\alpha/_{\alpha'}} = \tau_{HN}\left[\sin\left(\frac{\pi a}{2 + 2b}\right)\right]^{-\frac{1}{a}}\left[\sin\left(\frac{\pi ab}{2 + 2b}\right)\right]^{\frac{1}{a}}. \tag{16}$$

Temperature evolution of the structural relaxation times—in the supercooled liquid region—usually shows non-Arrhenius like behaviour. Therefore, in order to parameterize it VFT equation (Eq. 12) is frequently used. By extrapolating the VFT fit to 100 s, one can determine the glass transition temperature using the operational definition $T_g = T(\tau_\alpha = 100\,\text{s})$. Consequently, by following the above procedure with

a series of samples with various concentrations, one is able to experimentally determine the concentration dependence of the glass transition temperatures (presented on the example of FLU-KVA systems in Fig. 16b). This dependence will serve as the basis for the identification of a saturated solution (solubility limit) instead of the G-T prediction.

Consecutive part strictly corresponds to the second step of the Mahieu's approach—annealing of the sample at elevated temperature in order to re-crystallize the excess amount of the drug from the supersaturated solution.

4.1 Isothermal Dielectric Measurements

In the following subsection of this chapter, step by step instruction, on how to determine the drug's solubility within the polymer matrix utilizing Broadband Dielectric Spectroscopy, will be provided. For this purpose, FLU-KVA composition was chosen as the representative example.

Taking into account that demixing process (re-crystallization of the excess amount of the drug from the supersaturated solution) is the crucial step in discussed solubility determination, annealing should be performed well above the glass transition temperature—in the supercooled liquid region (preferably higher or close to the temperature onset of crystallization). Therefore, during the dielectric measurements the structural relaxation peak will be well visible in the experimental window. Furthermore, as was already stated in this book, when the re-crystallization of the neat amorphous component starts, the intensity of the α-process peak will decrease. However, when observed re-crystallization refers to the amorphous drug from the drug-polymer ASD system, then in addition to mentioned decrease, one can expect the shift of the structural relaxation process towards lower (in case of low-T_g drug and high-T_g polymer system) [96] or higher frequencies (in case of high-T_g drug and low-T_g polymer). The representative example of discussed phenomenon can be observed in Fig. 17a, in case of the re-crystallization from the FLU + 13 wt.% KVA system. Observed shift (towards lower frequencies) is caused by the weakening of the plasticization effect (i.e. an increase in the global mobility associated with a decrease in T_g of the binary system compared with the initial concentration) due to the decreasing amount of amorphous drug in the mixture. When the re-crystallization of the excess amount of the small molecule (herein FLU) from the supersaturated solution stops—leaving saturated (partially amorphous) solution, one can still observe, on the dielectric spectrum one well-resolved loss peak—α'-process (see Fig. 17a).

When no further changes in molecular dynamics, such as drop in intensity or horizontal shifts, can be observed, the sample should be cooled down and re-measured during heating up to the temperature of the performed isothermal crystallization, as can be seen in Fig. 17b (in discussed example $T = 353$ K). Described above additional measurement is necessary to cover wide temperature range of the relaxation time related to the α'-process. Next, based on the HN fitting procedure performed on the dielectric loss spectra obtained during mentioned procedure, one can determine the
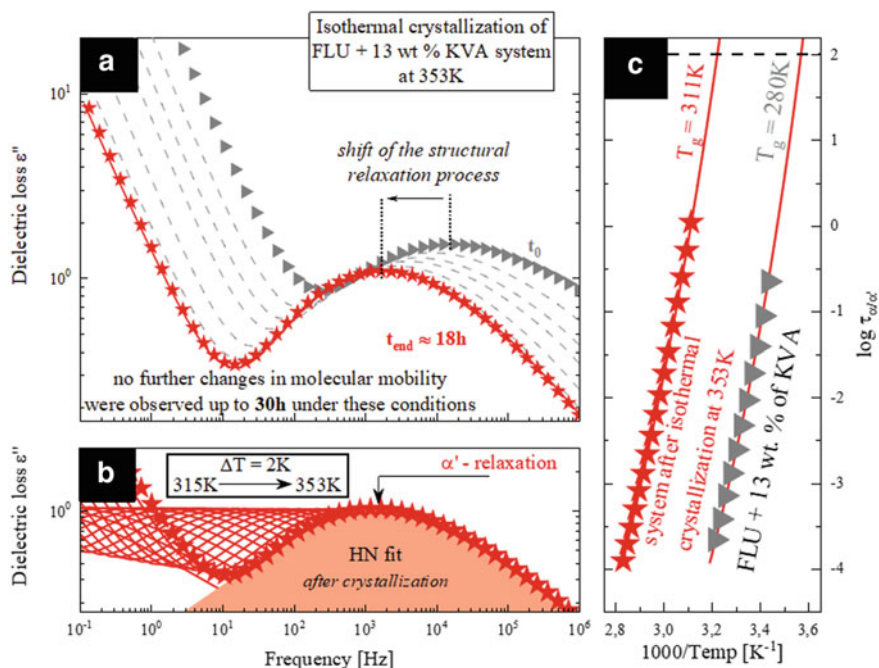
Fig. 17 Panel **a** presents the dielectric spectra obtained during the isothermal crystallizations registered at 353 K. t_0 indicates the first recorded spectrum at the set temperature, which does not correspond to the beginning of the crystallization. Panel **b** presents dielectric spectra obtained during additional measurements performed after isothermal crystallization at 353 K. Red shaded area corresponds to the HN fit of the partially re-crystallized sample. Panel **c** shows relaxation map of the fully amorphous FLU + 13 wt.% of KVA sample as well as the samples after isothermal crystallization at 353 K (grey triangles and red stars respectively). Temperature dependence of τ_α in the supercooled liquid has been described by VFT equations (red solid lines)

temperature dependence of the relaxation times of the sample after re-crystallization $(\tau_{\alpha'}(T))$. Further investigations focus mainly on the determination of the glass transition temperature of the sample obtained after isothermal re-crystallization. This can be done, by extrapolation of its VFT fit to 100 s ($T_g = T(\tau_\alpha = 100 \text{ s})$). Once the glass transition temperature of this stable system (saturated solution) is determined, its concentration can be easily established. It can be done by comparing the obtained $T_g's$ value to the experimentally determined concentration dependence of the glass transition temperatures. As can be seen in Fig. 18 the saturated composition of FLU-KVA determined at 353 K contains 62 wt.% of FLU.

To obtain the solubility limit line, in the wide temperature range, the above procedure should be repeated for different isothermal re-crystallization temperatures.

Before advancing to the next part of this chapter, the main difference between the two discussed techniques should be highlighted. By utilizing the DSC, one can obtain the information about the sample's concentration at two specific time points: before the re-crystallization begins and when it is finished. At the same time, by following the
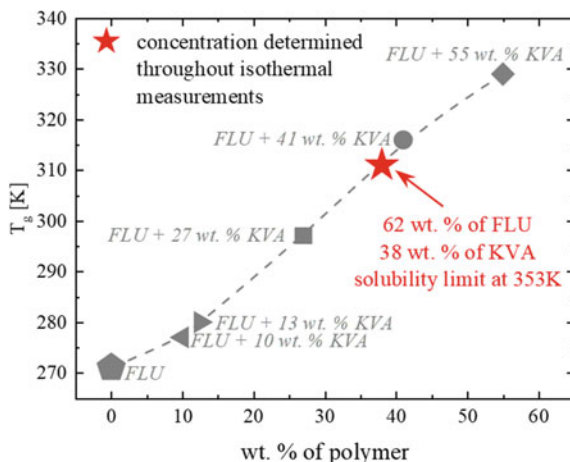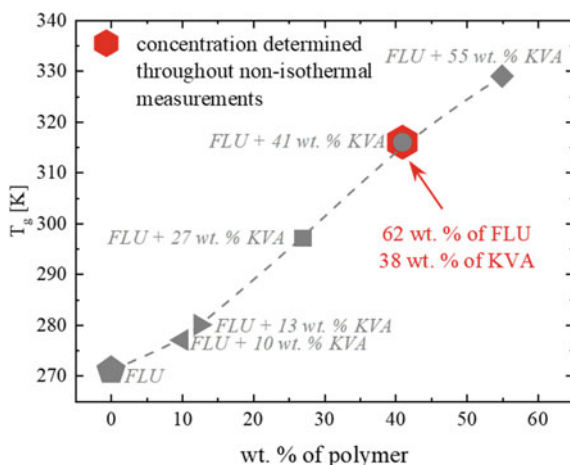
Fig. 18 Presents concentration dependence of the glass transition temperatures of FLU-KVA ASD systems, determined utilizing BDS. Grey pentagons, triangles pointing left, triangles pointing right, squares, circles and diamonds are assigned to the neat amorphous FLU, FLU + 10 wt.% of KVA, FLU + 13 wt.% of KVA, FLU + 27 wt.% of KVA, FLU + 41 wt.% of KVA and FLU + 55 wt.% of KVA respectively. Red star refers to the concentrations determined via isothermal measurements at 353 K

exact same procedure via BDS, one can additionally obtain the information—besides the initial and final glass transition temperatures—about the molecular dynamics of the examined system (in wide frequency and temperature range) before, during and after the re-crystallization process. Based on the subtle changes in molecular mobility of the examined system one can, not only monitor the progress but also determine the exact time when re-crystallization ceases [96].

It has to be pointed out that both approaches provide results that are in perfect agreement with each other. Therefore, it seems that the dielectric modification of the well-known Mahieu's protocol, provides the alternative experimental technique to the calorimetric measurements, but the basic principle remains the same. It should be pointed out that dielectric approach gives one more possibility of estimating polymers' ability to dissolve API. This phenomenon, related to the solubility determination, can be observed during non-isothermal dielectric studies [33, 97]. The following subsection will focus on this subject.

4.2 Non-isothermal Dielectric Measurements

Beginning with the statement that non-isothermal measurements are, without a doubt, significantly less time consuming than isothermal ones and at the same time they provide somehow similar results, they earn their place in this chapter. At this point, it has to be mentioned that discussed method of non-isothermal measurements can be
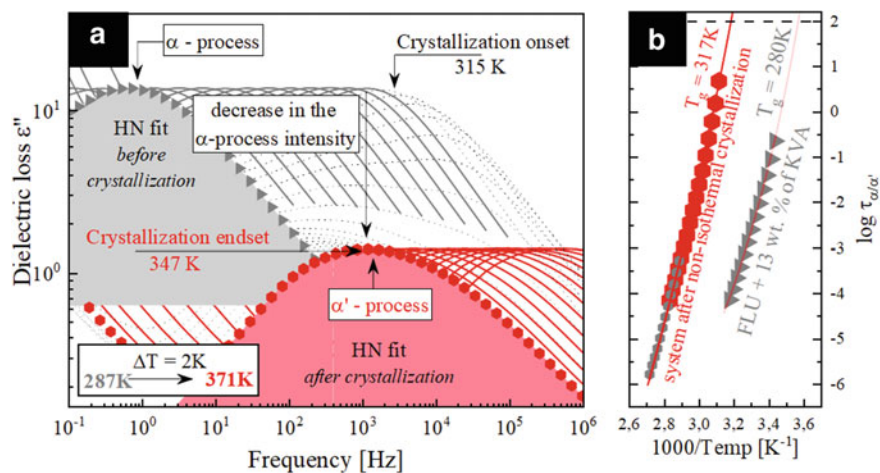
Fig. 19 Panel **a** presents dielectric spectra obtained during non-isothermal measurements performed on the fully amorphous sample. Grey shaded area refers to the HN fit of the fully amorphous sample. Red shaded area corresponds to the HN fit of the partially re-crystallized sample. C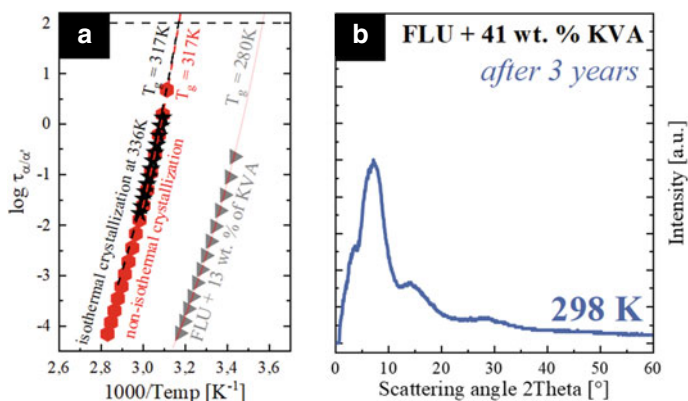rystallization was marked as the dotted spectra. Panel **b** shows the temperature dependence of the relaxation times of the fully amorphous FLU + 13 wt.% of KVA sample (grey triangles) as well as the samples after non-isothermal crystallization (grey hexagons) and partially re-crystallized sample re-measured after previous cooling (red hexagons). Temperature dependence of τ_α in the supercooled liquid has been described by the VFT equations (red solid lines)

considered as not quantitative but qualitative. Taking into account the situation when the same drug is dissolved within the different polymeric matrixes, one can, in a fast and easy way, determine the mutual relation between their dissolving properties [97].

In order to perform this assessment, one should follow the procedure described below. For this purpose, the representative examples of FLU-based ASDs were chosen. During the non-isothermal dielectric measurements, above the sample's T_g, the α-relaxation peak shifts towards higher frequencies (grey spectra in Fig. 19a). By analysing these dielectric loss spectra, $\tau_\alpha(T)$—related to the fully amorphous sample—can be determined (grey triangles in Fig. 19b). Throughout further heating of the sample, at some certain temperature (herein 315 K) supersaturated drug-polymer solution, starts to re-crystallize (see dashed loss spectra in Fig. 19a). At this point the observer should notice following phenomenon's occurring simultaneously to further heating [20, 33, 36, 97]: (i) rapid decrease of the intensity of the loss peak that reflects sample's re-crystallization; (ii) shift of the relaxation peak towards lower frequencies, associated with the changes in the drug-polymer concentration (as the result of the re-crystallization of the excess amount of the drug from the supersaturated solution), (iii) shift of the relaxation peak towards higher frequencies as the temperature is rising. When no further changes, in the intensity of the loss peak, could be observed and at the same time remaining α-relaxation peak, once again, shifts only towards higher frequencies during heating (see red spectra in Fig. 19a), it can be assumed that the crystallization process is over. This can suggest

that the excess amount of the drug re-crystallized leaving concentration that does not display any tendency towards re-crystallization during non-isothermal studies [33]. By analysing these dielectric loss spectra the temperature dependence of the relaxation time related to the α'-relaxation ($\tau_{\alpha'}(T)$) can be determined (grey hexagons in Fig. 19b).

To improve the accuracy of the VFT fitting procedure and in consequence the accuracy of the $T'_g s$ determination, the sample should be cooled down and re-measured during heating to cover wide temperature range of the $\tau_{\alpha'}(T)$. Data obtained by this additional procedure is presented in Fig. 19b as red hexagons. Once the glass transition temperature is determined, from the extrapolation of its VFT fit to 100 s, this concentration can be easily identified by the comparison its T_g value to the experimentally determined concentration dependence of the glass transition temperature of the ASD systems (see Fig. 20).

By proceeding with this method while employing different polymeric matrixes, one can determine the relationship in the apparent solubility of the amorphous drug dispersed within them. Based on the studies performed on FLU dispersed in PVP, KVA and PVAc [33, 97], following dependence was established: PVP > KVA > PVAc (see Fig. 21). This result would imply that the highest amount of the FLU can be dissolved in the PVP matrix and the lowest in the PVAc.

Fig. 20 Presents concentration dependence of the glass transition temperatures of flutamide-based ASD systems, determined utilizing BDS. Grey pentagons, triangles pointing left, triangles pointing right, squares, circles and diamonds are assigned to the neat amorphous FLU, FLU + 10 wt.% of KVA, FLU + 13 wt.% of KVA, FLU + 27 wt.% of KVA, FLU + 41 wt.% of KVA and FLU + 55 wt.% of KVA respectively. Red hexagon refers to the concentrations determined via non-isothermal measurements

Fig. 21 Presents concentration dependence of the glass transition temperatures of FLU-based ASD systems. Pentagon is assigned to the neat amorphous flutamide, and the triangle pointing down, star and triangle pointing up indicates the PVP, KVA and PVAc respectively. Red hexagons correspond to the concentrations determined via non-isothermal measurements
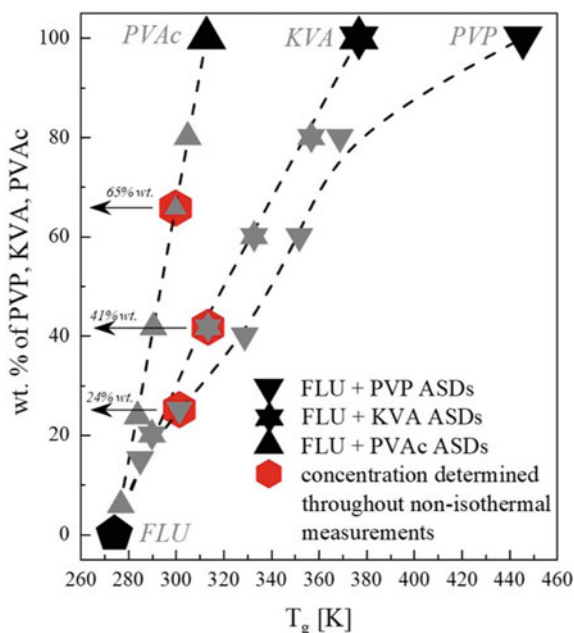
Even though described above procedure results in obtaining certain concentration (that does not show any tendency towards further re-crystallization during non-isothermal measurements) it is not directly linked to any certain temperature. Therefore, one cannot really state that concentration A (determined via non-isothermal measurements) is the solubility limit at a temperature equal to B.

However, by utilizing isothermal measurements in a series of trials and errors, this exact concentration was determined as the solubility limit at a specific temperature (well above the room temperature), as can be seen in Fig. 22a. Secondly, what in fact is more important, this particular concentration (i.e. which was determined via non-isothermal studies of the FLU-KVA mixture [33]—the first sample prepared based on this method) does not revealed any tendency towards re-crystallization at room temperature, for nearly 3 years (up to date), as indicated by long-term stability studies utilizing powder X-ray diffraction (see Fig. 22b).

At the end of this subsection, it should be pointed out that the discussed method of non-isothermal measurements was already successfully applied in the case of amorphous aripiprazole-based ASD systems [20]. In the recalled case of ARP dispersed in SOP as well as KVA, the results of the discussed non-isothermal BDS measurements allowed to determine the better excipient for the Hot Melt Extrusion purposes. BDS was initially used to qualitatively assess the solubility of the pharmaceutical within two different polymeric matrices (during non-isothermal measurements). Then, the specific solubility limit was determined in order to validate examined systems from the HME point of view. As it turns out the 70 wt.% of the KVA ensures both high physical stability of the ARP as well as the appropriate viscosity for the HME.

Fig. 22 Panel **a** shows temperature dependence of the relaxation times of the fully amorphous FLU + 13 wt.% of KVA sample (grey stars) as well as the samples after non-isothermal (red hexagons) and isothermal crystallization (black circle). Temperature dependence of τ_α in the supercooled liquid has been described by VFT equations (solid lines). Panel **b** presents the X-ray diffraction patterns for FLU + 41 wt.% of KVA at $T = 298$ K. The absence of sharp Bragg peaks indicates the full amorphousness of the sample. Up-to-date result was provided by *K. Jurkiewicz* according to the procedure described in ref. [33]

What is more both isothermal and non-isothermal dielectric measurements used to determine drug-excipient solubility limit are not limited to the drug-polymer mixtures. Analogous measurements were conducted in drug-drug systems as presented in case of FLU in a binary mixture with BIC.[36] What indicates on the universal potential of this method.

References

1. Shah VP, Amidon GL (2014) AAPS J 16:894
2. Lee VH, Hussain AS, Yu LX, Amidon GL, Polli JE, Zhao H, Mehta MU, Conner DP, Shah VP, Lesko LJ, Chen M (2002) Pharm Res 19
3. Thayer AM (2010) Chem Eng News Arch 88:13
4. Babu NJ, Nangia A (2011) Cryst Growth Des 11:2662
5. Laitinen R, Löbmann K, Strachan CJ, Grohganz H, Rades T (2013) Int J Pharm 453:65
6. Kawakami K (2012) Adv Drug Deliv Rev 64:480
7. Amidon GL, Lennernäs H, Shah VP, Crison JR (1995) Pharm Res 12:413
8. Forster A, Hempenstall J, Rades T (2001) J Pharm Pharmacol 53:303
9. Hancock BC, Parks M (2000) Pharm Res 17:397
10. Murdande SB, Pikal MJ, Shanker RM, Bogner RH (2010) J Pharm Sci 99:1254
11. Shah N, Sandhu H, Choi DS, Chokshi H, Malick AW (2014) Amorphous solid dispersions
12. Descamps M (2016) Disordered Pharmaceutical Materials

13. Williams H, Trevaskis N, Charman S, Shanker R, Charman W, Pouton C, Porter C (2013) Pharmacol Rev 65:315
14. Bhugra C, Pikal MJ (2008) J Pharm Sci 97:1329
15. Van den Mooter G, Wuyts M, Blaton N, Busson R, Grobet P, Augustijns P, Kinget R (2000) Eur J Pharm Sci 12:261
16. Knapik-Kowalczuk J, Wojnarowska Z, Rams-Baron M, Jurkiewicz K, Cielecka-Piontek J, Ngai KL, Paluch M (2017) Mol Pharm 14:2670
17. Bhardwaj SP, Arora KK, Kwong E, Templeton A, Clas SD, Suryanarayanan R (2013) Mol Pharm 10:694
18. Bhardwaj SP, Suryanarayanan R (2012) Mol Pharm 9:3209
19. Knapik-Kowalczuk J, Tu W, Chmiel K, Rams-Baron M, Paluch M (2018) Mol Pharm 15:2455
20. Knapik-Kowalczuk J, Chmiel K, Jurkiewicz K, Wojnarowska Z, Kurek M, Jachowicz R, Paluch M (2019) Mol Pharm 16:1742
21. Knapik J, Wojnarowska Z, Grzybowska K, Jurkiewicz K, Stankiewicz A, Paluch M (2016) Mol Pharm 13:1308
22. Kaushal AM, Bansal AK (2008) Eur J Pharm Biopharm 69:1067
23. Zhou D, Zhang GGZ, Law D, Grant DJW, Schmitt EA (2002) J Pharm Sci 91:1863
24. Marsac PJ, Konno H, Taylor LS (2006) Pharm Res 23:2306
25. Grzybowska K, Capaccioli S, Paluch M (2016) Adv Drug Deliv Rev 100:158
26. Hancock BC, Shamblin SL (2001) Thermochim Acta 380:95
27. Shamblin SL, Hancock BC, Dupuis Y, Pikal MJ (2000) J Pharm Sci 89:417
28. Shamblin SL, Tang X, Chang L, Hancock BC, Pikal MJ (2002) J Phys Chem B 103:4113
29. Gupta P, Chawla G, Bansal AK (2004) Mol Pharm 1:406
30. Schönhals A, Kremer F (2003) Broadband dielectr. Spectrosc. Springer Berlin Heidelberg, Berlin, Heidelberg, pp 35–57
31. Paluch M, Rams-Baron M, Tajber L, Knapik-Kowalczuk J, Chmiel K, Wojnarowska Z (2018) Mol Pharm 15:1928
32. Rams-Baron M, Pacult J, Jedrzejowska A, Knapik-Kowalczuk J, Paluch M (2018) Mol Pharm 15
33. Chmiel K, Knapik-Kowalczuk J, Jurkiewicz K, Sawicki W, Jachowicz R, Paluch M (2017) Mol Pharm 14:3370
34. Kremer F, Schönhals A (2003) Broadband dielectric spectroscopy
35. Knapik J, Wojnarowska Z, Grzybowska K, Tajber L, Mesallati H, Paluch KJ, Paluch M (2016) Mol Pharm 13:1937
36. Pacult J, Rams-Baron M, Chmiel K, Jurkiewicz K, Antosik A, Szafraniec J, Kurek M, Jachowicz R, Paluch M (2019) Eur J Pharm Sci
37. Avrami M (1939) J Chem Phys 7:1103
38. Avrami M (1940) J Chem Phys 8:212
39. Kaminski K, Adrjanowicz K, Wojnarowska Z, Dulski M, Wrzalik R, Paluch M, Kaminska E, Kasprzycka A (2011) J Phys Chem B 115:11537
40. Avramov I, Avramova K, Rüssel C (2005) J Cryst Growth 285:394
41. Szczurek J, Rams-Baron M, Knapik-Kowalczuk J, Antosik A, Szafraniec J, Jamróz W, Dulski M, Jachowicz R, Paluch M (2017) Mol Pharm 14:1071
42. Grzybowska K, Paluch M, Grzybowski A, Wojnarowska Z, Hawelek L, Kolodziejczyk K, Ngai KL (2010) J Phys Chem B 114:12792
43. Kolodziejczyk K, Paluch M, Grzybowska K, Grzybowski A, Wojnarowska Z, Hawelek L, Ziolo JD (2013) Mol Pharm 10:2270
44. Adrjanowicz K, Zakowiecki D, Kaminski K, Hawelek L, Grzybowska K, Tarnacka M, Paluch M, Cal K (2012) Mol Pharm 9:1748
45. Sarode AL, Sandhu H, Shah N, Malick W, Zia H (2013a) Mol Pharm 10:3665
46. Leuner C, Dressman J (2000) Eur J Pharm Biopharm 50:47
47. Crowley MM, Zhang F, Repka MA, Thumma S, Upadhye SB, Battu SK, McGinity JW, Martin C (2007) Drug Dev Ind Pharm 33:909
48. Solanki N, Gupta SS, Serajuddin ATM (2018) Eur J Pharm Sci 111:482

49. Sarode AL, Sandhu H, Shah N, Malick W, Zia H (2013b) Eur J Pharm Sci 48:371
50. Gupta SS, Solanki N, Serajuddin ATM (2016) AAPS Pharm Sci Tech 17:148
51. Bochmann ES, Üstüner EE, Gryczke A, Wagner KG (2017) Eur J Pharm Biopharm 119:47
52. Bochmann ES, Steffens KE, Gryczke A, Wagner KG (2018) Eur J Pharm Biopharm 124:34
53. Knapik J, Wojnarowska Z, Grzybowska K, Hawelek L, Sawicki W, Wlodarski K, Markowski J, Paluch M (2014) Mol Pharm 11:4280
54. Szklarz G, Adrjanowicz K, Dulski M, Knapik J, Paluch M (2016) J Phys Chem B 120:11298
55. Schammé B, Couvrat N, Malpeli P, Dudognon E, Delbreilh L, Dupray V, Dargent É, Coquerel G (2016) Int J Pharm 499:67
56. Grzybowska K, Chmiel K, Knapik-Kowalczuk J, Grzybowski A, Jurkiewicz K, Paluch M (2017) Mol Pharm 14:1154
57. Grzybowska K, Paluch M, Wlodarczyk P, Grzybowski A, Kaminski K, Hawelek L, Zakowiecki D, Kasprzycka A, Jankowska-Sumara I (2012) Mol Pharm 9:894
58. Kaminska E, Tarnacka M, Wlodarczyk P, Jurkiewicz K, Kolodziejczyk K, Dulski M, Haznar-Garbacz D, Hawelek L, Kaminski K, Wlodarczyk A, Paluch M (2015) Mol Pharm 12:3007
59. Kaminska E, Adrjanowicz K, Tarnacka M, Kolodziejczyk K, Dulski M, Mapesa EU, Zakowiecki D, Hawelek L, Kaczmarczyk-Sedlak I, Kaminski K (2014) Mol Pharm 11:2935
60. Fung MH, DeVault M, Kuwata KT, Suryanarayanan R (2018) Mol Pharm 15:1052
61. Jensen KT, Blaabjerg LI, Lenz E, Bohr A, Grohganz H, Kleinebudde P, Rades T, Löbmann K (2016) J Pharm Pharmacol 68:615
62. Karagianni A, Kachrimanis K, Nikolakakis I, Karagianni A, Kachrimanis K, Nikolakakis I (2018) Pharmaceutics 10:98
63. Knapik-Kowalczuk J, Tu W, Chmiel K, Rams-Baron M, Paluch M (2018) Mol Pharm 15
64. Knapik J, Wojnarowska Z, Grzybowska K, Jurkiewicz K, Tajber L, Paluch M (2015) Mol Pharm 12:3610
65. Löbmann K, Strachan C, Grohganz H, Rades T, Korhonen O, Laitinen R (2012) Eur J Pharm Biopharm 81:159
66. Mohapatra S, Samanta S, Kothari K, Mistry P, Suryanarayanan R (2017) Cryst Growth Des 17:3142
67. Mesallati H, Tajber L (2017) Pharm Res 34:2425
68. Baghel S, Cathcart H, O'Reilly NJ (2016) J Pharm Sci 105:2527
69. Szafraniec J, Antosik A, Knapik-Kowalczuk J, Kurek M, Syrek K, Chmiel K, Paluch M, Jachowicz R (2017) Int J Pharm 533:470
70. Marsac PJ, Li T, Taylor LS (2009) Pharm Res 26:139
71. Andrews GP, Abu-Diak O, Kusmanto F, Hornsby P, Hui Z, Jones DS (2010) J Pharm Pharmacol 62:1580
72. Ogawa N, Hiramatsu T, Suzuki R, Okamoto R, Shibagaki K, Fujita K, Takahashi C, Kawashima Y, Yamamoto H (2018) Eur J Pharm Sci 111:205
73. Szafraniec J, Antosik A, Knapik-Kowalczuk J, Chmiel K, Kurek M, Gawlak K, Paluch M, Jachowicz R (2018) Int J Pharm 542
74. Altamimi MA, Neau SH (2018) Powder Technol 338:576
75. Aho J, Edinger M, Botker J, Baldursdottir S, Rantanen J (2016) J Pharm Sci 105:160
76. Yang F, Su Y, Zhang J, DiNunzio J, Leone A, Huang C, Brown CD (2016) Mol Pharm 13:3494
77. Repka MA, Gerding TG, Repka SL, McGinity JW (1999) Drug Dev Ind Pharm 25:625
78. Mistry P, Amponsah-Efah KK, Suryanarayanan R (2017) Cryst Growth Des 17:2478
79. Aso Y, Yoshioka S, Kojima S (2004) J Pharm Sci 93:384
80. Rumondor ACF, Stanford LA, Taylor LS (2009) Pharm Res 26:2599
81. Mahieu A, Willart J-F, Dudognon E, Danède F, Descamps M (2013) Mol Pharm 10:560
82. Lehmkemper K, Kyeremateng SO, Degenhardt M, Sadowski G (2018) Pharm Res 35:25
83. Rask MB, Knopp MM, Olesen NE, Holm R, Rades T (2016) Eur J Pharm Sci 85:10
84. Rask MB, Knopp MM, Olesen NE, Holm R, Rades T (2018) Int J Pharm 540:98
85. Li S, Tian Y, Jones DS, Andrews GP (2016) AAPS Pharm Sci Tech 17:200
86. Tian Y, Booth J, Meehan E, Jones DS, Li S, Andrews GP (2013) Mol Pharm 10:236
87. Flory PJ (1953) Principles of polymer chemistry. Cornell University Press

88. Nishi T, Wang TT (1975) Macromolecules 8:909
89. Tamagawa RE, Martins W, Derenzo S, Bernardo A, Rolemberg MP, Carvan P, Giulietti M (2006) Cryst Growth Des 6:313
90. Sun Y, Tao J, Zhang GGZ, Yu L (2010) J Pharm Sci 99:4023
91. Park K, Evans JMB, Myerson AS (2003) Cryst Growth Des 3:991
92. Mohan R, Lorenz H, Myerson AS (2002) Ind Eng Chem Res 41:4854
93. Qian F, Huang J, Hussain MA (2010) J Pharm Sci 99:2941
94. Tao J, Sun Y, Zhang GGZ, Yu L (2009) Pharm Res 26:855
95. Havriliak S, Negami S (1967) Polymer (Guildf) **8**:161
96. Chmiel K, Knapik-Kowalczuk J, Paluch M (2019) Eur J Pharm Biopharm (In press)
97. Chmiel K, Knapik-Kowalczuk J, Jachowicz R, Paluch M (2019) Eur J Pharm Biopharm 136:231

Ordering Transitions in Short-Chain Alcohols

Alejandro Sanz

Abstract Alcohols present fascinating properties, both static and dynamic, to a large extent due to the presence of a hydrogen-bonded network. In the liquid state, hydrogen bonds (HB) are continuously forming and breaking on a timescale of 10^{-11} s at room temperature. Thus, these substances exhibit a rich dynamic behaviour at different time and length scales. Alcohols are considered complex systems in which structural and dynamic fluctuations in the HB network play a key role in the relaxation dynamics, as well as on the structural development. Revealing the interplay between the structural ordering and the relaxation dynamics during crystallization in short-chain alcohols is of paramount importance. One of the most powerful experimental methods to tackle this problem is dielectric spectroscopy (DS), not only because it offers information about characteristic time scales, but also because it allows obtaining information about the static properties of the system, at least in an indirect manner. In this chapter, we go through some of the most representative examples that illustrate the crystallization in short-chain alcohols by using dielectric spectroscopy, making special emphasis on those works in which dielectrics has been combined simultaneously with neutron diffraction (ND). This singular approach allows the crystal development to be tracked by means of ND, and the dynamic changes occurring in the disordered phase by DS, providing in this manner a complete picture of the structural ordering process.

Keywords Crystallization · Neutron diffraction · Alcohols · Hydrogen-bonded liquids · Plastic crystals

A. Sanz (✉)
Glass and Time, IMFUFA, Department of Science and Environment, Roskilde University, P.O. Box 260, 4000 Roskilde, Denmark
e-mail: asanzparras@gmail.com

Abbreviations

CNT   Classical nucleation theory
DS   Dielectric spectroscopy
G_{crys} Gibbs free energy of the crystalline state
G_{liq} Gibbs free energy of the liquid state
HB   Hydrogen bond
JMAK Johnson–Mehl–Avrami–Kolmogorov
MW   Maxwell–Wagner effect
ND   Neutron diffraction
PC   Plastic crystal
SCL   Supercooled liquid
T_g Glass transition temperature

1 Introduction

In this chapter, we will describe how dielectric spectroscopy techniques have contributed for a better understanding of the structure-dynamics correlations in low molecular weight alcohols. We will focus on the transformation of liquid short-chain alcohols into solid phases with periodic order, with especial attention paid to crystallization processes. Unlike liquids, where molecular entities exhibit rotational and translational mobility, in the true crystalline state, molecular motions are restricted to small oscillations about fixed positions in a regular lattice.

According to thermodynamics, crystallization would be possible as soon as the difference between the Gibbs free energy of the crystal G_{crys} and that of the liquid G_{liq} is negative [1–3]. Let us remind that the Gibbs free energy combines the internal energy of the system H and the entropy S, being the latter modulated by temperature as follows:

$$G = H - TS \qquad (1)$$

In most cases, ordering transitions get triggered by a reduction of the internal energy at temperatures below the corresponding melting point, although entropy-driven transitions into more ordered phases may also take place [4]. In these latter cases, freezing processes proceed via a partial ordering of the molecular entities while density remains almost constant. This is then understood to be produced by some molecular rearrangements allowing the stabilization of the new phase due to an increase in entropy instead of through a minimization of the internal energy. Freezing transitions in short-chain alcohols corresponding to both scenarios will be reviewed in the sections below.

The first step in crystallization requires overcoming the energy barrier of creating tiny crystalline seeds by thermal random fluctuations. During this process, termed

nucleation, tiny seeds of crystals are formed that will continue to grow by advancing the liquid/crystal interface across the remaining liquid medium. Molecular mobility of the mother phase, surface tension of the liquid/crystal interface, intermolecular attractions, purity of the sample and its interactions with the environment, are known to govern the crystallization tendency of supercooled liquids [5–8]. Crystallization is therefore a complex phenomenon, in which, apart from the thermodynamic driving force, several factors are simultaneously involved.

Along with the thermodynamic barrier to nucleation and crystal growth, it is well established that the molecular mobility plays a critical role in the crystalline development, although the exact nature of this interrelationship is still a matter of debate [9]. Most of the examples discussed in the present chapter relate to ordering transitions near the glass transition temperature, T_g, where the transport of molecules across the liquid/crystal interface for creating new crystalline layers is the limiting factor. Since it is directly related to the molecular dynamics, crystal growth is very dependent on temperature. One of the theoretical frameworks that, with some degree of approximation, have successfully explained the liquid-to-crystal transition is the classical nucleation theory (CNT) [10–13]. A detailed description of the theory is beyond the scope of the present chapter, but it may be useful to point out that the kinetic barriers for nucleation, ΔG_D, and growth, ΔE, can be expressed in terms of the self-diffusion coefficient as follows:

$$\exp\left(-\frac{\Delta G_D}{k_B T}\right) \propto D, \tag{2}$$

$$\exp\left(-\frac{\Delta E}{k_B T}\right) \propto D. \tag{3}$$

The kinetic contributions for nucleation and crystal growth can also be given by the reciprocal shear viscosity, η^{-1}, assuming the Stokes-Einstein relation holds [6].

Due to the presence of hydroxyl groups, the intermolecular interactions in alcohols are largely dominated by the directional character of hydrogen bonds (HB), resulting in supramolecular structures that form and break continuously on an approximate timescale of 10^{-11} s at room temperature [14, 15]. The structure, thermodynamics and dynamics of alcohols will, therefore, depend critically on the properties of the HB network. To quote IUPAC [16], "*the hydrogen bond is an attractive interaction between a hydrogen atom from a molecule or a molecular fragment X–H in which X is more electronegative than H, and an atom or a group of atoms in the same or a different molecule, in which there is evidence of bond formation.*" In the specific case of alcohols, each hydroxyl group can form up to three bonds, one involving the hydrogen atom and two involving the oxygen. As mentioned above, the HB network has a dynamic or *living* character, where the HB's are continuously forming and disintegrating, giving as a result a rich variety of motifs depending on the molecular architecture, temperature and pressure [17]. With the purpose of understanding the dynamics of the structural fluctuations in these supramolecular networks, a great

effort has been made over the past decades, in particular by utilizing dielectric spectroscopy methods [18]. Alcohols are extremely active in dielectric spectroscopy given the high dipole moment of hydroxyl groups, which constitutes an important benefit when dielectrics is employed for the study of crystallization processes, in particular during the late stages of the phase transition where a small fraction of mobile phase remains surrounded by the growing crystals [19, 20].

One of the most relevant features in liquid monohydroxy alcohols is the presence of a strong dielectric dispersion located at lower frequencies than that corresponding to the universal structural relaxation observed in all kinds of liquids. Due to its narrow shape, this strong peak is known as the Debye peak. There is a general consensus on the connection between the Debye peak and the dynamic character of the HB network. In Fig. 1 we show the dielectric loss as a function of frequency for supercooled isopropanol at 130.5 K, where the most intense process located at the low-frequency flank of the spectrum corresponds to the Debye peak. The Debye peak does not possess the main features of the typical structural or α relaxation and different models have been proposed for explaining its origin but commonly associated with the hydrogen bonding network dynamics [21–24]. For instance, according to the wait-and-switch model, first a molecule of the network switch its position to reorient itself but it must wait until a favourable condition for reorientation exists in the network [14, 22, 23, 25, 26]. Under the framework of this model, the mean relaxation time of the Debye peak is expected to depend inversely upon the number density of available hydrogen bonding sites [27].

The formation of superstructures via HB's is corroborated by the presence of a pre-peak at wave-vector values below the main peak (intermolecular correlations) in the static structure factor. These pre-peaks stem from the intermolecular aggregates via hydroxyl groups interactions and it is a well-documented signature in monohydroxy alcohols [28, 29] (Fig. 2).

In this chapter, we will pay special attention to the main results obtained by using a peculiar experimental setup that allows one to perform simultaneously dielectric

Fig. 1 Imaginary part of the dielectric susceptibility for isopropanol at 130.5 K. Solid black line is the total fit of the experimental data (○) using a Debye, Cole–Davidson and log-normal distribution function for describing the primary, alpha and beta relaxations respectively
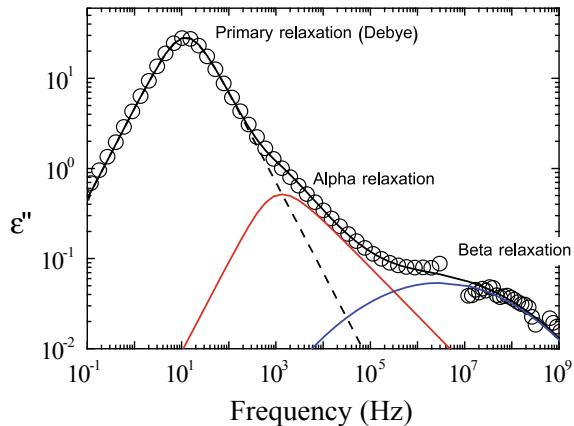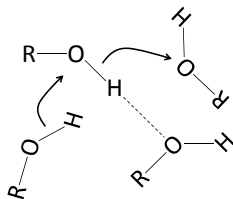
Fig. 2 Schematic description of the cooperative dynamics in a HB network. Hydroxyl groups of different molecules abandon and enter (molecule oriented favourably for a "switch") continuously the network

spectroscopy and neutron diffraction experiments with the main purpose of monitoring crystallization processes in real-time [30]. By means of this experimental approach, one can get information on both the crystal development through neutron diffraction (ND), and the dynamic changes occurring in the disordered (mobile) phase by dielectric spectroscopy, in this way, providing a complete picture of the ordering process.

We will also review, in the author's subjective view, the most relevant works in the field of crystallization of low molecular weight alcohols by using standard dielectric spectroscopy techniques.

2 Simultaneous Neutron Diffraction and Dielectric Spectroscopy During Crystallization of Liquids

As a result of the collaboration between the Institute for the Structure of Matter (CSIC, Madrid, Spain) and the neutron source facility Institute Laue-Langevin (Grenoble, France), in the early 2000s, a novel experimental setup to obtain information on structural and dynamic changes in liquids during crystallization was developed [30]. The setup consists of a sample cell that allows performing simultaneous measurements of neutron diffraction and dielectric spectroscopy. By carrying out these simultaneous experiments, information can be obtained from both phases, amorphous and crystalline, and therefore it can provide a complete description of the static and dynamic modifications occurring during a crystallization process. By utilizing this combined cell, from this point on ND-DS technique, it is possible to acquire in parallel the frequency-dependent complex dielectric permittivity and neutron diffraction patterns. In DS, one measures the complex dielectric permittivity, $\varepsilon * (\omega) = \varepsilon'(\omega) - i\varepsilon''(\omega)$, with ε' the real part of the permittivity and ε'' the so-called dielectric loss. In the particular case of the ND-DS cell, the complex permittivity was calculated through measurements of the complex impedance by placing the liquid sample in a container between two metallic electrodes of area A separated a distance d and subjected to an alternating electric field of angular frequency ω. A schematic description of the NS-DS setup is illustrated in Fig. 3. The liquid is placed in a
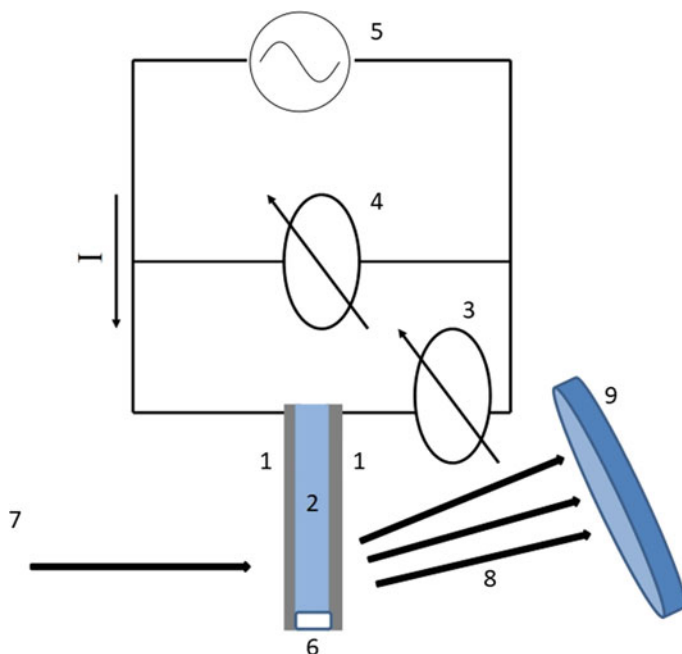
Fig. 3 Schematic view of the simultaneous dielectric spectroscopy and neutron diffraction technique. (1) Electrodes of area A, (2) sample of thickness d, (3) current analyzer, (4) voltage analyzer, (5) alternating voltage generator, (6) insulating spacer, (7) incoming neutron beam, (8) diffracted neutron beam, and (9) neutron detector

container made of anodized aluminium (50 µm thick). Anodized aluminium was chosen since is an appropriate material to give a weak neutron intensity absorption, and also because it becomes insulating. Two standard aluminium layers acting as electrodes separated by a Teflon® spacer and connected through the cap to the wires are connected to a Stanford lock-in amplifier SR830 with a dielectric interface and control unit from Novocontrol. Electrodes are glued to the cap by cryogenic glue. The set formed by the cap, the electrodes and the spacers encloses the liquid by means of an indium ring and four screws.

A Teflon® spacer keeps the electrodes in place at a distance of 3 mm. By changing the shape of the spacer, the volume of liquid can be varied if necessary in order to vary the sample capacitance as well.

All results shown in this section were obtained through experiments carried out on the 2-axes diffractometer *D1B* at the Institut Laue Langein (ILL). The ND-DS cell was designed as simple and compact as possible to fit in the D1B cryostat ($\phi = 25$ mm), covering the capacitor an area nearly equal to the neutron beam size. This cell can be used in the rest of the cryostats and instruments of the ILL which generally have a diameter $\phi = 50$ mm. The neutron wavelength was set at $\lambda = 2.52$ Å and the data were normalized to the monitor for accounting for fluctuations
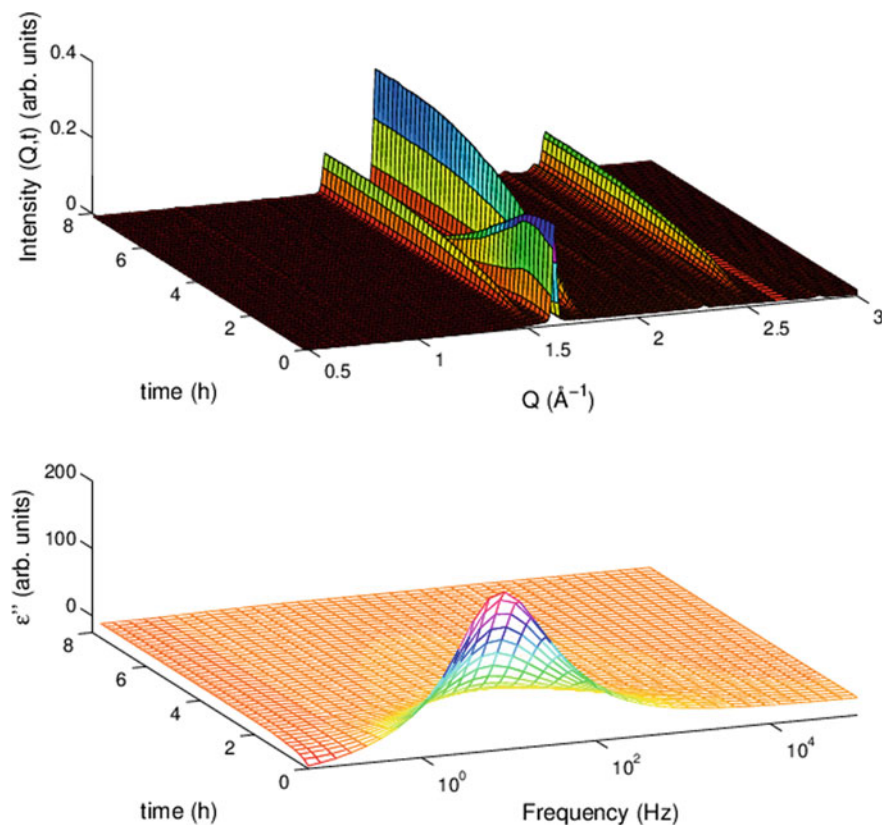
Fig. 4 Simultaneous neutron diffraction (top) and dielectric spectroscopy (bottom) data obtained by using the ND-DS setup for the transformation of plastic crystal ethanol into the monoclinic crystalline phase at 115 K. Experiment carried out on the diffractometer D1B at the ILL

in the intensity of the beam. As an example of the possibilities of the ND-DS setup, Fig. 4 presents the temporal evolution of the diffraction pattern (top) and alpha relaxation curve for ethanol during isothermal annealing at 115 K. More precisely, it shows the transformation from the rotationally disordered plastic crystal into the monoclinic crystal state [31]. Neutron intensity is plotted against the scattering vector $Q = 4\pi \sin(\theta)/\lambda$, where λ is the neutron wavelength and 2θ the scattering angle.

2.1 Crystallization of 2-Propanol by ND-DS Measurements

Isopropanol (2-propanol) is a monohydroxy alcohol with a glass transition temperature (T_g) at ambient pressure of 115 K. Of paramount importance is to establish the principal correlations between the molecular mobility and the growing structure

during crystallization above T_g, with particular interest on the role played by the HB network on the crystallization process [27].

It is worthy to remind that neutron diffraction is a type of coherent scattering and, consequently, the sample to be measured must have a high coherent cross-section. For this reason, deuterated isopropanol (2-propanol d8, 99% of deuterium) was used. The sample was quenched in the glassy state at 75 K from room temperature and different crystallization temperatures above T_g were reached on heating. The evolution of the ND-DS data during the crystallization of supercooled isopropanol at 134 K is shown in Fig. 5. The formation of a crystalline lattice and the concomitant destruction of the liquid mobile phase have a strong impact on both neutron diffraction and dielectric spectroscopy data. Regarding diffraction, as crystallization proceeds, several Bragg peaks stem at the expense of the typical amorphous halo observed in disordered matter that decreases progressively [27]. In parallel, the dielectric dispersion decreases in intensity as the fraction of mobile dipoles in the system becomes smaller in accordance to the theory of dielectric relaxation that relates directly the dielectric strength to the density of relaxing entities. As expected for a true crystalline phase with rotational and translational order, the area of the dielectric dispersion totally vanishes when the crystallization kinetics is over.

Dielectric loss data were described by two Cole–Davidson functions: (i) a primary relaxation at low frequencies (Debye peak) attributed to the hydrogen-bond network dynamics, and (ii) a secondary relaxation which is assigned to the alpha process. The dielectric dispersion curves are then fitted to the following expression, $\varepsilon'' = \mathrm{Im}[\varepsilon*] = \mathrm{Im}\big[\varepsilon_\infty + \sum_{x=\mathrm{I,II}} \Delta\varepsilon_x (1 + (i\omega\tau_x))^{-c_x}\big]$, with $\Delta\varepsilon$ the dielectric strength, c the shape parameter which describes the asymmetric broadening of the relaxation time distribution function, and τ the central relaxation time [32].

A major advantage of performing simultaneous DS and ND measurements is the possibility of correlating dynamic properties with the fraction of crystalline phase in an unambiguous way, that is, both quantities being generated under exactly the same conditions, precluding unwanted external effects associated with different sample environments. It was shown that the dependence of the dielectric strength with the degree of crystallinity for the primary and alpha relaxations was quite different as indicated in Fig. 6. From the very early stages of crystallization, a dramatic decrease of $\Delta\varepsilon_\mathrm{I}$ is observed which is interpreted as a depletion of the HB network.

Provided that the relaxing species being lost from the network are directly transferred to the crystalline phase in a linear fashion, a two-phase scenario for the dielectric strength denoted in Fig. 6 by a continuous line, should be expected. The strong deviation from the two-phase model for the Debye peak is interpreted as due to the existence of an intermediate step between the situation in which the molecule is in the network and that in which it occupies a position in the crystal. This indicates that the breakage of the HB network is a necessary but not sufficient step for nucleation [27]. On the other hand, the alpha relaxation shows an almost linear dependence of $\Delta\varepsilon$ with crystallinity, much closer to the two-phase behaviour indicating that the relaxing species contributing to the alpha process which are lost in the amorphous phase are almost completely transferred to the crystalline phase. It is important to remark that the fraction of crystallinity is calculated by describing the diffraction

Fig. 5 Simultaneous ND (bottom) and DS (top) data as a function of time during isothermal annealing of isopropanol at 134 K. ND patterns are represented as a function of the scattering angle. DS spectra are given for every time as a function of frequency
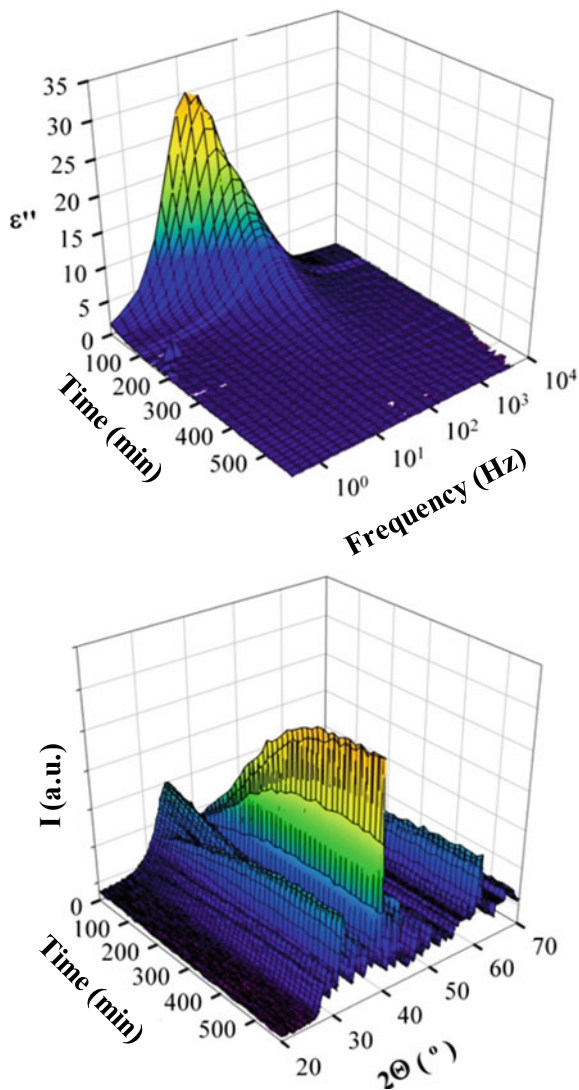
patterns as a linear combination of the fully crystallized (last pattern) and initial amorphous (first pattern) contributions [33].

In relation to the location of the relaxation process with crystallinity, both contributions shift towards higher frequencies as crystallization proceeds, suggesting an enhancement of the dynamics as the crystal phase grows. The disruption of the HB network, as a first step of the crystalline nucleation, involves more available sites in the network and, consequently, shorter waiting times for new molecules entering the network. This would explain the displacement of the Debye peak towards higher frequencies, in particular during the early stages of crystallization. The increment
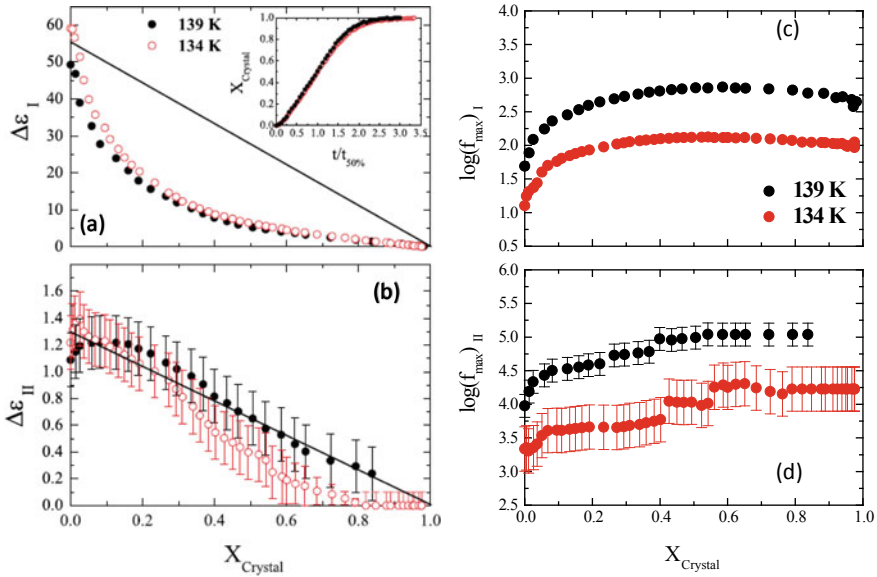
Fig. 6 Correlation between dynamic magnitudes and degree of crystallinity for 2-propanol during isothermal crystallization at 134 and 139 K. **a** Dielectric strength for the Debye peak; **b** Dielectric strength for the alpha relaxation; **c** Frequency of the maximum loss for the Debye peak; **d** Frequency of the maximum loss for the alpha relaxation. The inset on panel (**a**) presents the evolution of crystallinity with normalized time for the two studied temperatures. Reprinted with permission from Ref. [27]. Copyright (2004) by the American Physical Society

of $f_{(max)II}$ (alpha process) with crystallinity is interpreted consistently as being due to a depletion of relaxing species from the HB network. Establishing and analogy between the number of HB's in the network and the density of cross-links in polymeric systems, it is plausible to interpret the acceleration of the cooperative motions associated to the alpha process with the progressive distortion of the HB network during the early stages of the ordering transition [33, 34]. In summary, the results presented in Fig. 6 indicate that a breakage of the hydrogen-bonded network occurs at a first step in the formation of crystals during the crystallization of isopropanol [27].

2.2 Partial and Total Ordering of Supercooled Liquid Ethanol by Simultaneous ND-DS Measurements

Unlike the scenario presented above for 2-propanol, the phase behaviour in supercooled liquid ethanol is more complex. Besides the ordinary crystal state with rotational and translational order, at temperatures near T_g, ethanol forms another structural phase with intermediate order between the true crystalline and liquid state.
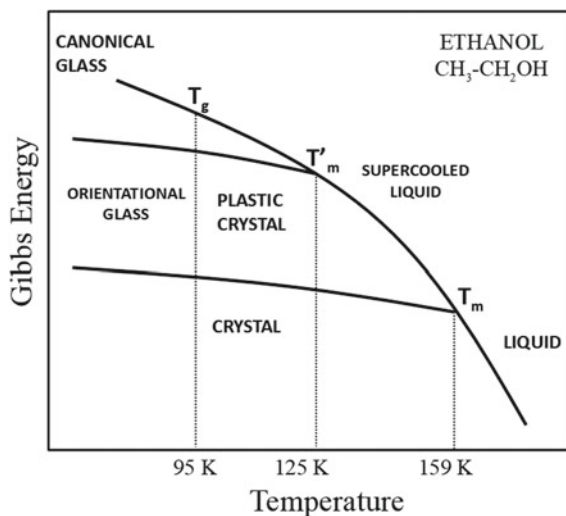
This metastable phase presents translational order, in which the centre of mass of the molecular species remains fixed at the nodes of a crystalline lattice, but it lacks rotational order. It is important to note that the rotational mobility in orientationally disordered crystals gets frozen at a characteristic T_g, transforming into the so-called orientational glass with random molecular orientations. As indicated in Fig. 7, both the supercooled liquid and plastic crystals phases form their respective glasses at the same temperature and very close densities [35]. The formation of these rotationally disordered crystals, commonly named plastic crystals, is fairly common in organic substances with small steric hindrance to molecular reorientation and some degree of intrinsic disorder [36, 37]. An increase of the rotational mobility (increase of rotational entropy) provides the necessary stabilization of these metastable phases.

Figure 8 presents the corresponding neutron diffractograms for the supercooled liquid, plastic crystal and stable monoclinic phase. A rigorous neutron and X-ray diffraction study by Bermejo et al. [39], revealed that the structure of plastic crystal ethanol corresponds to a cubic lattice (BCC), with two independent molecules per unit cell.

A precise experimental protocol must be followed in order to explore the formation of such structural phases. Liquid ethanol at room temperature must be cooled rapidly (cooling rate > 6 K/min) to temperatures below T_g, with the purpose of avoiding crystallization on cooling. In this particular case, the sample was quenched to 75 K. If supercooled liquid (SCL) ethanol is annealed between 105 and 110 K, the plastic crystal (PC) is formed. Finally, the plastic crystal phase tends to crystallize into a fully-ordered monoclinic phase at temperatures above 115 K.

Before we start discussing the main results obtained using the ND-DS technique, the transformation from SCL into the PC phase was previously investigated by standard real-time dielectric spectroscopy [40]. In this work, Benkhof and co-authors already pointed out that PC ethanol forms in a narrow temperature window around
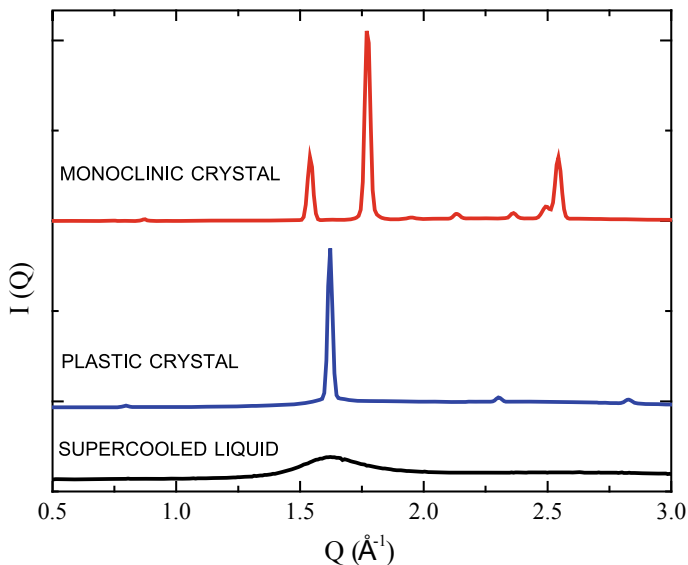
Fig. 8 Neutron diffractograms of deuterated ethanol (CD_3CD_2OD) corresponding to the stable monoclinic crystal (115 K), metastable plastic crystal (115 K) and metastable supercooled liquid (105 K). Data collected on the D1B instrument (ILL)

105 K, although excluding kinetic factors, the formation of the PC phase should be possible between T_g and 115 K approximately. It was reported that the dielectric spectra for the two PC and SCL phases were rather similar, with the exception of the time constant, indicating that the slow dynamics of PC and that of SCL ethanol probed by dielectric spectroscopy are basically identical.

The transformation of SCL ethanol into the PC phase at a fixed temperature of 105 K is discussed here below. Selected simultaneous ND patterns and DS spectra are displayed in Fig. 9. A remarkable observation is the transformation of the dielectric relaxation upon annealing. The main relaxation associated with the liquid phase is centred around 1 Hz and decreases in intensity as the metastable PC phase grows. In parallel, a new relaxation appears at lower frequencies due to the mobile nature of the plastic crystal phase. This process induced by pure reorientations of ethanol molecules presents slower relaxation times than that of SCL because of the translational constraints imposed by the BCC lattice.

In order to elucidate unequivocally the fraction of sample transformed into the PC phase, the diffraction patterns can be described as a linear combination of two contributions, corresponding to ordered (N_{PC}) and disordered (N_{SCL}) phases:

$$I(Q, t) = I_{PC}(Q) + [1 - N_{PC}(t)]I_{SCL}(Q), \tag{4}$$

Fig. 9 Selected snapshots during isothermal transformation of SCL ethanol (CD3CD2OD) into PC phase. Simultaneous DS curves (**a**) and ND patterns (**b**) are presented during annealing at 105 K. ND patterns are represented as a function of the scattering vector Q. DS spectra are given for every time as a function of frequency. Every pattern was recorded with an acquisition time of 10 min. Annealing time is indicated in hours. Reprinted with permission from Ref. [41]. Copyright (2011) by the American Physical Society
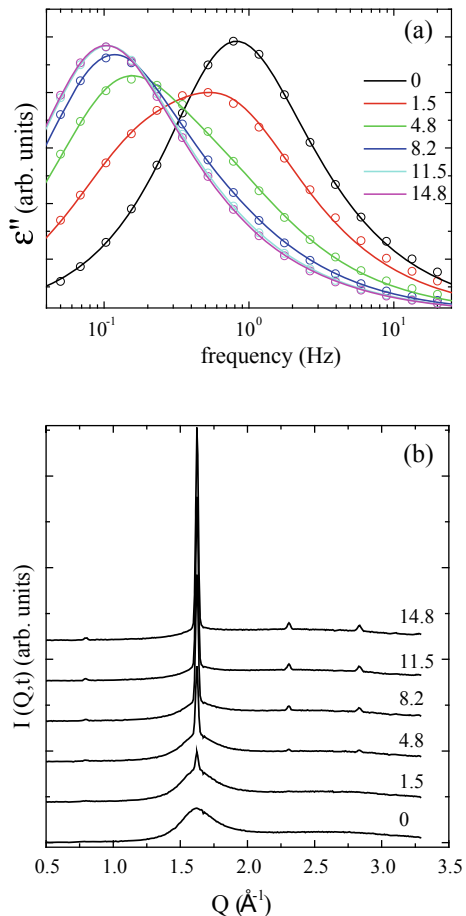
where I_{PC} is the intensity from the Bragg peaks and I_{SCL} the intensity from the amorphous halo. In Fig. 10, the time dependence of the fraction of PC phase at 105 and 109 K shows the typical sigmoidal shape for an overall crystallization process. The values of N_{PC} along the phase transition, calculated by Eq. 4, are described in terms of the Johnson−Mehl−Avrami−Kolmogorov (JMAK) model [42–45]. According to this model, the kinetics of crystallization can be expressed as follows:

$$N(t) = 1 - \exp\left(-\left(\frac{t - t_0}{\tau_{crys}}\right)^n\right), \tag{5}$$

with $N(t)$ the fraction of transformed phase under isothermal conditions, t_0 the induction time, n is a dimensionless exponent related to the nature of the nucleation phenomenon and dimension of the crystal growth, and τ_{crys} the characteristic

Fig. 10 Fraction of plastic crystal phase during isothermal annealing of supercooled deuterated ethanol at 105 and 109 K. Solid lines correspond to the best fit of the experimental data to the JMAK equation (Eq. 5)
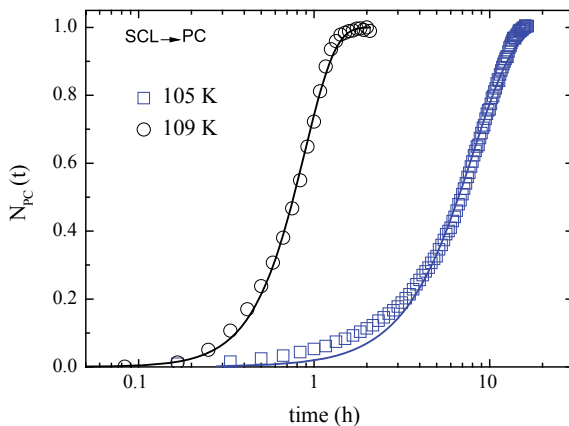
crystallization time. Fits of the experimental data to the JMAK equation are shown in Fig. 10 as continuous lines. Values of the exponent n close to 2 were found for both temperatures. A physical interpretation of the values of n for the transformation of SCL ethanol into the PC phase is beyond the scope of the present section.

As mentioned earlier, thanks to the ND-DS approach, one can correlate in a single experiment dynamic and static properties. It was found that the values of N_{PC} were noticeably lower when estimated by ND than those calculated by using dielectric strength, especially for intermediate crystallization times. This mismatch is interpreted considering that, although a portion of ethanol molecules are relaxing at a slower rate as compared to the fully disordered SCL phase, these are not attached to the ordered BCC lattice yet. Assuming the fraction of the new phase is unequivocally obtained by ND data, the following strategy was proposed to describe the dielectric spectra over time. The existence of an additional phase, presumably associated with an intermediate step of the partial ordering of SCL ethanol into the rotator phase (PC) was proposed. Dielectric loss data can be described by a weighted superposition of three Cole–Davidson modes: $\varepsilon''(\omega, t) = N_{PC}(t)\varepsilon''_{PC}(\omega) + N_{PRE}(t)\varepsilon''_{PRE}(\omega) + N_{SCL}(t)\varepsilon''_{SCL}(\omega)$, where the subscripts stand for the initial *SCL* and final *PC* phases, and also for the proposed precursor (PRE) phase.

The results shown in Fig. 11 demonstrate that previous to the growth of the crystalline lattice of the plastic crystal phase, the formation of a precursor or intermediate phase through a liquid-liquid phase separation takes place. Once this precursor phase is formed, subsequent (plastic) crystalline nucleation and growth is expected to develop [41].

Following the experimental protocol shown below and according to the phase diagram illustrated in Fig. 7, the stable monoclinic phase can be formed from the plastic crystal by heating the sample above 110 K approximately (Fig. 12).

Figure 4 displays ND-DS data for the transformation of deuterated ethanol from its PC form into the stable monoclinic phase [31]. During the isothermal transition from the rotator phase to the stable monoclinic lattice, an acceleration of the cooperative
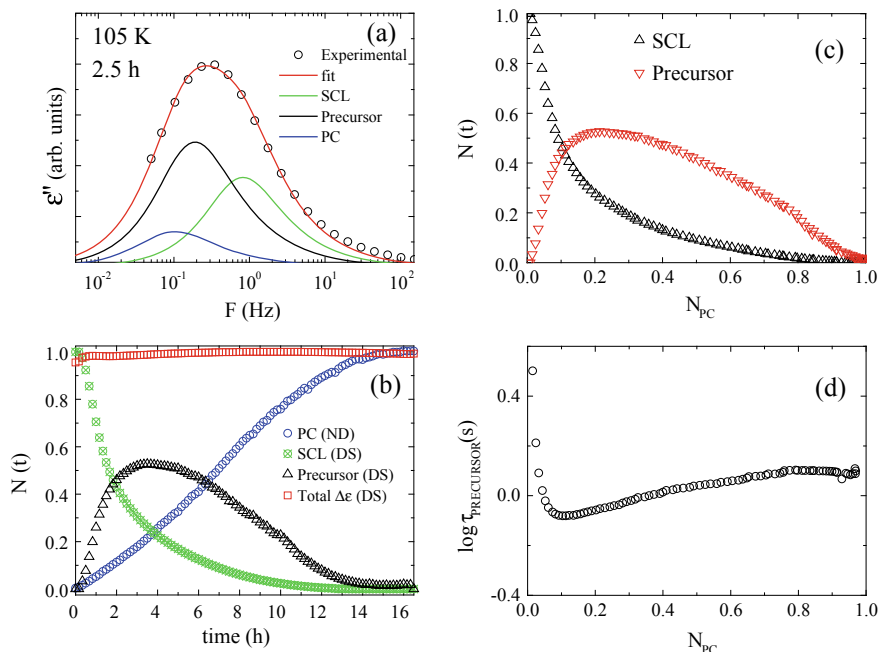
Fig. 11 **a** Fitting of the dielectric relaxation curve for annealing time of 2.5 h during transformation of SCL ethanol into PC at 105 K. **b** Time evolution of the fraction associated with the coexisting phases calculated by ND and DS. Normalized total dielectric strength is also shown for comparison. **c** Normalized dielectric strength to its initial value for the SCL and interface relaxations of deuterated ethanol as a function of the PC volume fraction. **d** Characteristic relaxation time for the main relaxation assigned to the precursor phase against the fraction of PC phase estimated by ND. Reprinted with permission from Ref. [41]. Copyright (2011) by the American Physical Society
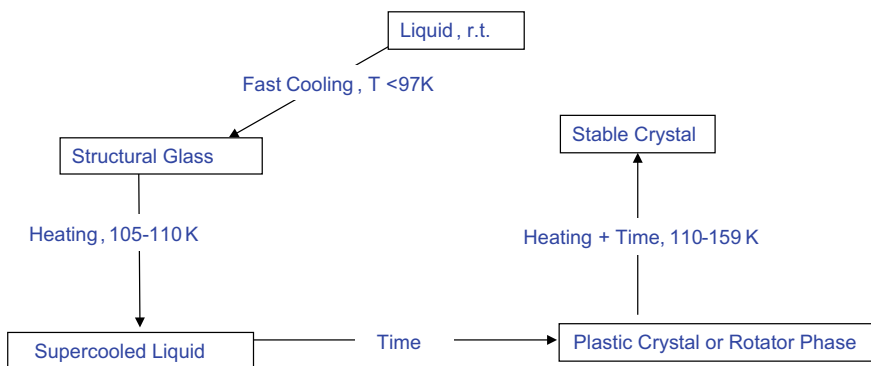
Fig. 12 Thermal protocol for controlling the structural order in ethanol. Isothermal annealing is employed to facilitate the transformation of supercooled liquid ethanol into the plastic crystal phase, as well as the final transition of the PC phase into the stable monoclinic state

motions related to the main dielectric relaxation is observed, as well as evidences of
the necessity of a deep reorganization of the HB network as a precursor step of the
overall crystallization process, similar to what is found for the ordinary crystallization
of isopropanol from the supercooled liquid state. As an example, two dielectric
spectra at different crystallization times are presented in Fig. 13. Two Cole–Davidson
functions were used to fit the experimental data to account for the primary (Debye
peak) and secondary (alpha) relaxations. The vertical dotted line in Fig. 13 is a guide
to help the reader to highlight the displacement of the maximum loss towards higher
frequencies as crystallization proceeds. Since the primary relaxation dominates the
spectrum, the fitting procedure was carried out by keeping slight constrains on the
shape and relaxation time of the secondary process. More precisely, the values of the
relaxation time for the secondary process were kept fixed during the fitting procedure.
This strategy was chosen in order to control the validity and physical reliability of
the resulting fits. Regarding the rest of fitting parameters, it was possible to let vary
the area and shape parameter c, the latter ranging between 0.25 and 0.5, obtaining in
this way satisfactory fits [31].

Dynamic features of PC ethanol might be unequivocally correlated to the fraction
of monoclinic phase (N_{MC}). The values of N_{MC} were estimated by ND data by
fitting the experimental neutron scattering patterns to a similar expression to Eq. 4.
In Fig. 14a, one observes a speeding up of the primary relaxation as soon as the
monoclinic crystals start to grow up to volume fractions of 0.8 approximately. Only
for large volume fractions of monoclinic phase, the primary relaxation time of the
remaining plastic crystal ethanol seems to keep constant or slightly increase. The

Fig. 13 Combination of two Cole–Davidson functions for describing the dielectric loss spectra of deuterated ethanol during the transition from the plastic crystal into the monoclinic phase at a fixed temperature of 115 K. Black solid lines correspond to the total fit, red solid lines represent the primary or Debye relaxation, and blue solid lines stand for the α process
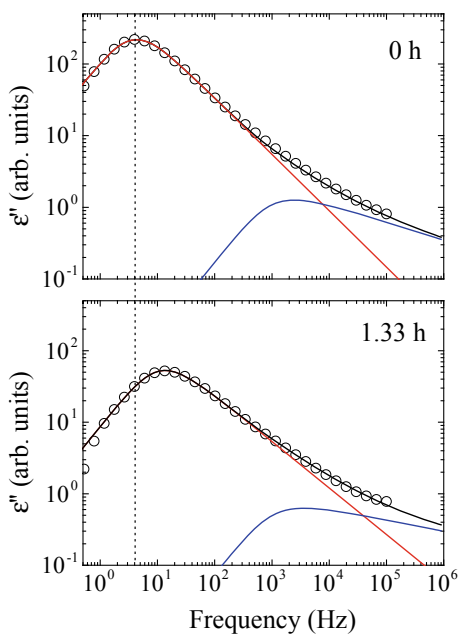
Fig. 14 a Relaxation time of
the primary relaxation of
plastic crystal ethanol as a
function of monoclinic phase
fraction (NMC).
b Normalized dielectric
strength for primary and
alpha relaxations against
N_{MC}. Reprinted from Ref.
[31] with the permission of
AIP Publishing
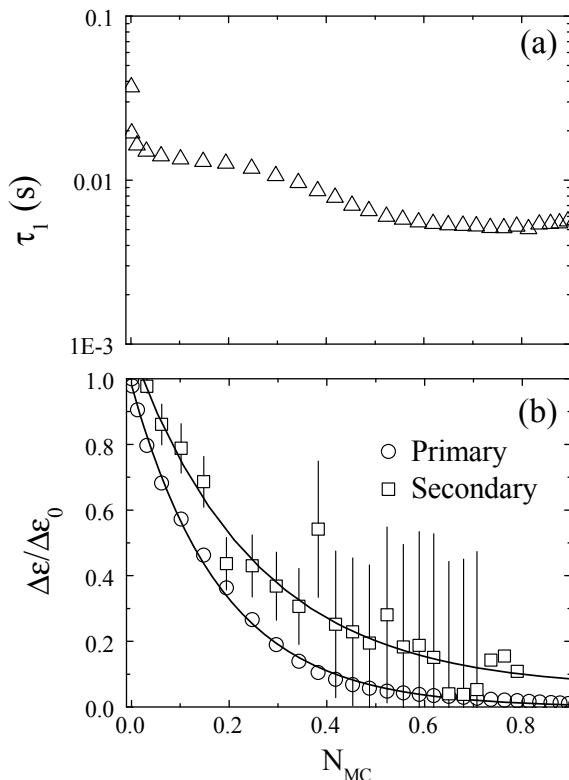
bottom panel of Fig. 14 shows the variation of the normalized dielectric strength for
the Debye peak against monoclinic volume fraction. Data for the alpha relaxation
is also included. Departure from linearity is detected for the prominent Debye peak
and considering that it arises from the dynamic character of the HB network, these
results reveal that the disruption of the network is not directly correlated to the
transfer of molecules into the new phase. The secondary relaxation shows a less
strong dependence, telling that the amplitude of the secondary relaxation shows
a closer relationship to linearity with the vanishing of the plastic crystal phase.
Nevertheless, also for the alpha relaxation, the dependence of the dielectric strength
with N_{MC} exhibits a clear curvature, unlike the purely linear fashion observed in
isopropanol crystallization. On the basis of that behaviour, it is highly plausible that
the geometrical restriction imposed by the BCC lattice that strongly controls the
nature of the intermolecular hydrogen bonding forces makes the alpha relaxation
more sensitive to distortions of the HB network.

By means of molecular dynamics simulations, it has been proposed that the reori-
entation of the ethanol molecules that occupy the BCC lattice in the rotator phase
is not totally random [46], being the orientation of the ethanol species governed by

the formation of HB's with the surrounding molecules. Given that whole body reorientation is the main contribution to the dielectric response of supercooled ethanol, the dynamics for SCL and PC is essentially the same, only differing in the time scale which is slightly slower for the rotator phase due to the spatial restrictions imposed by the positional order [40, 47]. During the phase transition from PC into the monoclinic crystal state, the mobility of the former experiences dramatic changes, in particular at the initial stages of crystallization, in contrast to other low molecular weight glass formers where the location and broadening of the main dielectric process remain nearly unchanged in the course of crystallization [48, 49]. Based on the results presented above, it is postulated that a dynamic transition from PC to SCL-like configuration through a deep reorganization of the HB network should take place along the pathway followed by the ethanol molecules as they diffuse from the mother phase and finally attach to the monoclinic crystalline front [31].

3   Structural Ordering in Short-Chain Alcohols by Standard Dielectric Spectroscopy Techniques

In this section, we will review several examples on the study of crystallization kinetics in short-chain alcohols by standard dielectric spectroscopy methods. We will mainly focus on isothermal processes. Different works have been published over the past years with the main purpose of establishing correlations between structure and dynamics during crystallization. To the author´s knowledge, dielectric spectroscopy has been employed for monitoring the crystallization of materials such as n-butanol [20], glycerol [49–51], salol [52], sorbitol [53], and pharmaceuticals compounds such as Biclotymol [54]. In these examples, one finds mono- and poly-alcohols, that is, systems showing a prominent Debye peak at low frequencies and others where this relaxation is absent due to the cancellation of macro-dipoles, although the view connecting solely the Debye relaxation in monohydroxy alcohols with the presence of macro-dipoles has been recently challenged [55].

Hecksher and co-workers studied systematically the crystallization of n-butanol at different temperatures with two different dielectric cells. In this work, the authors invoked Maxwell–Wagner effects to explain the peak shift towards higher frequencies and the strong reduction in intensity of the dielectric loss observed in the course of crystallization [20]. The depletion of the dielectric strength is especially pronounced for the strong Debye relaxation during the early stages of the phase transition. Hecksher and co-workers proposed that under the framework of the Maxwell-Wagner model, the crystallization of n-butanol can be interpreted by a transition from primarily growth of crystal spheres to growth of a crystal layer.

This picture was supported by describing the crystallization kinetics data in terms of the JMAK model, suggesting a transition from higher dimensional growth to a lower one [20] (Fig. 15).
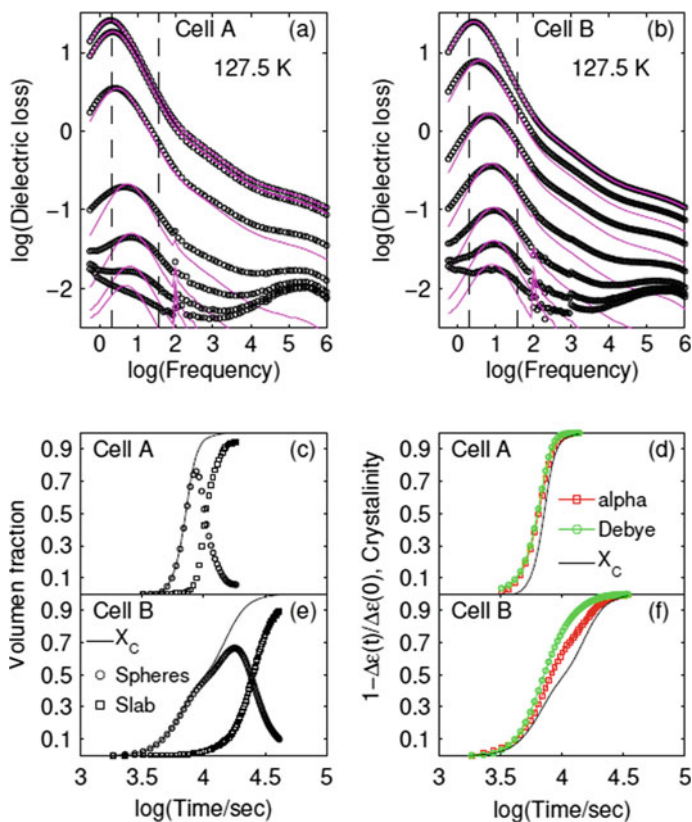
Fig. 15 **a**, **b** show a selection of curves together with fits (magenta lines) to the Maxwell-Wagner model for different dielectric cells during crystallization of n-butanol. The dashed vertical lines mark the frequency interval used for the fit. **c**, **e** show the volume fraction taken up by the spherical crystallites (circles) and the crystal slab (squares) as a function of time for dielectric cell A (**c**) and cell B (**e**). The solid line is the total crystal volume fraction. **d**, **f** Total crystal volume fraction from the MW fit (black line) as well as the normalised relaxation strength of the Debye process (in green) and alpha process (in red) as a function of time for dielectric cell A (**d**) and cell B (**f**). Reprinted from Ref. [20], with the permission of AIP Publishing

3.1 Isothermal Crystallization of Glycerol

Glycerol is a polyalcohol with three hydroxyl groups along the aliphatic chain. Glycerol (propane-1,2,3-triol), with chemical structure shown in Fig. 16, is a paradigmatic glass former and is considered the "fruit fly" of the glass-forming system community. A vast collection of articles on the dynamic properties of glycerol in connection to the glass transition problem can be found in the literature. The dynamics of glass-forming glycerol has been investigated by a multitude of techniques accessing to a broad range of time scales [56–59]. An extremely low tendency to crystallization in the supercooled window explains why glycerol has been historically chosen as case

Fig. 16 Thermal protocol for inducing the transformation of liquid glycerol into the crystalline phase. Nucleation of crystalline seeds is promoted by annealing at 190 K during 19 h. Crystal growth takes place at 230 K after fast heating from 190 K. Adapted with permission from Ref.[49]. Copyright AIP Publishing
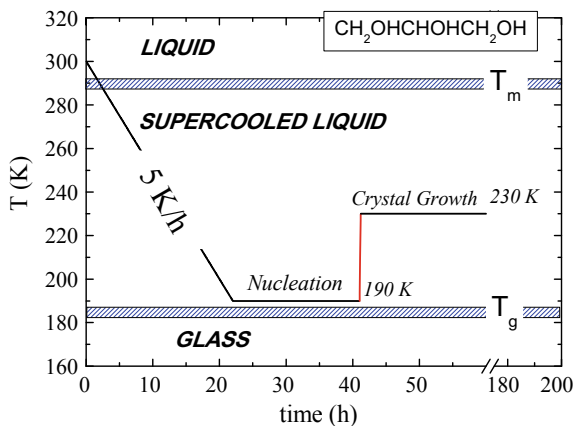
study for the understanding of liquid dynamics. For this reason, little attention has been paid to its crystalline phase. However, a precise control of the thermal history and purity of the sample facilitates the transformation of supercooled glycerol into a solid phase whose structure still remains unclear [50, 60, 61].

In this section, we will describe a systematic study on the nucleation and crystal growth of supercooled glycerol by real-time dielectric spectroscopy measurements. The dielectric cell consisted of two parallel metal plates separated by a Kapton® spacer of 0.25 mm thickness. The dielectric cell was filled with dry glycerol under nitrogen flow inside a glove bag. A detailed description of the dielectric spectroscopy setup and sample environment control can be found elsewhere [62, 63]. The thermal protocol followed to induce the ordering transition of supercooled liquid glycerol is presented in Fig. 16.

The formation of crystalline nuclei takes place by isothermal annealing at 190 K. This annealing was monitored by DS and there was no sign of crystal growth since the dielectric loss intensity remained constant. A slight decrease of the real part of the complex permittivity was detected but whether this reduction is a consequence of changes at the molecular level associated with crystal nucleation or simply slow geometrical adjustments of the capacitor due to mismatch of sample and spacer thermal-expansion coefficients is hard to elucidate [49]. Figure 17 demonstrates the efficiency of isothermal annealing at 190 K in the formation of crystalline nuclei. Here, the crystal growth at 230 K becomes faster for previous longer waiting times at 190 K, proving that a higher density of pre-existing nuclei results in a faster crystallization afterwards.

Selected snapshots of the time evolution of the dielectric loss in supercooled glycerol during crystallization at 230 K are displayed in Fig. 18. As mentioned earlier, sample was annealed at 190 K during 19 h to induce the formation of crystalline seeds. The reduction of the fluctuating dipoles density as glycerol crystallizes, is clearly reflected in the imaginary part of the complex permittivity. The low-frequency dispersion detected in the dielectric loss is assigned to pure ohmic conduction. This

Time evolution of the maximum intensity of the loss peak during crystal growth of glycerol at 230 K for samples without previous annealing (blue circles) or after annealing at 190 K for 5 h (red triangles) or 19 h (black squares). Data are normalized to the initial value. Reprinted from Ref. [49] with the permission of AIP Publishing
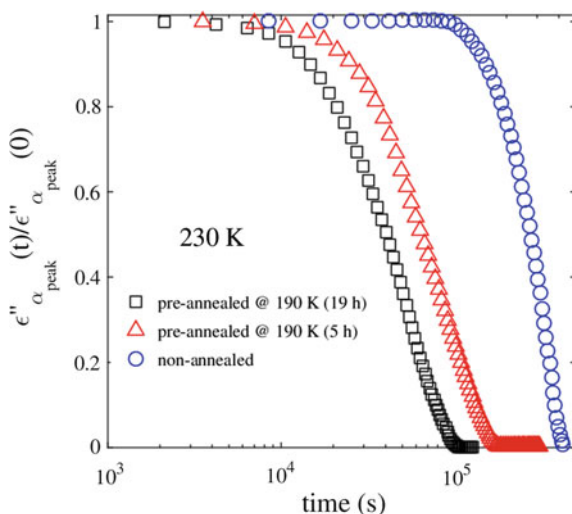
Fig. 18 Crystal growth in supercooled glycerol at 230 K monitored by dielectric spectroscopy. Sample was previously annealed during 19 h at 190 K
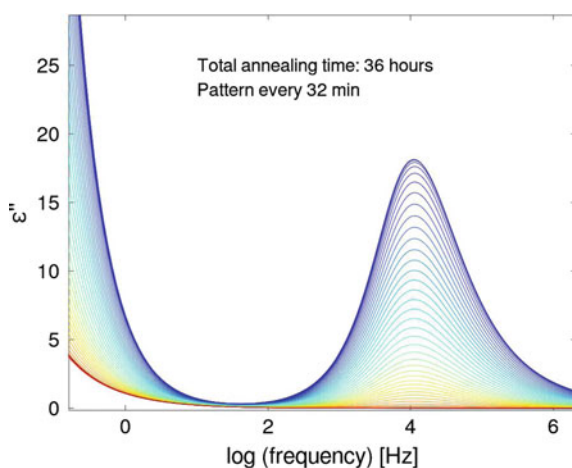
process decreases approximately at the same rate as the relaxation peak. A decrease in dc-conductivity upon crystallization is in line with arguments that inversely correlate the conduction of free charges with viscosity according to the Debye-Stokes-Einstein relation. Since crystalline glycerol presents a larger shear viscosity in comparison with the supercooled liquid [60], a larger viscosity for the composite material during crystallization is expected. This would explain why the dc-conductivity decreases, in spite of the characteristic relaxation time of the liquid remains unchanged. Besides, there is a significant modification of the charge-transport mechanism as revealed by the onset of a sub-linear power law as crystallization proceeds. Apart from the total extinction of the structural relaxation when crystallization ended, it is important to

remark that the location of the alpha peak remained unchanged during the whole process, suggesting that the intrinsic nature of the structural relaxation of glycerol remains unaltered in the course of crystallization.

Over the past years, the solidification of glycerol near T_g has been the subject of discussion and some authors have speculated on the existence of a glacial phase [60], similar to that shown by other molecular liquids such as triphenyl phosphate and n-butanol [64–66]. Elucidating the microscopic structure of the glacial phase in those systems has been the subject of intense research activity during the past decades [64, 65, 67]. Either a second amorphous state or a frustrated crystal with a high degree of defects and disorder could explain the existence of the so-called glacial phases. Two years later, by employing time-resolved neutron scattering, Yuan and co-authors [61] aimed to unravel the structural nature of this solid-like in glycerol, revealing, in agreement with one of the interpretations given by Möbius et al., the formation of nano-crystals at temperatures near T_g.

Several dielectric experiments were performed during isothermal annealing of supercooled glycerol at 230 K. Fresh samples were used each time. Only one single case was reported that did not show the typical behaviour of crystallization processes. The ordering process did not proceed to the end, and a small fraction of liquid phase (~1%) got trapped between the crystalline domains. To illustrate this aborted crystallization, in Fig. 19 (top) we present the evolution of the α relaxation as a function of crystallization time. Contrary to the data set shown in Fig. 18, a residual and stable peak was detected once the transition terminated. Such coexistence between crystallites and disordered domains giving rise to a relaxation process is a well-known and

Fig. 19 (Top) Dielectric loss in logarithmic scale as a function of frequency at different crystallization times during isothermal annealing of glycerol at 230 K. (Bottom) Time dependence of the crystalline volume fraction at 230 K for the complete (red squares) and aborted (black circles) crystallization processes. The inset zooms in the late stages to highlight the frustrated crystallization shown in the top panel. Reprinted from Ref. [49] with the permission of AIP Publishing
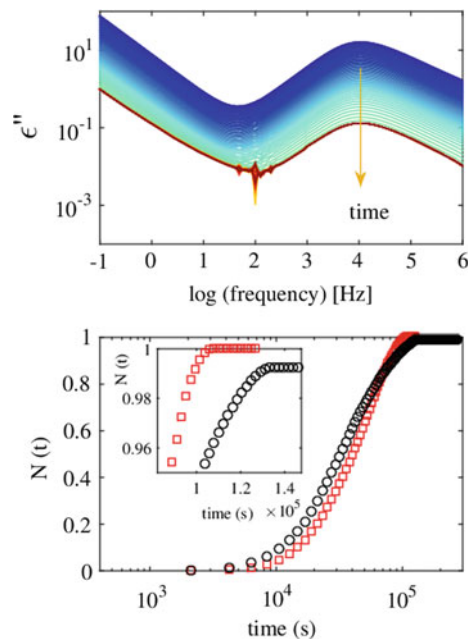
general phenomenon in the field of semi-crystalline polymers [68]. Here, the stability of this residual relaxation was confirmed over more than 24 h without any indication of losing intensity, broadening, or shifting in frequency. It is worth mentioning that the dynamics of this remaining liquid phase was studied as a function of temperature and showed features very close to the pure liquid material. The fraction of transformed phase at different times was calculated from the maximum intensity of the loss peak by the following expression:

$$N(t) = \frac{\varepsilon''_{\alpha\text{peak}}(0) - \varepsilon''_{\alpha\text{peak}}(t)}{\varepsilon''_{\alpha\text{peak}}(0) - \varepsilon''_{\alpha\text{peak}}(\infty)}, \tag{6}$$

where $\varepsilon''_{\alpha\text{peak}}(0)$ is the value of the loss peak for the pure liquid, $\varepsilon''_{\alpha\text{peak}}(t)$ takes the corresponding values at different times, and $\varepsilon''_{\alpha\text{peak}}(\infty)$ corresponds to the value of the dielectric loss at the same frequency for the pure crystal [49]. Our dielectric data reveal that liquid glycerol, through a nucleation step at 190 K and subsequent crystal growth at 230 K, transforms into a new phase. In most cases, total disappearance of the relaxation suggests that glycerol transforms into the standard orthorhombic crystalline phase [69]. The fact that in one of the samples studied here (Fig. 19), the end of crystallization was suddenly aborted during the late stages, could explain prior results that speculated the formation of a glacial phase in which metastable nanocrystals were embedded in a liquid matrix [60, 61, 70]. The data shown here just show an unfinished ordering process that resulted in a small fraction of sample remaining in the liquid state surrounded by a crystalline network. As indicated previously by other authors, the strong dependence of the crystallization ability of supercooled glycerol on the thermal history [61], could rationalize the different scenarios presented in Fig. 19 [49].

We have mentioned earlier that the relaxation dynamics in glycerol is almost unaffected by crystallization. This lack of dynamical signature upon crystallization indicates that the changes in the HB network as well as the conformational changes of glycerol molecules that had taken place during the ordering process are very local [49].

By following a similar thermal protocol, the ordering transition in supercooled glycerol was explored in a broader temperature range. The evolution of the complex dielectric permittivity with annealing time at 220 K is displayed in Fig. 20 [51]. One observes a much slower kinetics in comparison to the annealing at 230 K and a complete extinction of the relaxation at the end of the phase transition. It is important to remark that the location of the alpha peak does not shift during the whole crystallization process. The formation of the standard orthorrombic crystalline phase was corroborated by heating the fully crystallized sample. The thermal evolution of the permittivity was monitored upon heating. An abrupt jump in the permittivity was detected around 291 K (Fig. 21). This temperature corresponds to the melting point of the orthorhombic structure of glycerol.

The kinetics of crystal growth was analyzed in terms of the JMAK model. Figure 22 presents the crystallization kinetics at selected temperatures and the first

Fig. 20 Complex dielectric permittivity of supercooled glycerol upon crystal growth at 220 K. Imaginary (top) and real (bottom) parts of the complex permittivity are represented as a function of frequency at different stages of crystallization as indicated in the bottom panel. Reprinted with permission from Ref. [51]. Copyright (2017) American Chemical Society
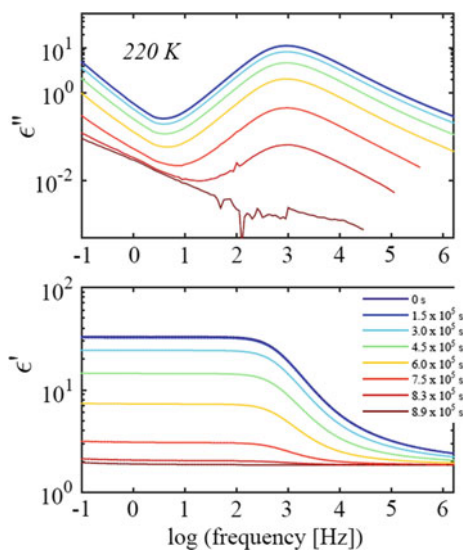
Fig. 21 Real part of the dielectric permittivity at 10 kHz as a function of temperature for samples of glycerol crystallized at 230 and 240 K. Dashed lines are guides to the eye
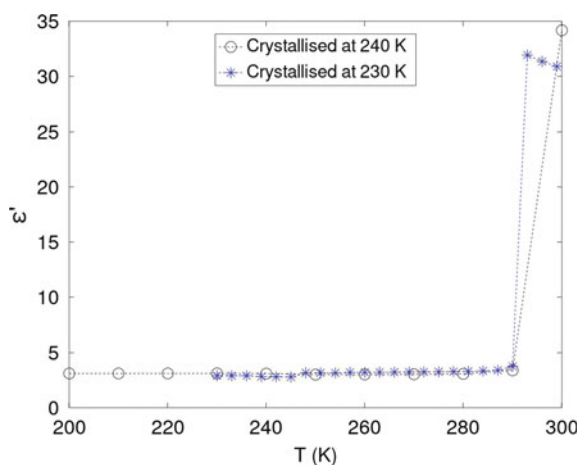
derivative of $N(t)$ with respect to $\ln(t - t_0)$. In all cases, the numerical differentiation gave a well-resolved maximum at the characteristic crystal growth time. The values of n in Eq. 5, were within a range of 1.3 and 2.2, and assuming that crystal growth started from a pre-existing collection of nuclei created at 190 K, this indicates that crystals probably grew in two dimensions [51].

With the purpose of gaining more insight on glycerol's morphology during crystallization, the Maxwell–Wagner model for dielectric heterogeneous systems can be applied [71]. According to the Maxwell–Wagner model, the shape and distribution of the crystals across the sample determine the resulting composite dielectric permittivity. The calculation of the fraction of crystalline phase by using Eq. 6 is based
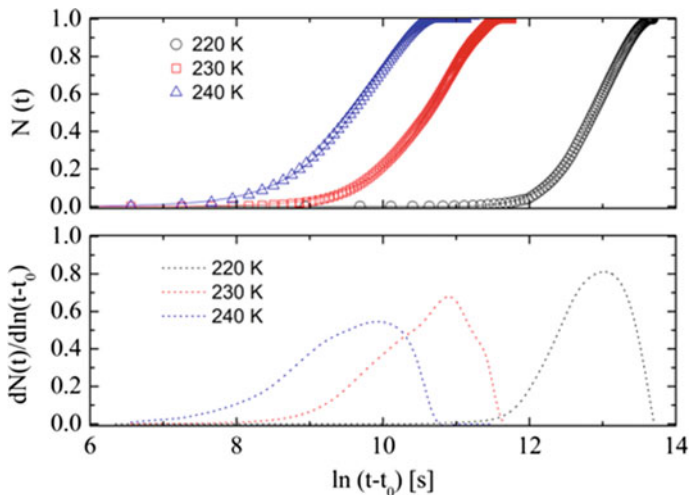
Fig. 22 Evolution of the normalized dielectric loss peak intensity ($N(t)$) (top) and its first derivative (bottom) as a function of $\ln(t - t_0)$ for crystallization processes at 220, 230, and 240 K

on the assumption that the dielectric permittivity of the liquid/crystal system is an additive quantity from the two domains. For crystals growing longitudinally from one electrode to the other in discrete spots separated by gaps remaining in the liquid phase, the permittivity of the heterogeneous crystal/liquid material is correctly calculated by means of Eq. 6 [51]. Different morphologies were considered to predict the experimental data, but a successful result was only achieved for a picture where crystallites are dispersed in a continuous liquid phase in which percolation pathways of disordered domains persist during crystallization [51]. Using a mean-field approach, the permittivity for this model can expressed as follows:

$$\varepsilon_{\text{total}}^*(t) = \varepsilon_l^* \frac{2\varepsilon_l^* + \varepsilon_c^* - 2N\left(\varepsilon_l^* - \varepsilon_c^*\right)}{2\varepsilon_l^* + \varepsilon_c^* + N\left(\varepsilon_l^* - \varepsilon_c^*\right)}, \tag{7}$$

where N corresponds to the fraction of crystalline phase, ε_l^* is the permittivity for the pure liquid and ε_c^* is the permittivity of the fully crystallized sample [20, 51]. Examples of fitting the experimental data to Eq. 7, together with the dependence of the crystalline volume fraction as a function of the dielectric strength by using Eqs. 6 and 7, are presented in Fig. 23. The first approach (Eq. 6) does not imply Maxwell-Wagner effects. Nevertheless, the inset in Fig. 23 shows that both models give similar results that only differ by up to a 10% at the intermediate stages of the phase transition. In order to unravel this discrepancy, it would be of great help to use diffraction methods coupled simultaneously with relaxation techniques.

In Fig. 24, the dielectric τ_α and the shear viscosity data for supercooled glycerol, extracted from the article by Schröter and Donth [72], are plotted against the crystal
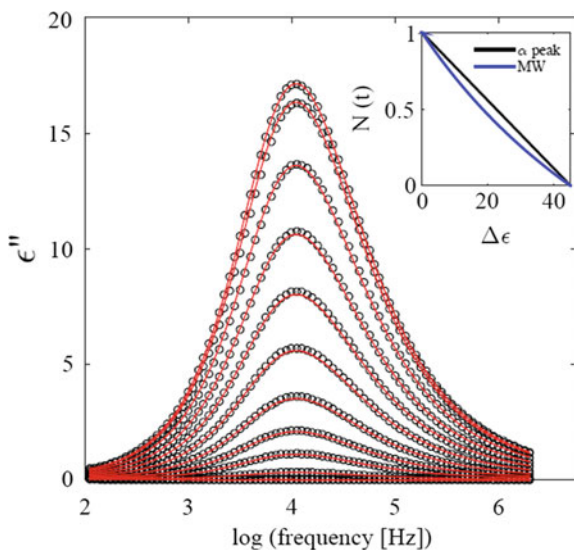
Fig. 23 Fit of Eq. 7 (red solid lines) to the experimental data (○) during the transformation of liquid glycerol into the crystalline phase at 230 K. Crystallization time advances from top to bottom. Snapshots every 3 h approximately. The inset displays the evolution of the crystalline volume fraction as a function of the dielectric strength according to Eq. 6 (linear combination of amorphous and crystalline domains) and Eq. 7 (Maxwell–Wagner effect). Reprinted with permission from Ref. [51]. Copyright (2017) American Chemical Society
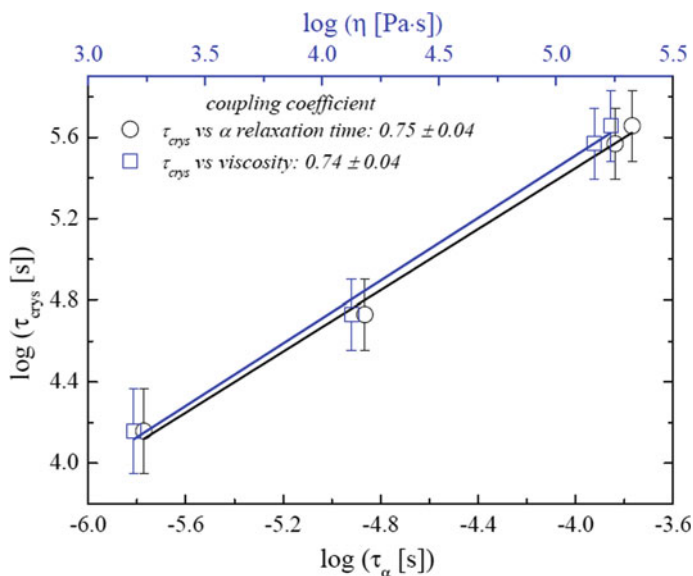
Fig. 24 Evolution of the characteristic crystallization time on a double x-axes representation against τ_α (alpha relaxation time) and shear viscosity (data from Ref. [72]). Solid lines represent linear fits. Reprinted with permission from Ref. [51]. Copyright (2017) American Chemical Society

growth time τ_{crys}. Almost the same correlation is observed. The coupling coefficient is quantified as the slope of the linear dependence of $\log(\tau_\alpha)$ or $\log(\eta)$ with $\log(\tau_{\text{crys}})$. The linear fits in Fig. 24 yielded coupling coefficients with values of 0.75 and 0.74 for τ_α and viscosity, respectively, revealing a strong connection between the structural relaxation time (viscosity) and the kinetics of crystal growth. It is demonstrated that supercooled glycerol can transform into the crystalline state via nucleation and crystal growth without significant modifications of the structural dynamics in the remaining liquid phase during the whole process. Moreover, this work shows evidence of the relation between different dynamic properties of the bulk liquid (relaxation time, viscosity and diffusion) and the kinetics of crystal growth [51]. The results shown in this section indicate that molecular mobility, although not solely, is the principal factor governing the crystal growth in supercooled glycerol near T_g.

4 Isothermal Crystallization of Glycerol

References

1. Debenedetti PG (2006) Nature 441(7090):168–169
2. Descamps M, Dudognon E (2014) J Pharm Sci 103(9):2615–2628
3. Jones RAL (2002) Soft condensed matter. OUP, Oxford
4. Cabrillo C, Bermejo FJ, Jiménez-Ruiz M, Fernández-Díaz MT, González MA, Martín y Marero D (2001) Phys Rev B 64(6):064206
5. Adrjanowicz K, Koperwas K, Szklarz G, Tarnacka M, Paluch M (2016) Cryst Growth Des 16(12):7000–7010
6. Ediger MD, Harrowell P, Yu L (2008) J Chem Phys 128(3):034709
7. Koperwas K, Adrjanowicz K, Wojnarowska Z, Jedrzejowska A, Knapik J, Paluch M (2016) Sci Rep 6:36934
8. Sanz A, Nogales A, Ezquerra TA (2010) Macromolecules 43(1):29–32
9. Adrjanowicz K, Grzybowski A, Grzybowska K, Pionteck J, Paluch M (2013) Cryst Growth Des 13(11):4648–4654
10. Frenkel J (1932) Phisik Zeit Sowjetunion 1:498–510
11. Baus MJ (1987) Statistical mechanical theories of freezing: an overview
12. Turnbull D, Fisher JC (1949) J Chem Phys 17(1):71–73
13. Zanotto ED (1992) Braz J Phys 22(2):77–85
14. Guàrdia E, Martí J, Padró JA, Saiz L, Komolkin AV (2002) J Mol Liq 96–97:3–17
15. Sillrén P, Swenson J, Mattsson J, Bowron D, Matic A (2013) J Chem Phys 138(21):214501
16. Arunan E, Desiraju Gautam R, Klein Roger A, Sadlej J, Scheiner S, Alkorta I, Clary David C, Crabtree Robert H, Dannenberg Joseph J, Hobza P, Kjaergaard Henrik G, Legon Anthony C, Mennucci B, Nesbitt David J (2011) Pure Appl Chem 83:1637

17. Johari GP (2013) J Chem Phys 139(2):026101
18. Böhmer R, Gainaru C, Richert R (2014) Phys Rep 545(4):125–195
19. Dobbertin J, Hannemann J, Schick C, Pötter M, Dehne H (1998) J Chem Phys 108(21):9062–9068
20. Jensen MH, Alba-Simionesco C, Niss K, Hecksher T (2015) J Chem Phys 143(13):134501
21. Gainaru C, Meier R, Schildmann S, Lederle C, Hiller W, Rössler EA, Böhmer R (2010) Phys Rev Lett 105(25):258303
22. Petong P, Pottel R, Kaatze U (1999) J Phys Chem A 103(31):6114–6121
23. Sato T, Buchner R (2003) J Chem Phys 118(10):4606–4613
24. Wang L-M, Shahriari S, Richert R (2005) J Phys Chem B 109(49):23255–23262
25. Kaatze U, Behrends R, Pottel R (2002) J Non-Cryst Solids 305(1):19–28
26. Sagal MW (1962) J Chem Phys 36(9):2437–2442
27. Sanz A, Jiménez-Ruiz M, Nogales A, Martín y Marero D, Ezquerra TA (2004) Phys Rev Lett 93(1):015503
28. Stewart GW, Morrow RM (1927) Phys Rev 30(3):232–244
29. Tomšič M, Jamnik A, Fritz-Popovski G, Glatter O, Vlček L (2007) J Phys Chem B 111(7):1738–1751
30. Jiménez-Ruiz M, Sanz A, Nogales A, Ezquerra TA (2005) Rev Sci Instrum 76(4):043901
31. Sanz A, Nogales A, Puente-Orench I, Jiménez-Ruiz M, Ezquerra TA (2014) J Chem Phys 140(5):054510
32. Schönhals A, Kremer F (2002) Broad band dielectric spectroscopy. Springer, Berlin
33. Sanz A, Nogales A, Ezquerra TA, Soccio M, Munari A, Lotti N (2010) Macromolecules 43(2):671–679
34. Kramarenko VY, Ezquerra TA, Šics I, Baltá-Calleja FJ, Privalko VP (2000) J Chem Phys 113(1):447–452
35. Haida O, Suga H, Seki S (1977) J Chem Thermodyn 9(12):1133–1148
36. Amoureux JP, Noyel G, Foulon M, Bée M, Jorat L (1984) Mol Phys 52(1):161–171
37. Brand R, Lunkenheimer P, Loidl A (1997) Phys Rev B 56(10):R5713–R5716
38. Talón C, Ramos MA, Vieira S, Cuello GJ, Bermejo FJ, Criado A, Senent ML, Bennington SM, Fischer HE, Schober H (1998) Low-temperature specific heat and glassy dynamics of a polymorphic molecular solid. Phys Rev B 58(2):745–755
39. Bermejo FJ, Criado A, Fayos R, Fernández-Perea R, Fischer HE, Suard E, Guelylah A, Zúñiga J (1997) Phys Rev B 56(18):11536–11545
40. Benkhof S, Kudlik A, Blochowicz T, Rössler E (1998) J Phys Condens Matter 10(37):8155–8171
41. Sanz A, Nogales A, Puente-Orench I, Jiménez-Ruiz M, Ezquerra TA (2011) Phys Rev Lett 107(2):025502
42. Shiryayev AN (1992) Selected works of A. N. Kolmogorov: Volume II Probability theory and mathematical statistics (Shiryayev AN, ed). Springer, The Netherlands, Dordrecht, pp 188–192
43. Johnson WA (1939) Trans AIME 135:416–459
44. Avrami M (1939) J Chem Phys 7(12):1103–1112
45. Avrami M (1940) J Chem Phys 8(2):212–224
46. González MA, Bermejo FJ, Enciso E, Cabrillo C (2004) Phil Mag 84(13–16):1599–1607
47. Jiménez-Ruiz M, González MA, Bermejo FJ, Miller MA, Birge NO, Cendoya I, Alegría A (1999) Phys Rev B 59(14):9155–9166
48. Massalska-Arodz M, Williams G, Thomas DK, Jones WJ, Dabrowski R (1999) J Phys Chem B 103(20):4197–4205
49. Sanz A, Niss K (2017a) J Chem Phys 146(4):044502
50. Ryabov YE, Hayashi Y, Gutina A, Feldman Y (2003) Phys Rev B 67(13):132202
51. Sanz A, Niss K (2017b) Cryst Growth Des 17(9):4628–4636
52. Kołodziejczyk K, Tarnacka M, Kamińska E, Dulski M, Kamiński K, Paluch M (2016) Cryst Growth Des 16(3):1218–1227
53. Minoguchi A, Nozaki R (2002) J Non-Cryst Solids 307–310:246–251
54. Tripathi P, Romanini M, Tamarit JL, Macovez R (2015) Int J Pharm 495(1):420–427

55. Gainaru C, Figuli R, Hecksher T, Jakobsen B, Dyre JC, Wilhelm M, Böhmer R (2014) Phys Rev Lett 112(9):098301
56. Schneider U, Brand R, Lunkenheimer P, Loidl A (2000) Phys Rev Lett 84(24):5560–5563
57. Lunkenheimer P, Loidl A (2002) Chem Phys 284(1):205–219
58. Wuttke J, Hernandez J, Li G, Coddens G, Cummins HZ, Fujara F, Petry W, Sillescu H (1994) Phys Rev Lett 72(19):3052–3055
59. Vispa A, Busch S, Tamarit JL, Unruh T, Fernandez-Alonso F, Pardo LC (2016) Phys Chem Chem Phys 18(5):3975–3981
60. Möbius ME, Xia T, van Saarloos W, Orrit M, van Hecke M (2010) J Phys Chem B 114(22):7439–7444
61. Yuan H-F, Xia T, Plazanet M, Demé B, Orrit M (2012) J Chem Phys 136(4):041102
62. Igarashi B, Christensen T, Larsen EH, Olsen NB, Pedersen IH, Rasmussen T, Dyre JC (2008a) Rev Sci Instrum 79(4):045106
63. Igarashi B, Christensen T, Larsen EH, Olsen NB, Pedersen IH, Rasmussen T, Dyre JC (2008b) Rev Sci Instrum 79(4):045105
64. Kobayashi M, Shimizu R, Tanaka H (2015) J Phys Chem B 119(35):11768–11782
65. Kurita R, Tanaka H (2005) J Phys Condens Matter 17(27):L293–L302
66. Krivchikov AI, Hassaine M, Sharapova IV, Korolyuk OA, Jiménez-Riobóo RJ, Ramos MA (2011) J Non-Cryst Solids 357(2):524–529
67. Kurita R, Tanaka H (2004) Science 306(5697):845
68. Nogales A, Denchev Z, Ezquerra TA (2000) Macromolecules 33(25):9367–9375
69. Bermejo FJ, Criado A, de Andres A, Enciso E, Schober H (1996) Phys Rev B 53(9):5259–5267
70. Zondervan R, Xia T, van der Meer H, Storm C, Kulzer F, van Saarloos W, Orrit M (2008) Proc Natl Acad Sci 105(13):4993–4998
71. Richert R (2010) Dielectric spectroscopy and dynamics in confinement. Eur Phys J Spec Top 189(1):37–46
72. Schröter K, Donth E (2000) Viscosity and shear response at the dynamic glass transition of glycerol

Isothermal and Non-isothermal Crystallization in Liquid Crystals as Seen by Broadband Dielectric Spectroscopy and Differential Scanning Calorimetry

Małgorzata Jasiurkowska-Delaporte

Abstract Being composed of shape-anisotropic molecules, liquid crystals (LCs) differ from simple liquids in that they demonstrate a tendency to orientate in specific directions and form various mesophases. Upon cooling, these partially ordered liquid crystalline phases can either vitrify or crystallize. Upon heating from a glassy state, LCs, like other low molecular weight systems and polymers, have been found to undergo so-called cold crystallization. This chapter discusses the findings of broadband dielectric spectroscopy (BDS) and differential scanning calorimetry (DSC) studies of the isothermal and non-isothermal crystallization kinetics of the supercooled nematic (N) and chiral nematic (N*) states of, respectively, 2,7-bis(4-pentylphenyl)-9,9-diethyl-9H-fluorene (5P-EtFLEt-P5) and S,S-2,7-bis(4-pentylphenyl)-9,9-dimethylbutyl-9H-fluorene (5P-Am*FLAm*P5). The isothermal melt and cold crystallization processes at selected temperatures T_c above the glass transition temperature T_g ($1.07T_g \leq T_c \leq 1.17T_g$) are compared in 5P-EtFLEt-P5. It was found that 5P-EtFLEt-P5 and 5P-Am*FLAm*P5 display different types of non-isothermal cold crystallization. Finally, the paper discusses the crystallization behavior occurring in the well-ordered smectic B phase (SmB) of 4-n-butyloxybenzylidene-4′-n′-octylaniline (BBOA) under various thermal conditions. The DSC analysis revealed two different crystallization mechanisms for fast and slow cooling.

Keywords Liquid crystals · Molecular dynamics · Non-isothermal crystallization · Isothermal crystallization · Broadband dielectric spectroscopy · Differential scanning calorimetry

M. Jasiurkowska-Delaporte (✉)
Institute of Nuclear Physics Polish Academy of Sciences, 31342 Krakow, Poland
e-mail: Malgorzata.Jasiurkowska-Delaporte@ifj.edu.pl

119

Abbreviations

5P-EtFLEt-P5	2,7-Bis(4-pentylphenyl)-9,9-diethyl-9H-fluorene
5P-Am*FLAm*P5	S,S-2,7-bis(4-pentylphenyl)-9,9-dimethylbutyl-9H-fluorene
BBOA	4-N-butyloxybenzylidene-4′-n′-octylaniline
BDS	Broadband dielectric spectroscopy
CONDIS	Conformationally disordered crystals
DSC	Differential scanning calorimetry
GN	Glass of nematic phase
GN*	Glass of chiral nematic phase
HN	Havriliak–Negami
Is	Isotropic state
LCs	Liquid crystals
POM	Polarizing optical microscopy
N	Nematic
N*	Chiral nematic
ODIC	Orientationally disordered crystal
SmB	Smectic B
VFT	Vogel–Fulcher–Tammann

1 Introduction

Owing to their remarkable optical and physical properties, liquid crystals (LCs) have attracted great attention from both academia and industry. In addition to their widespread use in displays and electrically driven optical switches, LCs have also found novel applications in a range of areas, including medicine [1–3], pharmacy [4] and sensing [5]. The simplest, and the most commonly used, form of LC is the nematic phase (N), in which molecules tend to align in a single direction. However, a chiral or *choresteric* form also exists (N*), comprising both an orientational molecular order and a spontaneous macroscopic helical superstructure with a twist axis orthogonal to the local director. As the temperature decreases, many thermotropic LCs form smectic phases which display layered structures that can be classified according to the degree of molecular order (A, B, E, F, G, etc.).

On cooling, LCs have been shown to form vitreous states characterized by partial ordering; such states differ from those of amorphous materials, such as "conventional" glasses. Calorimetric studies by Sorai and Seki [6] first identified vitrification of the nematic phase; following this, a glass-forming ability was reported for various smectic phases, including smectic G (SmG) [7], smectic B (SmB) [8, 9] and smectic E (SmE) [10–12]. BDS studies have indicated that cold crystallization can take place after softening the glass upon heating [13]; this was identified for the first time for

liquid crystals for chiral isooctyloxycyanobiphenyl [14]. Further studies on crystallization phenomena in LCs suggest that they may be dependent on the thermal history of the sample and the structure of the initial phase [15–19].

Mesogenic compounds like LCs can solidify not only to fully ordered crystals. They can also form orientationally disordered crystal (ODIC) where molecules are positioned in long-range ordered arrays but have rotational freedom, and conformationally disordered crystals (CONDIS) displaying long-range positional and long-range orientational order. These partially ordered phases can form a vitreous state and, by doing so, preserve some degree of order. The dielectric relaxation pattern of a certain phase depends on the arrangement of molecules, their orientations and packing. Figure 1 summarizes the molecular motions possible in different types of order.

This chapter examines the relaxation dynamics and kinetics of isothermal and non-isothermal crystallization processes in (i) the nematic phase of 2,7-bis(4-pentylphenyl)-9,9-diethyl-9H-fluorene (5P-EtFLEt-P5) [20] and the chiral nematic phase of S,S-2,7-bis(4-pentylphenyl)-9,9-dimethylbutyl-9H-fluorene (5P-Am*FLAm*P5), and contrasts them with (ii) the highly ordered smectic B phase (SmB) of 4-n-butyloxybenzylidene-4′-n′-octylaniline (BBOA). Due to their electroluminescent properties, fluorene-containing LCs are promising materials for organic light-emitting diode (OLED) displays [21]; however, the further development of LC devices requires a thorough understanding of the crystallization processes taking place under various thermal conditions.
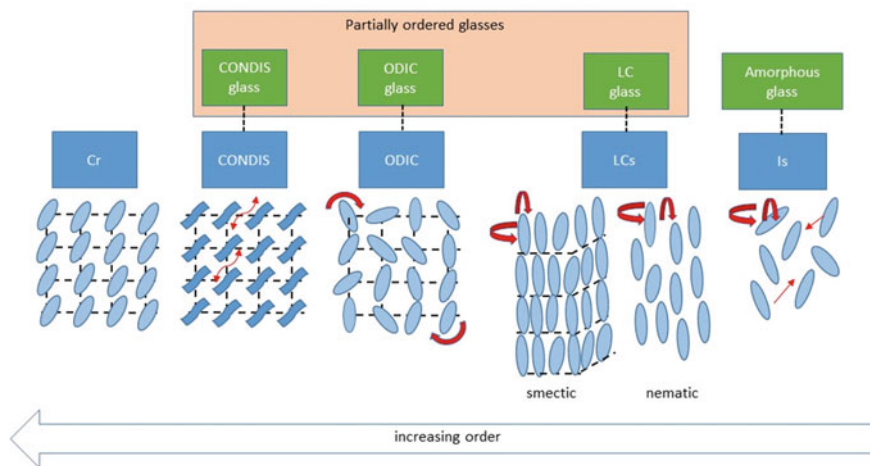
Fig. 1 Different states of the matter classified according to its degree of order. Possible molecular motions as denoted by arrows

2 Experimental Details

The examined liquid crystals (5P-EtFLEt-P5 [20], 5P-Am*FLAm*P5 [22], BBOA [23], purity > 99.5%) were kindly supplied by Prof. P. Kula, the Military University of Technology in Warsaw, and used as received.

Thermal analysis was carried out for several cooling/heating rates using a DSC 2500 Differential Scanning Calorimeter (TA Instruments, New Castle, Delaware, USA). A 6–7 mg sample of the material was placed in an aluminum pan, which was sealed before measurement. An empty aluminum pan was used as the reference.

The phase transitions of the investigated compounds were also verified: Samples with a thickness of about 50 µm were placed under a bipolar PI polarizing light microscope (PZO, Poland) to observe the temperature evolutions of the textures. The temperature of the sample was controlled with an uncertainty of 0.1 K by means of a Linkam THM 600 using a flow of liquid nitrogen. The increase of the degree of crystallinity $D(t)$ over the course of the change in temperature was determined by the graphical analysis of textures using GIMP (freeware graphics software). Based on the percentage share of the crystalline fraction in the whole texture layer, the value of $D(t)$ is estimated as the ratio of the texture area $S_{Cr}(t)$ corresponding to the new crystalline phase and the total surface area of the texture S:

$$D(t) = \frac{S_{Cr}(t)}{S} \tag{1}$$

Broadband dielectric measurements were performed using a high-precision dielectric analyzer (ALPHA analyzer; Novocontrol Technologies, Montabaur, Germany) in the frequency range of 0.1–10^7 Hz in combination with a Novocool temperature controller, providing temperature stability greater than 0.1 K. Prior to the BDS measurements, LC powder was heated up to the isotropic phase; the heating took place between two circular electrodes 10 mm in diameter which were separated by Teflon spacers to avoid a short circuit. To describe the detected relaxation processes, the empirical Havriliak–Negami function was fitted to the absorption spectra:

$$\varepsilon^*(\omega) = \varepsilon'(\omega) - i\varepsilon''(\omega) = \varepsilon + \sum_{k=1}^{3} \frac{\Delta\varepsilon_k}{\left(1 + \left(i\omega\tau_{HN_k}\right)^{a_{HN_k}}\right)^{b_{HN_k}}} + \frac{0}{\omega\varepsilon_0} \tag{2}$$

where ε' and ε'' are the real and imaginary parts of the complex dielectric permittivity, $\Delta\varepsilon_i$ and τ_{HNi} are the dielectric strength and the macroscopic relaxation time of process i and σ_0 is dc-conductivity. The a_H and b_H are related to the limiting behavior of the complex dielectric function at low and high frequencies [24]:

$$\varepsilon'(0) - \varepsilon'(\omega) \sim \omega^m; \varepsilon'' \sim \omega^m \text{ for } \omega \ll 1/\tau_{HN} \quad \text{with } m = a_{HN} \tag{3}$$

$$\varepsilon'(\omega) - \varepsilon'_\infty \sim \omega^{-n}; \varepsilon'' \sim \omega^{-n} \text{ for } \omega \gg 1/\tau_{HN} \quad \text{with } n = a_{HN}b_{HN} \tag{4}$$

where $\varepsilon'(0)$ and ε'_∞ describe the value of ε' at the low and high frequency limits, respectively. The n and $(1 - m)$ parameters [25, 26] indicate the cooperativity of the reorienting molecules in the local and long-range scales. In some crystalline phases, the relaxation spectra were obscured by Ohmic conductivity; to eliminate this undesirable contribution, the relaxation spectra were analyzed according to Wübbenhorst and Turnhout [27, 28] which is based on the approximation

$$\varepsilon''_{\text{der}} = -\frac{\pi}{2}\frac{\partial \varepsilon'(\omega)}{\partial \ln \omega} \approx \varepsilon'' \tag{5}$$

The derivative of dielectric loss spectra $\varepsilon''_{\text{der}}(f)$ ($\omega = 2\pi f$, where f is the frequency of the external electric field) was fitted with the analytical derivative of Havriliak–Negami function $\partial \varepsilon'_{HN}/\partial \ln \omega$

$$\frac{\partial \varepsilon'_{HN}}{\partial \ln \omega} = -\frac{a_{HN} b_{HN} \Delta\varepsilon (\omega\tau)^{a_{HN}} \cos\left[\frac{a_{HN}\pi}{2} - (1+b)\theta_{HN}\right]}{[1 + 2(\omega\tau)^{a_{HN}} \cos\left(\frac{\pi a_{HN}}{2}\right) + (\omega\tau)^{2a_{HN}}]^{1+\frac{b}{2}}} \tag{6}$$
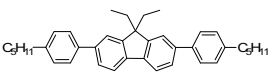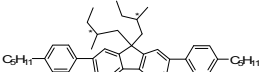
where

$$\theta_{HN} = \arctan\left[\sin(\pi a_{HN}/2)/\left((\omega\tau)^{-a_{HN}} + \cos(\pi a_{HN}/2)\right)\right] \tag{7}$$

3 Phase Diagrams of Investigated Mesogenic Fluorene Derivatives with Nematic Phases

The studied mesogenic fluorene derivatives (Table 1) are glass-forming systems of comparable glass transition temperatures (T_g); they possess very similar molecular structures, differing only by the chain attached to the fluorine moieties. In

Table 1 Chemical details of nematic liquid crystals under study

Sample	Molecular structure	Dipole moment [D][a]	Clearing point [K]	Glass transition temperature [K][b]
5P-EtFLEt-P5		0.7	376	255
5P-Am*FLAm*P5		0.32	298	253

[a]The resultant dipole moment calculated by semiempirical methods
[b]T_g temperature determined from DSC measurements

contrast to the non-chiral 5P-EtFLEt-P5 compound substituted by diethyl chains, the asymmetric 9,9-dimethylbutyl substitution in 5P-Am*FLAm*P5 molecules induces chirality in the nematic phase. The differential scanning calorimetric (DSC) thermograms and the phase sequences obtained by means of polarizing optical microscopy (POM) are shown in Fig. 2.

It can be seen that in the nematic phase (N), 5P-EtFLEt-P5 displays vitrification for even very slow cooling rates, such as 0.1 K/min. This inhibition of crystal formation is presumably associated with energetic flustration between locally favored nematic ordering and the thermodynamic stability of the crystalline state [29]. Upon heating, the nematic glass softened and cold crystallization to the Cr1 phase was observed, followed by transformation from Cr1 to Cr2 phase. A particularly complex phase diagram strongly dependent on cooling/heating rate was seen for 5P-Am*FLAm*P5: (i) At higher cooling rates ($\phi \geq 5$ K/min), vitrification of chiral nematic phase (N*) was observed with cold crystallization to the Cr2 phase occurring upon heating; in contrast, (ii) slow cooling ($\phi < 5$ K/min) results in the formation of the glass-forming Cr1 phase.

4 Molecular Dynamics in 5P-EtFLEt-P5 and 5P-Am*FLAm*P5

The dielectric properties of the investigated compounds are determined by the low molecular dipole moment (Table 1) associated with the fluorene unites. Figure 3 presents the dielectric loss spectra $\varepsilon''(f)$ of 5P-EtFLEt-P5 and 5P-Am*FLAm*P5, respectively, in the glass of N and N* phases, as well as in the metastable nematic phases. The structural α-relaxation process is generally ascribed to the reorientation of molecules around the short axis. For 5P-EtFLEt-P5, the temperature dependence of the shape parameter $n = a_H \, b_H$ indicates a substantial increase in local cooperativity on approaching T_g whereas the long-range correlation parameter, measured as $1 - m$ ($m = a_H$), is temperature insensitive. In the case of 5P-Am*FLAm*P5, both the short- and long-range correlations are temperature independent. Two secondary β and γ processes are ascribed, respectively, to the small-angle rotational diffusion of molecules around the short axis and to librations around the long axis [20]. Interestingly, the relaxation processes were also detected in the Cr1 and Cr2 crystalline forms of 5P-Am*FLAm*P5. Examples of dielectric loss spectra are given in Fig. 4.

As ionic conductivity represented such a strong contribution in the dielectric spectra of Cr1 in 5P-Am*FLAm*P5 (see Fig. 4a), the relaxation times of the high-temperature I-process were determined by fitting Eq. 6 to the derivative dielectric spectra (Fig. 4b). To expose the second relaxation process (II), observed in Cr1 at the lower temperatures, the results are presented in the temperature domain (Fig. 4a). The relaxation rates of the II-process were determined according to the maximum dielectric loss versus temperature $\varepsilon''(T)$ at a fixed frequency. The value of $\varepsilon''(T)$ maximum was designated by fitting a Gaussian function to the data as reported
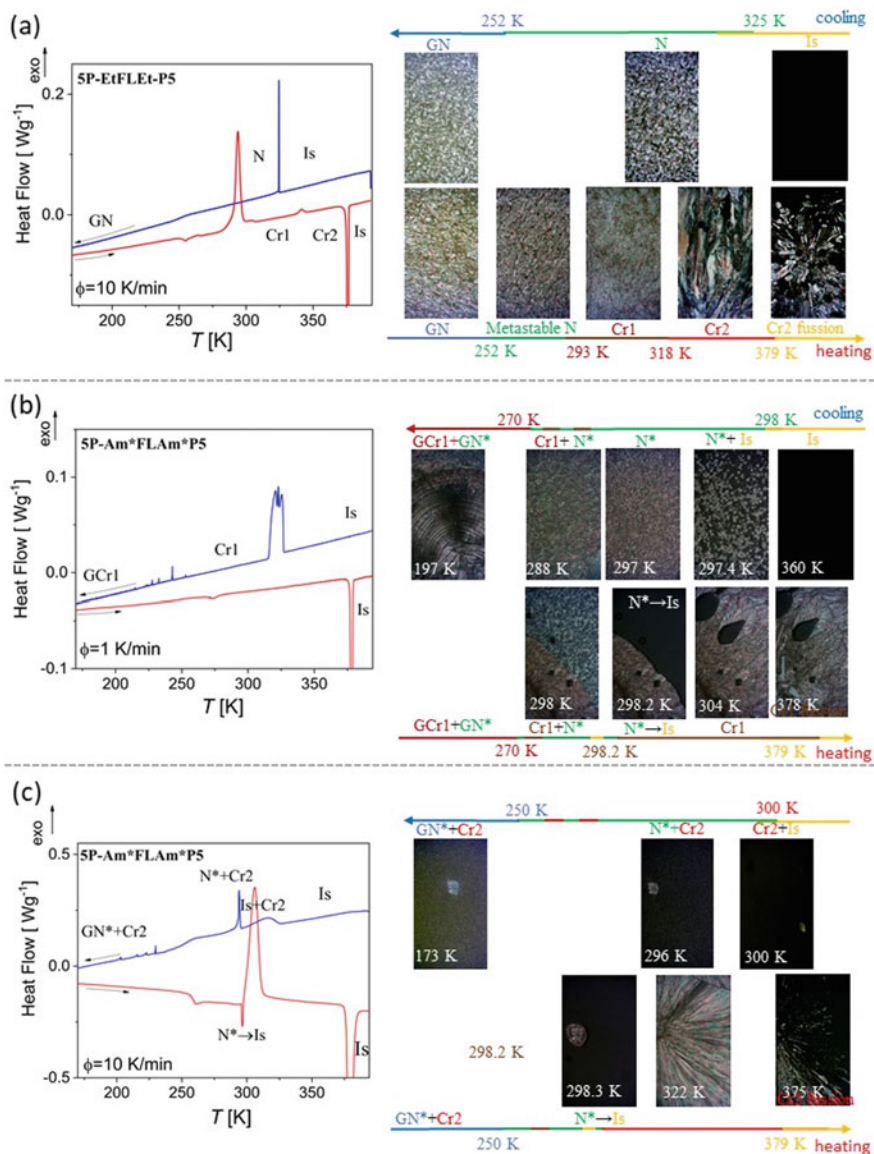
Fig. 2 DSC curves (left) and phase sequence obtained by POM observation (right) for (**a**) 5P-EtFLEt-P5 for a cooling/heating rate of ϕ = 10 K/min and (**b**) 5P-Am*FLAm*P5 for a cooling/heating rate ϕ = 1 K/min (**c**) and ϕ = 10 K/min. Adapted with permission from Refs. [20, 30]. ([20] Copyright © 2018 American Chemical Society and [30] kind permission of The European Physical Journal (EPJ))
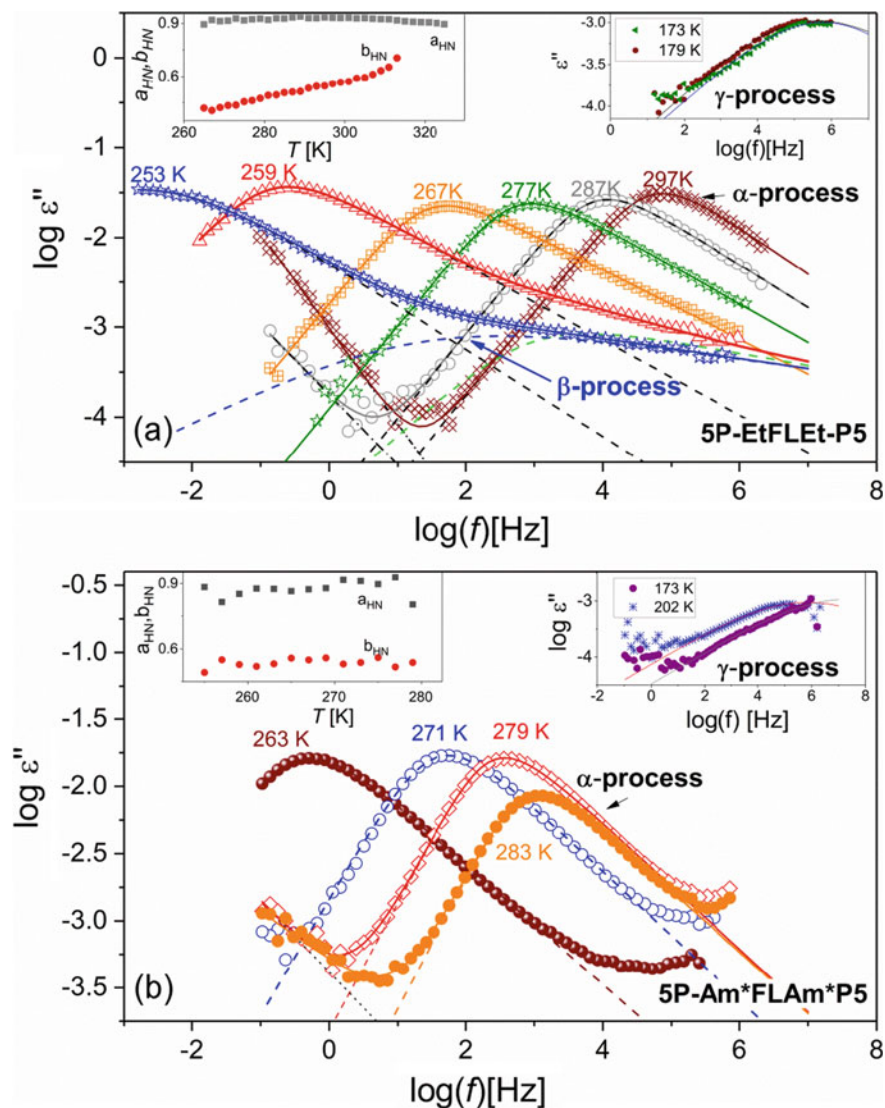
Fig. 3 Frequency-dependent dielectric loss spectra $\varepsilon''(f)$ of glass-forming nematic liquid crystals 5P-EtFLEt-P5 (**a**) and 5P-Am*FLAm*P5 (**b**) at selected temperatures. The left insets present temperature evolution of the shape parameters of the α-relaxation process. The right insets show secondary relaxation process for selected temperatures. Adapted with permission from [20, 30] ([20] Copyright © 2018 American Chemical Society and [30] kind permission of The European Physical Journal (EPJ))
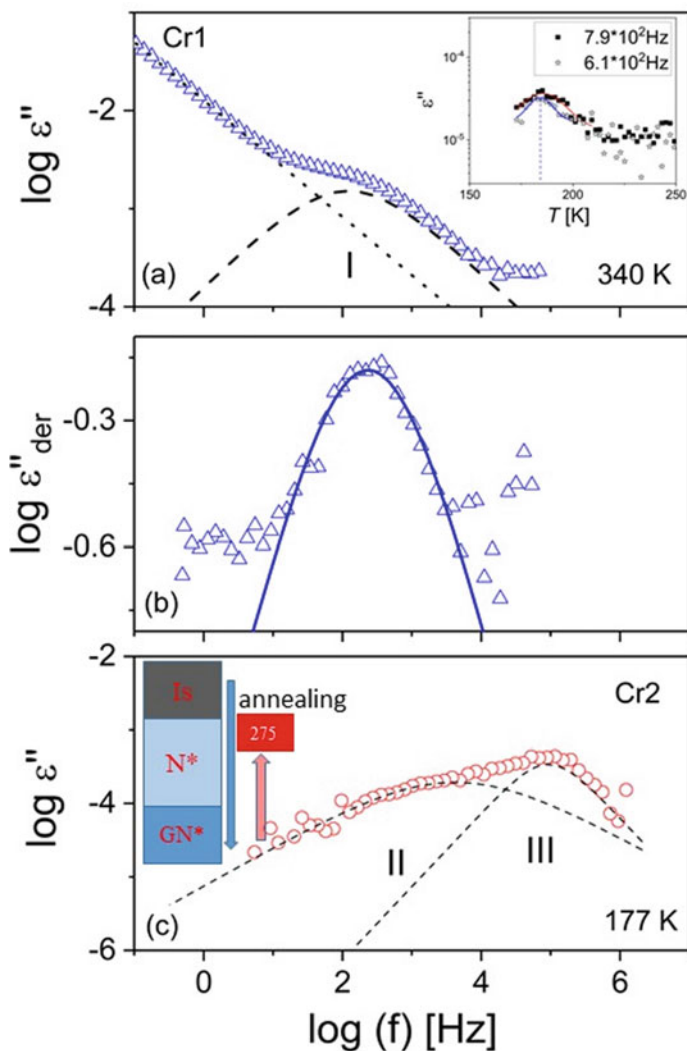
Fig. 4 **a** Dielectric loss spectrum $\varepsilon''(f)$ measured in the Cr1 at 340 K upon cooling for 5P-Am*FLAm*P5. The inset shows the imaginary part of dielectric function versus temperature. **b** The fit of derivative dielectric loss spectra $\varepsilon''_{der}(f)$. **c** $\varepsilon''(f)$ spectrum measured in Cr2 phase at 177 K. The scheme presents the thermal treatment carried out to obtain the Cr2 phase: The material was first cooled down with a rate of 10 K/min to the GN* state than the Cr2 crystal was obtained by annealing at 275 K. Adapted from [30] (kind permission of The European Physical Journal (EPJ))

previously [31, 32]. Two relaxation processes denoted as II and III (Fig. 4c) were found in the Cr2 phase.

The temperature dependencies of the relaxation rates of all processes revealed for 5P-EtFLEt-P5 and 5P-Am*FLAm*P5 in the low-frequency regime are given in Fig. 5. The temperature dependence of the α-relaxation rate ($1/\tau_\alpha$) is well described by the empirical Vogel–Fulcher–Tammann (VFT) equation

$$\tau_\alpha = \tau_\infty \exp\left(\frac{D_f T_0}{T - T_0}\right) \tag{8}$$

where τ_∞ is the so-called pre-exponential factor, D_f is a constant corresponding to so-called fragility index m_f, i.e., the measure of the response of glass-forming systems to temperature changes, and T_0 denotes the Vogel temperature. The VFT fit parameters are reported in Table 2. The m_f and D_f parameters are related to each other by $m_f = 16$
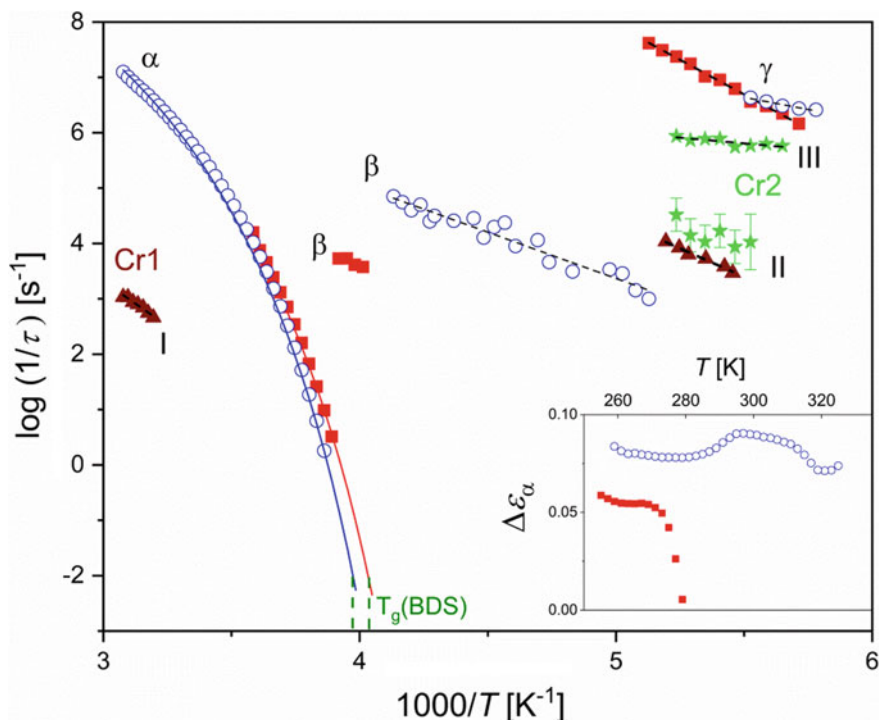
Fig. 5 Thermal activation plots of the structural α and secondary (β and γ) relaxation processes for 5P-EtFLEt-P5 (open symbols) and 5P-Am*FLAm*P5 (full symbols). The Roman numerals (I, II, III) denote relaxation processes in the crystalline phases Cr1 and Cr2 of 5P-Am*FLAm*P5. The inset presents the temperature dependence of dielectric strength $\Delta\varepsilon_\alpha$ of the α-processes. Data were taken from Refs. [20, 30] with permission ([20] Copyright © 2018 American Chemical Society and [30] kind permission of The European Physical Journal (EPJ))

Table 2 Parameters of the VFT fits for τ_α and the fragility index m_f

Sample	VFT parameters			
	τ_0 [s]	D_f	T_0 [K]	m_f
5P-EtFLEt-P5	$1.5 \cdot 10^{-12}$	5.6 ± 0.5	214 ± 7	121 ± 5
5P- Am*FLAm*P5	$3 \cdot 10^{-12}$	5.8 ± 1.4	210 ± 3	117 ± 6

$+ 590/D_f$ [33]. The high fragility of the investigated liquid crystalline glass formers suggests a strong tendency toward crystallization upon heating from the vitreous state; this could be associated with the large structural reorganization of material taking place with temperature changes in the vicinity of the glass transition [34, 35]. The secondary β and γ relaxations and the processes in the crystalline phases exhibit Arrhenius-like thermal activation. In 5P-Am*FLAm*-P5, the process (II) detected in the Cr1 phase crystal is split into two processes in the Cr2 phase, indicating an increase in the degree of anisotropy of the molecular motions [36]. It is expected that molecular movement will be strongly restricted in the Cr1 and Cr2 phases; this is most likely due to the efficient packing in both crystalline phases, as evidenced by the high melting entropy value ($\Delta S_{\mathbf{Cr1-Is, Cr2-Is}} \approx 69 \, \text{kJmol}^{-1}\text{K}^{-1}$). The existence of molecular motion suggests that these crystalline phases are not fully ordered. Based on the structure of the 5P-Am*FLAm*-P5 molecules and the direction of the effective molecular dipole moment, the motion observed in the Cr1 and Cr2 phases could be ascribed to a small twisting movement by conformationally disordered fluorene groups (as in CONDIS crystals). The dense molecular packing also favors collective motions. The activation entropy ($\Delta S^{\#}$) and activation enthalpy ($\Delta H^{\#}$) of the relaxation processes were calculated on the basis of the Starkweather analysis described elsewhere [37]. The results confirm the cooperativity of the molecular motions in the crystalline phases: Positive values of $\Delta S^{\#}$ and $\Delta S^{\#}$ were obtained for processes II ($\Delta S^{\#} = 0.17 \, \text{kJmol}^{-1}\text{K}^{-1}$, $\Delta H^{\#} = 28.8 \, \text{kJmol}^{-1}$) and III ($\Delta S^{\#} = 0.21 \, \text{kJmol}^{-1} \, \text{K}^{-1}$), $\Delta H^{\#} = 19.3 \, \text{kJmol}^{-1}$.

5 Crystallization in Fluorene Derivatives with Nematic Phases

The kinetics of crystallization in 5P-EtFLEt-P5 and 5P-Am*FLAm*P5 under various thermal conditions are discussed in this section.

5.1 Comparison of Isothermal Melt and Cold Crystallization Kinetics in 5P-EtFLEt-P5

This study was motivated by previous findings demonstrating differences in the crystallization kinetics of various polymers characterized by a crystalline state on cooling and heating. These findings revealed that at identical temperatures, cold crystallization is generally faster than melt crystallization. Nevertheless, no universal trend was found for other crystallization parameters, including the crystallization activation energy and Avrami exponent n_A. The 5P-EtFLEt-P5 liquid crystal offers a rare opportunity to investigate both melt and cold isothermal crystallizations: The thermal treatment protocols are presented in Fig. 6a, b.
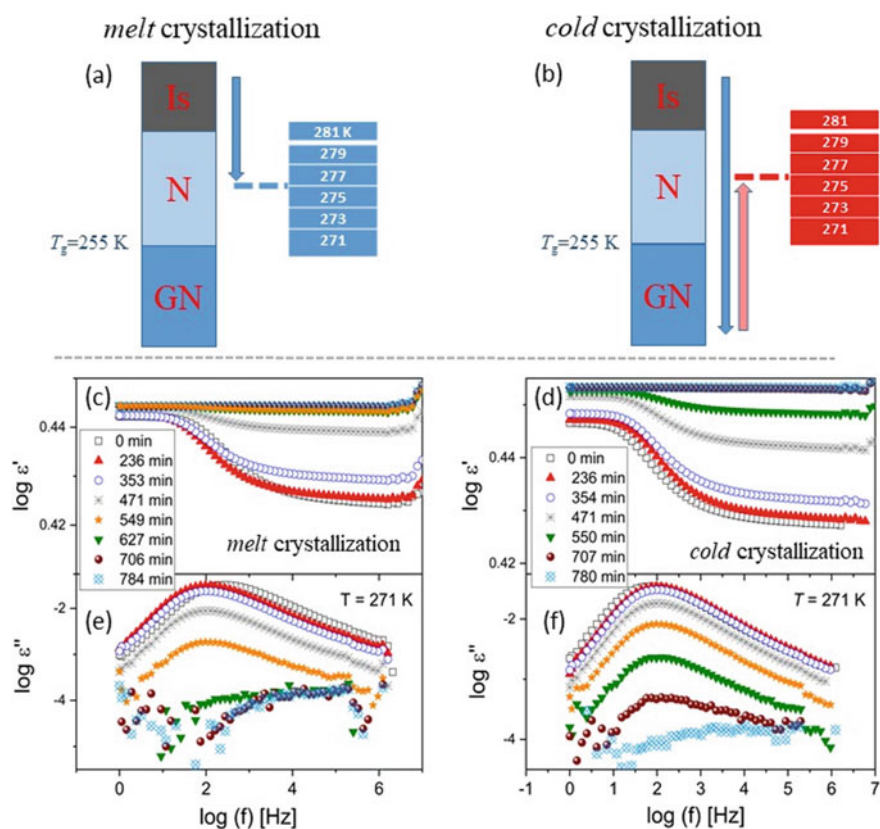
Fig. 6 Schemes presenting thermal treatment applied in order to study isothermal melt (**a**) and cold crystallization (**b**) and dielectric spectra of the real ε' (**c**, **d**) and imaginary ε'' (**e**, **f**) parts of the complex dielectric permittivity as a function of frequency measured at 271 K during isothermal melt and cold crystallization as indicated for 5P-EtFLEt-P5. Adapted with permission from [20]. Copyright © 2018 American Chemical Society

The melt crystallization was examined by directly cooling the material at a rate of 10 K/min from the isotropic state at 385 K to a selected temperature. In the case of cold crystallization, the sample was first quenched below T_g and then heated to the selected measurement temperature. The changes of the dielectric spectra occurring over time during melt and cold crystallization at 271 K are shown in Fig. 6(c–f). As crystallization proceeds, the dielectric loss spectra maximum can be seen to shift toward lower frequencies in the first case, while the opposite trend can be seen in the second. This indicates that the molecular motions around the short molecular axis slowed during the melt crystallization phase and that that molecular dynamics was enhanced during cold crystallization (Fig. 7).

An increase of the degree of crystallinity was determined by following changes of the dielectric strength (Fig. 8a) which are caused by a reduction in the number of fluctuating dipoles:

$$\Delta\varepsilon_N = \frac{\varepsilon'(0) - \varepsilon'(t)}{\varepsilon'(0) - \varepsilon'(\infty)} \tag{9}$$

where $\varepsilon'(0)$, $\varepsilon'(t)$ and $\varepsilon'(\infty)$ are the values of the dielectric permittivity at, respectively, the beginning of the observation, after time t and at the end. The kinetics of crystallization under isothermal conditions was described in terms of the classic Avrami approach and the analytical method proposed by Avramov. According to the Avrami model, the time dependence of $\Delta\varepsilon_N$ is given by
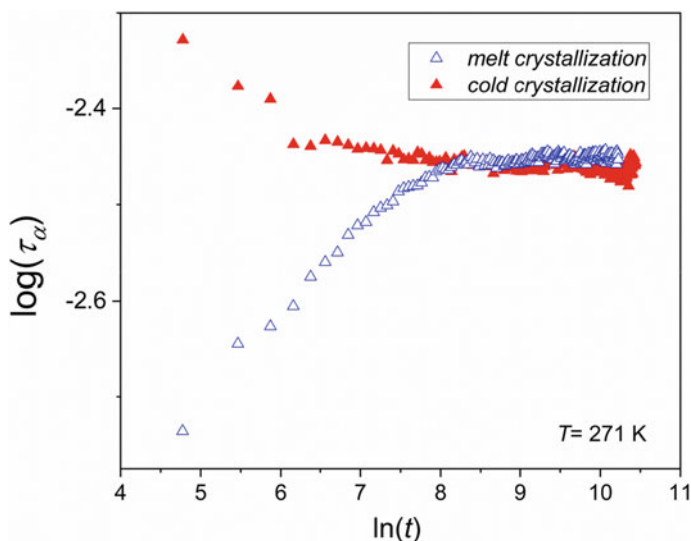
Fig. 7 Variation of the relaxation time as a function of crystallization time observed during melt and cold isothermal crystallization at 271 K. Adapted with permission from [20], supplementary materials (Copyright © 2018 American Chemical Society)
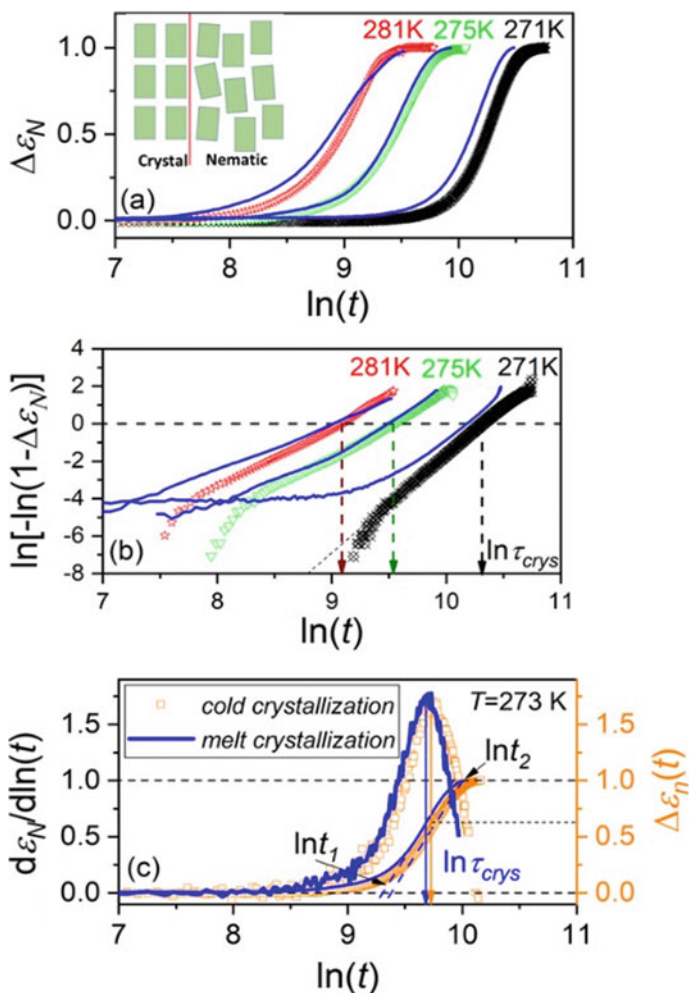
Fig. 8 Comparison of data obtained for melt and cold isothermal crystallization in 5P-EtFLEt-P5 at selected temperatures as indicated. **a** The normalized dielectric strength $\Delta\varepsilon_N(t)$ as a function of time during isothermal crystallization. The schematic representation of the crystal/nematic interface is shown in left corner of the panel. **b** Avrami plot: $\ln[-\ln(1-\Delta\varepsilon_N)]$ versus $\ln(t)$ for the data presented in the upper panel. **c** Avrami–Avramov plot: time dependence of normalized dielectric strength $\Delta\varepsilon_N(t)$ and its derivative versus the natural logarithm of the time at $T = 273$ K. Adapted with permission from [20] (Copyright © 2018 American Chemical Society)

$$\Delta\varepsilon_N(t) = 1 - \exp\left(-K(t - t_0)^{n_A}\right) \tag{10}$$

where K denotes a constant depending on the crystallization temperature and geometry of the sample, t_0 is the induction time and n is the Avrami exponent depending

on the type of nucleation and the dimensionality of crystal growth. The Avrami plot is shown in Fig. 8b.

Equation (10) can be presented as

$$\Delta\varepsilon_N(t) = 1 - \exp\left[-\left(\frac{t - t_0}{\tau_{\text{cryst}}}\right)^{n_A}\right] \qquad (11)$$

where $\tau_{\text{crys}} = K^{-1/n}$ refers to the characteristic time of the process. To determine the parameters according to the Avramov procedure, the first derivative of $\Delta\varepsilon_N(t)$ was plotted as a function of $\ln(t)$ (Fig. 8c). The characteristic crystallization time is obtained from the maximum of the derivative of $\Delta\varepsilon_N$ and the required condition ensuring $t_0 = 0$ is fulfilled for the situation $\Delta\varepsilon_N = 1 - e^{-1} = 0.63$. The n_A parameter can also be estimated from the formula:

$$n_A = \frac{e}{\ln t_2 - \ln t_1} \qquad (12)$$

where t_1 and t_2 are shown in Fig. 8c.

The comparison of data obtained for melt and cold crystallization revealed that, contrary to the results reported previously for polymers, for 5P-EtFLEt-P5 the crystallization process from the nematic melt state was faster than that observed for cold crystallization. As the molecules at the nematic/crystal interface are properly oriented to join the crystal and they do not need to align during the crystallization process (Fig. 8a), these findings can be attributed to the fact that orientational order of molecules is higher in the nematic phase achieved upon cooling than in the metastable nematic phase obtained when the glass softens [38, 39]. Similar acceleration of the crystallization process associated with the liquid crystalline order has also been observed for some other polymeric compounds [40].

5.2 Kinetics of Isothermal Cold Crystallization Process in 5P-EtFLEt-P5 and 5P-Am*FLAm*P5: Molecular Mobility, Morphology and Thermodynamic Properties

For 5P-Am*FLAm*-P5, it was only possibly to perform the isothermal experimnents using BDS for cold crystallization, due to very short duration of the crystallization process from the melt nematic N* state. Example of experimental data and the results of Avrami analysis are given in Fig. 9. According to the classical theory of crystallization, characteristic crystallization time is affected by kinetic and thermodynamic factors [41]. By studying the correlation between dynamic properties and crystallization rates for a large number of materials, Ediger et al. [42] demonstrated that coupling coefficient ζ, associated with decoupling of the crystal growth time from viscosity due to dynamic heterogeneity, is related to fragility m_f thus: $\zeta \approx 1.1-0.005m_f$. The extent of correlation between molecular mobility and the crystallization
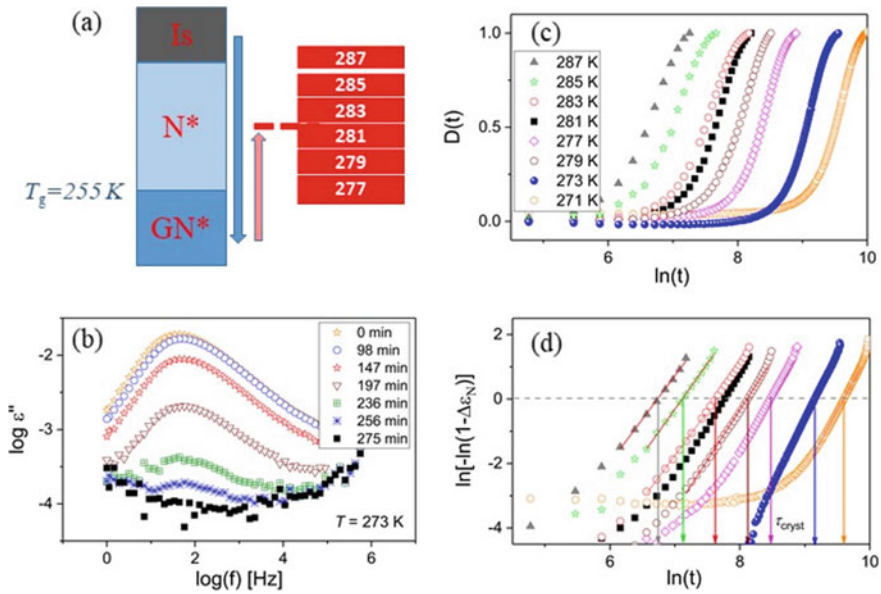
Fig. 9 a A scheme presenting thermal treatment protocol applied to study the cold crystallization process of the Cr2 phase in 5P-Am*FLAm*P5. **b** Dielectric loss spectra in the course of isothermal crystallization of the Cr2 phase at 273 K. **c** Normalized dielectric strength $\Delta\varepsilon_N(t)$ as a function of time during isothermal crystallization at selected temperatures, as indicated. **d** Avrami plot: $\ln[-\ln(1-\Delta\varepsilon_N)]$ versus $\ln(t)$ for the data presented in panel **b**. Adapted from [30] with kind permission of The European Physical Journal (EPJ)

rates was quantified as the slope of the linear dependence of $\ln(\tau_{cryst})$ against $\ln(\tau_\alpha)$ (Fig. 10b). The value of $\varsigma \approx 0.51$ obtained for 5P-Am*FLAm*P5 is slightly higher than that found for 5P-EtFLEt-P5 ($\varsigma \approx 0.44$) at the temperature range $T_c < 1.1T_g$. In both cases, the estimation agrees well with the value predicted based on the fragility index m_f. At $T > 277$, a fall in the coupling coefficient value was observed ($\varsigma \approx 0.2$); this hints at the role of the kinetic factor in the crystallization in the nematic phase of 5P-EtFLEt-P5 being reduced in favor of thermodynamic driving force mechanism.

The values of the crystallization activation energy (E_c) for the investigated LCs were determined by fitting the Arrhenius function to the temperature dependence of $\ln(\tau_{cryst})$ (Fig. 11a). For 5P-EtFLEt-P5, the energy of crystallization in the N phase significantly increases from $E_c \approx 32$ kJ/mol to $E_c \approx 100$ kJ/mol below 277 K, which suggests a change in the crystallization mechanism. In the case of isothermal crystallization in N* of 5P-Am*FLAm*P5 taking place above the glass transition temperature, E_c was found to be 114 ± 6 kJ/mol.

The Avrami parameter n_A was found to fall from 4 to 2.8 as the crystallization temperatures increased, indicating that the N* phase of 5P-Am*FLAm*P5 underwent spherical growth in three dimensions. More pronounced variation of n_A values was revealed for 5P-EtFLEt-P5 ($n_A \approx 5$ at 271 K), indicating the formation of bundle-like or sheaflike crystallites; the value of n≈3 suggests the presence of spherically
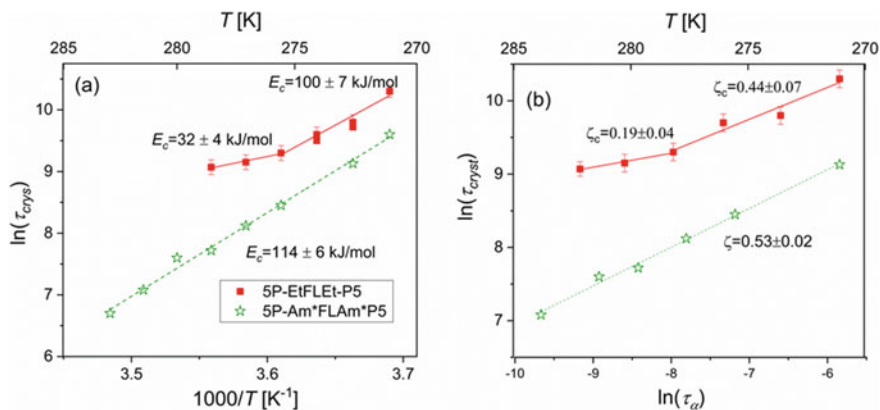
Fig. 10 a Temperature dependence of crystallization rates $\ln(\tau_{\text{cryst}})$ for isothermal cold crystallization in N and N* phases of 5P-EtFLEt-P5 and 5P-Am*FLAm*P5, respectively. **b** The crystallization rates $\ln(\tau_{\text{cryst}})$ as a function of α-relaxation time (τ_α). Data adapted with permission from Refs [20, 30] (kind permission of The European Physical Journal (EPJ))
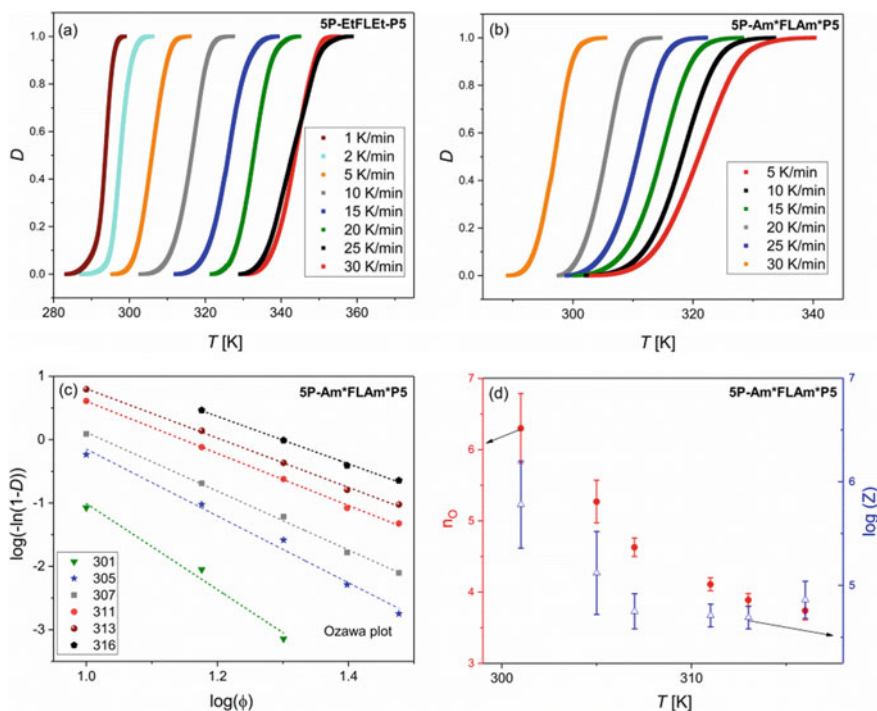
Fig. 11 Crystallization degree $D(T)$ as a function of temperature determined from DSC measurements at different heating rates ϕ for **a** 5P-EtFLEt-P5 and **b** 5P-Am*FLAm*P5. The panel **c** shows Ozawa plots. **d** Temperature dependence of Ozawa parameters for 5P-Am*FLAm*-P5. Data taken with kind permission of The European Physical Journal (EPJ) from Ref [30]

growing crystalline centers at 281 K. This also indicates isotropic growth took place at higher temperatures, whereas a large anisotropy in the growth rate, manifested by some faces growing faster than others (resulting in spiky crystals), was found at low temperatures. Further details about crystal growth were obtained by analyzing the difference of entropy between the melt and crystalline states. According to Jackson, materials displaying a large entropy of crystal fusion ($\Delta_m S > 4R$, where R is the gas constant), as it was observed in the case of studied LCs ($\Delta_m S \approx 68$ Jmol^{-1} K^{-1} for 5P-Am*FLAm*P5 and $\Delta_m S \approx 192$ Jmol^{-1} K^{-1} for 5P-EtFLEt-P5), show a flat melt/crystal interface growing laterally by either screw dislocation or surface nucleation growth.

5.3 The Non-isothermal Cold Crystallization Process in 5P-EtFLEt-P5 and 5P-Am*FLAm*P5 as Observed by DSC

The tendency of the investigated fluorene derivatives to vitrify or crystallize was verified by DSC measurement for different rates of temperature changes (ϕ). For 5P-EtFLEt-P5, vitrification of the nematic phase was observed followed by cold crystallization in a metastable N state upon heating—this was found for all tested cooling/heating rates ($1 \leq \phi \leq 30$); in contrast, the chiral nematic phase of 5P-Am*FLAm*P5 formed glass only upon cooling at a $\phi \geq 5$ K/min. Additionally, upon heating, the metastable N* of the latter first transformed to an isotropic phase and then underwent crystallization (see Fig. 2c). The relative degree of the non-isothermal crystallization (D) for each value of ϕ can be estimated by integrating the crystallization peaks of DSC curve [43]:

$$D(T) = \frac{\int_{T_0}^{T} \left(\frac{\mathrm{d}H}{\mathrm{d}T}\right)\mathrm{d}T}{\int_{T_0}^{T_\infty} \left(\frac{\mathrm{d}H}{\mathrm{d}T}\right)\mathrm{d}T} \tag{13}$$

where $\mathrm{d}H/\mathrm{d}T$ is the heat flow and T_0 and T_∞ denote the temperatures at which the crystallization process, respectively, starts and ends. The evolution of the degree of crystallization $D(T)$ in the course of cold crystallization for 5P-EtFLEt-P5 and 5P-Am*FLAm*P5 over changes in temperature is presented in Fig. 11. The results were subjected to the Ozawa equation [44], which is based on the assumption that non-isothermal crystallization is composed of infinitesimally small isothermal crystallization steps. By following that the time variable t in the Avrami model can be replaced with the quotient of temperature and heating rate T/ϕ

$$\log(-\ln(1-D)) = \log Z(T) - n_O \log(\phi) \tag{14}$$

where D is the relative degree of non-isothermal crystallization, n_O denotes the Ozawa exponent that gives information about the dimensionality of the crystal and $Z(T)$ is

the Ozawa crystallization rate. For fixed temperatures, the plots of $\log(-\ln(1 - D))$ versus $\log(\phi)$ are linear, with the slope being the parameter n_O and the intercept with the y-axis corresponding to $\log(Z(T))$ (inset Fig. 11c). The values of n_O were found to range from 6.1 to 3.7 with increasing temperature, suggesting the presence of considerable anisotropy in growth, resulting in the production of spiky crystals (bundle-like or sheaflike crystallites) at slow heating rates and isotropic growth upon fast heating [41]. Due to the broad temperature range of crystallization in 5P-EtFLEt-P5, it was not possible to determine a reasonable number of points to construct the Ozawa plot.

The activation energy of crystallization E_c was calculated by means of an equation proposed by Kissinger [45]:

$$\ln \frac{\phi}{T_p^2} = C - \frac{E_c}{RT_p} \tag{15}$$

and by Augis and Bennett [46]:

$$\ln \frac{\phi}{T_p - T_o} = C_{AB} - \frac{E_c}{RT_p} \tag{16}$$

where C and C_{AB} denote fitting parameters, ϕ refers to the cooling/heating rate, T_p is the maximum crystallization peak and T_o indicates the onset temperature of crystallization. The discrepancies between the crystallization activation barriers (E_c) estimated from two models are comparable within error limits. For 5P-EtFLEt-P5, the crystallization energy values $E_c \approx 90$ kJ/mol at 293–306 K (points corresponding to 1 K/min $\leq \phi \leq$ 5 K/min) and $E_c \approx 30$ kJ/mol at 317–344 K (points corresponding to 5 K/min > $\phi \geq$ 30 K/min) are consistent with findings obtained for isothermal crystallization (Fig. 12). They also confirm that diffusive and thermodynamic factors play dominant roles at low and high temperatures, respectively. Similar behavior was identified for crystallization in nematic phase of other liquid crystal [41]. A different scenario was observed for 5P-Am*FLAm*P5: Upon heating from the glassy state, the metastable N* phase transformed to an isotropic state which then crystallized. The activation energy of non-isothermal crystallization in such a condition ($E_a \approx 54$ kJ/mol) is less than half that observed for metastable N* in the isothermal experiment ($E_a \approx 114$ kJ/mol). This difference can be attributed to the lower viscosity of the material in the liquid state than in the N* phase, which facilitates molecular diffusion.

6   Crystallization in a Liquid Crystal with Smectic Phase

This part of the chapter presents the crystallization of 4-n-butyloxybenzylidene-4′-n′-octylaniline (BBOA) in the smectic B phase (SmB) under various thermal conditions. The SmB phase is an orthogonal hexagonal phase, occurring in two forms: the SmB$_{Cr}$ phase, characterized by strong interlayer correlation, and the SmB$_{hex}$ phase, in which
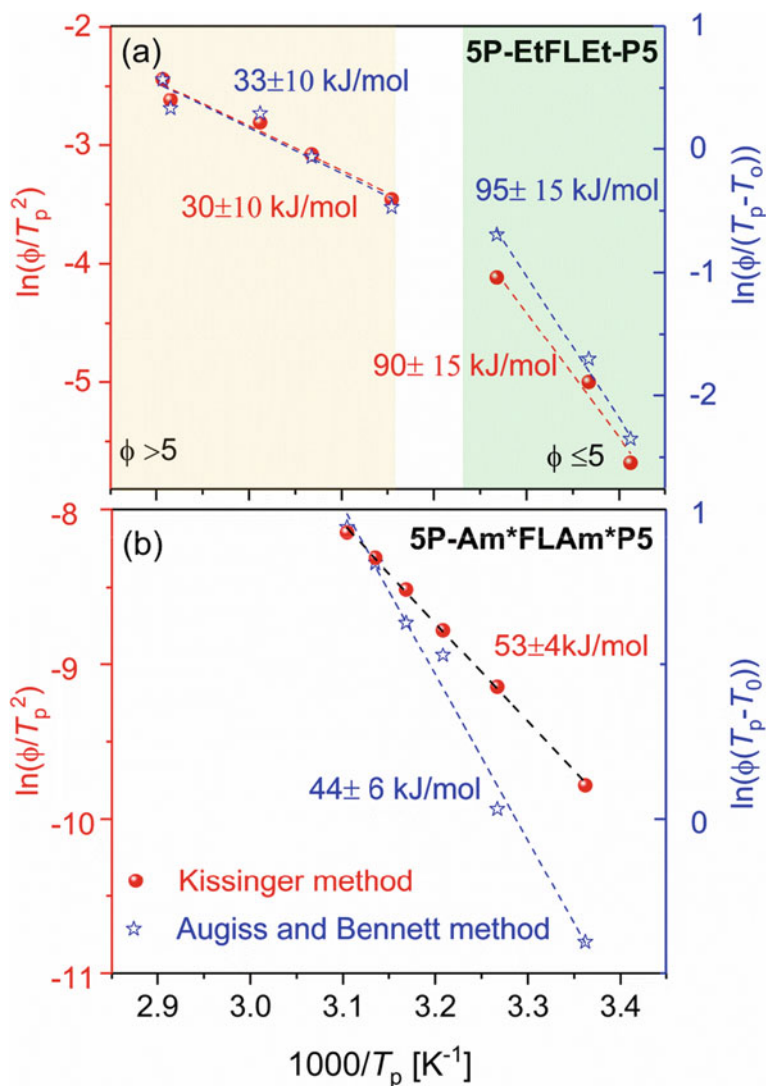
Fig. 12 Kissinger and Augis and Bennett plots for non-isothermal cold crystallization of **a** Cr1 in the nematic phase of 5P-EtFLEt-P5 and **b** Cr2 in isotropic phase of 5P-Am*FLAm*-P5. The figure presents unpublished data for 5P-EtFLEt-P5 and data for 5P-Am*FLAm*-P5 taken with permission (The European Physical Journal (EPJ)) from Ref [30]

this is absent [47]. The existence of both SmB phases in BBOA was confirmed by X-ray studies. Molecular dynamics investigations by BDS revealed that the transition from SmB_{hex} to SmB_{Cr} is also characterized by retardation of the rotational motions of molecules around their short axis and an increase in corresponding activation energy [9]. Moreover, the glass transition in the highly ordered SmB_{Cr} phase is

manifested by Vogel−Fulcher−Tammann (VFT)-type temperature dependence of structural relaxation time $\tau(T)$.

6.1 Non-isothermal Melt Crystallization Process in SmB$_{cr}$

DSC curves of BBOA for various cooling/heating rates are shown in Fig. 13. Upon cooling, the isotropic phases found at higher temperatures are followed by four mesophases: N-SmA-SmB$_{hex}$-SmB$_{cr}$ as identified also by POM textures. In the next phase transition, parts of SmB$_{cr}$ crystallize and the remainder vitrifies. Crystallization is completed after the glass softens during subsequent heating. At heating rates of $\phi \geq 5$, complex cold crystallization in SmB$_{cr}$ was found, as indicated by the presence of a broad exothermal peak with three maxima at around 241, 249 and 261 K. These findings are in agreement with adiabatic calorimetry studies, which found that two metastable crystalline states undergo transformation to a stable crystalline phase [48].
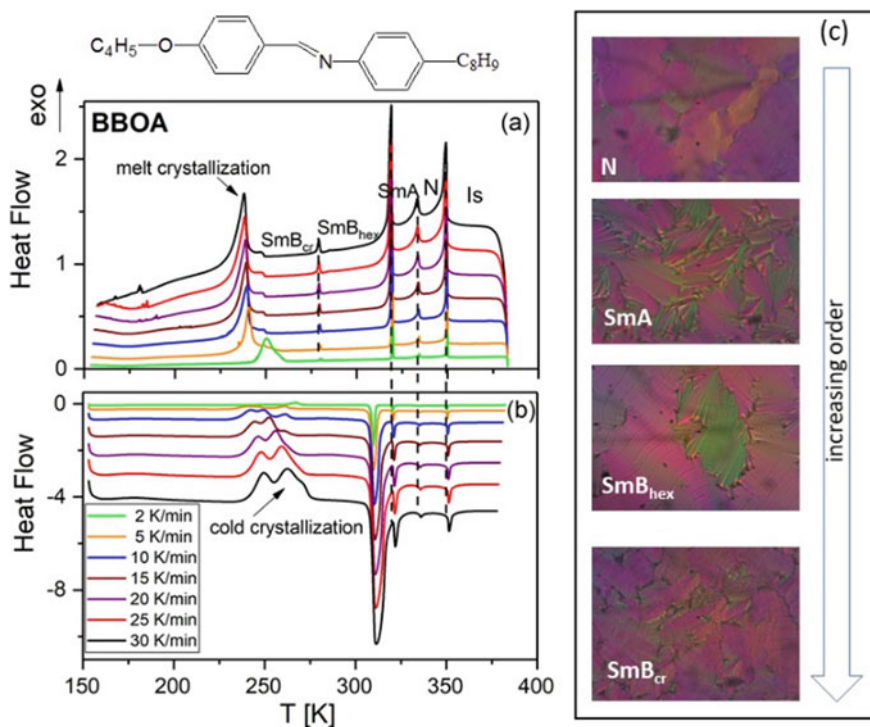
Fig. 13 Thermograms of BBOA measured at various rates of cooling **a** and heating **b**. **c** POM textures of various liquid crystalline states as indicated. Adapted with permission from [15] (according to an open access Creative Commons CC BY license)

The temperature dependences of the crystallization degree D in the course of non-isothermal crystallization (see Fig. 14) upon cooling were obtained according to Eq. 13. As the sample does not fully crystallize on cooling, and cold crystallization in the metastable SmB_{cr} occurs upon heating, the value obtained from Eq. 13 was multiplied by the ratio of the peak area on cooling and heating. The highest degree of crystallization upon cooling, $D = 89\%$, was achieved for $\phi = 2$ K/min; at faster cooling rates, this value decreased to $D = 13\%$ for $\phi = 30$ K/min.

The crystal growth in SmB_{cr} during cooling was also observed using polarized microscopy (POM). An increase of crystalline fraction was obtained from the graphical analysis of the BBOA textures as described in the experimental section. Visually, the crystalline centers were found to appear gradually with decreasing temperature and develop evenly in all directions (see Fig. 14). The crystallization temperature T_c
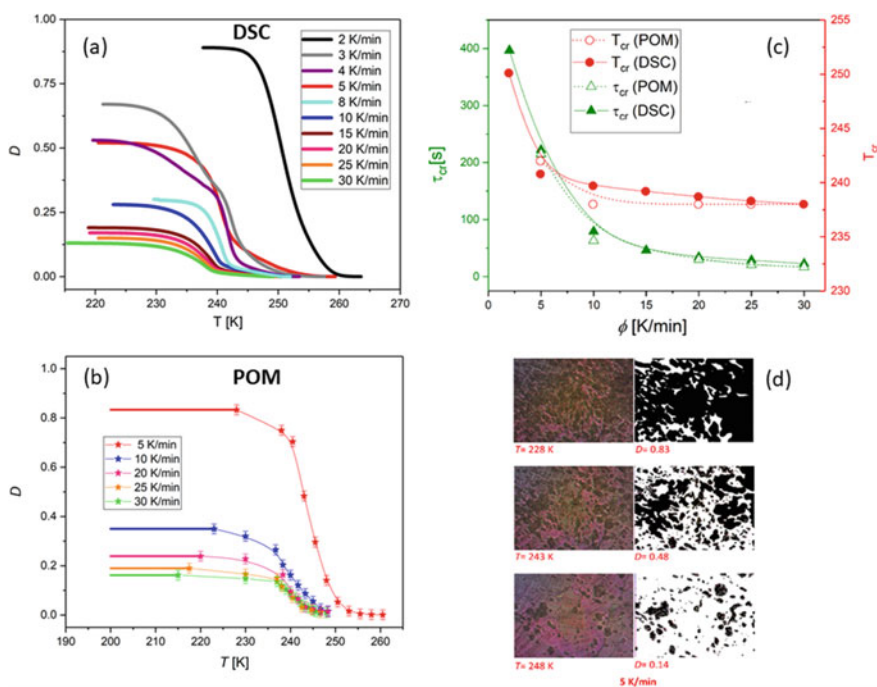
Fig. 14 Analysis of non-isothermal melt crystallization in BBOA. **a** The crystallization degree $D(T)$ versus temperature determined based on DSC measurements with different cooling rates ϕ. **b** Evolution of $D(T)$ with decreasing temperature obtained from the graphical analysis of the textures for various cooling rates. **c** Comparison of the crystallization temperature τ_c and crystallization characteristic time τ_{cr} obtained by DSC and POM studies. τ_{cr} was assumed as the time needed to achieve 63% of the maximal degree of crystallinity. **d** Texture changes during crystallization of the sample cooled at a rate of 5 K/min. Unless explicitly stated otherwise, the error bars are smaller than the symbols. Adapted with permission from [15] (according to an open access Creative Commons CC BY license)

and crystallization characteristic time τ_{cr} derived by POM investigations agree with the values determined by thermogram analysis.

Polarized microscopy was also employed to exam how the crystallization process, started upon cooling, proceeds upon heating. The evolution of the degree of crystallinity over time $D(t)$ in the course of experiment is presented in Fig. 15. It was found that $D(t)$ follows the same Avrami curve on heating as for the crystallization process taking place on cooling. This suggests that total crystallization, not being restricted by the partial vitrification of the sample, would occur at the same time as incomplete crystallization upon cooling.

To determine the activation energy of non-isothermal crystallization in SmB_{cr}, the findings were analyzed according to Kissinger and Augis–Bennett equations. Two significantly different values of E_c were found: $\approx$175 kJ/mol for slow cooling (3K/min $\leq \phi \leq$ 5 K/min) and $\approx$305 kJ/mol for fast cooling (5K/min $> \phi \geq$ 30K/min). This difference suggests that two different cooling rates act by two different mechanisms of crystallization (Fig. 16). Also, the Ozawa model (Eq. 14) describes only data regarding crystallization upon cooling at $\phi \geq$ 10 K/min (see Fig. 17a). The fact that the value of $\log(Z(T))$ decreases with increasing temperature indicates that melt non-isothermal crystallization occurs for fast cooling in the diffusion-controlled region.
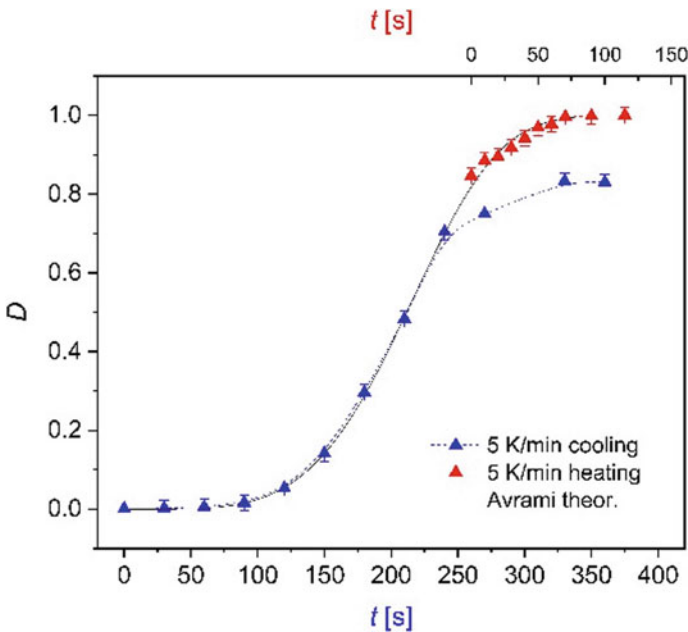
Fig. 15 Time dependence of the degree of crystallinity $D(t)$ observed for BBOA by POM on cooling (partial crystallization) and heating at a rate of 5 K/min. The black line denotes the theoretically predicted Avrami curve. Adapted with permission from [15] (according to an open access Creative Commons CC BY license)
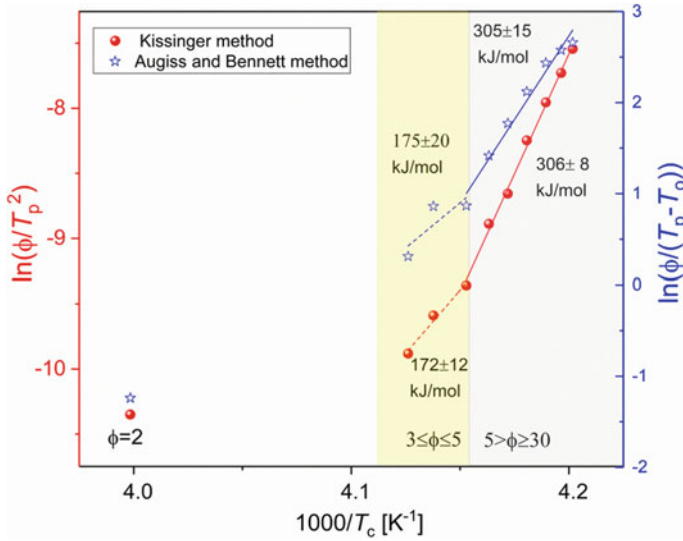
Fig. 16 Kissinger and Augis and Bennett plots as indicated for the crystallization process observed for BBOA upon cooling. Adapted with permission from [15] (according to an open access Creative Commons CC BY license)
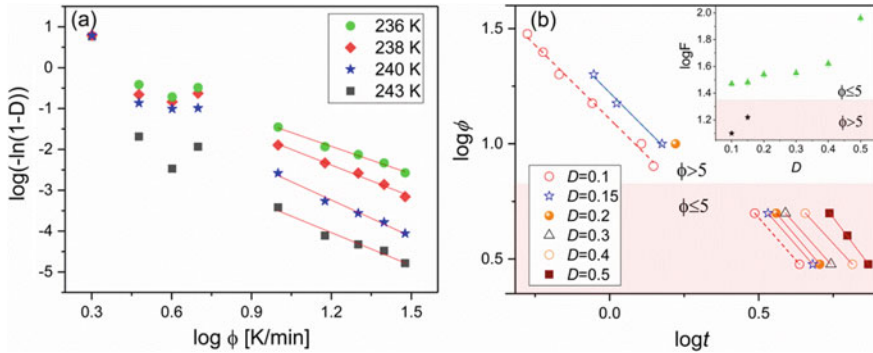
Fig. 17 **a** Analysis of DSC data obtained for the non-isothermal melt crystallization in SmB_{cr} of BBOA according to Ozawa and **b** according to Mo: plots of $\log\phi$ versus $\log t$ for a fixed degree of crystallinity D during non-isothermal crystallization in the SmB phase. The inset presents $\log F$ versus the crystallinity D. Adapted from [15] (according to an open access Creative Commons CC BY license)

Finally, the non-isothermal crystallization process was analyzed according to Mo et al. [49, 50] which combines the Ozawa and Avrami equations as below:

$$\log Z(t) - n_o \log \phi = \log k + n_A \log t \tag{17}$$

$$\log \phi = \log F - a \log t \qquad (18)$$

where a is the ratio of the Avrami exponent n_A to the Ozawa n_O exponent and $F = (Z/k)^{\frac{1}{n_O}}$ is associated with the cooling/heating rate. Figure 17b shows cooling rate as a function of crystallization time for the fixed degree of crystallinity D. Two different linear dependences of log$t$ versus logφ were revealed for 3K/min $\le \phi \le 5$ K/min and 5K/min $> \phi \ge 30$K/min. The log Z values increase as the fraction of the new phase (D) develops. Together, these results further indicate that the forms of crystallization associated with slow and fast cooling are underpinned by different mechanisms.

6.2   Isothermal Melt Crystallization in SmB$_{cr}$

The isothermal crystallization in the SmB$_{cr}$ phase was monitored at several selected temperatures using BDS for a sample which had been previously cooled from an isotropic state (Fig. 18). The τ_{cryst} value was found to increase with temperature (Fig. 19), which indicates that the crystallization process is restricted by the nuclei formation. The activation energy ($E_a \approx 205$ kJ/mol) identified for the isothermal process is consistent with that obtained for a non-isothermal experiment under slow cooling ($\phi \le 5$). These findings are also consistent with POM observations suggesting a continuous nucleation mechanism [51]. Hence, it appears that both isothermal crystallization in the temperature range 274–281 K and the non-isothermal process taking place at $\varphi \le 5$ K/min are driven by thermodynamic factors. The Avrami exponent (n_A) changes from 2.8 to 2.3 with decreasing temperature, but is predicted to be 3 for the homogeneous growth of the spherulitic nuclei. In this sense, the reduction in dimensionality observed for the non-isothermal experiment ($2.24 \le n_o \le 2.67$) can be attributed to the confinement effect imposed on the layered SmB$_{cr}$ by crystalline domains [9]. Similar findings were reported for the crystallization of some materials enclosed in nanopores and for thin polymeric films [52].

7   Conclusion

The study examines the isothermal and non-isothermal crystallization processes taking place in the isotropic and nematic phases of two mesogenic fluorene derivatives (5P-EtFLEt-P5 and 5P-Am*FLAm*P5) and in the highly ordered smectic B of 4-n-butyloxybenzylidene-4′-n′-octylaniline (BBOA) by means of BDS, DSC and POM methods.

5P-EtFLEt-P5 was found to have a higher tendency to vitrify than crystallize, even for cooling rates as low as 0.1 K/min: Crystallization of the melt nematic state can be achieved only by isothermal annealing for several hours. It was found that
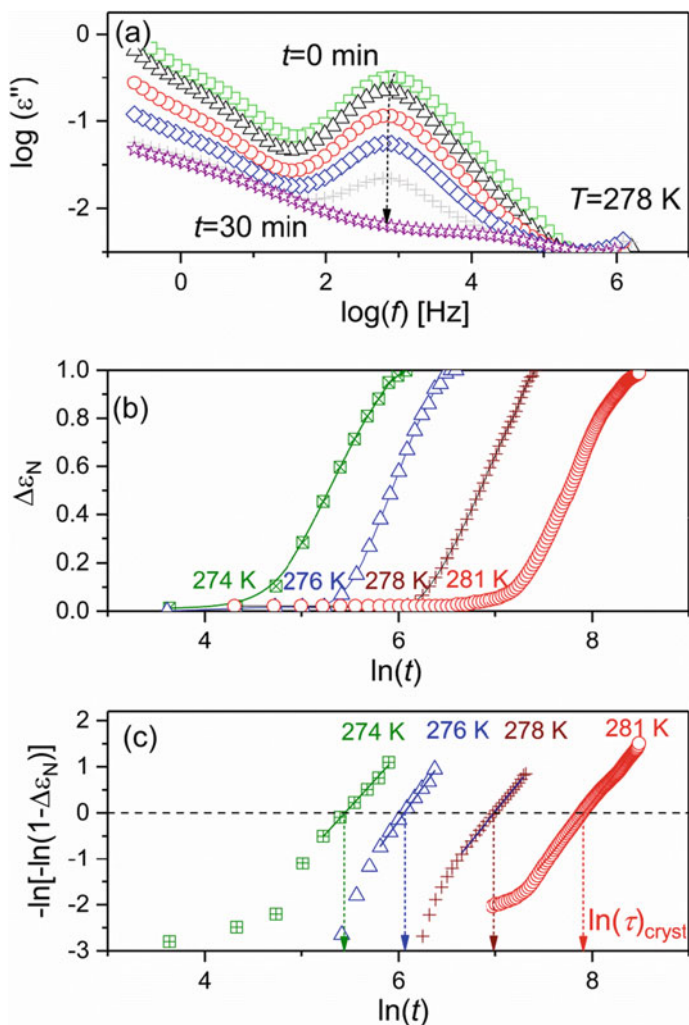
Fig. 18 a Evolution of dielectric loss spectra upon isothermal melt crystallization of BBOA at 278 K. The arrow indicates the direction of changes in the $\varepsilon''(f)$ during the crystallization process. **b** The normalized dielectric strength ($\Delta\varepsilon_N$) versus time during isothermal crystallization at 274, 276, 278 and 276 K. **c** Avrami plot of $\Delta\varepsilon_N(t)$ for the data presented in the panel **b**. Adapted with permission from [15] (according to an open access Creative Commons CC BY license)
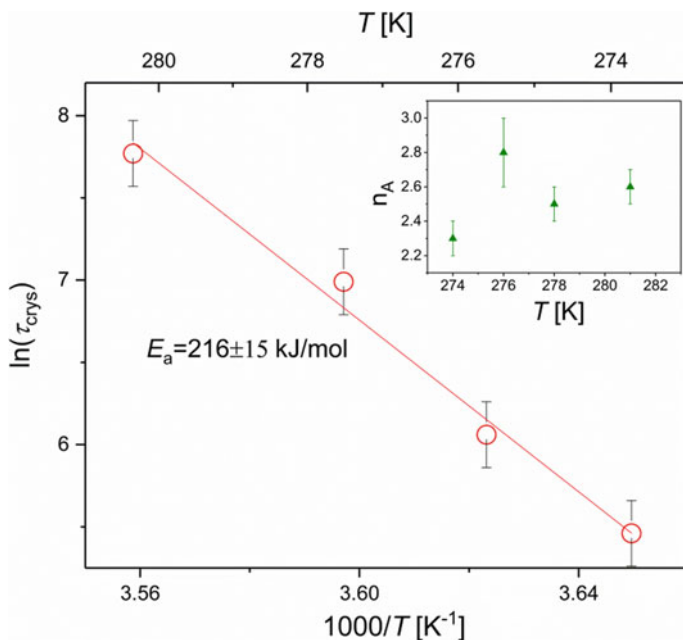
Fig. 19 Characteristic crystallization time (τ_{cryt}) as a function of reciprocal temperature for the isothermal melt crystallization from (SmB$_{\text{cryt}}$) of BBOA. The inset presents the Avrami exponent n_A versus temperature. Adapted with permission from [15] (according to an open access Creative Commons CC BY license)

the crystallization process from the nematic melt state to Cr1 phase was faster than that observed for cold crystallization after softening of glass of nematic phase on heating. The phase diagram of 5P-Am*FLAm*P5 demonstrated a strong dependence on cooling rate: A sample in the chiral nematic (N*) phase forms a glassy state when cooled at $\phi \geq 5$ K/min but undergoes crystallization of Cr1 at $\phi < 5$ K/min. Both materials crystallize upon heating when the glass softens. The crystals in 5P-EtFLEt-P5 display greater order than these found in 5P-Am*FLAm*P5, as evidenced by a higher fusion entropy value. The relaxation processes observed by BDS in the crystalline forms of 5P-Am*FLAm* indicate that the phases are conformationally disordered crystals (CONDIS). No such molecular motions were detected in the crystalline phases of 5P-EtFLEt-P5.

The energy barrier for isothermal cold crystallization of Cr1 in the metastable N phase of 5P-EtFLEt-P5 was found to increase from $E_c \approx 32$ kJ/mol to $E_c \approx 100$ kJ/mol for lower crystallization temperatures. This is consistent with studies performed under non-isothermal conditions, demonstrating $E_c \approx 32$ kJ/mol on fast heating (5 K/min > $\phi \geq 30$ K/min, corresponding to crystallization at 317–344 K) and $E_c \approx 90$ kJ/mol on slow heating (1 K/min $\leq \phi \leq 5$ K/min, corresponding to crystallization at 317–344 K). The change in the crystallization energy was attributed to the fact that the crystallization process is dominated by thermodynamic and kinetic factors

at high and low temperatures, respectively. A different crystallization behavior was observed for 5P-Am*FLAm*P5: On heating from the glassy state, the metastable N* phase transforms to an Is state which then undergoes crystallization to the Cr2 crystal. The activation energy of non-isothermal crystallization in the Is phase ($E_a \approx 54$ kJ/mol) is significantly lower than for isothermal crystallization in the N* phase ($E_a \approx 114$ kJ/mol). This can be attributed to the material having lower viscosity in the isotropic state than in the N* phase, thus better facilitating molecular diffusion. It was found that both compounds displayed a correlation between molecular dynamics and isothermal crystallization kinetics in the vicinity of the glass transition temperature.

Complex crystallization was also observed for BBOA. During cooling, part of the SmB_{cr} phase crystallizes and the remainder vitrifies; the crystallization is completed upon subsequent heating, when the glass softens. POM investigations found that the degree of crystallinity increases upon heating, and that it follows the same Avrami curve observed for crystallization upon cooling. DSC examination found the non-isothermal melt crystallization in the SmB_{cr} phase is driven by two factors depending on cooling rate: (i) thermodynamic forces at lower cooling rates (3K/min $\leq \phi \leq$ 5K/min), with the energy barrier $E_a \approx 175$ kJ/mol, and (ii) diffusion mechanism at higher cooling rates (5K/min $> \phi \geq$ 30K/min), with $E_a \approx 305$ kJ/mol. The isothermal melt crystallization process in SmB_{cr}, tested between 274 and 281 K, is restricted by the formation of nuclei. The isothermal and non-isothermal crystallization processes occurring at $\phi \leq 5$ K/min have similar activation energy ($E_a \approx 205$ kJ/mol), which suggests that both processes are controlled by the same mechanism. The Avrami and Ozawa parameters of crystal growth observed for isothermal ($2.3 \leq n_A \leq 2.8$) and non-isothermal ($2.24 \leq n_o \leq 2.67$) experiments are reduced in the smectic phase with respect to the three-dimensional process; this may be due to the constraints placed on the SmB_{cr} fractions by the surrounding crystalline domains.

These findings may have considerable value in future research on LCs and their applications; however, further studies are required on the relationship between the structure of the mesophase and the kinetics of its crystallization.

References

1. Vallamkondu J, Corgiat E, Buchaiah G, Kandimalla R, Reddy P (2018) Cancers (Basel) 10:462
2. Woltman SJ, Jay GD, Crawford GP (2007) Nat Mater 6:929

3. Woltman SJ, Jay GD, Crawford GP (2007) Liquid crystals: frontiers in biomedical applications. WORLD SCIENTIFIC

4. Stevenson CL, Bennett DB, Lechuga-Ballesteros D (2005) J Pharm Sci 94:1861

5. Schenning APHJ, Crawford GP, Broer DJ (eds) (2017) Liquid crystal sensors, Series: liquid crystals book series. CRC Press, Boca Raton, FL

6. Sorai M, Seki S (1973) Mol Cryst Liq Cryst 23:299

7. Johari GP (1982) Philos Magaz B 46:549

8. Uhrich D, Aimiuwu V, Ktorides P, LaPrice W (1975) Phys Rev A 12:211

9. Jasiurkowska-Delaporte M, Napolitano S, Leys J, Juszyńska-Gałązka E, Wübbenhorst M, Massalska-Arodź M (2016) J Phys Chem B 120:12160

10. Jasiurkowska M, Ściesiński J, Czub J, Massalska-Arodź M, Pełka R, Juszyńska E, Yamamura Y, Saito K (2009) J Phys Chem B 113:7435

11. Jasiurkowska M, Zieliński PM, Massalska-Arodź M, Yamamura Y, Saito K (2011) J Phys Chem B 115:12327

12. Jasiurkowska-Delaporte M, Massalska-Arodź M (2017) J Mol Liq 241:355

13. Leslie-Pelecky DL, Birge NO (1994) Phys Rev B 50:13250

14. Massalska-Arodź M, Williams G, Thomas DK, Jones WJ, Dabrowski R (1999) J Phys Chem B 103:4197

15. Jasiurkowska-Delaporte M, Rozwadowski T, Juszyńska-Gałązka E (2019) Crystals 9:1

16. Padmaja S, Ajita N, Srinivasulu M, Girish SR, Pisipati VGKM, Potukuchi DM (2010) Zeitschrift Fur Naturforsch - Sect a J Phys Sci 65:733

17. Rozwadowski T, Massalska-Arodź M, Kolek Ł, Grzybowska K, Bąk A, Chłędowska K (2015) Cryst Growth Des 15:2891

18. Georgopoulos D, Kripotou S, Argyraki E, Kyritsis A, Pissis P (2015) Mol Cryst Liq Cryst 611:197

19. Deptuch A, Jaworska-Gołąb T, Marzec M, Urbańska M, Tykarska M (2019) Phase Transit 92:126

20. Jasiurkowska-Delaporte M, Rozwadowski T, Dmochowska E, Juszyńska-Gałązka E, Kula P, Massalska-Arodź M (2018) J Phys Chem B 122:10627

21. Aldred MP, Eastwood AJ, Kelly SM, Vlachos P, Contoret AEA, Farrar SR, Mansoor B, O'Neill M, Tsoi WC (2004) Chem Mater 16:4928

22. Dmochowska E, Bombalska A, Kula P (2019) Liq Cryst 1

23. Rao NVS, Potukuchi DM, Pisipati VGKM (1991) Mol Cryst Liq Cryst 196:71

24. Kremer F, Schönhals A (2003) Broadband dielectric spectroscopy

25. Jonscher AK (1981) J Mater Sci 16:2037

26. Jonsher AK (1983) Dielectric relaxation in solids. Chelsea Dielectrics Press, London

27. Wübbenhorst M, Van Turnhout J (2002) J Non Cryst Solids 305:40

28. Van Turnhout J, Wübbenhorst M (2002) J Non Cryst Solids 305:50

29. Syme CD, Mosses J, González-Jiménez M, Shebanova O, Walton F, Wynne K (2017) Sci Rep 7:42439

30. Jasiurkowska-Delaporte M, Rozwadowski T, Juszyńska-Gałązka E, Krawczyk J, Dmochowska E, Kula P, Massalska-Arodź M (2019) Eur Phys J E 42:121

31. Sharma RP, Green PF (2017) Macromolecules 50:6617

32. Madkour S, Szymoniak P, Radnik J, Schönhals A (2017) ACS Appl Mater Interfaces 9:37289

33. Bohmer R, Ngai KL, Angell CA, Plazek DJ (1993) J Chem Phys 99:4201

34. Shintani H, Tanaka H (2006) Nat Phys 2:200

35. Kawakami K, Harada T, Yoshihashi Y, Yonemochi E, Terada K, Moriyama H (2015) J Phys Chem B 119:4873

36. Meersman F, Geukens B, Wübbenhorst M, Leys J, Napolitano S, Filinchuk Y, Van Assche G, Van Mele B, Nies E (2010) J Phys Chem B 114:13944

37. Starkweather HW, Avakian P (1992) J Polym Sci Part B Polym Phys 30:637

38. Descamps M, Dudognon E (2014) J Pharm Sci 103:2615

39. Jackson KA (2004) Kinetic processes. Wiley-VCH Verlag GmbH & Co. KGaA, Weinheim, FRG

40. Kim SO, Koo CM, Chung IJ, Jung HT (2001) Macromolecules 34:8961
41. Gutzow JWP, Ivan S, Schmelzer (1995) The vitreous state: thermodynamics, structure, rheology, and crystallization, 2nd edn. Springer, Berlin
42. Sanz A, Niss K (2017) Cryst Growth Des 17:4628
43. Henderson DW (1979) J Non Cryst Solids 30:301
44. Ozawa T (1971) Polymer (Guildf) 12:150
45. Kissinger HE (1956) J Res Natl Bur Stand (1934) 57:217
46. Augis JA, Bennett JE (1978) J Therm Anal Calorim 13:283
47. Górecka E, Chen L, Pyżuk W, Krówczyński A, Kumar S (1994) Phys Rev E 50:2863
48. Juszyńska E, Jasiurkowska M, Massalska-Arodź M, Takajo D, Inaba A (2011) Mol Cryst Liq Cryst 540:127
49. Liu Y, Wang L, He Y, Li S (1998) J Polym Sci Part B Polym Phys 36:1305
50. Liu T, Mo Z, Wang S, Zhang H (1997) Polym Eng Sci 33:568
51. Zhou D, Zhang GGZ, Law D, Grant DJW, Schmitt EA (2008) Mol Pharm 5:927
52. Napolitano S, Wübbenhorst M (2006) Macromolecules 39:5967

Control of Crystallization Pathways by Electric Fields

Karolina Adrjanowicz and Ranko Richert

Abstract Polar molecular materials subject to high electric fields of magnitude E lead to situations which are usually characterized by dipole energies (μE) that remain small compared with the thermal energy, i.e., $\mu E << k_B T$. As a result, typical nonlinear dielectric effects are very small and electric fields are expected to have little impact on the net molecular orientation and on thermodynamic potentials. Nevertheless, static electric fields in the range from 40 to 200 kV cm^{-1} were observed to impact the crystallization dynamics and pathway of a polar molecular glass-former: vinyl ethylene carbonate (VEC), a derivative of propylene carbonate. Various temperature/field protocols have been employed to reveal the effect of a static electric field on the crystallization behavior of VEC. The volume fraction of the liquid state is measured via the dielectric permittivity. The rate of crystallization could be accelerated by more than a factor of 10, either by applying a field near the glass transition temperature, T_g, and then taking the sample to a higher crystallization temperature T_c without field, or by taking the sample directly from $T > T_m$ to T_c, where T_m is the melting temperature, and then applying an electric field. Interestingly, crystallization promoted by electric fields gave rise to a new polymorph that could not be obtained in the absence of an electric field. The signature of this new structure is a melting temperature that was observed to be 20 K below that of the ordinary crystal of VEC. Because VEC is a simple polar molecule, these field-induced features are expected to occur in many other materials having sufficient permanent dipole moments. Our results highlight the important role of an external electric field as additional control variable to influence the crystallization tendency of molecular glass-formers, and provide new opportunities in pharmaceutical science or organic electronics.

Keywords High electric fields · Dielectric relaxation · Crystal polymorphs

K. Adrjanowicz
Institute of Physics, University of Silesia, 75 Pulku Piechoty 1a, Chorzow 41-500, Poland
e-mail: karolina.adrjanowicz@us.edu.pl

R. Richert (✉)
School of Molecular Sciences, Arizona State University, Tempe, Arizona 85287, USA
e-mail: Ranko.Richert@asu.edu

Abbreviations

BDS	Broadband dielectric spectroscopy
ε_∞	High-frequency limit dielectric constant
ε_s	Static dielectric constant
J	Nucleation rate
MWS	Maxwell–Wagner–Sillars
PC	Propylene carbonate
RMS	Root mean square
T_g	Glass transition temperature
T_m	Melting temperature
TTT	Time-temperature-transformation
u	Crystal growth rate
VEC	Vinyl ethylene carbonate

1   Introduction

Crystallization is an important aspect in designing materials and understanding their behavior [1–4]. It is a process that can prevent glass formation, the transition to the amorphous solid that forms by cooling a supercooled liquid to below the glass transition temperature T_g. In some cases, crystallization can also be driven to lead to different polymorphs, i.e., different crystal structures of the same chemical compound which will have different properties. Tailoring the outcome of a crystallization process or preventing it altogether is usually done by modifying the temperature T, its rate of change $q = dT/dt$, or by applying pressures beyond the ambient level. This work is concerned with how a static electric field influences the crystallization outcome.

For understanding the process of crystallization, it is important to realize that two separate steps are involved: nucleation and crystal growth. For typical molecular materials, the nucleation rate $J(T)$ and the crystal growth rate $u(T)$ can follow very different patterns on the temperature scale, as indicated in Fig. 1.

According to the standard Gibbs theory of nucleation, a critical nucleus size is required before further growth remains a thermodynamically favored process [5]. The difference in the chemical potentials μ between melt and crystal phase, $\Delta\mu = \mu^{\text{melt}} - \mu^{\text{crystal}}$, determines the thermodynamic driving force for crystallization, with $\mu^{\text{crystal}} < \mu^{\text{melt}}$ for temperatures $T < T_m$. According to this classical theory of homogeneous nucleation, the free energy involved in forming a nucleus is the sum of a volume term, $-V\rho\Delta\mu$, and a surface term, $A\sigma$. For a spherical nucleus with volume $V = 4\pi r^3/3$ and surface area $A = 4\pi r^2$, the free energy as a function of radius r is $\Delta G = 4\pi r^2\sigma - 4\pi r^3\rho\Delta\mu/3$. The barrier to nucleation, ΔG_{max}, then controls the nucleation rate J, and this maximum of ΔG is reached when the radius equals its critical value $r_c = 2\sigma/\rho\Delta\mu$, where $d\Delta G/dr = 0$, see Fig. 2. In this framework, it
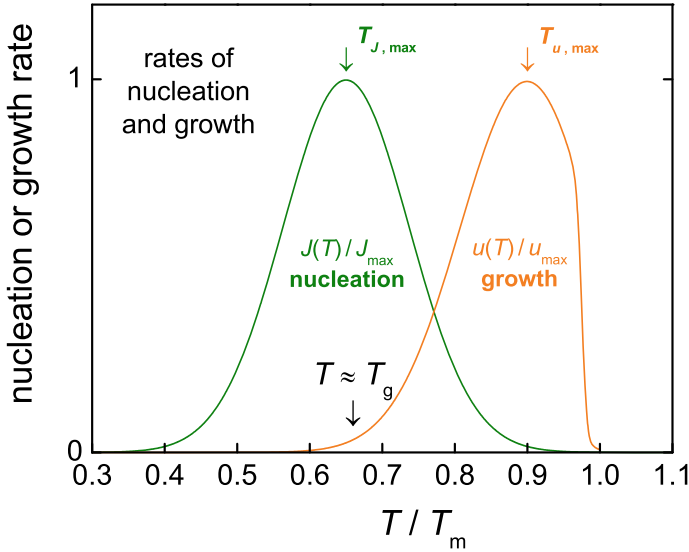
Fig. 1 Schematic representation of a typical temperature dependence of the nucleation rate $J(T)$ and the growth rate $u(T)$. The temperature scale is reduced to the melting point T_m, and the glass transition temperature T_g is positioned at $2T_m/3$, near a common value for molecular materials

is easy to realize that an electric field will modify the nucleation rate via the value of the thermodynamic driving force $\Delta\mu$, as the field-induced shift of the chemical potentials will differ for the crystal and the liquid state. According to basic models [6–9], the direction of change of ΔG_c depends mainly on the relation of the dielectric constants of crystal and liquid, $\varepsilon^{\mathrm{cryst}} > \varepsilon^{\mathrm{liquid}}$ or $\varepsilon^{\mathrm{cryst}} < \varepsilon^{\mathrm{liquid}}$.

Once crystal nuclei that exceed the critical size are present, a main factor in the growth rate is the dynamics that controls material transport towards crystal surfaces and reorientation. In the case of sufficiently polar molecules, an electric field can be assumed to affect crystal growth rates by providing preferential dipolar and thus molecular orientation. For most molecular materials, the energy preference (μE) for aligning a dipole in field direction remains small compared with thermal fluctuations ($k_B T$), and even at the dielectric strength or breakdown field of the material, one still has $\mu E/k_B T < 0.1$ [10]. This is indicative of only a small departure of $\langle\cos\theta\rangle$ from zero, where θ is the angle between dipole and field.

An alternative but common way to indicate crystallization rates and their competition with glass formation are the time-temperature-transformation (TTT) curves [11], for which examples are shown in Fig. 3, including an idea of how an electric field could modify this behavior by accelerating the crystallization rate.

The dashed lines in this graph indicate various constant cooling rates, and entering an area of a "nose" (solid lines) gives rise to a given volume fraction of crystals. In
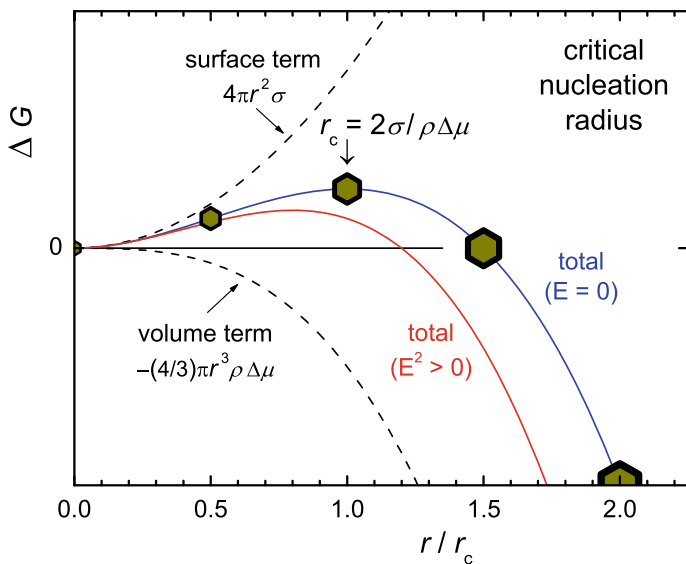
Fig. 2 Schematic representation of Gibbs' approach to homogeneous nucleation in terms of the change in free energy with crystal nucleus radius r. The dashed curves indicate the separate contributions from a surface and a volume term to the total free energy, shown as solid blue curve for the field-free case ($E = 0$). The solid red curve labeled ($E^2 > 0$) shows a possible effect of an electric field on the free energy, and in this case, the electric field promotes crystallization
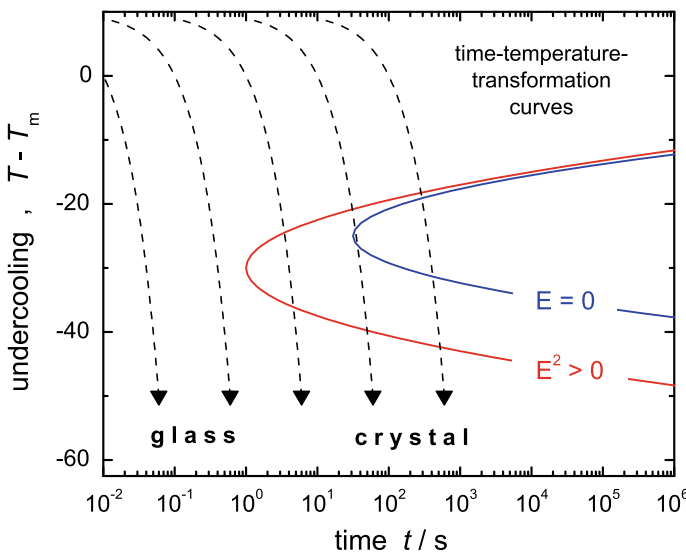
Fig. 3 Schematic representation of time-temperature-transformation (TTT) curves for various cooling rates $q = dT/dt$. Both solid curves are for the same crystal volume fraction, but the blue one is for the field-free case ($E = 0$), the red one is for an electric field ($E^2 > 0$) that promotes crystallization

the present example of Fig. 3, the high-field is assumed to lead to faster crystallization, thus requiring a higher cooling rate to avoid exceeding a certain extent of crystallization.

Predicting the effect of an electric field on crystallization is not an easy task. On the basis of the field effect on $\Delta\mu$, both the nucleation rate J and the crystal growth rate u [12]:

$$J \propto D \exp\left(-\Delta G_c(E)\big/k_BT\right) \tag{1a}$$

$$u \propto D\left[1 - \exp\left(-\Delta\mu(E)\big/k_BT\right)\right] \tag{1b}$$

will change with the application of an external electric field E. In both expressions, the prefactor is a matter of the diffusion constant D rather than viscosity η [13, 14]. The sensitivity of thermodynamic potentials, free energy F and entropy S, to an electric field is governed by [15]:

$$\Delta_E F = \tfrac{1}{2}\varepsilon_s\varepsilon_0 E^2 \tag{2a}$$

$$\Delta_E S = \tfrac{1}{2}\left(\partial\varepsilon_s\big/\partial T\right)_V \varepsilon_0 E^2 \tag{2b}$$

where ε_s is the static dielectric constant and ε_0 the permittivity of vacuum. Both ε_s and $(\partial\varepsilon_s/\partial T)$ differ substantially between liquid and crystal phases for polar materials. Qualitatively, the above discussion for a field's impact on homogeneous nucleation could apply equally to heterogeneous nucleation, where nuclei form on the surface of a foreign material. Here, however, a necessary factor to consider is how the attachment to foreign objects limits the ability of the field to orient the nuclei, which could affect the formation of polar crystals in the bulk liquid.

The above expressions clearly indicate a dependence of both J and u on the field E, but generally, the information needed to obtain the magnitude of the effect is not available. Eq. 2 does imply that larger field effects are expected for polar materials, i.e., those with large ε_s and thus larger $\partial\varepsilon_s/\partial T$. As a result of these considerations, the best approach to assessing how electric fields impact crystallization is by experimental evidence, based upon single-component molecular materials with relatively high dielectric constant [16].

1.1 Observing Crystallization by Dielectric Techniques

Key quantities in study of crystallization are the volume fractions of the crystalline and liquid material, and how these change with time [17]. The dielectric constant, ε_s, of a liquid connects the polarization $P = \varepsilon_0(\varepsilon_s - 1)E$ to the electric field E that

induced this polarization. In a polar liquid in which molecules carry a permanent dipole moment μ, this polarization is comprised of two components. One is electronic polarization leading to a permittivity ε_∞ which is approximately equal to the square of the refractive index, $\varepsilon_\infty \approx n^2$. For a given compound, ε_∞ is mostly a matter of the density, and therefore this contribution to polarization is not so different for liquid and crystalline states. The situation is different for the dipole orientation contribution to polarization, which rests on the orientational degrees of freedom of dipoles and adds the amount of $\Delta\varepsilon = \varepsilon_s - \varepsilon_\infty$, which can be much larger than ε_∞ itself. The feature that is exploited in the context of crystallization studies is that, to a very good approximation, the crystalline state does not contribute to the dielectric relaxation amplitude $\Delta\varepsilon$. With these approximations, $\Delta\varepsilon^{crystal} = 0$ and $\varepsilon_\infty^{crystal} = \varepsilon_\infty^{liquid}$, the dielectric technique is assumed to yield the volume fraction of the liquid via:

$$\frac{\upsilon^{liquid}}{\upsilon^{total}} = \frac{\Delta\varepsilon^{mixture}}{\Delta\varepsilon^{liquid}} \tag{3}$$

For liquids with moderate polarity, say $\Delta\varepsilon < \varepsilon_\infty$, Eq. 3 may serve as a good approximation to the liquid volume fraction, $\upsilon^{liquid}/\upsilon^{total}$. For materials with large dielectric constants, the situation of a partly crystallized sample is that of a mixture of a volume υ^{liquid} of liquid with dielectric constant ε_s with a volume $\upsilon^{crystal}$ with a much lower dielectric constant ε_∞. The problem inherent in this situation is that the dielectric contributions of the two distinct phases do not simply add to the total dielectric constant, ε_{mix}, observed for the mixture. Instead, the dielectric permittivity of such heterogeneous systems has to be determined by a proper mixing formula [18, 19]. One simple example is the Maxwell–Wagner–Sillars (MWS) theory [20, 21], which determines the frequency dependent permittivity of the composite, $\varepsilon_c^*(\omega)$, from those of the filler, $\varepsilon_f^*(\omega)$, and the matrix, $\varepsilon_m^*(\omega)$, for a given filler volume fraction φ and filler shape characterized by its depolarization factor n. For the static limit and designating the crystal as filler, we have the special case $\varepsilon_c^*(\omega) = \varepsilon_{mix}$, $\varepsilon_f^*(\omega) = \varepsilon_\infty$, and $\varepsilon_m^*(\omega) = \varepsilon_s$, with $\varphi = \upsilon^{crystal}/\upsilon^{total}$. For this case, the MWS relation reads:

$$\varepsilon_{mix} = \varepsilon_s \frac{[n\varepsilon_\infty + (1-n)\varepsilon_s] + \phi(1-n)[\varepsilon_\infty + \varepsilon_s]}{[n\varepsilon_\infty + (1-n)\varepsilon_s] - \phi n[\varepsilon_\infty + \varepsilon_s]} \tag{4}$$

where ε_s and ε_∞ refer to the permittivities of the pure liquid. The result is based on mean-field approximations and valid only for volume fractions $\varphi < 0.2$.

Examples of this nonlinear mixing effect are shown in Fig. 4, indicating that the deviations from the often assumed linearity are more severe for high dielectric constant liquids, and that disk-like spheroids can result in a significant reduction of the apparent crystal volume fraction relative to the actual value. For instance, for the $\varepsilon_s = 80$ and $n = 2/3$ case, a reduction of $(\varepsilon_{mix} - \varepsilon_\infty)/(\varepsilon_s - \varepsilon_\infty)$ from 1.0 to 0.8 would be interpreted as crystal volume fraction of $\varphi = 20\%$ based on linearity, whereas the MWS calculation yields $\varphi = 8\%$. Note again that more sophisticated approaches are required for accurate predictions for higher crystal content, $\varphi > 20\%$. The conclusion
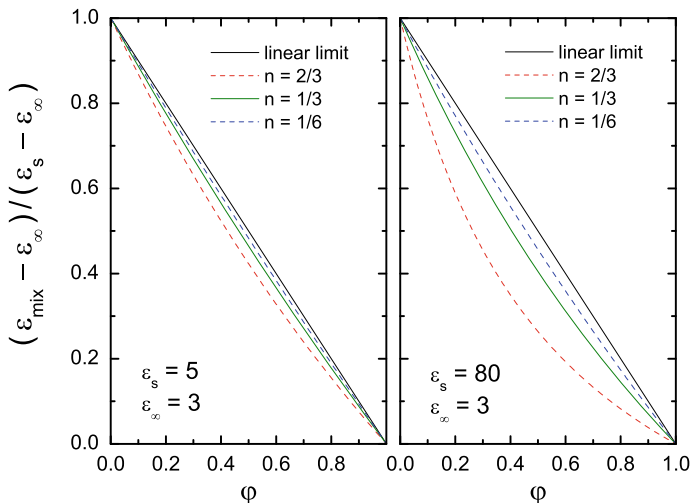
Fig. 4 Calculation of the permittivity $\varepsilon_{\mathrm{mix}}$ versus filler volume fraction φ of a crystalline filler (ε_{∞}) in a liquid matrix (ε_s) on the basis of the MWS theory. The two panels are for systems of different polarity, $\varepsilon_s = 5$ and $\varepsilon_s = 80$, as indicated, but using a common value $\varepsilon_{\infty} = 3$. The various values for n reflect different filler particle shapes: prolate (needles, $0 \le n \le 1/3$), spherical ($n = 1/3$), and oblate (disks, $1/3 \le n \le 1$) with respect to the field lines

from these considerations is that truly quantitative measures are not to be expected from dielectric relaxation data of polar liquids as regards the crystal volume fraction and thus the crystal growth dynamics, unless the proper corrections are applied. Still, broadband dielectric spectroscopy (BDS) is a powerful tool to explore crystallization behavior [22–26].

2 Experiments

The material employed for the results [16] discussed in this chapter is 4-vinyl-1,3-dioxolan-2-one or vinyl ethylene carbonate (VEC), which is also referred to as "vinyl-PC". It was supplied from Sigma-Aldrich with a nominal purity of 99% and used as received. Temperature control of samples during dielectric measurements was realized with a nitrogen gas cryostat and Novocontrol Quatro controller. Low field dielectric relaxation measurements were performed using a Solartron SI-1260 gain/phase analyzer together with a transimpedance amplifier DM-1360 for increasing current sensitivity. Such measurements were used to characterize samples in terms of α-relaxation time, glass transition temperature, the magnitude of dc-conductivity, and dielectric relaxation amplitude, $\Delta\varepsilon(T)$. The latter is needed to calibrate the sample thickness for determining the electric field for a given voltage in the context of high-field studies. For these low field experiments, a spacer-free capacitor that consists of

two parallel invar-steel plates of 18 mm diameter and fixed distance of 79 μm was used [27].

High static electric fields were applied using a Trek PZD-700 high-voltage amplifier which boosts the generator voltage of the Solartron SI-1260 by a factor of 200. The current was detected via the voltage drop across an RC-shunt, which is connected to the analyzer via a buffer amplifier and a dc-blocking capacitor with $C_0 = 220$ nF. The buffer amplifier is meant to protect the analyzer from sample failure, as it tolerates voltages up to 500 V_p without time limit. With this system, the dielectric response of the sample can be measured for frequencies between 1 Hz and 100 kHz. The capacitor cell used for high-field experiments consists of two spring-loaded polished stainless-steel disks (17 and 20 mm diameter), separated by a Teflon ring of 25 μm thickness. The Teflon ring leaves an inner area of 14 mm diameter which is filled with the sample.

The nominal electrode separation of the high-field cell is defined by the 25 μm thickness of the Teflon spacer, but the actual electrode distance could be different. Uncertainties in the electrode separation d will translate into uncertainties in the magnitude of the dc bias field $E = V/d$. The actual electrode separation d can be determined from the ratio of ε' (at $\nu = 10$ kHz) measured in the high-field cell and invar-steel cell, the latter serving as reference value because its geometry is well defined. This approach provides electric fields with an accuracy of about $\pm 5\%$. The kinetics of crystallization was monitored on the basis of changes in the dielectric response of the sample at a fixed frequency of $\nu = 10$ kHz, with or without the presence of a dc bias field, in time steps of 5 seconds. The amplitude (RMS) of the ac measuring field was set to 20% of the applied dc bias field in each high-field experiment. Therefore, all ac field amplitudes result in responses within the linear regime. Further details can be found elsewhere[16].

A variety of protocols have been employed regarding the change of temperature versus time and the range in which a high dc electric field has been applied. The different $T(t)$ and $E(t)$ schemes are identified schematically in Fig. 5, and are labeled A through D for reference used below.

All temperature profiles begin and end above the melting point T_m, and after the final melting, all field-induced changes turned out fully reversible. In these graphs, T_c refers to "crystallization temperature", i.e., the temperature at which the progress of crystallization is monitored as a function of time under isothermal conditions.

2.1 Results and Discussion

The crystallization behavior of VEC at zero electric field is illustrated in Fig. 6. After melting, the permittivity was recorded during cooling at a rate of -2 K min^{-1}, and then during subsequent heating at $+0.3$ K min^{-1}. The cooling scan reveals no crystallization, as the level of $\varepsilon'(\nu = 10$ kHz) follows the expected $\varepsilon_s \propto 1/T$ behavior for $T > 195$ K, while the decrease at lower temperature is the result of the relaxation time, τ_α, exceeding the reciprocal test frequency of 10 kHz.
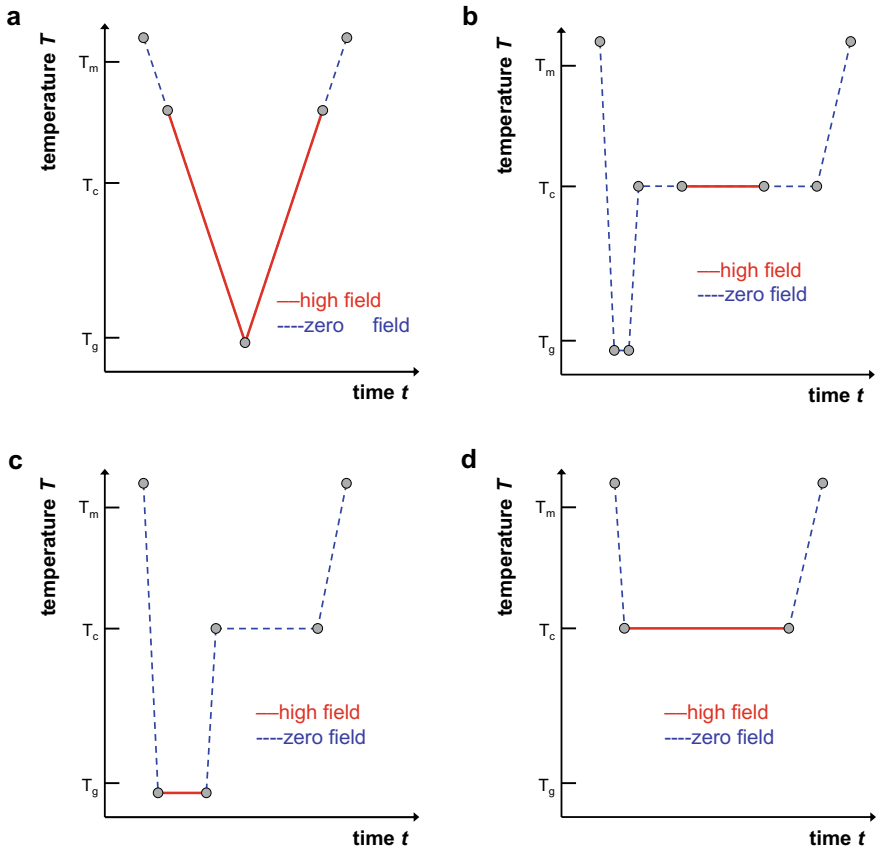
Fig. 5 Schematic representation of the temperature protocols used in the high-field experiments, with the red solid lines indicating the segments for which the sample was subject to high electric fields, while no bias field was applied for the dashed blue segments (see text for details). The temperatures marked are the melting temperature T_m, the crystallization temperature T_c, and the glass transition temperature T_g

Subsequent heating starting below $T_g = 171$ K yields the red curve in Fig. 6, which displays crystallization setting in as soon as the liquid state is reached at $T \approx 195$ K. Between 195 and 227 K, the heating curve remains below the cooling data, indicating that some volume fraction is in the crystalline state. At about 215 K, the value of $\varepsilon'(\nu = 10$ kHz$)$ has dropped to very near the level of ε_∞, revealing the completion of crystallization and the lack of liquid remaining in this sample.

From this heating curve, one would estimate the fastest crystal growth kinetics to be located near 210 K, where the drop of ε' is steepest. The explanation for the lack of crystallization when cooling near 210 K is that nucleation had been very ineffective at temperatures $T > 210$ K, so that there are no nuclei with critical size that grow to a considerable volume fraction. The effective crystal growth on heating is then the
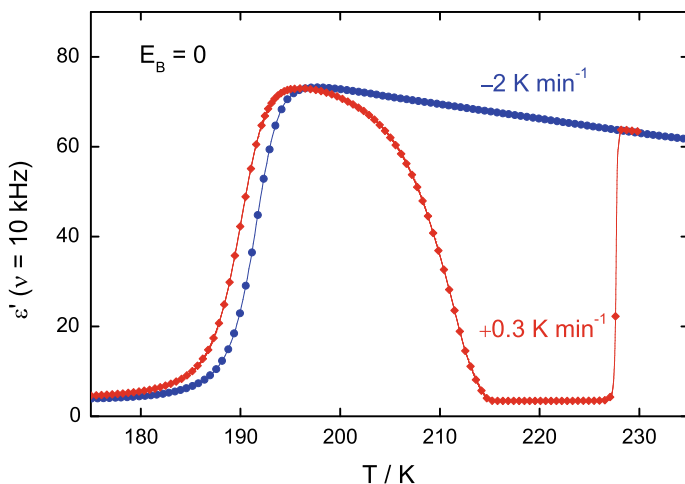
Fig. 6 Dielectric permittivity ε' measured at a frequency $\nu = 10$ kHz, for cooling (blue circles) and subsequent heating (red diamonds) of VEC. Upon heating at zero bias field, $E_B = 0$, crystallization proceeds between 195 and 215 K, followed by complete melting at $T_m = 227$ K

result of nucleation occurring near T_g. This behavior is typical for many molecular liquids and consistent with the nucleation and growth curves depicted schematically in Fig. 1, where nucleation is most effective near T_g, while growth is fastest where the structural relaxation times have reached values of order $\tau_\alpha \approx 100$ ns.

The experiment leading to the results of Fig. 6 is repeated, but with an electric bias field of $E_B = 37$ kV cm^{-1} applied continuously for $T < 210$ K on cooling and for $T < 225$ K on heating, thus using protocol "A" of Fig. 5. These high-field results are shown in Fig. 7.

As a consequence of the field, crystallization upon reentering the liquid phase is faster, and in this case practically complete at $T = 200$ K, rather than at $T = 215$ K for the zero-field case. More interestingly, there is a melting process at $T = 209$ K, whereas no such feature is visible for the zero-field experiment in Fig. 6. Above about 210 K, the liquid gained by melting at $T_{m2} = 209$ K quickly recrystallizes, and those crystals melt completely at the ordinary melting point of $T_{m1} = 227$ K, where the liquid recovers the original static dielectric constant. The latter observation implies that all field-induced changes are entirely reversible upon melting the sample.

Two conclusions can be drawn from comparing the crystallization scenarios with and without a bias field. First, crystallization kinetics of VEC are more rapid in the presence of a static electric field, and second, crystals are formed that are distinct from the ones obtained at zero field in that their melting temperature is shifted by about 20 K. Although independent evidence is not available, it seems reasonable to assume that crystals with a different melting point would have a different structure relative to the ordinary field-free case. This means that electric fields can induce polymorphism regarding crystal structures which had not been observed before for VEC.
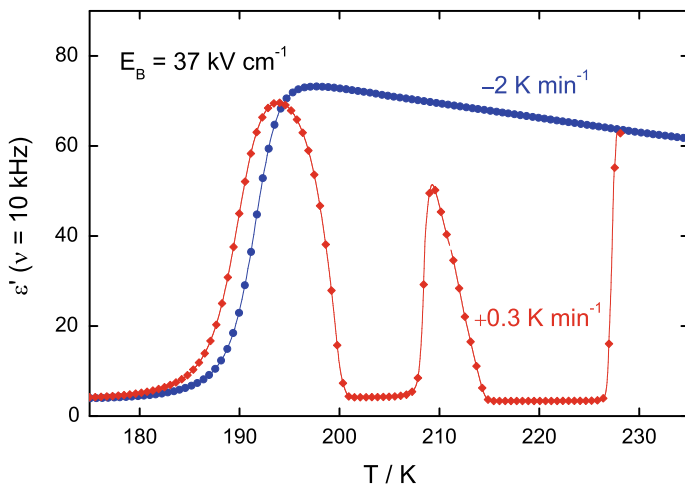
Fig. 7 Dielectric permittivity ε' measured at a frequency $\nu = 10$ kHz, for cooling (blue circles) and subsequent heating (red diamonds) of VEC while subject to an electric bias field of $E_B = 37$ kV cm^{-1}. Upon heating at this field, crystallization proceeds between 195 and 200 K, followed by partial melting at $T_{m2} = 209$ K and eventually complete melting at $T_{m1} = 227$ K

While the above observations derived from Figs. 6 and 7 clearly establish a significant field effect on crystallization outcomes, they do not distinguish which rate is mostly modified by the field, nucleation or crystal growth. For a systematic evaluation of how a field modifies the temperature-dependent rate $J(T)$ and $u(T)$, the set of protocols outlined in Fig. 8 could be used.
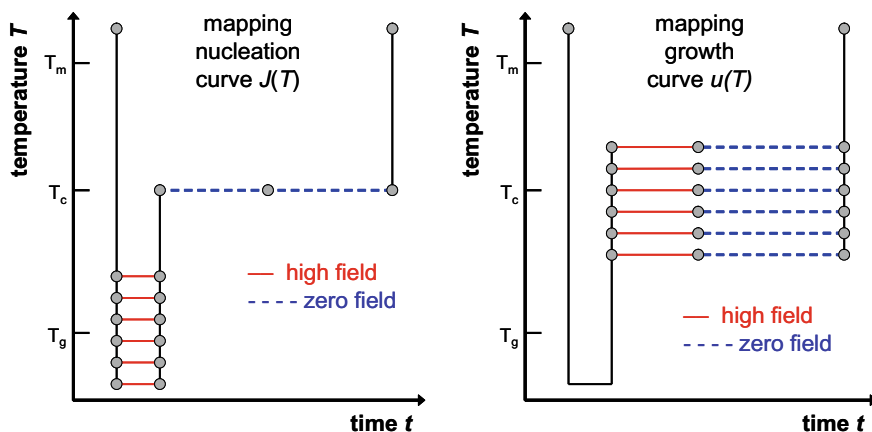
Fig. 8 Schematic representation of temperature protocols that could be used to map either the nucleation curve $J(T)$ or the crystal growth curve $u(T)$, both for a high dc electric field

For a more detailed characterization of the field effect on VEC, protocol "B" from Fig. 5 has been employed. Here, the sample is cooled to $T = T_g + 2$ K = 173 K, and the heated to $T_c = 198$ K, all without a dc field applied. As expected based on the field free results of Fig. 6, the liquid crystallizes slowly under these isothermal conditions, and according to the solid line in Fig. 9, all VEC has turned into a crystalline state after about 14,000 s. The same temperature cycle has been repeated, but after about 20% of the material had crystallized at T_c, a bias field is switched on until about 50% crystallinity is achieved, using fields of 51, 127, and 199 kV cm^{-1} in three different experiments. Clearly, the rate of crystallization is accelerated with increasing dc field. The situation in Fig. 9 is that nucleation and some growth of the ordinary zero-field crystals had occurred prior to applying the dc field, such that approximately 20% of the volume is crystalline. Therefore, the faster crystallization could be accelerated crystal growth of already existing nuclei or a high rate of nucleation, or both.

Interestingly, when the field is switched off at the point at which about half the volume is crystalline, i.e., $\varepsilon'(\nu = 10$ kHz$) \approx 30$ in Fig. 9, the crystallization rate does not return to the much slower level that prevailed before applying the field. This could be seen as consistent with field-induced nucleation at $T = T_c$, rather than field controlled growth rates of existing crystallites.

Following the isothermal scans at T_c for various fields shown in Fig. 9, a temperature scan from T_c to $T > T_m$ was performed for each of the four field cases, and these results are compiled in Fig. 10. As for the case of using protocol "A" of Fig. 5,
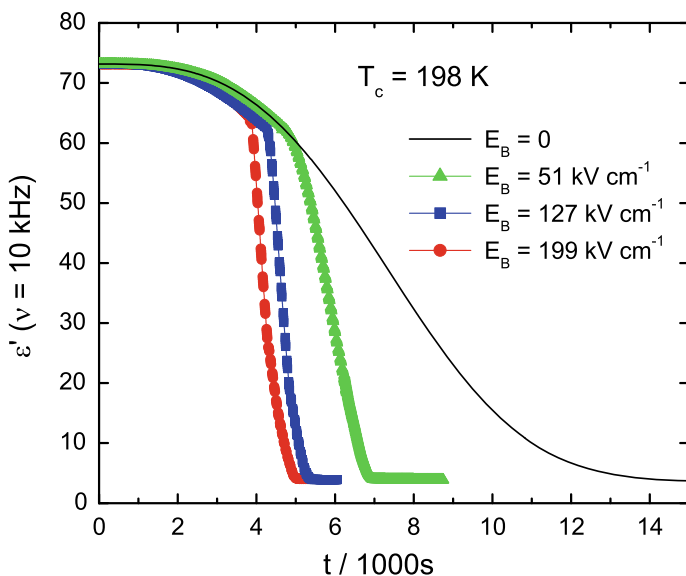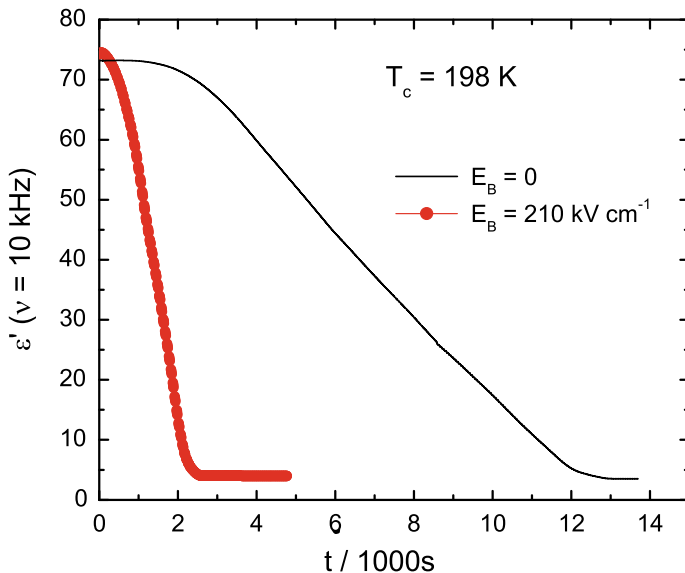

Fig. 9 Dielectric permittivity ε' measured at a frequency $\nu = 10$ kHz, measured isothermally at T_c = 198 K using the protocol "B" of Fig. 5. For each of the four separate experiments, the indicated field was applied when ε' reached 20 % of ε_s, and removed again when ε' reached 50% of ε_s
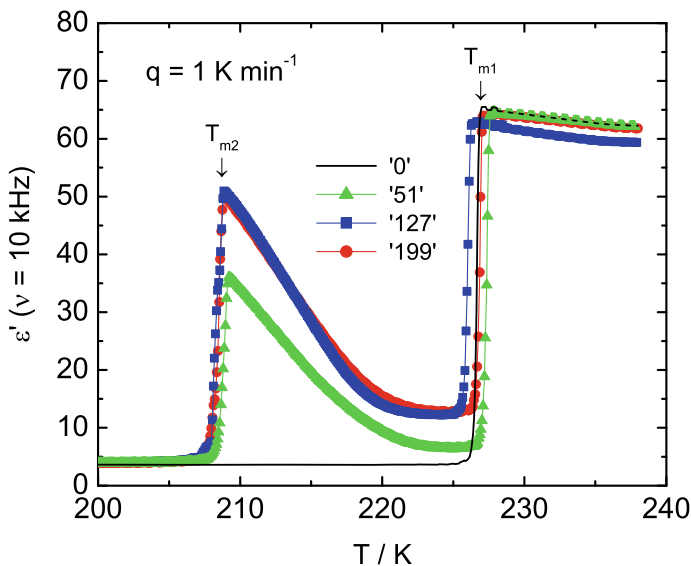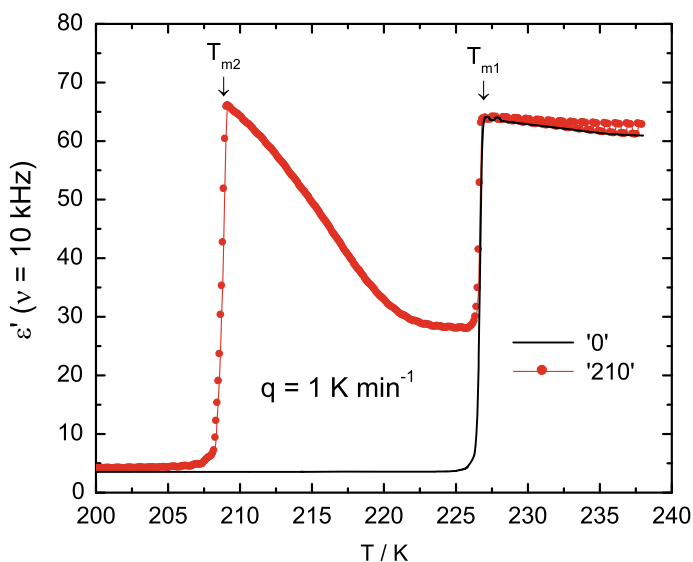
Fig. 10 Dielectric permittivity ε' measured at a frequency $\nu = 10$ kHz, recorded during heating at a rate of $q = 1$ K min^{-1} from $T_c = 198$ K to $> T_m$ without the presence of a static field. These scans are performed directly following the respective measurement of Fig. 9, labeled using the value of the previously applied field in units of kV cm^{-1}

again a melting at 209 K is observed, but because that melting step does not reach the value of ε_s, it is reasonable to conclude that a large volume fraction was occupied by the field-induced crystal type that melts at $T_{m2} = 209$ K, while approximately the amount that crystallized prior to applying the field in Fig. 9 remained the ordinary crystal type that then melts at $T_{m1} = 227$ K. As a result of these existing nuclei, the liquid formed by melting at T_{m2} quickly crystallizes to convert most of the volume to the ordinary crystal type before the temperature reaches T_{m2}.

A further test of the field effect is based on protocol "C" of Fig. 5, where a dc field is applied only at temperatures near the glass transition, namely at $T = T_g + 2$ K $= 173$ K, where structural mobility is strongly inhibited. Applying a field of 210 kV cm^{-1} at 173 K for one hour has a considerable impact on the crystallization rate that is then observed at $T_c = 198$ K without a dc field. This is demonstrated by the symbols in Fig. 11, when comparing with the solid line that is measured following the same temperature protocol but without subjecting the sample to a high electric field. After field treatment near T_g, the crystallization rate at T_c is about five times faster than the zero-field case. Based on the ε' values at $t = 0$ in both cases, i.e., with and without applying a field near T_g, practically no crystal growth has occurred prior to reaching T_c.

As before, temperature scans from T_c to $> T_m$ are performed in order to assess the melting behavior of the two crystalline samples obtained after completing the time scans of Fig. 11. Expectedly, the $E_B = 0$ case remains crystalline, i.e., $\varepsilon'(\nu = 10$ kHz$)$

Fig. 11 Dielectric permittivity ε' measured at a frequency $\nu = 10$ kHz, measured isothermally at $T_c = 198$ K using the protocol "C" of Fig. 5, annealing the sample for 1 hour at $T_g + 2$ K = 173 K while a field of 210 kV cm^{-1} or zero field was applied. The sample was not subject to a dc field at other temperatures, $T > 173$ K

$\approx \varepsilon_\infty$, until the temperature reaches $T_{m1} = 227$ K, where the entire material melts, see Fig. 12. The interesting feature of the high-field counterpart is that it reveals not only some melting at T_{m2}, but the liquid signal (ε_s) is recovered entirely at T_{m2}. This implies that the field-induced crystal structure (type 2) had been nucleated in a highly selective fashion, whereas the volume fraction of the ordinary crystal (type 1) had to be negligible. The observation in Fig. 12 that the liquid crystallizes effectively at temperatures exceeding T_{m2} indicates that some nucleation of type 1 crystals occurred even in the presence of the high-field applied in the very viscous regime. In the absence of such type 1 nuclei, the crystallization rate should be practically zero.

The question remains whether the VEC sample can be crystallized entirely into the new type 2 polymorph, such that no further crystallization sets in after melting at the lower $T_{m2} = 208$ K. As indicated above, this requires avoiding temperatures at which the type 1 crystal nucleation is effective. To this end, we follow protocol "D" of Fig. 5, where the temperature never dips below T_c after melting. In the absence of a dc field, it is observed that holding the sample at $T_c = 198$ K for 15,000 s (4.2 h) still does not reveal any onset of crystallization. This shows that the nucleation curve $J(T)$ does not extend into the T_c range, because the zero-field crystallization rate at T_c was considerable after nucleating at lower temperatures, see Figs. 6, 9, and 11. This absence of crystallization at T_c for protocol "D" at zero field can be seen as solid line in Fig. 13. By contrast, applying a dc field at T_c generates relatively rapid

Fig. 12 Dielectric permittivity ε' measured at a frequency $\nu = 10$ kHz, recorded during heating at a rate of $q = 1$ K min^{-1} from $T_c = 198$ K to $> T_m$ without the presence of a static field. These scans are performed directly following the respective measurement of Fig. 11, labeled using the value of the previously applied field in units of kV cm^{-1}
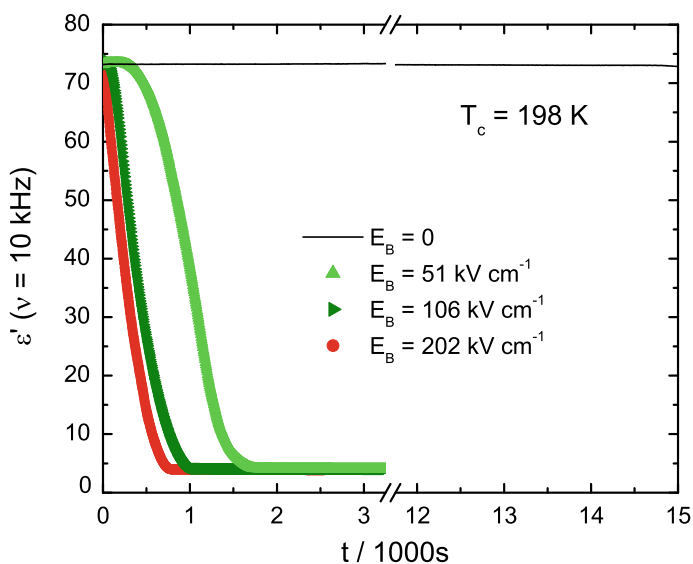
Fig. 13 Dielectric permittivity ε' measured at a frequency $\nu = 10$ kHz, measured isothermally at $T_c = 198$ K using the protocol "D" of Fig. 5, where the sample was not taken below T_c. Different symbols are for different amplitudes of the dc field E_B as indicated, while the solid line is for the zero-field case. Note the break in the time axis
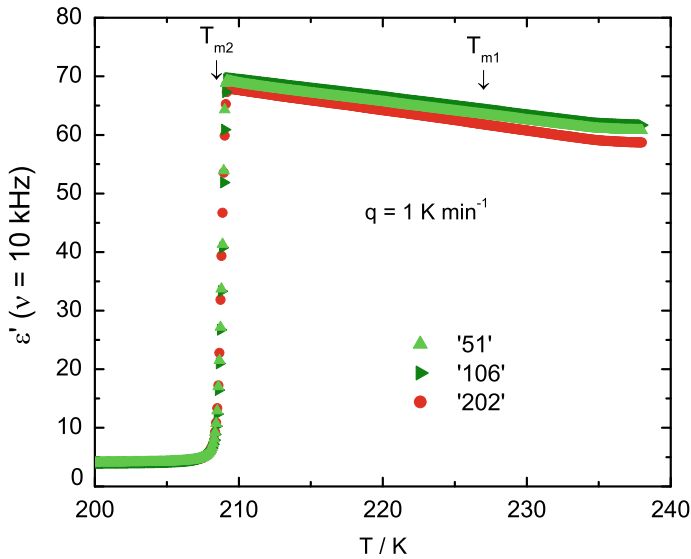
Fig. 14 Dielectric permittivity ε' measured at a frequency $\nu = 10$ kHz, recorded during heating at a rate of $q = 1$ K min^{-1} from $T_c = 198$ K to $> T_m$ without the presence of a static field. These scans are performed directly following the respective measurement of Fig. 13, labeled using the value of the previously applied field in units of kV cm^{-1}

crystallization, within about 1500 s for any of the three fields used, see symbols in Fig. 13.

The results of the temperature up scan following the crystallization measurements of Fig. 13 are shown in Fig. 14. Regardless of field amplitude, the curves clearly show that the samples convert from 100% crystalline to fully liquid at $T_{m2} = 208$ K and that there is no discernable crystallization occurring at temperatures $T > T_{m2}$. Accordingly, the curves are featureless at the ordinary melting temperature T_{m1}. This is a strong indication of the complete absence of type 1 crystal nuclei in the course of this protocol "D" of Fig. 5.

The evidence presented above provides information on how a high dc field affects the nucleation, $J(T)$, and growth, $u(T)$, curves relative to the typical zero-field case outlined in Fig. 1. The results of the protocols "B", "C", and "D" of Fig. 5 demonstrate that in the presence of a high bias field, nucleation of type 2 crystals is occurring both at low temperatures near T_g and at the much higher temperature T_c, where no field-free nucleation is observed. Another way of expressing this is to state that the nucleation curve, $J(T)$, is widened considerably towards higher temperatures in the presence of an electric field. Crystal growth appears to remain ineffective at low temperatures even if a high field is applied, which is quite expected as the field has little impact on the structural relaxation time and viscosity.

Indications that static external electric fields could affect the crystallization process had been reported previously [28–30]. For example, relatively small electric fields of 2-8 kV cm^{-1} applied during the crystallization of proteins increased the nucleation and growth rate [31–33]. Electric fields have also been made responsible for shifting preference towards one polymorphic form of glycine over another when crystallized from solution [34, 35]. In terms of the origin of these field-induced effects, contributions from field-dependent thermodynamic potentials [6–8] as well as field-induced orientations have been discussed [36, 37]. In general, the detailed mechanism involved in such field effects on crystallization have not been identified [38].

In the case of crystallization from solution, e.g., water, the field effect may be indirect through structural changes in the solvent. In the present case of VEC, the situation is simpler as this is a pure substance with no significant tendency to form supermolecular structures by directional bonding (such as hydrogen bonds). VEC is a simple liquid in the sense that its high dielectric constant of about 79 (at $T = 183$ K) [39] is largely determined by the high molecular dipole moment of $\mu = 4.76$ D [40], with no indication of strong orientational dipole correlation that leads to effective dipoles larger than μ. This means that using $\mu = 4.76$ D, $E = 200$ kV cm^{-1}, and $T = 200$ K as parameters, the value of $\mu E/k_\mathrm{B}T$ will not exceed 0.1 for the experiments on VEC. Therefore, strong overall molecular orientation is not expected. The connection between net orientation, $\langle \cos\theta \rangle$, and field E is the Langevin relation which is approximately $\langle \cos\theta \rangle = a/3$ for a dipole gas, with $a = \mu E/k_\mathrm{B}T$. Regardless of these considerations, even fields as small as 37 kV cm^{-1} give rise to substantial changes in the crystallization rates and outcomes, see Fig. 7.

It is a reasonable question to ask whether the observations shown here are specific to VEC or possibly of a more general nature. VEC is a compound of a family of derivatives of propylene carbonate (PC), which are highly polar materials [41]. PC itself is a simple liquid in the sense that the Kirkwood correlation factor is near unity in the viscous regime [42], and similar behavior may be expected for its vinyl derivative VEC. Therefore, in the absence of properties that are highly particular for VEC apart from a considerable polarity, it is likely that the field effects outlined here may be found in numerous other substances. Many pharmaceutical materials have similarly high dielectric constants, and field-induced alternative crystal structures may provide materials with the same chemistry but improved shelf-life, bioavailability, and solubility [43, 44].

Other systems for which static electric fields are expected to impact crystallization outcomes and generate new polymorphs are those that already show more that one crystal structure [45] in the absence of a field. A prime example of such a case is ROY, a pharmaceutical precursor compound, 5-methyl-2-[(2-nitrophenyl)amino]-3-thiophenecarbonitrile, that is named for its red, orange, and yellow crystals. ROY is known to form 10 different crystal structures under ambient conditions [46]. Computationally, many more stable structures have been predicted [47], and chances are that some of these might be found by crystallization under the influence of static electric fields.

2.2 Summary and Conclusion

In summary, it has been demonstrated that even moderate electric fields can have a considerable impact on the crystallization outcome for a neat, simple liquid such as VEC. In this case, static fields between 37 and 200 kV cm^{-1} led to an acceleration of crystallization kinetics, largely due to the nucleation curve extending towards higher temperatures in the presence of a field relative to the zero-field case. The crystals grown while a field is applied differ from the ordinary (type 1) crystals in that they melt already at $T_{m2} = 208$ K, i.e., about 20 K below the ordinary melting point at $T_{m1} = 227$ K. The strong dependence of the nucleation curve $J(T)$ on the electric field facilitates using temperature/field protocols that produce the new (type 2) crystal polymorph in a highly selective fashion, such that the liquid will crystallize entirely into a type 2 structure.

More systematic high field studies on VEC and other polar molecular systems have the potential to reveal the microscopic and thermodynamics origins of these field effects, which can be exploited to improve crystallization outcomes in terms of changing the kinetics or tailoring crystallization towards new or away from unwanted polymorphs.

References

1. Haleblian J, McCrone W (1969) J Pharm Sci 58:911
2. Lendlein A, Kelch S (2002) Angew Chem 41:2034
3. Novoa JJ, Braga D, Addadi L (eds) (2008) Engineering of Crystalline Materials Properties. Springer, Berlin
4. Myerson A (2002) Handbook of Industrial Crystallization. Butterworth Heinemann, Boston
5. Schmelzer JWP, Abyzov AS, Fokin VM, Schick C, Zanotto ED (2015) J Non-Cryst Solids 429:24
6. Kashchiev D (1972) J Cryst Growth 13–14:128–130
7. Kashchiev D (1972) Philos Mag.25:459–470
8. Isard JO (1977) Philos Mag 35:817–819
9. Ziabicki A, Jarecki L (1996) Macromol Symp 104:65–87
10. Richert R (2018) J Chem Phys 149:240901
11. Uhlmann DR, J. Non-Cryst Solids (1972) 7:337
12. Schmelzer JWP (2008) J Non-Cryst Solids 354:269–278
13. Ngai KL, Magill JH, Plazek DJ (2000) J Chem Phys 112:1887–1892
14. Ediger MD, Harrowell P, Yu L (2008) J Chem Phys 128:034709
15. Fröhlich H (1958) Theory of dielectrics. Clarendon, Oxford
16. Adrjanowicz K, Paluch M, Richert R (2018) Phys Chem Chem Phys 20:925
17. Jensen MH, Alba-Simionesco C, Niss K, Hecksher T (2015) J Chem Phys 143:134501
18. Scaife BKP (1989) Principles of Dielectrics. Clarendon Press, Oxford
19. Kremer F, Schönhals A (eds) (2002) Broadband Dielectric Spectroscopy. Springer, Berlin

20. Wagner KW (1914) Arch Electrotech 2:371
21. Sillars RW (1937) J Inst Electr Eng 80:378
22. Massalska-Arodz M, Williams G, Thomas DK, Jones WJ, Dabrowski R (1999) J Phys Chem B 103:4197
23. Alie J, Menegotto J, Cardon P, Duplaa H, Caron A, Lacabanne C, Bauer M (2003) J Pharm Sci 93:218
24. Adrjanowicz K, Kaminski K, Wojnarowska Z, Dulski M, Hawelek L, Pawlus S, Paluch M, Sawicki W (2010) J. Phys. Chem. B 114:6579
25. Ezquerra TA, Majszczyk J, Balta-Calleja FJ, López-Cabarcos E, Gardner KH, Hsiao BS (1994) Phys Rev B 50:6023
26. Adrjanowicz K, Grzybowski A, Grzybowska K, Pionteck J, Paluch M (2014) Cryst Growth Des 14:2097
27. Wagner H, Richert R (1999) J Phys Chem B 103:4071
28. Evans GJ (1984) Mat Lett 2:420
29. Kotsuki K, Obata S, Saiki K (2014) Langmuir 30:14286
30. Parks C, Koswara A, Tung H-H, Nere N, Bordawekar S, Nagy ZK, Ramkrishna D (2017) Cryst Growth Des 17:3751
31. Taleb M, Didierjean C, Jelsch C, Mangeot JP, Capelle B, Aubry A (1999) J Cryst Growth 200:575
32. Hammadi Z, Veesler S (2009) Prog Biophys Mol Biol 101:38
33. Nanev CN, Penkova A (2001) J Cryst Growth 232:285
34. Aber JE, Arnold S, Garetz BA, Meyerson AS (2005) Phys Rev Lett 94:145503
35. Di Profio G, Reijonen MT, Caliandro R, Guagliardi A, Curcio E, Drioli E (2013) Phys Chem Chem Phys 15:9271
36. Gattef E, Dimitriev Y (1979) Phil Mag B 40:233
37. Gattef E, Dimitriev Y (1981) Phil Mag B 43:333
38. Gutzow I, Schmelzer JWP (2013) The vitreous state: thermodynamics, structure, rheology, and crystallization. Springer, Heidelberg
39. Young-Gonzales AR, Adrjanowicz K, Paluch M, Richert R (2017) J Chem Phys 147:224501
40. Jedrzejowska A, Wojnarowska Z, Adrjanowicz K, Ngai KL, Paluch M (2017) J Chem Phys 146:094512
41. Jedrzejowska A, Ngai KL, Paluch M (2016) J Phys Chem A 120:8781
42. Simeral L, Amey RL (1970) J Phys Chem 74:1443
43. Lee AY, Erdemir D, Myerson AS (2011) Annu Rev Chem Biomol Eng 2:259
44. Bauer J, Spanton S, Henry R, Quick J, Dziki W, Porter W, Morris J (2001) Pharm Res 18:859
45. Bernstein J (2002) Polymorphism in Molecular Crystals. Oxford Univ. Press, New York
46. Yu L (2010) Acc Chem Res 43:1257
47. Habgood M, Sugden IJ, Kazantsev AV, Adjiman CS, Pantelides CC (2015) J Chem Theory Comput 11:1957

Dynamics of Water in Partially Crystallized Solutions of Glass Forming Materials and Polymers: Implications on the Behavior of Bulk Water

Silvina Cerveny and Jan Swenson

Abstract There is no simpler compound than water. It is the most copious substance on Earth and the most important constituent for life, as we know. There is also a continuous scientific interest due to its exceptional and infrequent properties, such as a density maximum at 4 °C (at atmospheric pressure), a high specific heat capacity, and a low viscosity under high pressure, among other macroscopic properties. The origin of the unusual properties of water is evidenced at lower temperatures in the no man's land temperature region (235–150 K), where bulk water cannot remain in an amorphous state. Instead, in this region, bulk water crystallizes in a complex phase diagram with more than 16 crystalline phases. Therefore, most of the work done so far on supercooled water focuses on the investigation of the dynamics when crystallization is suppressed using different types of confinements, such as nanocavities or by mixing water with other solutes (polymers, proteins, or DNA). On the contrary, in this chapter, we will use broadband dielectric spectroscopy to analyze the dynamics of aqueous solutions and confined water when it is partially crystallized, i.e., when liquid water and ice coexist. With this technique, it is possible to obtain information about the molecular relaxations in both amorphous and crystalline phases. We have analyzed the results of this semi-crystalline water and compared them with the response of supercooled water in fully amorphous solutions. Finally, we discuss the implications of these results on the behavior of bulk water.

Keywords Supercooled water · Ice · Crystallization · Dynamic crossover · BDS · NMR

S. Cerveny (✉)
Centro de Física de Materiales (CSIC-UPV/EHU)-Material Physics Centre (MPC), Paseo Manuel de Lardizabal 5 (20018), San Sebastián, Spain
e-mail: silvina.cerveny@ehu.es

Donostia International Physics Center (DIPC), Paseo Manuel de Lardizabal 4 (20018), San Sebastián, Spain

J. Swenson
Department of Physics, Chalmers University of Technology, 412 96 Göteborg, Sweden

Abbreviation

3PG	Tri-propylene glycol
ε^*, ε', ε''	Complex permittivity, real and imaginary part
ε_0	Dielectric permittivity of the vacuum
BDS	Broadband dielectric Spectroscopy
CC	Cole-Cole equation
DSC	Differential scanning calorimetry
LDA	Low-density amorphous ice
MCM-41	Mesoporous silica material
HB	Havriliak-Negami equation
NMR	Nuclear Magnetic Resonance
PVME	Poly (vinyl methyl ether)
PVP	Poly(vinyl pyrrolidone)
T_g	Glass transition temperature
T_{crist}, t_{crist}	Crystallization temperature and crystallization time
TMDSC	Temperature-modulated DSC mode
VFT	Vogel-Fulcher-Tammann equation

1 Introduction

Water is unquestionably the most significant and studied of all liquids, but at the same time, one of the least understood. The research on the physical and chemical properties of water is very broad because water is involved in several biological and industrial processes. Water is an excellent solvent for many chemical compounds and therefore called the "universal solvent" in the sense that it dissolves more substances than any other liquid. In addition, the chemical and physical reactions important to life are produced in the cells and most of them are water mediated [1, 2]. Water in the cell is involved in digestion, photosynthesis, or respiration and therefore, it has a role either as a reactant or as a product of a reaction.

At low temperatures (between 0 and −38 °C, depending on the cooling rate and cleanness of the water), water crystallizes more commonly in a hexagonal lattice, although it can also form a large number of distinct amorphous and crystalline solid phases [3], for instance high- and low-density amorphous ices (HDA and LDA, respectively). Since at low temperatures, the rate of many deterioration reactions is low, and freezing is used for tissue and food preservation [4]. However, during freezing, water tends to crystallize, which may cause damage on the microstructure of the solute. Thus, the behavior of frozen aqueous solutions of biopolymers [5–7], food [8], animal, or vegetable cells [9, 10], etc., has been the subject of considerable investigations since it is involved in several fields of the food industry, biomedical technologies as well as in protocols of pharmaceuticals storage. In fact, the freezing of water into ice can be the origin of numerous problems when considering

biological materials. For instance, in frozen food, the increment in the concentration of water solutions that does not freeze (partial crystallization of the water causes freeze-concentration of the amorphous part of the solution) cause a reduction of the water activity [11, 12]. On the other hand, cells may be damaged by the presence of ice because it will expand and burst the cell wall destroying the tissues. In fact, the strategy of several insects, plants, or animals to overcome the problem of water crystallization in extreme environments is to use compounds in their body fluids (for instance the sugar trehalosa [13] or anti-freeze proteins [14]) to prevent crystallization. In this case, the solutes act as protection against freezing (cryoprotectant or super-cooling agents). Therefore, one strategy the nature enforces to avoid water crystallization is to mix the water molecules with some solute. Another way to avoid crystallization of water at low temperatures is to confine water in porous materials. This brings a geological perspective to the problem of water crystallization. Water is a very mobile molecule and can easily change its aggregation state (liquid, vapor, and solid) depending on temperature. This fact impacts on minerals like quartz or mineral clays since a water phase transition could affect the structure of rigid materials.

The temperature range where bulk water crystallizes is called the "no man's land" because it is inaccessible to liquid bulk water [15, 16] (although nowadays by using very fast measurements it has been possible to enter into the no man's land and study the structure of water down to 227 K [17]). This "no man's land" temperature range comprises from 150 to 235 K at ambient pressure. It has been proposed that this temperature range include a liquid–liquid critical point [16], which explains the water anomalies [18]. Above this temperature (i.e., between 235 and 273 K), water is in the supercooled state, whereas below this temperature range, water is in the glassy state (see Fig. 1). There are several structural and dynamical studies of water at low temperatures and it is not the purpose of this chapter to review all of them (there are some compressible reviews in the literature about this topic [19–23]). The purpose here is instead to provide a physical picture of the dynamics of water in solutions when water partially crystallizes.

It is well-known that the relaxation data for confined supercooled water exhibits a dynamic crossover in its temperature dependence [22, 24]. This dynamic crossover is not only of essential importance for understanding the dynamic properties of supercooled water in solutions or under confinement, it is also of importance for understanding the most possible relaxation scenario for supercooled bulk water [23]. Bulk water behaves as a fragile liquid down to about 235 K, where crystallization occurs. A fragile glass-forming liquid exhibits a highly non-Arrhenius temperature
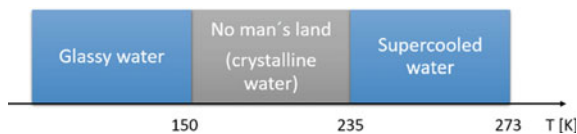
Fig. 1 States of water at different temperatures. In the temperature region between 150 and 235 K, water is crystalline and no bulk liquid is possible

dependence, typical for ionic and van der Waals systems, whereas a strong super-cooled liquid shows a temperature dependence close to the Arrhenius law, which is typical for materials with strong (commonly covalent) bonds forming a network structure. It is well-established that: (1) water above approximately 233 K is one of the most fragile liquids studied [25] and (2) the temperature dependence of its viscosity (or structural relaxation time) seems to follow a power law diverging [26] at about 228 K. Therefore, a glass-transition temperature, T_g, substantially lower than 228 K can be obtained only if the fragile behavior above 233 K changes to a stronger Arrhenius-like temperature dependence slightly below 233 K. This is the reason why it has been proposed that supercooled water undergoes a fragile-to-strong (FS) transition around 228 K [25].

In fact, confined water (in hard- or soft- confinement systems) shows a similar dynamic crossover in a temperature range between 180 and 220 K depending on the system and experimental technique [22]. However, the origin of this dynamic crossover and its relation to bulk water is a subject of controversial discussions. Some studies indicate that the crossover is due to the existence of a fragile-to-strong transition at about 225 K, related to a transition from a high-temperature high density liquid (HDL) to a low-temperature low density liquid (LDL) [27]. Other studies attributed this dynamic crossover (sometimes observed at lower temperatures) to finite-size effects [28, 29], where the low temperature relaxation (below the crossover temperature) represents a local relaxation (β-relaxation) of the confined water molecules [24]. Lately, it has been proposed that the dynamical behavior changes in response to fractional freezing of the confined water [30–33]. In this chapter, we are interested in understanding the origin of a similar crossover in water solutions (i.e., in so-called soft confinement systems), and how it is affected by a partial crystallization of the water.

In this chapter, we are first reviewing some early work in this field and thereafter, we are providing new experimental results on partial crystallization of water in solutions of some polymers and liquids. We analyze the impact of crystallization temperature and time on the glass transition of the solutions by calorimetric measurements. Then, we are discussing the dynamics of amorphous water in solutions as seen by broadband dielectric spectroscopy. We elucidate how the dynamical behavior of the water is altered both during and after isothermal crystallization. Finally, we provide implications of these results on the behavior of bulk water.

2 Experimental Section

2.1 Calorimetric Experiments

The DSC measurements described in this chapter were performed using a DSC Q2000 from TA Instruments in both standard and temperature-modulated (TMDSC) modes. In the TMDSC mode, a periodic temperature perturbation is superimposed on a linear

heating or cooling. Samples weighing about 10–15 mg were prepared in hermetic pans. Standard DSC experiments were performed at heating and cooling rates of 5–10 K/min as indicated in each experiment. Modulated experiments were performed with a 0.4 K temperature amplitude, 60 s modulation period, and 5 K/min underlying heating rate. A helium flow rate of 25 mL/min was used all throughout.

2.2 Dielectric Experiments

Broadband dielectric spectroscopy (BDS) is a powerful technique to evaluate the dielectric properties of aqueous solutions and to assess the molecular dynamics on various time and length scales. In particular, using the changes in the dielectric permittivity, BDS can probe phase transformations. During crystallization of water, the dielectric permittivity decreases from that of liquid water (~80) to that of ice (~3.2).

To measure the complex dielectric permittivity, $\varepsilon^*(\omega) = \varepsilon'(\omega) - i\,\varepsilon''(\omega)$, we combined different dielectric techniques to obtain a wide spectral range (0.1 Hz–20 GHz). For the frequency range from 10^{-1} to 10^6 Hz, we used a Novocontrol Alpha Analyzer. The sample thickness for all measurements was 0.1 mm and the sample diameter was 30 mm.

To analyze the complex permittivity (ε^*), fitting of the imaginary (ε'') component was performed by the use of the phenomenological Havriliak–Negami function

$$\varepsilon^*(\omega) = \varepsilon'(\omega) + i\varepsilon''(\omega) = \varepsilon_\infty + \frac{\Delta\varepsilon}{\left[1 + (i\omega\tau)^\alpha\right]^\beta} \tag{7.1}$$

where $\Delta\varepsilon$ is the dielectric strength, ε_∞ the unrelaxed value of the dielectric constant, τ is the relaxation time, and $\omega = 2\pi f$ is the angular frequency. In Eq. 7.1, α and β are shape parameters ($0 < \alpha, \alpha\beta < 1$) which describe the symmetric and the asymmetric broadening of the equivalent relaxation time distribution function. By setting $\beta = 1$, a symmetrical function is obtained (Cole-Cole (CC) function), which is widely used to describe secondary relaxations in glassy materials [34]. At low frequencies, conductivity effects dominate and to account for that a power law term was added to the sum of CC and HN functions.

3 The Glass Transition Temperature and Cold Crystallization in Water Solutions of Synthetic Polymers

Differential scanning calorimetry (DSC) is a technique that measures the heat flow as a function of temperature or time at a given cooling or heating rate and it allows analyzing two essential characteristics of water solutions. From one side, the glass

transition temperature (T_g) can be determined, and on the other side, crystallization of water at sub-zero temperatures can be detected. At a given cooling rate and depending on water content, crystallization of water can be suppressed for all temperatures. This is the case for solutions with water content lower than 25 wt% where crystallization of water is inhibited on both cooling and heating cycles. However, at higher water content, crystallization on cooling or on heating (the so-called cold crystallization) can be detected. In general, cold crystallization occurs in solutions when the water content remains above 25 wt%.

Figure 2 shows a typical DSC trace for solutions of tri-propylene glycol (3PG) [35] at different water contents: $c_w = 0$ wt% (dry 3PG, Fig. 2a), $c_w = 10$ wt% (Fig. 2b) and $c_w = 50$ wt% (Fig. 2c). For $c_w = 0$ and 10 wt%, the samples are amorphous at all temperatures, i.e., no crystallization is observed on cooling or on heating cycles (Fig. 2b). For $c_w = 50$ wt%, the sample does not show crystallization on cooling at a fast rate but cold crystallization in the heating cycle is observed (Fig. 2c) followed by a broad melting in the temperature range between 245 and 260 K. This is also the case for $c_w = 40$ wt%. For all the water contents analyzed, the solutions show a glass transition (T_g). Figure 2d shows the effect of water content on the glass transition
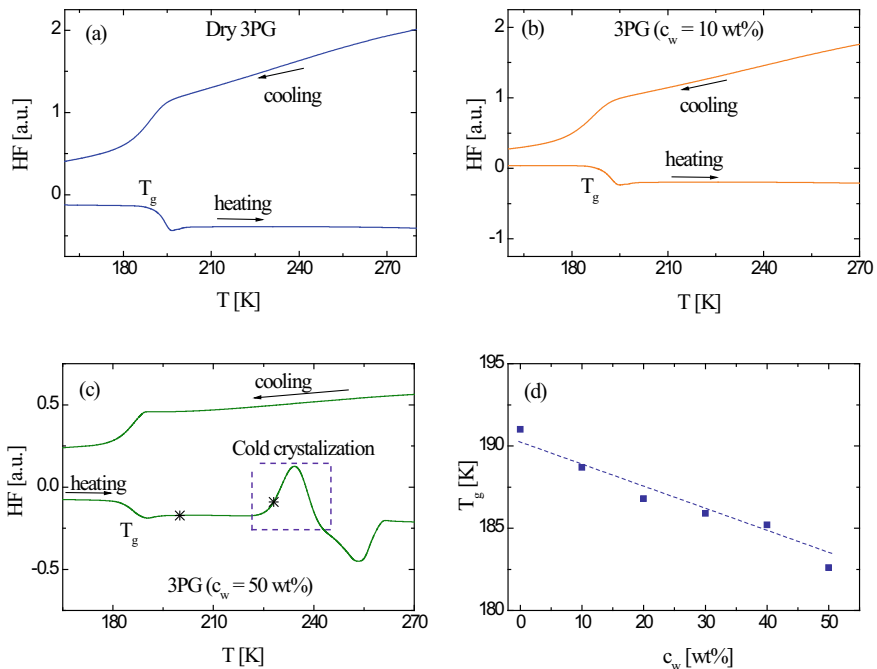
Fig. 2 Heat flow as a function of the temperature for 3PG-water solutions at a heating rate of 10 K/min. In **a** and **b**, samples are amorphous at all temperatures whereas in **c**, cold crystallization is observed. **d** Temperature dependence of the glass transition as a function of the water content. In **c**, the symbol * represents two crystallization temperatures. For the lower T_{cryst}, the crystallization proceeds slowly whereas for the high T_{cryst} the crystallization is produced much faster

temperature for these solutions including the dry oligomer. A linear dependence is observed up to $c_w = 50$ wt% with a maximum variation of T_g of 8 K between the dry and the 50 wt% sample. This variation indicates that water acts as plasticizer of 3PG molecules. Plasticization [36] increases the flexibility of the molecules (whether synthetic or biological molecules), allowing internal motions as well as shielding of solute-solute interactions. Because of plasticization, both the viscosity and glass transition temperature of the compounds decrease compared with those values of the dry system.

In the following, we analyze the variation of the T_g value under isothermal crystallization. In this case, the measurements were performed in the temperature-modulated mode because it allows separation of overlapping transitions and more accurate measurements of initial crystallinity. In this case, a different heating rate (5 K/min) compared with the measurements showed in Fig. 2 was used. Water crystallization takes place above T_g on the heating cycle due to the presence of some nucleation, which grows below the melting region during the cooling cycle. If the crystallization temperature (T_{cryst}) is close to T_g, the crystallization occurs more slowly than at higher temperatures.

The isothermal experiments were carried out over a series of crystallization temperatures (T_{cryst}) and crystallization times (t_{cryst}) in order to obtain different amounts of ice in each sample (see Table 1). Figure 3 shows the reversing heat flow for 3PG with a water content of 50 wt% at different T_{cryst} and t_{cryst} as indicated in the figure. The first scan (red trace in Fig. 3) shows the T_g value before crystallization. After this scan, the sample was maintained at a certain temperature (T_{cryst}) during some time (t_{cryst}) also indicated in the figure. After this time, we have measured again the glass transition of the semi-crystalline sample (green trace in Fig. 3) as well as the melting of the ice produced at higher temperatures. Table 1 shows the values of T_g for the first and second scans (i.e., before and after crystallization.

From Fig. 3, we observe that when T_{cryst} is very low (i.e., T_{cryst} is approximately $20°$ above the T_g value), the crystallization proceeds slowly and the T_g value does not appreciable change before and after crystallization (the portion of the water crystallized is very small). Accordingly, in the second scan, this small fraction of water is not participating in the glass transition phenomenon, and therefore the heat flow step decreases. However, in the case of the samples crystallized at the highest temperature (228 K for 50 wt% or 223 K for 40 wt%), the T_g variation between the amorphous and semi-crystalline states is about $2–4°$ (and much bigger for PVME or PVP solutions). If an appreciable part of the water crystallizes, the residual solution becomes freeze-concentrated and therefore the glass transition temperature increases. We will get back to these results after we have analyzed the dynamics of water in amorphous and semi-crystalline environments.

In addition to 3PG solutions, we also analyze the response of two polymers: poly (vinyl methyl ether) (PVME) and poly (vinyl pyrrolidone) (PVP) in solution with $c_w = 50$ and 55 wt%, respectively. As for 3PG, PVME shows a linear T_g concentration dependence whereas PVP shows a stronger T_g concentration dependence, as seen in Fig. 4.

Table 1 The glass transition temperature (T_g) for different solutions in the amorphous and semi-crystalline state

Sample	T_{cryst} [K]	T_{cryst} [h]	$T_{g,onset(before crystallization)}$ [K]	$T_{g,onset(after crystallization)}$ [K]	DTg [K]
3PG ($c_w = 50$ wt%)	200	8	184.1	184.4	0.3
3PG ($c_w = 50$ wt%)	201	4	184.3	184.9	0.6
3PG ($c_w = 50$ wt%)	228	2	184.5	188.2	3.7
3PG ($c_w = 40$ wt%)	203	8	186.5	186.5	0
3PG ($c_w = 40$ wt%)	218	8	187.1	189.5	2.4
3PG ($c_w = 40$ wt%)	223	6	186.7	189.9	3.2
PVME ($c_w = 50$ wt%)	210	1	190	190.5	0.5
PVME ($c_w = 50$ wt%)	210	8	190	199.5	9.5
PVP ($c_w = 55$ wt%)	215	2.5	204.4	205.9	1.5
PVP ($c_w = 55$ wt%)	215	8	204.4	221	16.6

$T_{g,onset(before crystallization)}$ and $T_{g,onset(after crystallization)}$ represents the T_g values in the amorphous and semi-crystalline states, respectively. ΔT_g represents the difference between these two values. Samples were crystallized at a temperature of T_{cryst} during t_{cryst}
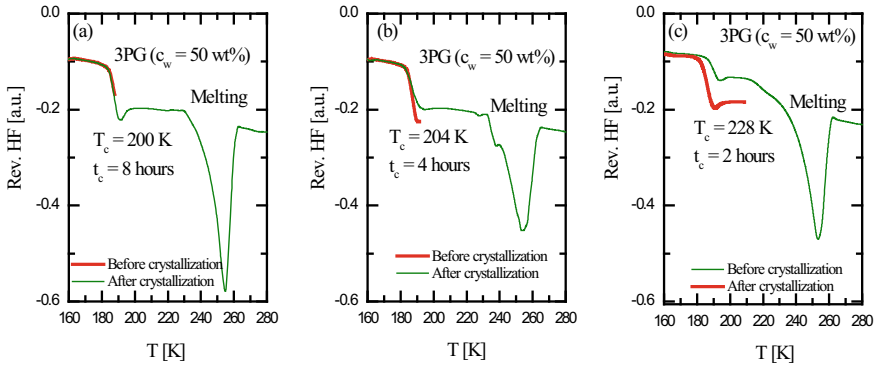
Fig. 3 a–c TMDSC data measured during heating at 5 K/min as a function of the temperature for 3PG solutions ($c_w = 50$ wt%) (see text for details). The red trace represents the first scan (before crystallization) whereas the green trace represents the second scan (after crystallization)
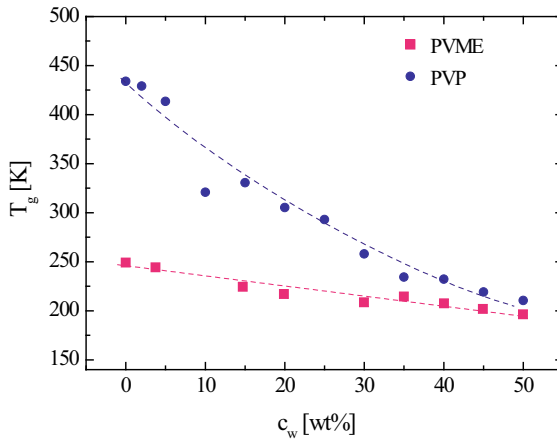
Fig. 4 Concentration dependence of the glass transition temperature (T_g) for poly (vinyl methyl ether) and poly (vinyl pyrrolidone). Adapted from Refs. [37] and [38] with permission

As a conclusion of this section, we have observed that the glass transition temperature of the partially crystallized solution changes or remains the same depending on the crystallization temperature: the lower T_{cryst} and t_{cryst} the minor change in T_g.

4 The Dynamics of Water in Amorphous Water Solutions at Low Temperatures by BDS

In this section, we review the dynamics of the aqueous solutions showed in Fig. 2 as seen by broadband dielectric spectroscopy when water remains amorphous for all temperatures. Isothermal data of the dielectric loss ε'' of amorphous 3PG–water mixtures are shown in Fig. 5a at different temperatures [35]. The dielectric response of these amorphous mixtures shows a prominent peak due to the reorientation of water molecules (water relaxation in Fig. 5b). In addition, a slower and weaker relaxation is also observed (α-relaxation in Fig. 5b). Therefore, the response of the amorphous samples can be described using a Havriliak–Negami equation to fit the α-relaxation and a Cole–Cole equation to fit the water relaxation in the sub-T_g range.

The relaxation times obtained from the fittings are shown in Fig. 6a for the sample 3PG with $c_w = 50$ wt%. A comparison with other water concentrations is also shown in Fig. 5b and c. As seen in Fig. 6a, the origin of the slow relaxation is the glass transition related structural α-relaxation of the solution, due to its Vogel–Fulcher–Tammann (VFT) temperature dependence and the fact that it reaches a time scale of about 100 s at the calorimetric T_g, as expected for the α-relaxation. The fast process (water relaxation in Figs. 5b and 6c) is displayed below T_g and shows an Arrhenius temperature dependence. This process is local in character, and therefore designated
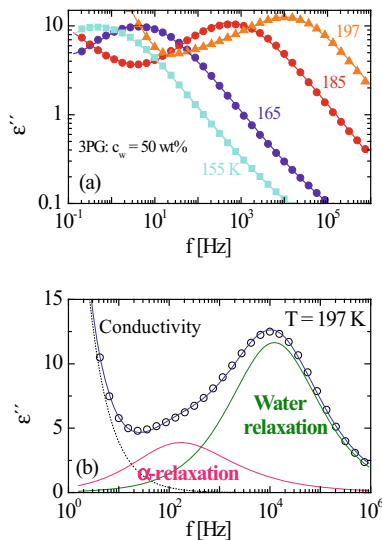
Fig. 5 **a** Loss component, ε'', of the complex permittivity, $\varepsilon^*(f)$, of an amorphous 3PG—water solution with $c_w = 50$ wt% at different temperatures. **b** Same as in (**a**) at T = 197 K, where both the α-relaxation and the water relaxation are observed. The lines through the data points correspond to least-squares fits to a superposition of a Havriliak–Negami and a Cole–Cole function for the α-relaxation and water relaxation, respectively
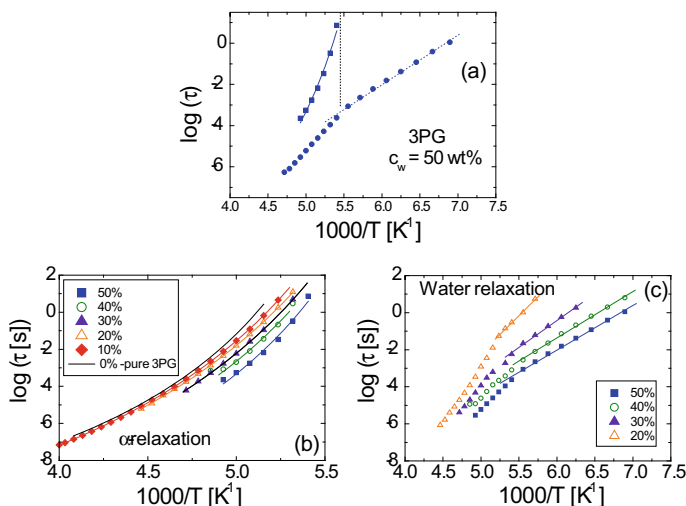
Fig. 6 Temperature dependences of the relaxation times for 3PG aqueous solutions at different water contents. **a** 3PG with 50 wt% of water in the temperature range where water is amorphous. **b** Relaxation times corresponding to the α-relaxation of the solutions that becomes faster at higher water contents. The solid lines are fits of the VFT equation to the data. **c** Relaxation times corresponding to the water process. The results of the Arrhenius fittings to the data are shown with solid lines. At temperatures close to the calorimetric T_g values there is a crossover in the temperature dependence of the water relaxation to a high-temperature non-Arrhenius behavior

as a β-relaxation. The intensity of this β-relaxation increases rapidly with increasing water concentration [35], and therefore this relaxation is mainly caused by water.

The main result of Fig. 5, with a significant relevance for bulk water, is the analysis of the temperature dependence of the relaxation times at high water content (but when water still remains amorphous). In this case, the relaxation times become similar to those in other solutions (i.e., this water relaxation is independent of the solute). For all the solutions analyzed, the temperature dependence of the relaxation time shows a crossover from a low-temperature Arrhenius behavior to a high-temperature non-Arrhenius behavior. The presence of this crossover has been observed in quite a lot of aqueous solutions and its origin has been controversially discussed in the literature [22, 29]. We will get back to this crossover and its origin latter in Sects. 7–9

The scenario here analyzed for 3PG solutions (i.e., the presence of two relaxations: a slower one associated with the α-relaxation of the solute and a faster one related to the relaxation of water molecules in the solution) is very similar to that found in several aqueous solutions previously analyzed in the literature [39–43] and also for the PVME–water solutions here and previously [37] analyzed. The condition to detect this behavior in any aqueous solution has been related to the variation of the glass transition temperature with the water concentration [44, 45]. When the solutes show a linear concentration dependence of T_g with the water concentration, as that shown in Fig. 4 for PVME (with a difference between the T_g of dry and wet solutes of
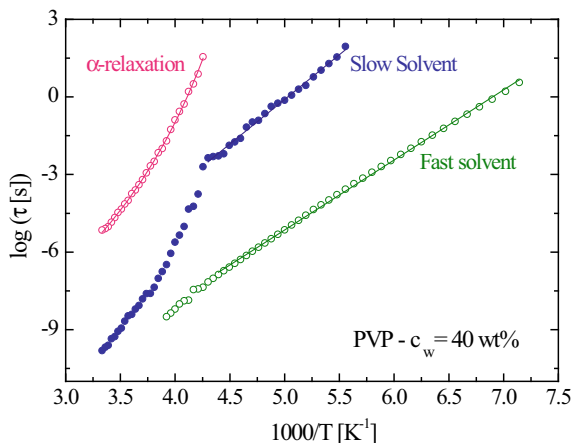
Fig. 7 Temperature dependences of the relaxation times for PVP aqueous solutions with 40 wt% of water in the temperature range where water is amorphous. The straight lines below T_g represent fits to the experimental data by the Arrhenius equation, whereas above T_g full lines represent VFT-fits to the experimental data. Adapted from Ref. [45] with permission

about 10 K), it is possible to observe a single water relaxation with the characteristics discussed above.

Different to PVME or 3PG solutions, PVP solutions show a different dynamical behavior. For PVP solutions (Fig. 7), we observe three relaxations [44]: the slowest is related to the α-relaxation of the solute and the two fastest are due to motions of water molecules [44]. It is important to note that in our previous works of PVP aqueous solutions [46–48], these two water relaxations were not reported (only the fast relaxation was included). In Fig. 7, we show the temperature dependence of the relaxation time of each relaxation process for PVP with 40 wt% of water. It is evident that the relaxation times of the slow solvent process and the solute exhibit the same temperature dependence in the high temperature range above T_g. Note that this slow solvent relaxation is not observed for 3PG or for PVME. In addition, for these solutions, the fast solvent relaxation shows a completely different temperature dependence than the solute relaxation (Fig. 7).

5 The Dynamics of Solutions During Isothermal Crystallization

There is quite a lot of information about the water dynamics in solutions when water remains amorphous at all temperatures. However, there is little information about the dynamical changes of the water during and after isothermal crystallization. Therefore, in this section, we address the dynamics of water in semi-crystalline solutions. BDS is a good technique to follow the dynamics of the amorphous solutions and

the dynamical alterations after crystallization. Even more, given that the isothermal crystallization of water is slow at certain temperatures, it is possible to follow the time evolution of the dielectric permittivity during crystallization.

To obtain a semi-crystalline sample, we selected a water content high enough to observe cold crystallization on heating. Water is able to crystallize at any temperature between the glass transition and the melting point (see Fig. 3c). This allows analyzing the dynamics of both the amorphous and semi-crystalline state of the same sample. In all the cases, the protocol is as follows:

1. We measure the dynamics of the amorphous sample up to a temperature where cold crystallization is not detected.
2. Then, we allow the sample to crystallize isothermally at a temperature T_{cryst} during some time (t_{cryst}).
3. After crystallization, we measure the dynamics of the semi-crystalline sample.

Figure 8 shows the time evolution of the dielectric permittivity during isothermal crystallization of 3PG at two water contents (50 wt% in Fig. 8a and 40 wt% in Fig. 8b). The main difference between the samples is that the crystallization was produced at $T_{cryst} = 200$ K in (a) and at a higher temperature $T_{cryst} = 218$ K in (b). For Fig. 8a at $t_{cryst} = 0$, we can observe the water relaxation at $f \sim 2 \times 10^4$ Hz. Increasing the
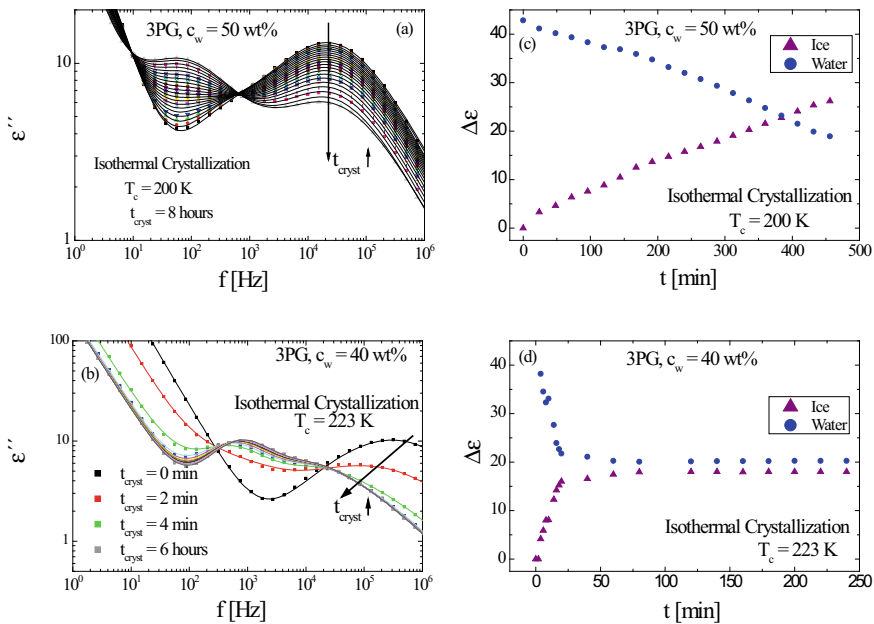
Fig. 8 a Loss component, ε'', of the complex permittivity, ε^*, during isothermal crystallization at $T_{cryst} = 200$ K during 8 h (**a**) and $T = 223$ K during 6 h in (**b**). Curves at $t = 0$ min (black boxes) represent the response of the amorphous material whereas the rest of the curves represent the dynamics after crystallization at different times (t_{cryst}). **c** and **d** relaxation strengths of the ice and water processes during isothermal crystallization

crystallization time, the water relaxation becomes progressively broader on the low frequency side and for longer times, there is a slow extra peak in the spectra ($f \sim$ 65 Hz). The dielectric strength corresponding to the water relaxation decreases with increasing crystallization time since part of the water turns into ice and therefore a fraction of the water dipoles do not contribute anymore to the dielectric response of water. On the other hand, the number of "ice" dipoles during crystallization increases and therefore the dielectric strength corresponding to the slow process also increases. The presence of this slow process does not depend on the crystallization temperature and it is independent of the solute, i.e., this extra process is also observed during the isothermal crystallization of PVP- or PVME–water solutions and it corresponds to the dielectric response of ice, as we will discuss latter.

In Fig. 8, we can observe two different behaviors depending on the crystallization temperature. For the sample in Fig. 8a, there is no change of the glass transition temperature between the amorphous and the semi-crystalline solution whereas in the second case (Fig. 8b), a change of 2.4° is produced in the T_g value (see T_g values in Table 1). In addition, in Fig. 8, a the peak maximum of water is not changing whereas in Fig. 8b, the relaxation time becomes slower after each cycle of crystallization.

The isothermal data during crystallization were fitted using the sum of three functions, two of them for describing the relaxations occurring in the amorphous fraction of the samples (a HN function for the α-relaxation and a CC function for the water relaxation). The third CC function was used to fit the new process at low frequencies ("ice relaxation" in Fig. 8b). When there is no change in the T_g value before and after crystallization, the relaxation times of the HN and CC functions of the α-relaxation and water relaxation, respectively, were fixed using the values of the amorphous sample. For these relaxations, $\Delta\varepsilon$ were free during the fitting as well as for the "ice relaxation" for which all the parameters were free. By contrast, for samples in which T_g changes are produced by the crystallization, all the parameters were free during the fitting. An example of the fitting can be seen in Fig. 9 for the amorphous ($t_{cryst} = 0$) and semi-crystalline sample ($t_{cryst} = 8$ h). Figure 8c and d show the time evolution of the relaxation strength of the ice and water relaxations for 3PG samples containing 50 and 40 wt% water, respectively. The lower the crystallization temperature (Fig. 8c) the longer it takes for water to crystallize (slow kinetics), and after 480 min, $\Delta\varepsilon_{water}$ of water has dropped to ~44%. At a higher crystallization temperature (Fig. 8d), the water crystallizes much faster ($\Delta\varepsilon_{water}$ of water has dropped ~52% after 25 min), and thereafter there is no more water crystallization.

Another example during isothermal crystallization is shown in Fig. 10 for PVME ($c_w = 50$ wt%) and PVP ($c_w = 55$ wt%). Both polymers were crystallized at high temperatures and therefore the crystallization proceed fast. In both cases, the water peak shown in the figure corresponds to the water relaxation for PVME and the fast water relaxation for PVP. As in the previous case, the intensity decreases and a shoulder is developed at lower frequencies. For PVME, the maximum of the water peak becomes slower after each cycle of crystallization (as in the case of 3PG) until ~1 decade is reached after 480 min. By contrast, for PVP, the water peak also becomes slower, but only ~0.4 decades in spite of the fact that the crystallization time is longer than for PVME and the glass transition value decreases more for PVP
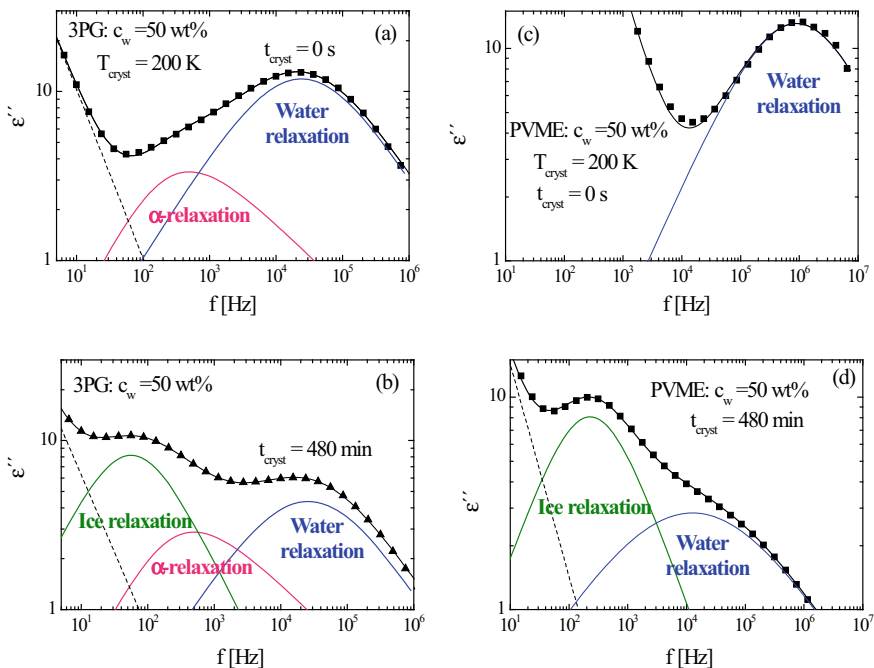
Fig. 9 **a** Loss component, ε'', of the complex permittivity, $\varepsilon^*(f)$, of the amorphous sample ($t_{cryst} = 0$), and after isothermal crystallization **b–d** indicated in each figure for 3PG and PVME solutions. A new relaxation process (ice relaxation) at low frequencies can be observed at longer crystallization times
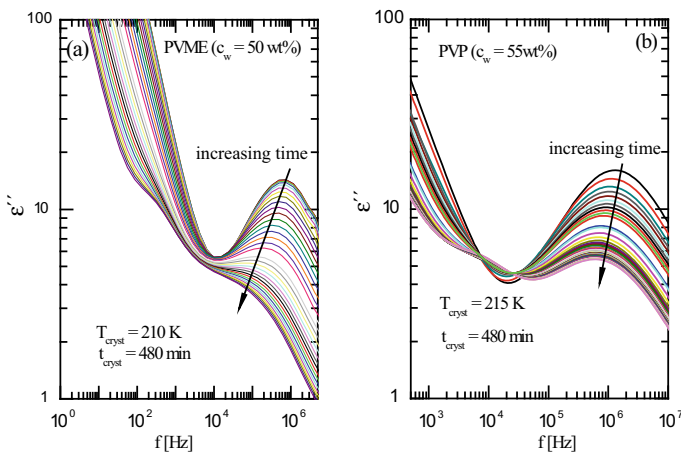

Fig. 10 Loss component, ε'', of the complex permittivity, $\varepsilon^*(f)$, of **a** PVME ($c_w = 50$ wt%) and **b** PVME ($c_w = 55$ wt%) at the T_{cryst} and t_{cryst} indicated in each figure

than for PVME. In the next two sections, we will analyze how the characteristics of the water dynamics changes under isothermal crystallization of the different systems here studied.

6 The Dynamics of Water Solutions After Isothermal Crystallization

Now, we analyze the dynamics of the semi-crystalline materials concentrating on the water and ice relaxations. Figure 11 shows the dielectric spectra of 3PG with $c_w = 50$ wt% in the amorphous (Fig. 11a) and semi-crystalline states (Fig. 11b). The semi-crystalline state was obtained by keeping $T_{cryst} = 200$ K during $t_{cryst} = 8$ h (480 min) and no change in the glass transition temperature was observed. Similar results were obtained for the other water concentrations and for crystallization temperatures for which T_g remains the same. As mentioned above, the intensity of the dielectric loss of water in the amorphous state (a) is smaller than in the semi-crystalline mixture (b) since a portion of the amorphous water turns into ice during isothermal crystallization. The fitting procedure was already explained in Fig. 9 for 3PG solutions. This procedure was also used to fit the data of PVP and PVME solutions.

Figure 12 shows the shape factors and relaxation strengths for the ice and water relaxations in the amorphous and semi-crystalline states of this sample (3PG, $c_w =$
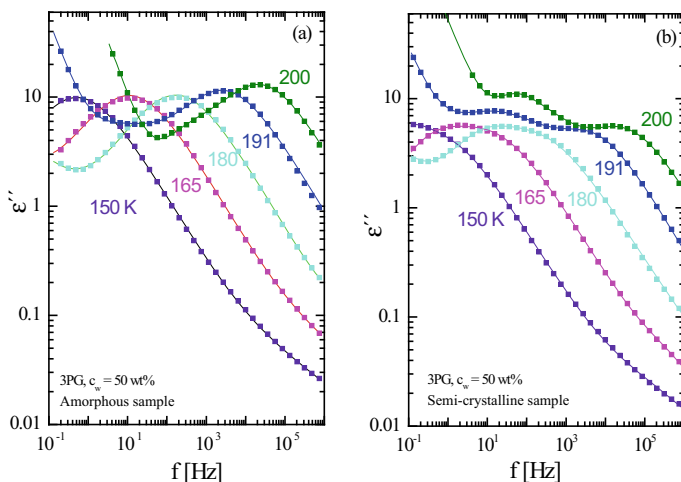
Fig. 11 **a** Loss component, ε'', of the complex permittivity, $\varepsilon^*(f)$, of the amorphous 3PG—water solution with $c_w = 50$ wt% at different temperatures. The lines through the data points correspond to least-square fits to a superposition of two Cole–Cole functions. **b** Same as in (**a**), but after isothermal crystallization at $T_{cryst} = 200$ K during $t_{cryst} = 8$ h. The solid lines through the data points correspond to least-square fits to a superposition of three Cole–Cole functions
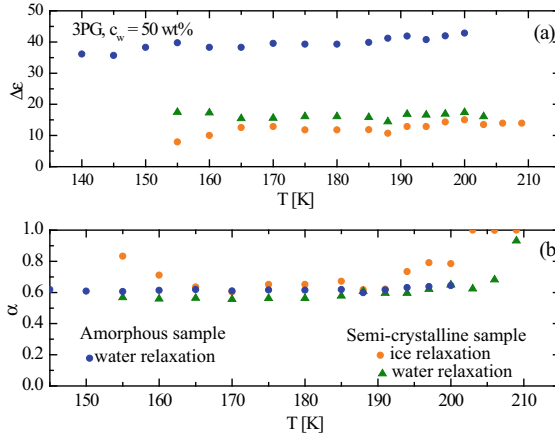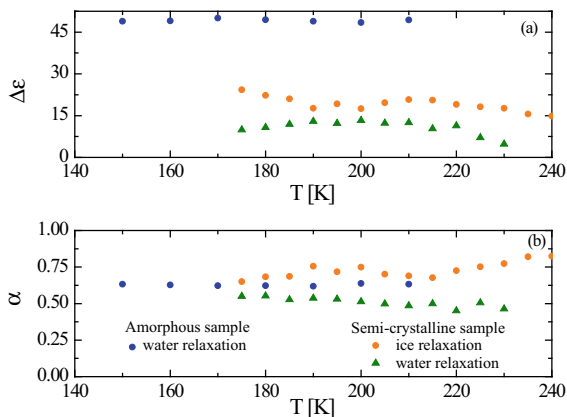
Fig. 12 **a** Relaxation strength and **b** shape factor of amorphous and semi-crystalline 3PG—water solution (c_w = 50 wt%). The glass transition temperatures of the amorphous and semi-crystalline materials are the same

50 wt%). As expected, the relaxation strength of water decreases whereas the α-parameter is only slightly lower in the crystallized material. This indicates that the environment of the water molecules is not significantly affected after crystallization, in spite of the fact that an increasing amount of water molecules becomes ice. Finally, Fig. 13 shows the temperature dependence of the water relaxation time as obtained
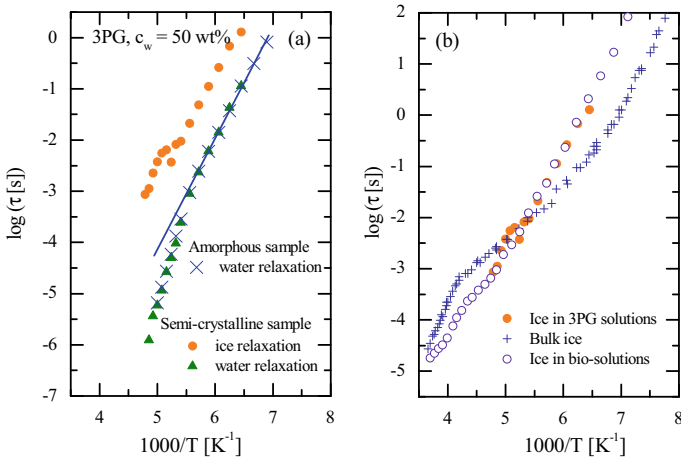
Fig. 13 **a** Temperature dependence of the water relaxation times of amorphous and semi-crystalline 3PG—water solution (c_w = 50 wt%). In orange symbols, the relaxation times of ice only observed in the crystalline material. **b** Comparison of the relaxation times of bulk ice (Ih) [49], ice in solutions of Bovine Serum Albumin (BSA) [50], collagen [51] and elastin [52], and ice in 3PG solutions after crystallization Adapted with permission

from the fittings. It can there be seen that the water relaxation time is unaffected by crystallization and correspondingly the crossover from the high-temperature non-Arrhenius behavior to the low-temperature Arrhenius dependence is obtained at the same temperature (approximately T_g) for the amorphous and semi-crystalline materials.

Regarding the ice relaxation, Fig. 13b compares the temperature dependence of the relaxation times of bulk ice [49], ice in solutions of bovine serum albumin (BSA) [50], collagen [52], and 3PG water solutions. We can observe that there is no difference in the relaxation times between solutions of proteins and 3PG, but the relaxation of bulk ice is different, as discussed in other publications [50–52].

We now present the results for samples crystallized at a high crystallization temperature (i.e., fast crystallization). As an example, we show the case for PVME ($c_w = 50$ wt%) using $T_{cryst} = 210$ K. In this case, the glass transition temperature of the amorphous (190 K) and semi-crystalline (200 K) materials changes by ~10 K (see Table 1). Figure 14 shows the shape factor and the relaxation strength of the water and ice relaxations. As in the case of 3PG, the relaxation strength of water decreases substantially and the shape factor becomes slightly lower in the semi-crystalline PVME solution. In Fig. 15, we show the temperature dependence of the relaxation times. It is clear that the relaxation times of the water process become slower (~1 decade) in the crystallized sample and, consequently, the crossover temperature also changes. However, in this case, the glass transition of the solution is changing, which implies that the crossover from the high-temperature non-Arrhenius dependence to the low-temperature Arrhenius behavior of the water relaxation is produced at a higher temperature (approximately T_g) in the semi-crystalline material.

It is not obvious why the crystallization temperature has this large effect on both T_g and the relaxation time of the amorphous water. Possibly larger clusters of ice are formed, i.e., a micro-phase separation of the freeze concentrated solution and the

Fig. 14 **a** Relaxation strength and **b** shape factor of amorphous and semi-crystalline PVME–water solution ($c_w = 50$ wt%)
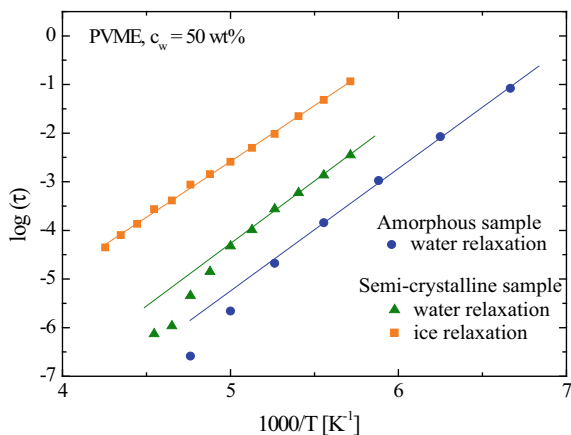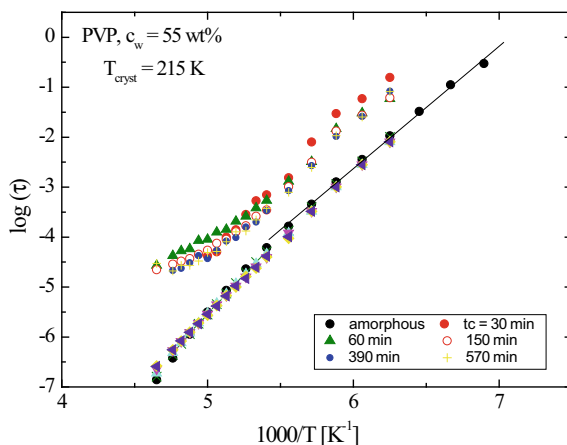
Fig. 15 Temperature dependences of the relaxation times of an amorphous PVME–water mixture with $c_w = 50$ wt% and after isothermal crystallization during $t_{cryst} = 360$ min at $T_{cryst} = 210$ K

ice regions occurs at a higher crystallization temperature due to a larger mobility of both water and solute molecules. Given that the T_g of the solutions is increasing after crystallization, as showed in Table 1, crystallization of water generates dehydration of the PVME molecules. This behavior was also observed for crystallization of glycerol water solutions [53]. At crystallization temperatures close to T_g, it is possible that the overall structure of the solution remains the same, with the exception that a fraction of the water transforms from an amorphous network to a crystalline network. However, this may have a lower effect on T_g and the relaxation time of the remaining amorphous water.

Finally, we present the dynamical results of water in PVP solutions, in which two relaxations of water molecules are observed in the amorphous material. In the case presented here, the glass transition temperature under isothermal crystallization at $T = 215$ K, shows an increase of 16.6 K from the amorphous to the semi-crystalline material. Therefore, we also expect, as in the case of the PVME solution shown in Fig. 15, a change in the dynamics of water after crystallization. Figure 16a shows the dielectric response at $T = 180$ K (a temperature lower than T_g) and Fig. 16b at $T = 215$ K (higher than T_g) for different crystallization times as indicated in the figure. Each curve in Fig. 16 represents a different material in the sense that each curve has a different crystallization time and therefore a different crystallization level. The relaxation times are independent of the crystallization time at temperatures lower than T_g, although the dielectric intensity decreases since water molecules turned into ice. At temperature higher than T_g ($T = 215$ K), the main loss peak in the semi-crystalline material shifts toward lower frequencies for 0.4 decade. From this observation, we can conclude that at temperatures lower than T_g the relaxation due to water molecules is not affected by the change of environment. Thus, the relaxation of the water below T_g is the same irrespective whether it is confined by the frozen polymer or the ice phase. However, above T_g, the relaxation times change slightly,
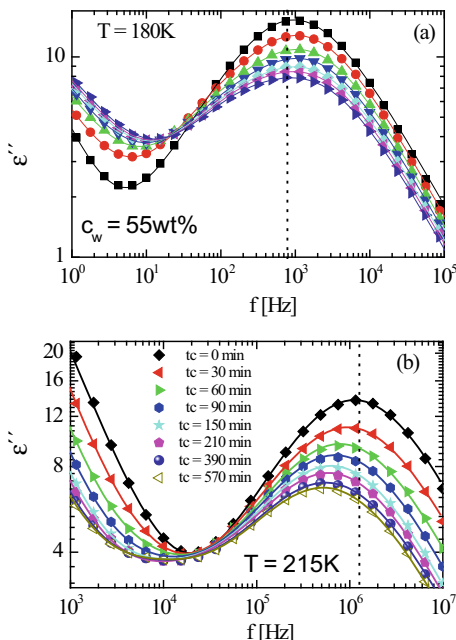
Fig. 16 Loss component, ε'', of the complex permittivity, $\varepsilon^*(f)$, of amorphous PVP–water solutions (black boxes) and after isothermal crystallization at $T_{cryst} = 215$ K at different times (0, 20, 60, 90 150, 210, 390, and 570 min, respectively) at two temperatures: **a** $T = 180$ K and **b** $T = 215$ K. Curves at t = 0 min (black boxes) represent the response of the amorphous material whereas the rest of the curves represents the dynamics after crystallization at different times (t_{ct})

although in a much milder way than the glass transition temperature changes with the crystallization time, as in the case of PVME. Figure 17 shows the relaxation times for the fast water relaxation and the "ice relaxation" for all these samples crystallized at different levels. Although, the relaxation time of the fast water relaxation becomes slightly slower with increasing crystallization time at 215 K (as shown in Fig. 16b), it is evident from Fig. 17 that this difference decreases and becomes vanishingly small at lower temperatures. Furthermore, the crossover temperature is not changing significantly, as in the case of PVME. The T_g difference in this case is 14 K, whereas the difference in the crossover temperature between the amorphous and the sample crystallized during 570 min is only 3 K. Even more, the "ice relaxation" is not similar to that showed in Figs. 12 and 14 for 3PG and PVME.

As a result, after isothermal crystallization of water in solutions, we find two different scenarios for the temperature dependence of the water relaxation time. When the amorphous solutions have a single water relaxation (3PG or PVME), the relaxation times and therefore the crossover temperature are changing with T_g (if there is no change of T_g, no change of the crossover temperature). However, when the amorphous solutions have two water relaxations, the relaxation times are not appreciable changing. This indicates that the temperature where the crossover

Fig. 17 Temperature dependences of the relaxation times of an amorphous PVP–water mixture with $c_w = 55$ wt% and after isothermal crystallization during $t_{cryst} = 30, 60, 150, 390$ and 570 min at $T_{cryst} = 215$ K

occurs is governed by the T_g of the solution in the case of solutions with a single water relaxation, but that it is independent of T_g when two water relaxations are present in the systems. The latter scenario suggests that the faster water relaxation in solutions exhibiting two water relaxations is an intrinsic water relaxation, which may also be present for water in hard confinements (Sects. 7 and 8 below) as well as in bulk water, as discussed in Sect. 9 below.

7 The Dynamics of Amorphous and Semi Crystalline Water in Hard Confinement Systems by BDS and NMR

In this section, we discuss the results of amorphous and semi-crystalline water confined in small cavities of porous materials (so-called hard confinements). Confinement of water was extensively analyzed in the literature using different types of mesoporous silica materials such as silica hydrogels, Vycor glasses, molecular sieves, mineral clays, graphite oxide, and cement-like materials. All these materials are hydrophilic (generally with hydroxyl groups on the surface) and exhibit an interconnected pore structure with a broad pore size distribution. These characteristics give often rise to an incomplete filling of the pores, and water—surface interactions are therefore highly promoted. However, a suitable model system to confine water is the mesoporous silica MCM-41, because it presents a very well-defined geometry of cylindrical pores with a narrow size distribution. The water dynamics seems to be less influenced by surface interactions in this case and a more "universal" relaxation behavior is obtained.
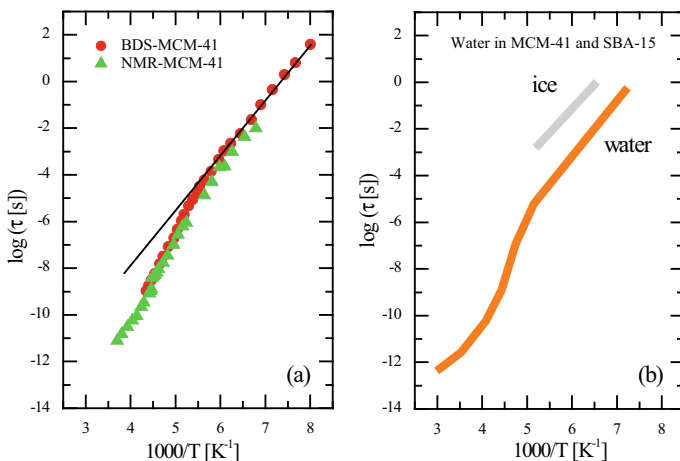
Fig. 18 **a** Temperature dependence of relaxation times determined from BDS [54] and NMR[33] of amorphous water confined in MCM-41 of the same pore diameter. **b** Temperature dependence of relaxation times for partially crystallized water confined in MCM-41 of different sizes. The two lines represent the results of the experiment on D_2O in MCM-41 with various pore diameters (2.1–6 nm). The fast relaxation represents the rotational motion of confined water (orange line) whereas the slow relaxation (grey line) represents the relaxation times of the ice phase

The dynamics of amorphous water confined in MCM-41 has been studied by both BDS [54, 55] and nuclear magnetic resonance [31, 32, 56] (NMR). The relaxation times of water exhibit a dynamic crossover at about 180 K, similar to that previously discussed for water solutions in Sect. 5 (see Fig. 18a).

If the pore diameter is ~2 nm or smaller, water remains amorphous for all temperatures. However, using a wider pore, a fraction of water crystallizes, as in the case of the water solutions analyzed in Sect. 2. Weigler et al. [33] explore the dynamics of water confined in MCM-41 of different sizes from 2.1 to 3.3 nm. The calorimetric response showed that crystallization of water confined in 2.1 nm is fully suppressed, but water confined in pore sizes of 3.3, 2.8 and even in 2.4 nm present crystallization on the cooling cycle. Increasing the pore size, a more pronounced freezing peak is shown and therefore more ice is produced in each sample. Thus, by increasing the pore size, it is possible to study the dynamics of amorphous water in samples of an increasing amount of ice. In particular, it was of interest [32, 33] to elucidate whether the dynamic crossover of the confined supercooled water is affected by crystallization.

The dynamics of such partially crystallized D_2O confined in MCM-41 of different pore sizes has been studied by 2H SLR and STE experiments. Figure 18b shows the relaxation times for these samples of different pore sizes and different levels of ice. As can be seen in the figure, the relaxation time is basically independent of the pore size and the level of crystallization. This result contrasts that previously obtained in ordinary solutions, as discussed in Sect. 6, but is similar to what was observed for

PVP, where two water relaxations were observed, as discussed in Sect. 7. In the next section, we will discuss the impact of all these results on bulk water.

8   The Implication of the Present Results for Bulk Water

In this section, we discuss likely implications of the findings presented above for water in both solutions and hard confinements. In the case of water in "ordinary solutions" (i.e., solutions with only a single water relaxation), we found that the dynamic crossover temperature of the water relaxation is strongly affected by the glass transition temperature. The dynamic crossover occurs at T_g of the solution irrespective of the degree of water crystallization. This observation suggests that the dynamic crossover is not an intrinsic property of the water in the solution, but rather caused by an immobilization of the solute matrix at T_g, which imposes a confinement effect of the water intercalated in the matrix. Thus, water in these kinds of solutions behaves as confined water only below T_g, and the water is furthermore affected by interactions with the solute matrix, causing the water relaxation to be slower at low water contents. This also implies that the water relaxation becomes slower if the effective water concentration decreases by freeze-concentration, as occurs during crystallization at a high temperature. This strong influence of the local environment on the water relaxation in these kinds of solutions indicates that the water relaxation cannot be considered as an intrinsic property of water, and therefore not be of strong relevance for bulk water.

However, for solutions exhibiting two water relaxations, such as solutions of PVP, the crossover temperature of the fast water relaxation is independent on the ice level and therefore independent on the T_g value. This is also the case for water in hard confinements, as can be seen in Ref. [33] where the degree of crystallization can be regulated by the pore size. Furthermore, in these two types of systems also the time scale and activation energy of the water relaxation are unaffected by the amount of ice in the systems. These findings indicate that the dynamical properties of this amorphous water can be considered as intrinsic properties of supercooled or glassy water. Hence, bulk water is then expected to exhibit similar dynamical properties in the same temperature range. Indeed, Amann-Winkel et al. [57] observed a dielectric relaxation process of low-density amorphous ice (LDA) that is almost identical to this "universal" relaxation of confined water. This strongly suggests that the low-temperature water relaxation we observe in both solutions exhibiting two water relaxations and in hard confinements is the same as for bulk water. Moreover, DSC studies of both crystalline and amorphous ices show that the calorimetric feature observed for LDA at 136 K [58] is identical to the calorimetric feature observed for hydrogen-disordered crystalline ice phases at a similar temperature [59]. Since this endothermic peak is not affected by isotope substitution of ^{16}O to ^{18}O, but significantly shifted for D_2O, it is also clear that this is due to an unfreezing of molecular reorientation dynamics, rather than related to translational motions of the oxygen atoms, which should be the case if it was a true glass-to-liquid transition.

This implies that the "universal" water relaxation we observed is not only the same for bulk water, but it also has the characteristics of a local reorientational motion in amorphous ice, i.e., the water we observe below the crossover temperature at about 180 K should be considered as amorphous ice rather than as a supercooled liquid [23].

9 Conclusion

In this chapter, we have presented old and new experimental data on the dynamics of water in semi-crystalline environments and we have compared with the dynamics of water in the amorphous state. By using broadband dielectric spectroscopy, we have analyzed the dynamics during and after crystallization at different crystallization temperatures and times. The dynamical behavior of both the solute and the remaining non-crystalline water is remarkably affected by the crystallization temperature. At a low crystallization temperature (just above T_g), there is basically no changes of the glass transition and its related structural relaxation or the low-temperature water relaxation, suggesting that some of the amorphous water transforms to crystalline water without affecting the overall structure of the solution or the hydration of the solute molecules. However, at a high crystallization temperature, the dynamics of both the solute (and therefore also the glass transition temperature) and the water is slowed down by the partial crystallization of the water. This is the typical behavior of freeze-concentrated solutions when the amorphous part of the solution is "dried out" by a micro-phase separation into ice regions and freeze-concentrated amorphous regions.

The differences in the dynamics described above for low and high crystallization temperatures occur for "ordinary" aqueous solutions exhibiting only one water relaxation. However, for solutions exhibiting two water relaxations, as commonly observed for biological systems and solutes for which the addition of water has a dramatic effect on T_g [44, 45], yet another dynamical behavior is observed. In this case, partial crystallization of the water does increase the glass transition temperature, as typical for freeze-concentrated solutions, but nevertheless the low-temperature water relaxation is not affected. This indicates that the fast water relaxation in this type of solutions may be considered as an intrinsic water relaxation. This conclusion is furthermore supported by the fact that an almost identical water relaxation is observed for both bulk water (or rather low-density amorphous ice) [57] and water confined in hard confinements with or without ice. Thus, there is no reason to believe that this common water relaxation should not have the same origin in the three mentioned types of systems. The "universality" of this water relaxation gives also further evidence for that it is of local character, in contrast to the viscosity related structural (α) relaxation.

References

1. Papoian GA, Ulander J, Wolynes PG (2003) J Am Chem Soc 125(30):9170–9178
2. Ben-Amotz D (2016) Annu Rev Phys Chem 67(1):617–638
3. Petrenko, V.F. and R.W. Whitworth, *Physics of Ice*. 2002: Oxford University Press
4. Li DM, Zhu ZW, Sun DW (2018) Trends Food Sci Technol 75:46–55
5. Agranovich D et al (2016) Colloids Surfaces B-Biointerfaces 141:390–396
6. Sasaki K et al (2014) J Chemical Phys 140(12):124506 (7 pp)
7. He ZY, Liu K, Wang JJ (2018) Acc Chem Res 51(5):1082–1091
8. Zhang X et al (2016) Food Anal Methods 9(11):3125–3132
9. Huebinger J et al (2016) Biophys J 110(4):840–849
10. Pearce RS (2001) Ann Bot 87(4):417–424
11. Chen G et al (2013) J Cereal Sci 57(1):120–124
12. Eckardt J et al (2013) J Cereal Sci 57(1):125–133
13. Gibney PA et al (2015) Proc Natl Acad Sci 112(19):6116–6121
14. Voets IK (2017) Soft Matter 13(28):4808–4823
15. Mishima O, Stanley HE (1998) Nature 396(6709):329–335
16. Poole PH et al (1992) Nature 360(6402):324–328
17. Kim KH et al (2017) Science 358(6370):1589–1593
18. Chaplin M (2006) Nat Rev Mol Cell Biol 7:861–866
19. Angell CA (1983) Annu Rev Phys Chem 34(1):593–630
20. Debenedetti PG (2003) J Phys: Condens Matter 15(45):R1669
21. Bellissent-Funel MC et al (2016) Chem Rev 116(13):7673–7697
22. Cerveny S et al (2016) Chem Rev 116(13):7608–7625
23. Swenson J (2018) Phys Chem Chemical Phys 20(48):30095–30103
24. Swenson J, Jansson H, Bergman R (2006) Phys Rev Lett 96:247802
25. Ito K, Moynihan CT, Angell CA (1999) Nature 398(6727):492–495
26. Speedy RJ, Angell CA (1976) J Chem Phys 65(3):851–858
27. Faraone A et al (2004) J Chem Phys 121(22):10843–10846
28. Cerveny S, Colmenero J, Alegria A (2006) Phys Rev Lett 97(18):189802
29. Swenson J, Cerveny S, Phys J (2015) Condens Matter 27:033102
30. Sattig M et al (2014) Phys Chem Chem Phys 16(36):19229–19240
31. Rosenstihl M et al (2015) J Non-Cryst Solids 407:449–458
32. Lederle C, Sattig M, Vogel M (2018) J Phys Chem C 122(27):15427–15434
33. Weigler M et al (2019) J Phys Chem B 123(9):2123–2134
34. Kremer F, Schönhals A (2003) Broadband dielectric spectroscopy. Springer, Berlin
35. Cerveny S et al (2006) J Chem Phys 124(19):194501
36. Immergut, E.H. and H.F. Mark, *Principles of Plasticization*, in *Plasticization and Plasticizer Processes*. 1965, American Chemical Society. p. 1–26
37. Cerveny S, Colmenero J, Alegría A (2005) Macromolecules 38(16):7056–7063
38. Cerveny S, Alegria A, Colmenero J (2008) J. Chem. Phys. 128(4):044901
39. Cerveny S, Alegria A, Colmenero J (2008) Phys Rev E: Stat Nonlinear Soft Matter Phys 77:031803
40. Sjostrom J et al (2011) J.Phys Chem B 115(33):10013–10017
41. Elamin K et al (2012) J Chem Phys 136(10):104508
42. Sudo S et al (2004) J Chem Phys 121(15):7332–7340

43. Tyagi M, Murthy SSN (2006) Carbohyd Res 341(5):650–662
44. Combarro Palacios I et al (2019) J Chem Phys 150(12):124902
45. Cerveny S, Swenson J (2019) J Chem Phys 150(23):234904
46. Cerveny S, Alegria, Colmenero J (2008) J Chem Phys 128(4)
47. Busselez R et al (2012) J Chem Phys 137(8):084902
48. Cerveny S et al (2010) J Non-Cryst Solids 356(52–54):3037–3041
49. Johari GP, Whalley E (1981) J Chem Phys 75(3):1333–1340
50. Shinyashiki N et al (2009) J Phys Chem B 113:14448–14456
51. Kurzweil-Segev Y et al (2017) J Phys Chem B 121(21):5340–5346
52. Gainaru C, Fillmer A, Bohmer R (2009) J Phys Chem B 113(38):12628–12631
53. Wang Q et al (2019) Phys Chem Chem Phys 21(20):10293–10299
54. Sjostrom J et al (2008) J Chem Phys 128(15):154503
55. Hedström J et al (2007) The Eur Phys J Special Top 141(1):53–56
56. Sattig M, M. Vogel, J. Phys. Chem. Lett., 2014. **5**(1): p. 174–178
57. Amann-Winkel K et al (2013) Proc Natl Acad Sci USA 110(44):17720–17725
58. Johari GP, Hallbrucker A, Mayer E (1987) Nature 330(6148):552–553
59. Shephard JJ, Salzmann CG (2016) J Phys Chem Lett 7(12):2281–2285

Order and Dielectric Relaxation During Polymer Crystallization

Aurora Nogales, Tiberio A. Ezquerra, Michelina Soccio, and Marianella Hernández

Abstract In the recent years Broadband Dielectric Spectroscopy (BDS) has been shown to be a powerful technique to investigate crystallization in complex fluids including liquids and polymers. Particularly attractive is when scattering and diffraction experiments are combined with dielectric spectroscopy during crystallization in real-time. In this chapter we will review the application of BDS to the study of polymer crystallization emphasizing those aspects related to the combination of X-ray scattering techniques, rendering information about the crystalline phase, with BDS providing information about the amorphous phase dynamics. In addition, we will show as well that both the α-relaxation and the β-relaxation can be used for probing polymer crystallization especially when they appear simultaneously and well resolved in the experimental frequency window. Although most of the applications of BDS to polymer crystallization involve thermal treatments we will show that BDS can be also used when other magnitudes like pressure, shear or strain are involved in the crystallization process.

Keywords Real time crystallization · Broadband dielectric spectroscopy (BDS) · Natural rubber · Strain induced crystallization

A. Nogales (✉) · T. A. Ezquerra
Instituto de Estructura de la Materia, IEM-CSIC, Serrano 121, Madrid 28006, Spain
e-mail: emnogales@iem.cfmac.csic.es

T. A. Ezquerra
e-mail: t.ezquerra@csic.es

M. Soccio
Dipartimento di Ingegneria Civile, Chimica, Ambientale e dei Materiali, Universitá di Bologna, Via Terracini 28, Bologna 40131, Italy
e-mail: m.soccio@unibo.it

M. Hernández
Instituto de Ciencia y Tecnología de Polímeros, ICTP-CSIC, Juan de la Cierva 3, Madrid 28006, Spain
e-mail: marherna@ictp.csic.es

195

Abbreviations

BDS   Broadband dielectric Spectroscopy
FK   Frölich-Kirkwood
HN   Havriliak Negami equation
NR   Natural rubber
PET   Poly(ethylene terephthalate) (PET)
PPS   Poly(propylene succinate)
PPT   Poly(pentamethylene terephthalate)
PTT   Poly(trimethylene terephthalate)
RAP   Rigid amorphous phase (RAP)
SAXS   Small Angle X-ray Scattering
WAXS   Wide Angle X-ray Scattering

1 Introduction

Nowadays polymers are ubiquitous in our everyday life. The world polymer materials production reached around 350 million tons in 2017 being about two-thirds of it related to semicrystalline polymers [1]. Similarly to other glass former materials by cooling a polymer from its viscoelastic liquid phase its specific volume, Fig. 1 a, linearly decreases with temperature until the glass transition temperature, T_g, is reached [2]. Below T_g a change in the specific volume decrease rate with temperature is observed. Before reaching T_g the polymer has to transit through the supercooled liquid state (SCL) temperature range defined by $T_g > T > T_m^0$ being T_m^0 the equilibrium melting temperature. In the SCL state the polymer can be thermodynamically unstable depending on chemical structure factors like branching, copolymerization
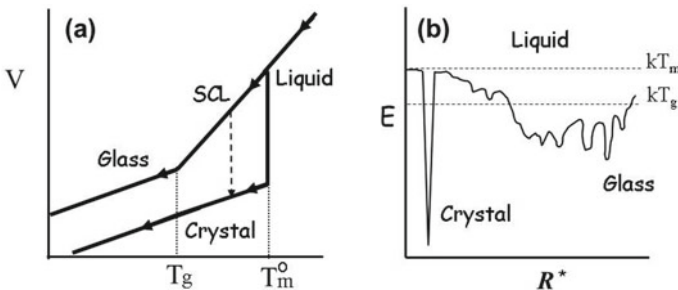
Fig. 1 **a** Schematic dependence of the specific volume (V) of a material as a function of the temperature indicating the liquid, supercooled liquid, glass and crystalline phases. **b** Energy landscape representation illustrating the energetic scenario for liquid, glass and crystalline phases. R* is a generalized configuration coordinate for the whole system. The dashed arrow in **a** indicates a possible liquid-crystal transition. See text for details

or tacticity since its free energy can be higher than that of the crystalline state. If this is the case, the supercooled liquid spontaneously suffers a first order liquid-to-crystal phase transition [3, 4]. Semicrystalline polymers usually adopt a characteristic folded chain crystalline lamellar morphology of nanometer dimensions when located in the supercooling temperature range. The lamellar morphology typically consists of stacks of laminar crystals with amorphous regions intercalated between them. While the crystalline phase provides strength to the material, the amorphous one is responsible of its toughness. Although extended chain crystals would be the thermodynamically most stable state, kinetic factors favor that polymer chains may fold several times forming crystalline lamellae [4–7]. From the point of view of the potential energy landscape [8], Fig. 1b, when the temperature decreases the crystalline phase is the one offering a minimum in energy. However, depending on cooling rate, the whole system cannot reach this state for kinetic reasons and fractions of the material become eventually trapped in local minima as an amorphous phase. While molecular dynamics is severely arrested in the crystalline phase, that of the fraction in local minima can exhibit both segmental and local dynamics above T_g [9].

If the polymer is quenched fast enough below T_g a fully amorphous state can be obtained where only local dynamics is allowed. In this case a semicrystalline state can be achieved by a thermal treatment process referred to as "cold crystallization" consisting in heating the glassy polymer above its T_g.

Experimentally in the past years Broadband Dielectric Spectroscopy (BDS) has been shown to be a powerful technique to investigate crystallization in complex fluids including liquids and polymers. Particularly attractive is when scattering and diffraction experiments are performed simultaneously with dielectric spectroscopy during crystallization in real-time [10–13]. The study of the isothermal polymer crystallization by dielectrics can be complemented with diffraction experiments using either X-rays[14–16] or neutrons [17].

In this chapter we will review the application of BDS to the study of polymer crystallization emphasizing those aspects related to the combination of X-ray scattering techniques, rendering information about the crystalline phase, with dielectrics providing information about the amorphous phase.

2 Probing Polymer Crystallization in Real-Time by Dielectric Spectroscopy

As far as polymers are concerned, BDS is very suitable to investigate molecular dynamics below and above T_g [18]. In particular, the segmental motions of the polymeric chains giving rise to the α-relaxation can be observed by BDS provided the polymer possesses dipolar moieties in its chemical structure. Pioneering work by Williams et al. showed that the dielectric α-relaxation can be used as a probe for crystallization since it is strongly sensitive to development of the crystalline phase [19]. The existence of a crystalline phase in a polymer material is reflected in the

dynamics of the α-relaxation mainly by three effects: i) a reduction of the dielectric strength, ii) a slowing down of the dynamics and iii) a modification of the shape of the relaxation [9, 14, 20]. Accordingly, the α-relaxation has been used extensively as a probe to follow in real-time the crystallization of polymer materials [17, 21–23], polymer thin films [24] and polymer liquid crystals [25, 26] among other polymer systems. Moreover, different ordered stages previous to crystallization have been discussed on the basis of dielectric experiments [27–30]. In the frequency domain, the α-relaxation appears as a maximum in the dielectric loss, ε'', and as a step in the dielectric constant, ε' [18]. As an example, Fig. 2a shows the variation with temperature of the dielectric loss spectra for initially amorphous poly(trimethylene terephthalate) [16]. The initial dielectric spectrum shows the α-relaxation associated with the segmental motions of chains in the amorphous phase above the T_g. As expected, the position in frequency of the relaxation maximum shifts to higher frequencies with increasing temperature. As the temperature rises there is a dramatic reduction of the intensity of the dielectric relaxation which is associated to the onset of crystallization. This effect is accompanied by a decrease of the area underneath the relaxation curve as a consequence of the reduction of the dielectric strength and by a significant shift of the maximum loss towards lower frequencies. At higher temperatures, the maximum further moves toward higher frequencies according to the temperature activated character of the α-relaxation. At even higher temperatures the contribution of the dc (direct current) electrical conductivity is observed by the increase of ε'' at low frequencies.

Scattering and diffraction techniques either with X-rays or with neutrons can provide structural information about the ordered regions in semicrystalline polymers at different length scales [4, 31]. Wide angle X-ray scattering (WAXS) allows the possibility of obtaining information about molecular order in the range of tenths of nanometers. Hence, WAXS can be useful to deal with crystalline structure determination and to estimate the crystallinity degree, X_c, defined as the amount of crystalline fraction in a semicrystalline polymer [3, 4, 7, 32]. Therefore, WAXS experiments can be used to visualize a crystallization process by monitoring the evolution with temperature of the WAXS patterns as illustrated in Fig. 2b. The two initial WAXS patterns show the typical broad maximum characteristic of an amorphous material. As temperature increases, crystallization is revealed by the appearance of Bragg peaks concurrently with the dramatic reduction of the intensity of the dielectric relaxation (Fig. 2a). In addition to WAXS, Small angle X-ray scattering (SAXS) enables to characterize structural features of semicrystalline polymers at length scales of the order of nanometers [31]. Figure 2c shows that crystallization is revealed by an increase of the scattered intensity at low angles in the SAXS patterns further developing into a well-defined maximum, commonly referred to as Long-spacing, revealing the presence of a periodicity between crystalline lamella and disordered domains. The experiments illustrated in Fig. 2 highlight that an improvement in the characterization of a crystallization process can be achieved by inter-correlating structural information, obtained by scattering about the crystalline phase, and molecular dynamics results about the amorphous phase obtained by BDS.

Fig. 2 **a** Evolution with increasing temperature of the dielectric loss spectra (ε'' versus frequency). **b** Wide Angle X-ray Scattering (WAXS) and **c** Small Angle X-ray Scattering (SAXS) of an initially amorphous poly(trimethylene terephthalate) sample. WAXS and SAXS intensities are represented as a function of the modulus of the scattering vector q. The three techniques have been carried out simultaneously [16]. The position of T_g has been highlighted by a dashed line "Adapted with permission from ref. [16]. Copyright (2019) American Chemical Society."
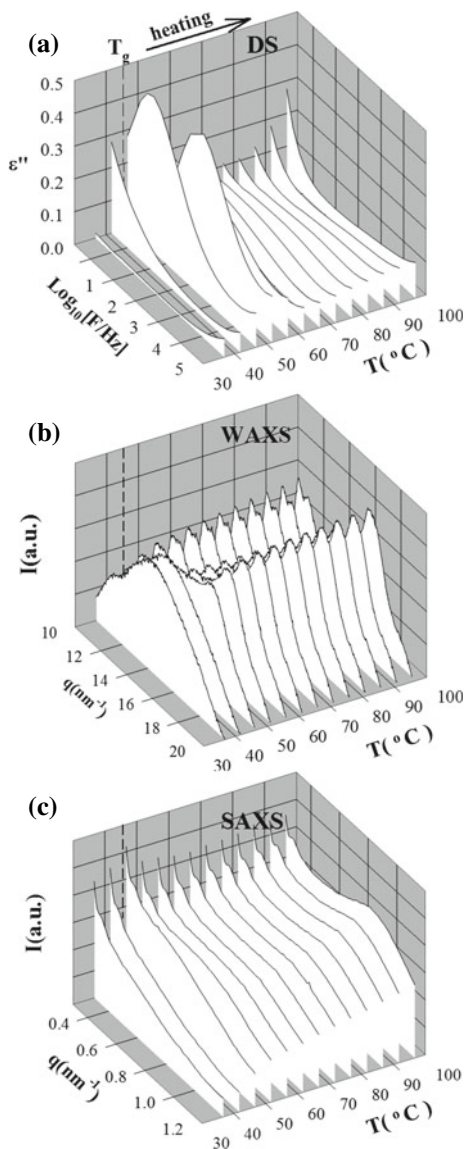
Of particular experimental interest is when dielectric and scattering experiments can be performed simultaneously. As a matter of fact the BDS, WAXS and SAXS experiments described in Fig. 2 were accomplished simultaneously by using synchrotron radiation for the scattering part [16]. For the sake of illustration, Fig. 3a shows a scheme of a typical set-up to measure SAXS, WAXS by using two position sensitive detectors at different distances from the sample [33] and BDS [10] simultaneously. The SAXS-WAXS-BDS (SWD) sample holder is schematized in Fig. 3b.
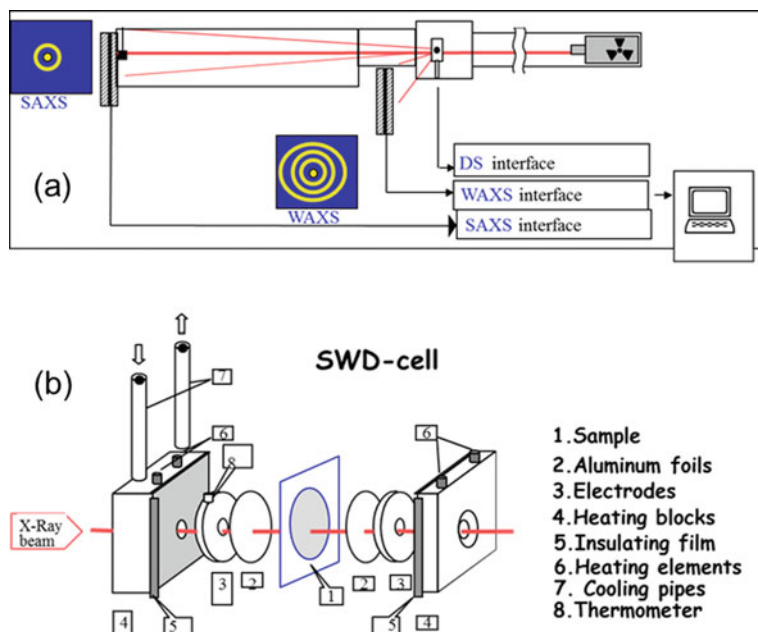
Fig. 3 **a** Scheme of a typical set-up for simultaneous measurements of SAXS, WAXS and BDS. **b** Schematic view of a sample cell (SWD) to accomplished BDS measurements simultaneously with SAXS and WAXS experiments [10]. "Adapted with permission from ref. [10]. Copyright (2020) AIP Publishing"

The polymer is placed between two metallic electrodes which are electrically insulated from the heating/cooling blocks. The X-ray beam can pass through the set-up by the holes machined in the electrodes and heating blocks. Different devices aimed to simultaneously measure BDS with other techniques including X-ray scattering and chip calorimetry [12], wide angle neutron scattering [34] or even inelastic neutron scattering under extreme pressure conditions [13] have been developed. This ongoing endeavor emphasized the added value of BDS when combined with other techniques in a simultaneous fashion to investigate ordering phenomena.

3 Isothermal Crystallization of Polymers as Revealed by Dielectric Spectroscopy

Dielectric spectroscopy can be used to monitor changes during isothermal polymer crystallization in real time. As mention above during crystallization the intensity of the α-relaxation typically decreases and its frequency of maximum loss shifts to lower values. Figure 4 (left panel) illustrates the time-resolved dielectric loss spectra collected during an isothermal crystallization at a crystallization temperature $T_c =$
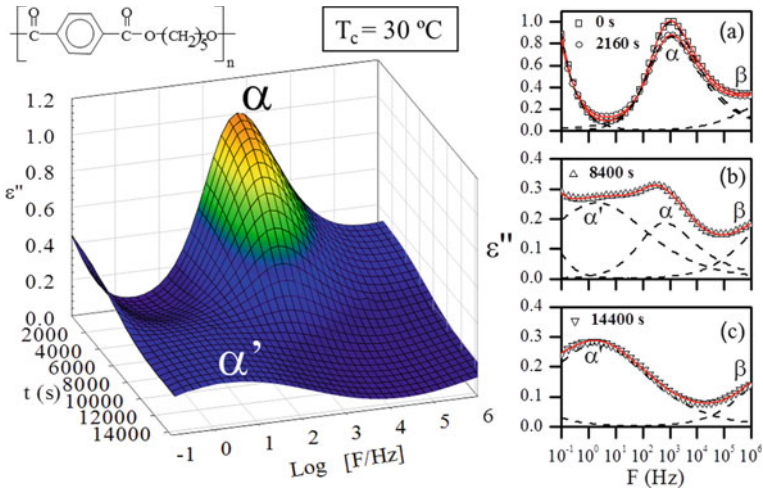
Fig. 4 (Left panel) Real time isothermal crystallization of initially amorphous poly(pentamethylene terephthalate) (PPT) at $T_c = 30°C$ as revealed by BDS, (ε'' data have been normalized to its maximum at $t = 0$ s). (Right panel) Selected isothermal ε'' data at different crystallization times (**a–c**). Continuous lines represent best fits according to HN equation. Dashed lines show the separated contribution of the different relaxation processes and conductivity. " Adapted with permission from ref. [35]. Copyright (2020) Elsevier."

$30°C$ of an initially amorphous poly(pentamethylene terephthalate) (PPT) sample ($T_g = 16°C$) [35]. The ε" data have been normalized to the maximum at $t = 0$ s. Figure 4b displays the dielectric loss spectra for selected times during crystallization. The initial amorphous state is characterized by a well resolved maximum in the spectrum associated to the α-relaxation. A small decrease of the α-relaxation intensity is observed in the initial stages of crystallization (Fig. 4a). This effect is associated to the induction period of crystallization and will be discussed in the next section. As crystallization develops, the α-relaxation changes significantly by the appearance of an additional slower process that can be well resolved in frequency (Fig. 4b). This slower relaxation can be ascribed to the segmental relaxation of a confined amorphous phase. As crystallization further proceeds the slower process becomes the main segmental process in the crystallized polymer (Fig. 4c).

The dielectric relaxations can be described in general by the HavriliakNegami (HN) equation[18, 36]:

$$\varepsilon'' = \mathrm{Im}\left[\varepsilon_\infty + \sum_{x=\alpha,\beta} \Delta\varepsilon_x \left[1 + (i\omega\tau_{\mathrm{HN}^x})^{b_x}\right]^{-c_x} - i\left(\frac{\sigma_{\mathrm{dc}}}{\varepsilon_{\mathrm{vac}}\,\omega}\right)^s\right] \qquad (1)$$

This equation describes the dependence of the dielectric loss, $\varepsilon´´$, with the angular frequency ω. Here $\Delta\varepsilon$ is the relaxation strength, τ_{HN} is the central relaxation time of the relaxation time distribution function, and b and c ($0 < b, c < 1$) are shape parameters which describe the symmetric and the asymmetric broadening of the relaxation time

distribution function, respectively. The last term corresponds to the contribution of the dc electrical conductivity, σ_{dc}, whose exponent is related to the conduction mechanism [18]. The average relaxation time (τ_{max}) value of the distribution can be calculated as follows:

$$\tau_{max} = \frac{1}{2\pi F_{max}} = \tau_{HN}\left[\sin\frac{b\pi}{2+2c}\right]^{-\frac{1}{b}}\left[\sin\frac{bc\pi}{2+2c}\right]^{\frac{1}{b}} \tag{2}$$

where F_{max} is the frequency at which the maximum in dielectric loss appears, and τ_{HN} is the central relaxation time of Eq. 1. A satisfactory description of the evolution of the segmental relaxation with crystallization time based on the HN formalism can be achieved considering separately the contribution of the different components present in the dielectric loss spectra as described by the dashed lines in Fig. 4. In general these include a dc conductivity and a β-relaxation contribution at lower and higher frequencies, respectively, in addition to the two α-relaxations [15, 16, 35, 37]. In Fig. 5 (left panel) the evolution with crystallization time of the different dielectric magnitudes has been represented for the data corresponding to Fig. 4. Figure 5a shows the WAXS patterns during crystallization revealing the appearance of Bragg maxima associated to the crystalline phase as crystallization time increases. An estimation of the crystallinity degree (X_c) in the sample can be obtained by considering the ratio of Bragg reflections contribution to the total scattered intensity [32, 35,
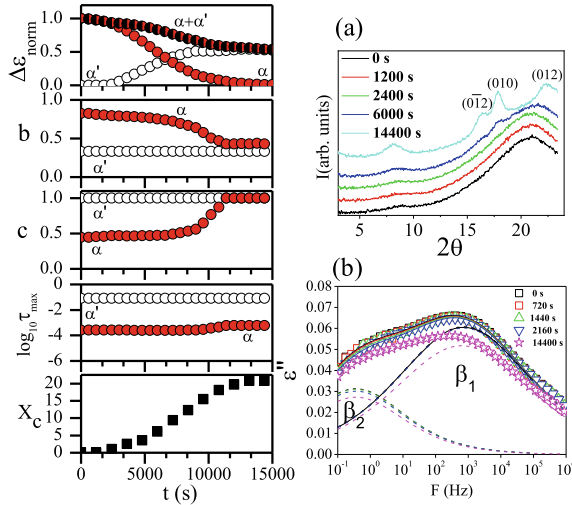
Fig. 5 HN equation parameters resulting from the fitting of the dielectric data of Fig. 3 for the α (•) and α′ (○) relaxations as a function of crystallization time. ($\Delta\varepsilon$) dielectric strength, (**b** and **c**) shape parameters, ($\log_{10}\tau_{max}$) relaxation time of maximum loss and (X_c) crystallinity degree. Dashed lines in **b** correspond to the contribution of the different β_1 and β_2 processes described by two independent Cole-Cole processes. The continuous line is the total fit considering the additive contribution of both processes. "Adapted with permission from ref. [35]. Copyright (2020) Elsevier."

38]. The evolution of the crystallinity with crystallization time typically presents a characteristic sigmoidal shape as shown in the bottom of the left panel of Fig. 5. As time increases the main effect is that the dielectric strength ($\Delta\varepsilon$) of the initial α-relaxation decreases whereas the α'-relaxation grows up. In addition, crystallization also affects the shape and frequency location of the α-relaxation. The b and c parameters decrease and increase, respectively, indicating broadening and symmetrization of the α-relaxation. The broadening parameter has been associated to large scale motions suggesting that these are dramatically affected by crystallization[39].

During crystallization not only segmental dynamics but also local dynamics, giving rise to the dielectric β-relaxation, can be significantly affected. The β-relaxation, observed below and above T_g, is a dielectric process faster than the α one and therefore appearing in a BDS experiment at higher frequencies [40].

To measure the β-relaxation in real-time at crystallization temperatures of interest is a difficult task since typically, as illustrated in Fig. 4, the maximum of the β-relaxation is located out of the frequency window covered by standard dielectric spectrometers. However some procedures can be used in order to achieve a quasi real-time description of the influence of crystallization in the β-relaxation. One of such protocols is illustrated in Fig. 6 as applied to the crystallization of poly(pentamethylene terephthalate) (PPT) at $T_c = 30°C$. Firstly, the β- relaxation is measured at a temperature where its maximum is well centered in the experimental frequency window, in the case of PPT $T = -85°C$. Secondly, the temperature is increased up to the crystallization temperature of interest where the α-relaxation can be well characterized and
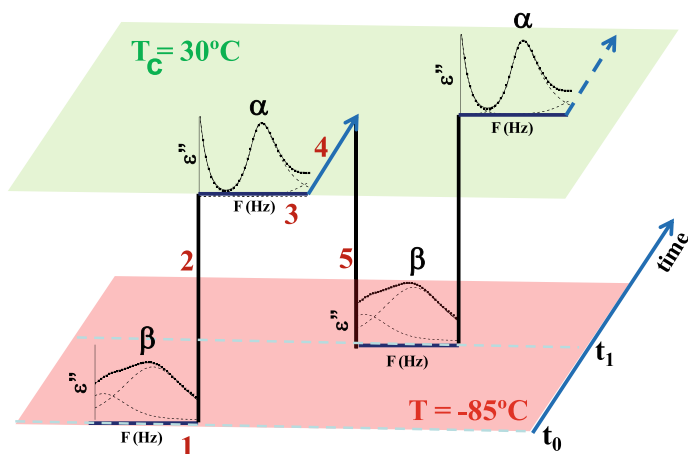
Fig. 6 Schematic description of a protocol useful to evaluate the effect of crystallization on the β-relaxation in quasi real-time: (1) The β relaxation is measured at a temperature where its maximum is well centered in the experimental frequency window. (2) The temperature is increased up to the crystallization temperature. (3) The α-relaxation is measured. (4) The polymer is allowed to crystallize for a controlled period of time. (5) The sample is rapidly cooled down back to the temperature where the β-relaxation was first characterized and another measurement is performed. The process can be repeated several times until the crystallization is considered to be finished

there the polymer is allowed to crystallize for a controlled period of time. Afterwards, the sample is rapidly cooled down back to the temperature where the β-relaxation was first characterized and another measurement is performed. It is worth noticing that at $T = -85°C$, the crystallization process can be considered interrupted since the temperature is well below the polymer T_g ($16°C$). The process can be repeated several times until the crystallization is considered to be finished.

Figure 5b shows the dielectric loss spectra of the β relaxation of PPT, measured at $T = -85°C$, collected by the described procedure for some characteristic crystallization times during the crystallization experiment at $T_c = 30°C$. Heating and cooling rates were $5°C/min$.

For PPT the β-relaxation, like for other aromatic polyesters, appears as a broad and multimodal relaxation composed of two processes designated as $β_1$ and $β_2$ in order of decreasing frequency [41, 42]. The β-relaxation of aromatic polyesters is typically multimodal and it is composed by contribution of the three conformationally flexible bonds of the repeating unit, namely, the aromatic ring carbon to ester carbon bond (CA-C), the ester ether oxygen to aliphatic carbon bond (O-C) and the aliphatic carbon-carbon bond (C-C) [43]. However, due to the small dipole moment of the C-C bond its relaxation is not likely to be detected by BDS. For PPT the faster mode ($β_1$) has been assigned to the relaxation of the O-C bond of the diol subunit and the slower one ($β_2$) to the relaxation of the aromatic ring carbon to ester carbon bond (CA-C) [35]. For PPT the β-relaxation can be described by the HN equation (Eq. 1) considering the contribution of two symmetric processes described in Fig. 5b by the dashed lines. In this case Eq. 1 is referred to as Cole − Cole equation. As far as crystallization is concerned at the early stages of the crystallization process the overall β-relaxation remains almost unaffected. As crystallization proceeds a net decrease of the dielectric strength of both components is observed. However while the Δβ of $β_1$ decreases by 18% with respect to its initial value, the Δβ of $β_2$ decreases by 12%. This effect can be explained considering the assignment of $β_1$ to the O-C bond which is a more mobile bond than the CA-C one and therefore is more affected by the crystalline phase.

Figure 7 represents, for the experiment presented in Fig. 4, the dependence of the total dielectric strength of the $α$ ($\Delta\varepsilon_\alpha + \Delta\varepsilon_{\alpha'}$) and of the β ($\Delta\varepsilon_{\beta 1} + \Delta\varepsilon_{\beta 2}$) relaxations normalized with respect to their initial values, as a function of crystallinity degree as evaluated by WAXS.

The dielectric strength of both relaxations, α and β, decreases linearly with crystallinity although the slopes are different being higher for the α-relaxation. In a first approximation one may consider the dielectric strength to be related to the amount of mobile amorphous phase and the crystallinity with the amount of material included in the crystals. The results for the β-relaxation show an inversely proportional dependence with the crystallinity degree (Fig. 7b). This effect, observed in several polymers [9, 44], suggests that the local dynamics of the material incorporated into the crystalline phase is significantly restricted. For the α-relaxation the decrease of the dielectric strength with crystallinity deviates from the slope -1 to be expected for a simple amorphous/crystal two phase model. This effect has been interpreted in the literature considering that during isothermal crystallization the restrictions to the segmental

Fig. 7 Evolution of the dielectric strength of the **a** α and **b** β relaxations with crystallinity, X_c for the cold crystallization of PPT(•) at $T_c = 30°C$. The data have been normalized to the initial value and correspond to $\Delta\varepsilon_\alpha^{norm} = \Delta\varepsilon_a + \Delta\varepsilon_{a'}$ (top panel) and $\Delta\varepsilon_\beta^{norm} = \Delta\varepsilon_{\beta1} + \Delta\varepsilon_{\beta2}$ (bottom panel). Additional data for PET [15] (□) and PTT [16] (○) have been included. The dashed and doted lines are a guide for the eye. "Adapted with permission from ref. [35]. Copyright (2020) Elsevier."
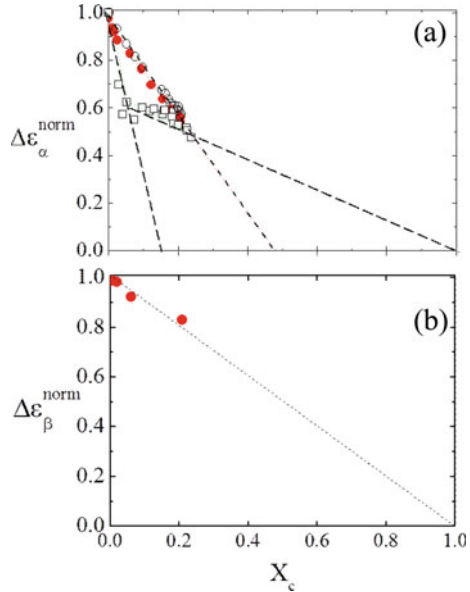
mobility not only affect to polymer segments included in the crystalline phase but also to other non-relaxing and non-crystallized segments which form a rigid amorphous phase (RAP) [45]. The RAP is a common structural feature of polymers with a medium degree of crystallinity and it is formed by polymer segments which relax at a significant slower rate than those of the amorphous phase. BDS measurements have evidenced the existence of a RAP in different aromatic polyesters [15, 16, 37, 45–49]. For the sake of comparison similar results for two aromatic polyesters PET [15] and PTT [16] have been included in Fig. 7a. As shown, the dielectric strength for PPT decreases lineally with X_c with the same slope for the whole investigate range suggesting that the rate of reduction of relaxing species is almost constant during crystallization. A qualitatively similar behavior is followed by PTT. However, for PET clearly two regimes with different slopes are observed in Fig. 7a. A similar behavior has been found for poly(butylene isophthalate) [37] and for poly(lactide) [49]. It has been proposed in the literature that for some polymers, like PET, cold crystallization proceeds by filling the space with a heterogeneous distribution of lamellar stacks separated by larger amorphous regions referred to as liquid pockets [15]. A schematic ideal picture of such a model is described in Fig. 8. In this case, it was proposed the RAP to be associated to the intra-lamellar amorphous regions, being the material in the inter-lamellar stacks amorphous regions (liquid pockets) the phase giving rise to the dielectric segmental relaxation. Accordingly, the initial strong decrease of the dielectric strength with crystallinity observed in PET (See Fig. 7a) can be associated to the immobilization of segments in the intra-lamellar stacks amorphous regions while the second weaker dependence can be associated to the formation of secondary lamellae in the liquid pockets. For PTT, and PPT the
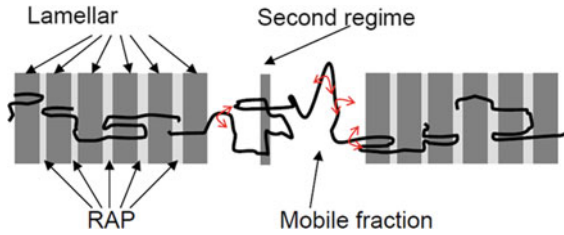
Fig. 8 Schematic ideal picture of a heterogeneous distribution of lamellar stacks separated by larger amorphous regions referred to as liquid pockets. The Rigid Amorphous Phase is associated to the intra-lamellar amorphous regions. The material in the inter-lamellar stacks amorphous regions (liquid pockets) give rise to the dielectric segmental relaxation. Secondary lamellae in the liquid pockets appear during a secondary regime of crystallization." Adapted with permission from ref. [37]. Copyright (2019) Elsevier."

dielectric strength reduction with crystallinity is weaker than for PET exhibiting a single regime. This can be interpreted considering a more homogeneous filling of the space by uniformly separated crystalline lamellae with absence of liquid pockets. In this case the RAP can be assigned to the crystalline-amorphous interface rather than to the whole inter-lamellar amorphous regions. As a matter of fact morphological studies for both PTT and PPT suggest a quite homogeneous crystal lamellae filling [50, 51]. It is worth mentioning that for aromatic polyesters of the type n-glycol terephthalate (nGT) the crystalline structure for 2GT (PET) exhibit unit cell with fully extended chain conformation while in those for 3GT(PTT), 4GT(PBT) and 5GT(PPT) the chain is contracted [52]. In principle one may speculate that these conformational differences of the crystals can affect the homogeneity of the lamellar crystal distribution although more experimental evidence is definitely needed.

4 Polymer Crystallization by Simultaneous Dielectric α and β-Relaxation Assessing

As discussed in the previous section, during crystallization not only the α-relaxation but also the β-relaxation is significantly affected. Early work by Coburn et al. about dielectric relaxation of poly(ethylene terephthalate) (PET), showed that the dielectric strength of the β-relaxation was inversely proportional to the amount of crystalline phase [9]. Accordingly, by measuring the β-relaxation during polymer crystallization one could, in principle, evaluate the amount of crystalline phase without the need of carrying out additional diffraction experiments. As mentioned above, to perform this while simultaneously measuring the α-relaxation can be difficult due to the relative frequency positions of α and β relaxations at the crystallization temperature of interest. However in some particular cases, like some low T_g aliphatic polyesters [28, 44], both α and β-relaxations may appear simultaneously in the covered frequency

range. This fact can enable a characterization during the crystallization of the structure development and of the segmental dynamics evolution by using the β-relaxation and the α-relaxation as probes, respectively. As an example, Fig. 9 (left panel) shows ε'' data collected during different stages of the cold crystallization of an aliphatic polyester, poly(propylene succinate) (PPS), ($T_g = -29°C$) [44]. In order to follow the crystallization process, a procedure as the one described in the previous section
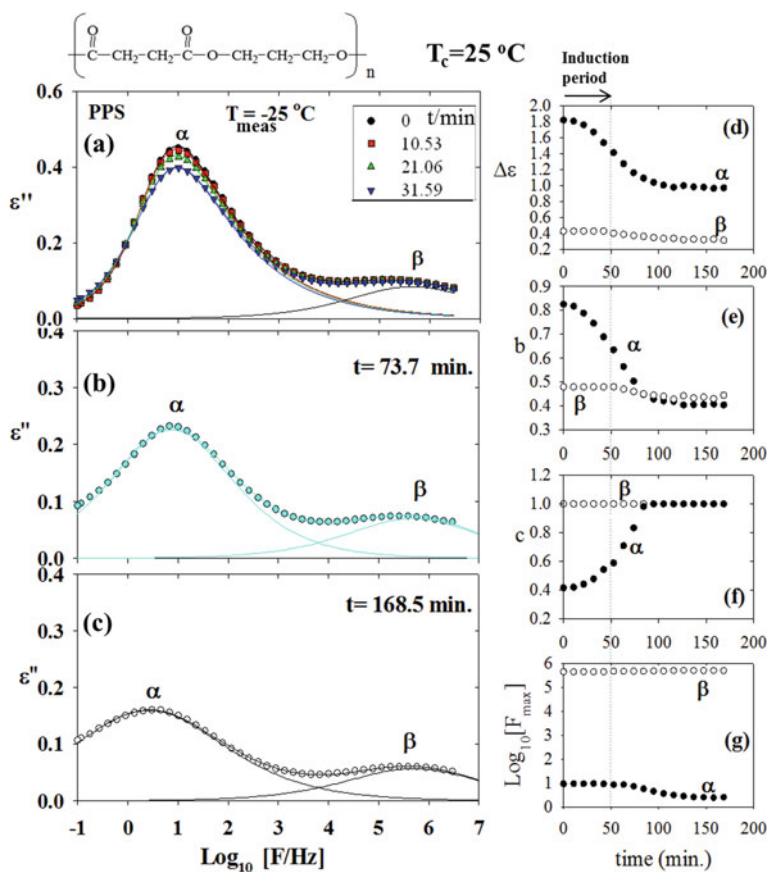
Fig. 9 (Left panel) Crystallization of initially amorphous poly(propylene succinate) (PPS) as revealed by BDS for different stages of crystallization including **a** the induction period and **b–c** later stages of crystallization. The polymer was held at a crystallization temperature of $T_c =$ 25°C for a controlled period of time and then rapidly cooled down to the measuring temperature ($T_{meas} = -25°C$). After performing a frequency swept at T_{meas} the sample is heated up back to T_c to wait for another time period. The procedure is repeated several times until the crystallization is considered terminated. Heating and cooling rates were 5°C/min. (Right panel) Results of the fittings of the HN equation to the dielectric data of the α (•) and β (○) relaxations: (*d*) dielectric strength ($\Delta\varepsilon$); (*e*) broadening parameter; (*f*) asymmetry parameter and (*g*) frequency of maximum loss. All parameters are represented as a function of crystallization time. Vertical dotted line indicates the limit of the induction period. " Adapted with permission from ref. [44]. Copyright (2019) Elsevier."

(Fig. 6) can be implemented. In this case, the polymer was held at the selected crystallization temperature, $T_c = 25°C$, for a controlled period of time and then rapidly cooled down to the measuring temperature ($T_{\text{meas}} = -25°C$). After performing a frequency sweep at the measuring temperature, lasting typically about 2 min, the sample is immediately heated up back to T_c to wait for another time period. This process is repeated several times until the crystallization is considered terminated. Heating and cooling rates were 5°C/min. At the measuring temperature both relaxation processes, α and β, are well resolved. The initial amorphous state is characterized by an intense α-relaxation and a less intense β-relaxation. In the early stage of crystallization, Fig. 9a, the α-relaxation clearly decreases in intensity with crystallization time while the β-relaxation remains nearly unaffected. Figure 9b, c show the evolution of the dielectric relaxations with crystallization time after the initial period until the completion of the crystallization process. Here, both α and β relaxations decrease with time. In addition, the F_{max} of the α relaxation exhibits a shift towards lower frequencies. The continuous lines in Fig. 9a–c correspond to the fits of the experimental data to Eq. 1. The β-relaxation can be described as being a symmetric process, $c = 1$, during the whole crystallization process. Figure 9 (right panel) shows the changes of the characteristic parameters as a function of crystallization time. It is worth mentioning the absence of a secondary α′-relaxation during crystallization as observed for the previously discussed PPT case (Fig. 4). This can be explained considering that, after completion of the crystallization process, the α-relaxation of the semicrystalline PPS sample is only about half an order of magnitude slower than the original one (Fig. 9), while for PPT the final segmental relaxation, α′, is almost four orders of magnitude slower than the initial one (Fig. 4). This fact provokes the α′ relaxation for PPS to merged with the α one. The general trend followed by the shape parameters of the α-relaxation are similar to that discussed in the previous paragraph: (i) a decrease of $\Delta\varepsilon_\alpha$ values associated to a reduction of the amorphous mobile phase due to a transfer to the crystalline phase, (ii) a broadening and concurrent symmetrization as reveled by evolution of the b_α and c_α parameters and (iii) a shift to lower values of the frequency of maximum loss, F_{max}, suggesting a slowing down of the amorphous phase dynamics due to the confinement exerted by the crystalline phase. The β-relaxation follows a similar trend although in contrast its maximum, F_{max}, remains essentially unaltered during crystallization. This last effect can be well understood considering the local character of the dynamics associated to the β-relaxation being therefore less affected by the crystalline phase [9, 40].

Considering that the dielectric strength of the β-relaxation is inversely proportional to the amount of the crystalline phase [9, 28, 44] then a characterization of structure development and dynamics could be possible by a single experiment. In this case the magnitude defined as $X_c^{\text{diel}} = 1 - \Delta\varepsilon_\beta/\Delta\varepsilon_\beta^0$ where $\Delta\varepsilon_\beta^0$ is the initial dielectric strength of the β-relaxation, can be used to estimate the crystallinity [28]. Figure 10 represents, for the data of PPS shown in Fig. 9, the dependence of $\Delta\varepsilon_\alpha$ as a function of X_c^{diel}.

The data reported in Fig. 10 clearly suggests the existence of three different regimes. First, an initial period where a significant reduction of $\Delta\varepsilon_\alpha$ takes place without a concurrent change in X_c^{diel}. The existence of this first regime where the $\Delta\varepsilon_\beta$
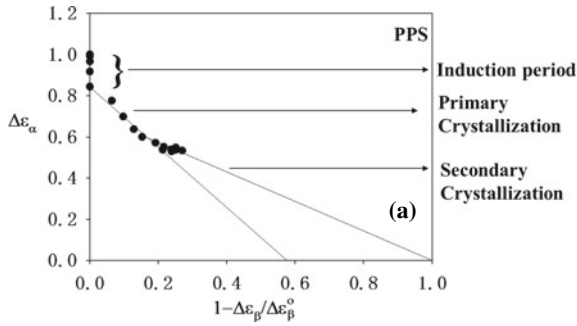
Fig. 10 Normalized dielectric strength $\Delta\varepsilon_\alpha$ as a function of $X_c^{\text{diel}} = 1 - \Delta\varepsilon_\beta/\Delta\varepsilon_\beta^0$ where $\Delta\varepsilon_\beta^0$ is the initial dielectric strength of the β-relaxation for the data shown in Fig. 9 for PPS. The straight lines are a guide for the eye. "Adapted with permission from ref. [44]. Copyright (2019) Elsevier."

remains nearly unchanged while a significant decrease of $\Delta\varepsilon_\alpha$, i.e. no increment in crystallinity is observed is a streaking fact of the crystallization experiments. Taking into account that $\Delta\varepsilon_\beta$ can be considered to be inversely proportional to the amount of crystalline phase then the first regime can be identified with an induction period of crystallization suggesting a modification of the segmental dynamics in the molten state with respect to the initial one. Several possibilities to account for this effect have been contemplated in the literature. One possibility is the formation of fringed micelle nuclei as expected when a spinodal liquid-liquid phase separation appears before crystallization [53, 54]. Another view, based on molecular simulation, is the formation in the induction period of crystallization of a type of precursor nuclei [55], which may act as physical cross-links of the amorphous phase and therefore modifying its dynamics. Regardless of the model invoked these results point towards the existence of precursors of crystallization in the induction period which has been an important topic in polymer crystallization in the recent years [53–57].

After the induction period, a second regime is observed in which a reduction of $\Delta\varepsilon_\alpha$ is accompanied by an increase of X_c^{diel}. Finally a third regime appears where the reduction of $\Delta\varepsilon_\alpha$ becomes directly inversely proportional to X_c^{diel}. Focusing our attention now on the second and third crystallization regimes, one can observe a qualitatively similar behavior previously illustrated in Fig. 7 for PET. Following a similar line of interpretation we can attribute the second period observed in Fig. 10 as corresponding to the primary crystallization in which the crystalline phase provoke a strong reduction in the amount of mobile material involved in the α-relaxation. As mention in the previous section, this fact can be understood assuming the formation of extra non-crystalline immobile RAP additional to the crystalline phase immobilized within the crystals and to the ordinary amorphous phase. The RAP can explain the strong reduction of $\Delta\varepsilon_\alpha$ for moderate increase of X_c^{diel} illustrated in Fig. 10 and reported for several polymers [35, 37, 44]. Within this view, the third regime corresponds to a secondary crystallization process where the reduction of $\Delta\varepsilon_\alpha$ becomes inversely proportional to X_c^{diel}. This trend has been interpreted by assuming that

during secondary crystallization the segmental immobilization induced by the crystalline phase is not as effective as in the previous period. As a matter of fact, in this period the amount of immobilized material runs in parallel to the amount of material incorporated to the crystals.

5 Polymer Crystallization Induced by Strain: The Case of Vulcanized Natural Rubber

Although temperature is the main variable involved in most of the studies in polymer crystallization also other magnitudes like pressure [58], shear [59] and strain [60] can play an important role in the crystallization process. A paradigmatic case for strain induced polymer crystallization is the one occurring in rubbers [61]. Natural rubber (NR) is a natural amorphous polymer ($T_g \approx -64^{\circ}$C) basically consisting of cis-1,4-isoprene units. NR is one of the most important natural materials present in many products of our everyday life. It possesses a unique microstructure consisting of different type of chain connections leading to the formations of a naturally occurring network formed by branch, star and network structures [62]. For most of the NR industrial applications it is compulsory to enhance both elasticity and tensile strength by converting the weak naturally occurring network into a more robust three-dimensional network [63]. This can be achieved by a process known as vulcanization by which cross-linking of the polymer chains is produced by covalent bonding formation typically by chemical reaction with sulfur [64]. As far as BDS is concern NR exhibits above its glass transition temperature two dielectric relaxation processes which are illustrated in Fig. 11a for a NR sample (Malaysian Rubber: Berhad, Malaysia, SMR CV60). Similarly to synthetic 1,4-cis-poly(isoprene) (PI) [65, 66], NR presents an asymmetry in its chemical structure inducing components of the dipolar moment parallel and perpendicular to the polymer chain. For this reason NR exhibits a standard segmental relaxation process, associated to the perpendicular dipole moment, and an additional slower one, referred to as normal mode, associated to the parallel dipole moment [65].

For vulcanized NR the dielectric relaxation process associated to the normal mode is suppressed as a consequence of the crosslinking (Fig. 11b). Therefore vulcanized NR exhibits above T_g only the α-relaxation associated to the segmental motions of the polymer chains [64, 67].

Natural rubber, similarly to other polymers, can crystallize by thermal treatment within the temperature window defined by its T_g and its melting point [68]. However the crystallization rate is rather slow reaching a maximum at $T_c \approx -20$°C [69]. It has been proposed that the mechanical performance of vulcanized NR originates from partial crystallization under the action of an extensional field. The formation of strain-induced crystals can be responsible of the tensile modulus enhancement observed when NR is subjected to fast deformations. The crystals are embedded into an amorphous phase forming a semicrystalline structure and orient themselves in

Fig. 11 Dielectric loss, ε'', spectra for **a** Natural rubber (Neat NR) and **b** Vulcanized natural rubber (Vulc NR)
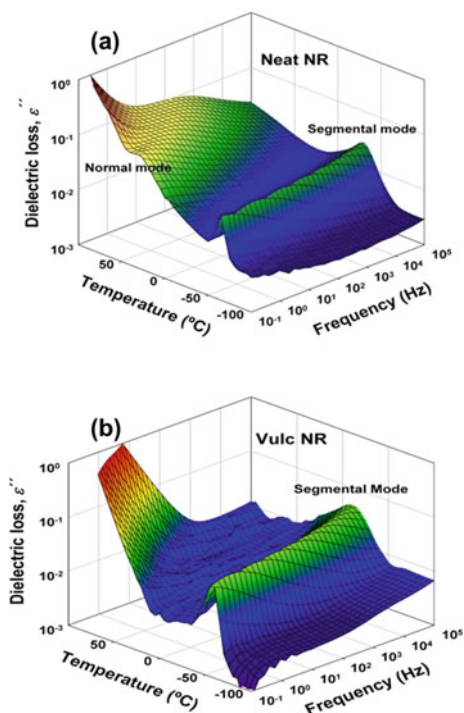
response to a macroscopic mechanical load [70]. Figure 12 shows one experiment of strain induced crystallization of a NR (Malaysian Rubber: Berhad, Malaysia, SMR CV60) sulfur vulcanized [71]. The tensile stress-strain curve of the vulcanized NR exhibits the characteristic mechanical behavior corresponding to a rubber -like elastomer (Fig. 12). It is proposed that the application of a tensile stress provokes a chain conformation change from a coiled to an extended configuration which at low strains is Hookean, i.e. linear relationship between stress and strain. However as stretching proceeds (strain ratio $\lambda > 3$) a significant increase in stress is observed characterized by a change in the slope of the stress-strain curve. This peculiar property of NR is mainly due to a crystallization process induced by stretching causing molecular alignment in the stretching direction. Strain induced crystallization can be quantitatively evaluated by Wide and Small Angle X-ray Scattering (WAXS and SAXS) [61, 71]. Different 2-dimensional WAXS patterns measured in NR samples stretched at different strain ratios are shown in Fig. 12. The corresponding 2-dimensional SAXS patterns are also shown at the bottom. For strain ratios between $\lambda = 0$ (initial non-stretched sample) and $\lambda = 2.5$ the patterns (insets (a) and (b)) exhibit a diffuse ring characteristic of an amorphous isotropic material. However at $\lambda \approx 3$ crystallization starts taking place as revealed by the presence of crystalline diffraction Bragg maxima. For higher strain ratios ($\lambda > 3$), the patterns (insets (d-g)) clearly show the diffraction maxima characteristic of an oriented crystalline phase which has been
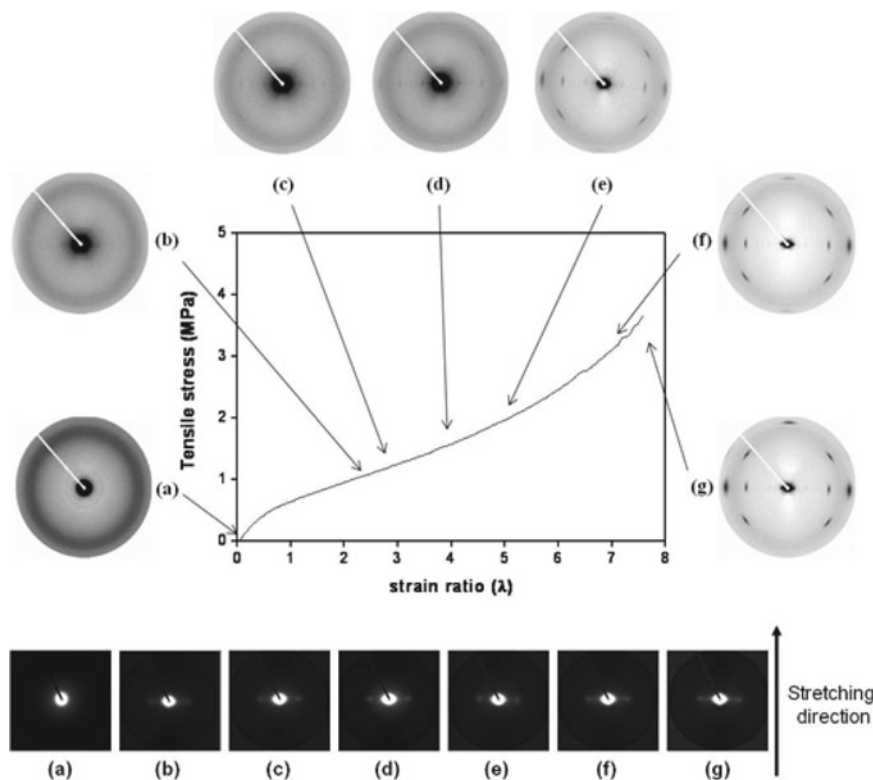
Fig. 12 Tensile stress-strain curve of a vulcanized NR sample stretched up to a strain ratio of $i = 7.5$. Insets correspond to WAXS patterns of NR upon stretching at room temperature at different strain ratios λ indicated by the arrows: **a** 0, **b** 2.5, **c** 3, **d** 4, **e** 5, **f** 7 and **g** 7.5. The corresponding SAXS patterns [72] are shown at the bottom. " Adapted with permission from ref. [71]. Copyright (2019) American Chemical Society."

induced by strain. Moreover, the Bragg peak intensities of these reflections increase with increasing strain. This effect can be better visualized by an azimuthal integration of the WAXS patterns represented in Fig. 13a. Here the $360°$ azimuthally integrated intensity has been represented as a function of the scattering vector $q = 4\pi/\lambda_w(\sin\theta)$ being λ_w the X-ray wavelength and 2θ the scattering angle. It is noteworthy that an amorphous halo always remains during the stretching process suggesting the presence of a significant amorphous phase.

The evolution with the strain ratio of the SAXS patterns (Fig. 12 bottom) shows that for $\lambda > 2$ the scattering tends to spread along the equator with increasing stretching. This suggests the appearance of density fluctuation elongated in the stretching direction. For strain rations $\lambda > 3$ a clear maximum appears in the equator concurrently with the appearance of the crystalline phase as revealed by the WAXS patterns. This maximum corresponds to the long spacing related to the average distance between the crystalline lamella separated by amorphous domains. The long
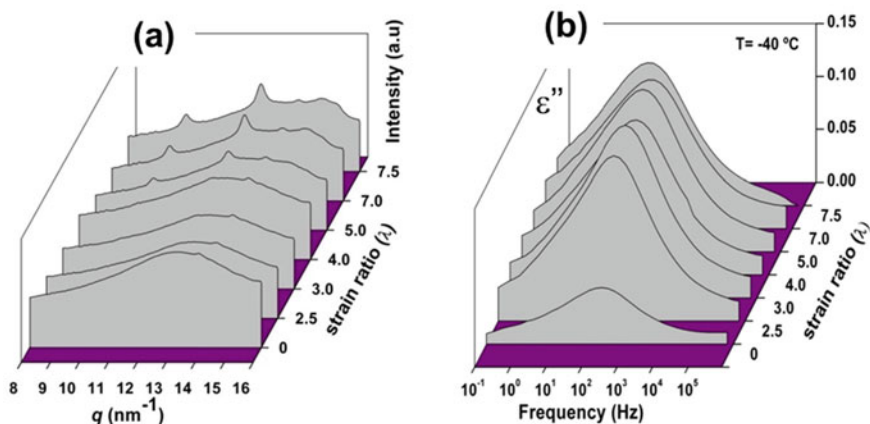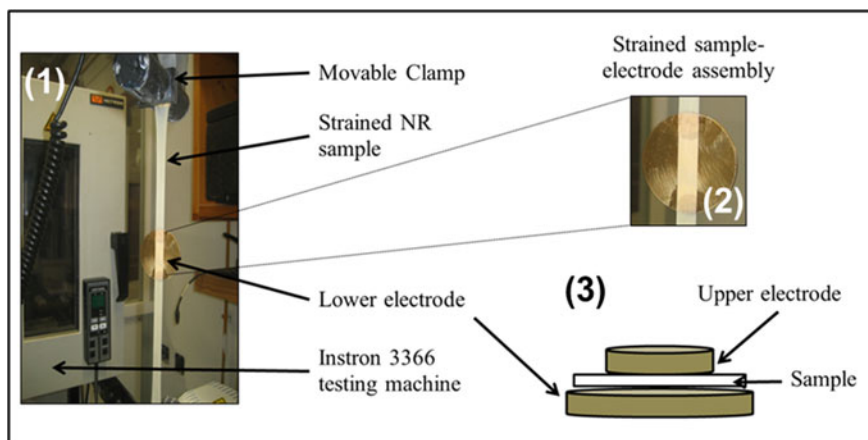
Fig. 13 (Upper panel) Scheme describing a experimental approach to evaluate the effect of strain induced crystallization in NR as characterized by BDS: (1) The vulcanized NR sample is subjected to uniaxial deformation at room temperature by using a dynamometer (strain ratio shown λ = 7.5). (2) Subsequently the elongated sample is glued either to a gold-plated electrode for BDS measurements or to a metallic frame for the X-ray scattering experiments. (3) The stretched sample-electrode set can be detached from the dynamometer clamps. (Lower panel): **a** Azimuthally integrated intensity of the WAXS patterns as a function of the scattering vector q and **b** Dielectric loss, ε'', as a function of frequency at different strain ratios (λ) for vulcanized NR [71]. "Adapted with permission from ref. [71]. Copyright (2019) American Chemical Society."

spacing value $L \approx 3.9$ nm estimated from the SAXS patterns remains almost constant for the whole strain ratio range explored.

The effect of strain induced crystallization in NR can be characterized by BDS according to the experimental procedure described in Fig. 13 (upper panel) [71, 73].

First, the vulcanized NR sample is subjected to uniaxial deformation at room temperature by using a dynamometer. In this way, samples with defined strain ratios

can be prepared. Subsequently, the elongated sample can be glued either to a gold-plated electrode for BDS measurements, or to a metallic frame for the X-ray scattering experiments. Finally, the stretched sample-electrode set can be detached from the dynamometer clamps. As mentioned above, vulcanized NR only exhibits above T_g the characteristic α-relaxation because the normal mode has been suppressed by the cross-linking induced by vulcanization. Therefore in order to assess the effect of stretching on the segmental dynamics of vulcanized NR the BDS experiments can be accomplished at a temperature at which the α-relaxation is well centered within the frequency window measured. As an example Fig. 13b shows dielectric loss spectra as measured at $T = -40°C$ for vulcanized NR at the different strain ratios. The dielectric loss data for different stretch ratios can be well fitted according to HN equation (Eq. 1) considering one relaxation process. Figure 14 (left panel) shows the frequency dependence of ε'' for stretched vulcanized NR at different strain ratios and the results of the fittings to the HN equation. The HN fitting parameters ($\Delta\varepsilon$, b, c and τ_{HN}) have been represented in Fig. 14 (right panel).

It is worth mentioning that the dielectric loss curves exhibit a systematic deviation from the fitting of the experimental results at low frequencies. This effect has been
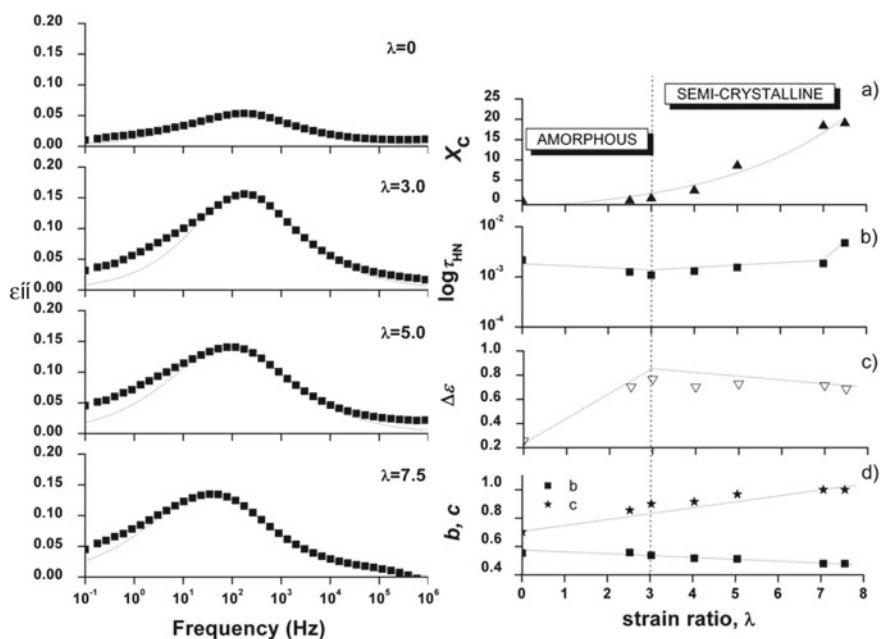
Fig. 14 (Left panel): Dielectric loss data, ε'', as a function of frequency at $T = -40°C$ for vulcanized NR samples stretched at different strain ratios as indicated. Dotted lines correspond to best HN fitting. (Right panel): **a** Crystallinity index (X_c), **b** segmental relaxation time (τ_{HN}), **c** dielectric strength ($\Delta\varepsilon$), and **d** dielectric shape parameters (b, c) as a function of strain ratio (λ) for vulcanized NR samples. Dotted lines are guides for the eye. "Adapted with permission from ref. [71]. Copyright (2019) American Chemical Society."
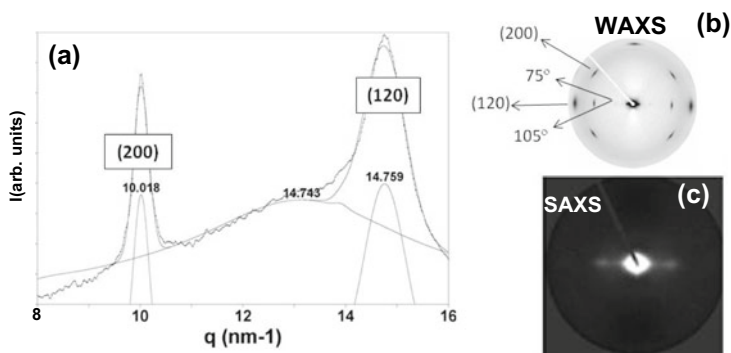
Fig. 15 **a** Example of an equatorial cake integrated intensity as a function of the scattering vector q taken from the WAXS pattern of stretched vulcanized NR at $\lambda = 7.5$. **b** WAXS image shows integration limits for the cake (from 75° to 105°). **c** Corresponding SAXS pattern at $\lambda = 7.5$ is also shown. "Adapted with permission from ref. [71]. Copyright (2019) American Chemical Society."

reported several times in the literature and attributed either to stearic acid [74] or to zinc oxide [64] both presents in the formulation of vulcanized NR rubber.

Information about the structure development upon stretching can be obtained from the WAXS experiments (Fig. 12). The strain induced crystalline structure developed by vulcanized NR corresponds to that of the monoclinic unit cell of poly(isoprene) [75, 76]. Different procedures have been proposed to evaluate quantitatively the strain-induced crystallinity from WAXS patterns. The most accepted one is based on the estimation of a crystallinity index based on the equator diffraction peaks [76]. As an example Fig. 15a shows the WAXS integrated intensity as a function of the scattering vector q for a strain ratio of $\lambda = 7.5$ for an angular cake between 75°–105° illustrated on the top of Fig. 15b.

The resultant patterns can be deconvoluted considering the diffraction peaks of the 200 and 120 reflections of the crystalline phase and the amorphous halo contribution to evaluate a mass fraction crystallinity index, X_c, from the ratio of the area under the crystalline peaks to the total scattered intensity. Calculated crystallinity index, X_c, for vulcanized NR samples as a function of the strain ratio are shown in Fig. 14a. Figure 15c shows the SAXS pattern for $\lambda = 7$ exhibiting a maximum corresponding to the long spacing related to the average distance between the crystalline lamella separated by amorphous domains at $L \approx 3.9$ nm.

The results suggest that for strain ratios $\lambda < 2.5$ vulcanized NR remains amorphous. However, strain-induced crystallization occurs for $\lambda > 2.5$ and the crystallinity index gradually increases with strain ratio. These results agree well with the significant change of slope observed in the stress-strain measurements (Fig. 12) and suggest that the polymer chains, which are initially coiled, stretch along the drawing direction and partially crystallize once a critical value is reached. According to Tosaka et al. [75] the network in vulcanized NR is expected to be composed of molecules with a broad distribution of chain lengths between the network points. By stretching, only the
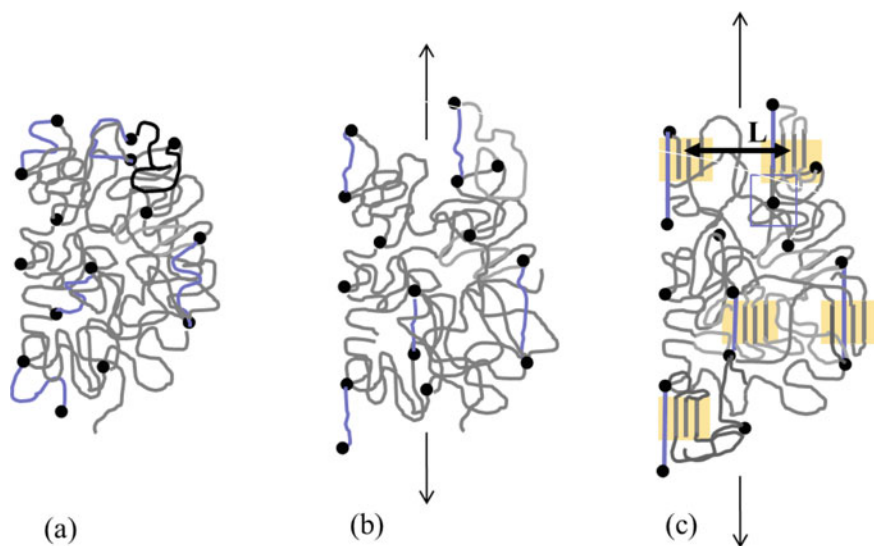
Fig. 16 Model of strain induced crystallization in vulcanized NR based on Tosaka et al. (see text for details). Short chains are drawn as blue lines. Filled circles represent cross-links. **a** Before deformation. **b** After deformation: short chains are fully stretched. **c** Crystallites are grown from the stretched chains. The experimental value of the long spacing, L, extracted from the SAXS experiments (Fig. 15c) has been added to the model for illustrative purposes

molecules of small chain length between the densely packed network points can be oriented and form crystallites, whereas the molecules of much longer chain lengths would remain in the random coil state. Some of the tie molecule chains which have overflown form fibrillary crystallites by the drawing process and hence, the degree of crystallinity can further increase by subsequent drawing. A schematic representation of this model is displayed in Fig. 16.

The effect of such amorphous to semicrystalline transition on the segmental dynamics of the stretched vulcanized NR samples can be discussed on the basis of the results shown in Fig. 14. The dependence of the dielectric magnitudes (Fig. 14 (right panel)) can be separated into two regimes. In a first regime, for $\lambda < 3$, where no crystallization is evidenced there is, however a dramatic increase of the dielectric strength, $\Delta\varepsilon$. In a second regime, for $\lambda > 3$, strain induced crystallization takes place the variation of the shape parameters with increasing strain ratio indicates a broadening of the relaxation for the segmental process. In this second regime, a decrease of $\Delta\varepsilon$ is observed. This type of behavior, that has been illustrated and discussed in the previous section, is the characteristic one expected for the polymer crystallization induced by thermal treatment where the crystalline domains slow down the segmental dynamics. Indeed, for vulcanized NR the relaxation time, τ_{HN}, tends to increase slightly with the strain once crystallization appears. A reduced segmental mobility is expected by the confinement effect exerted by the crystalline phase. In a

first approach changes in $\Delta\varepsilon$ can be discussed on the basis of the Frölich- Kirkwood (FK) equation:

$$\Delta\varepsilon \propto \frac{4\pi\rho N_A}{9kTM} g\mu^2 \propto \mu_{\text{eff}}^2 \tag{3}$$

where ρ is the density, μ is the dipole moment, M is the molecular weight of the repeating unit, N_A is Avogadro's number, k is the Boltzmann constant. The correlation factor, g, contains contributions of both inter and intra chain dipolar correlations and indicates the angular correlation between dipolar groups. The g factor is frequently referred to as a reduction factor since the term $g\mu^2 = \mu_{\text{eff}}^2$ corresponds to an effective dipole moment of the material. In the absence of correlation among dipoles, as for example in a gas, $g \approx 1$. For vulcanized NR in the first regime, $\lambda < 3$, an increase of the density induced by stretching is expected by. However, according to Eq. 3, the increment of $\Delta\varepsilon$ of about three times cannot be exclusively explained by this fact. In vulcanized NR the dipole moments contributing to the segmental relaxation are mainly perpendicular to the polymer chain [66]. In the undeformed state vulcanized NR, as most polymers different molecular conformations partially cancel the net dipolar contribution. However, stretching can counteract this effect by selective molecular orientation provoking the observed increase of the dielectric strength. Although the most favorable conformation of cis-1,4-polyisoprene should be that with alternating CH_3^- pendant groups in which dipoles should balance along the chain [77] recent molecular modelling shows that the molecular asymmetric unit of ordered cis-1,4-polyisoprene is a di-isoprene in which the two isoprene residues have distinctive, not symmetrically related conformations [78]. This suggests a possible increase of μ_{eff} by stretching in support of the observed increment of $\Delta\varepsilon$. In the second regime, $\lambda > 3$, crystallization should induce a net decrease of the dielectric strength since the crystalline phase lacks the segmental relaxation. Consequently the effect caused by stretching can be counterbalanced by that of crystallization producing almost no change in $\Delta\varepsilon$ for further stretching.

6 Conclusions

Broadband Dielectric Spectroscopy (BDS) is a powerful technique to investigate polymer crystallization in order to characterize modifications of the amorphous phase dynamics. Of special interest is the combination of BDS with scattering techniques probing structure development during crystallization in real time. During cold crystallization of polymers the α relaxation suffers significant modifications consisting of the appearance of a new segmental process (α') associated to the segmental relaxation of a confined amorphous phase coexisting with the initial one. By analysis of the evolution of the α-relaxation during crystallization, information about the type distribution of the crystal lamellar stacks, either homogeneous or heterogeneous, in

the sample can be obtained. During cold crystallization not only the α-relaxation but also the β-relaxation can be significantly affected by crystallization. The dielectric strength of β-relaxation linearly decreases with crystallinity suggesting that local dynamics is essentially arrested in the crystalline phase.

BDS can be used to follow in a straightforward manner the isothermal polymer crystallization of some low T_g polymers exhibiting at the same temperature both the α and the β relaxations in the measured frequency window. In these cases, by simultaneous measurement of the α and the β relaxations a characterization in a single experiment of the structure development, by the magnitude $X_c^{\text{diel}} = 1 - \Delta\varepsilon_\beta/\Delta\varepsilon_\beta^0$ where $\Delta\varepsilon_\beta^0$ is the initial dielectric strength of the β-relaxation, and of the dynamics evolution, by $\Delta\varepsilon_\alpha$, can be accomplished during the crystallization process. The results obtained suggest the existence of three differentiated regimes for crystallization as revealed by BDS. Initially there is an induction period where $\Delta\varepsilon_\alpha$ decreases without significant increase of the crystallinity. These results point towards the existence of precursors of crystals in the induction period of crystallization. After the induction time a primary crystallization period follows, in which $\Delta\varepsilon_\alpha$ decreases strongly with crystallinity. This effect supports the existence of a Rigid Amorphous Phase (RAP) formed by amorphous but immobile material in addition to the crystalline phase immobilized within the crystals and to the ordinary mobile amorphous phase. Finally there is secondary crystallization regime where $\Delta\varepsilon_\alpha$ decreases inversely proportional to crystallinity. Here, the segmental immobilization induced by the crystalline phase is not as effective as in the previous period and the amount of immobilized material runs in parallel to the amount of material incorporated to the crystals.

BDS can by also used to investigate strain induced polymer crystallization as occurring in vulcanized natural rubber whose segmental dynamics is significantly affected by uniaxial stretching. By combining BDS and X-ray scattering techniques three regimes have been characterized upon stretching. For low strains, stretching takes place without crystallization but with a dramatic increase of the dielectric strength which cannot be accounted for by considering an increase in density. The dielectric experiments suggest an increase of the effective dipole moment induced by upon stretching as the responsible for the increment in $\Delta\varepsilon_\alpha$. For intermediate strain ratios, crystallization takes place and the inclusion of segments into the crystalline phase counteracts the increment in $\Delta\varepsilon_\alpha$ provoked by stretching. The experiments support a model in which by stretching, only the molecules of small chain length between the densely packed network regions can be oriented and form crystallites, whereas longer molecules remain in the random coil state. In summary, BDS has contributed significantly to the understanding of crystallization. However, the continuous engagement of scattering techniques to investigate novel in situ and in-operando processes [79, 80] will require of complementary techniques. For sure BDS can be one of them.

References

1. PlasticsEurope-AISBL (2018). Available from: https://www.plasticseurope.org/en/resources/publications/619-plastics-facts-2018
2. Kovacs AJ (1958) J Polym Sci 30(121):131–147
3. Young RJ (ed) (1981) I.t. Polymers. London: Chapman and Hall
4. Strobl G (1996) The physics of polymers. Springer-Verlag, Berlin
5. Bassett DC (1981) Principles of polymer morphology. Cambridge University Press, Cambridge
6. Keller A (1957) Phil Mag 2(21):1171
7. Gedde UW (1995) Polymer physics. Chapman and Hall, London
8. Angell CA (1997) J Res Natl Inst Stan Technol 102(2):171–185
9. Coburn JC, Boyd RH (1986) Macromolecules 19(8):2238–2245
10. Sics I et al (2000) Rev Sci Instrum 71(4):1733–1736
11. Sanz A et al (2005) Phys B-Condens Matter 370(1–4):22–28
12. Wurm A, Minakov AA, Schick C (2009) Eur Polym J 45(11):3280–3289
13. Sanz A et al (2018) Rev Sci Instrum 89(2)
14. Ezquerra TA et al (1994) Phys Rev B 50(9):6023–6031
15. Alvarez C et al (2004) Polymer 45(11):3953–3959
16. Sanz A et al (2010) Macromolecules 43(2):671–679
17. Lund R et al (2008) Macromolecules 41(4):1364–1376
18. Kremer F, Schonhals A (eds) (2002) *Broadband dielectric spectroscopy*. Springer Verlag: Heidelberg, Germany
19. Williams G (1979) Adv Polym Sci 33:59–92
20. Nogales A et al (2000) Macromolecules 33(25):9367–9375
21. Cerveny S et al (2008) Macromolecules 41(22):8669–8676
22. Wang Y et al (2005) Macromolecules 38(11):4712–4718
23. Dionisio M et al (2005) Macromol Rapid Commun 26(17):1423–1427
24. Napolitano S, Wubbenhorst M (2006) Macromolecules 39(18):5967–5970
25. Georgiev G, Cebe P, Capel M (2005) J Mater Sci 40(5):1141–1152
26. Ezquerra TA et al (2005) J Non-Cryst Solids 351(33–36):2768–2772
27. Martin-Fabiani I et al (2013) Polymer 54(21):5892–5898
28. Soccio M et al (2007) Phys Rev Lett. 98(3)
29. Sangroniz L et al (2018) Macromolecules 51(10):3663–3671
30. Fukao K, Miyamoto Y (1997) Phys Rev Lett 79(23):4613–4616
31. Balta-Calleja FJ (1989) X-ray scattering of synthetic polymers. Elsevier, Amsterdam
32. Blundell DJ, Osborn BN (1983) Polymer 24(8):953–958
33. Rueda DR et al (2006) Rev Sci Instrum 77(3)
34. Jimenez-Ruiz M et al (2005) Rev Sci Instrum 76(4)
35. Soccio M et al (2014) Polymer 55(6):1552–1559
36. Havriliak S, Negami S (1967) Polymer 8(4):161–&
37. Sanz A et al (2006) Polymer 47(4):1281–1290
38. Denchev Z et al (2000) J Polym Sci Part B-Polym Phys 38(9):1167–1182
39. Schonhals A, Schlosser E (1989) Colloid Polym Sci 267(2):125–132
40. Ngai KL (2011) Relaxation and diffusion in complex systems. Springer, New York
41. Bravard SP, Boyd RH (2003) Macromolecules 36(3):741–748
42. Soccio M et al (2012) Macromolecules 45(1):180–188
43. Boyd SU, Boyd RH (2001) Macromolecules 34(20):7219–7229
44. Soccio M et al (2007) Polymer 48(16):4742–4750
45. Huo PT, Cebe P (1992) Macromolecules 25(2):902–909
46. Dobbertin J, Hensel A, Schick C (1996) J Therm Anal 47(4):1027–1040
47. Kalakkunnath S, Kalika DS (2006) Polymer 47(20):7085–7094
48. Huo PT, Cebe P (1992) Abs Pap Am Chem Soc 203:372–POLY
49. Laredo E et al (2013) Euro Polym J 49(12):4008–4019
50. Ivanov DA et al (2008) Macromolecules 41(23):9224–9233

51. Pi LW, Woo EM, Liu HL (2004) J Polym Sci Part B-Polym Phys 42(23):4421–4432
52. Hall IH, Pass MG, Rammo NN (1978) J Polym Sci Part B-Polym Phys 16(8):1409–1418
53. Imai M, Kaji K, Kanaya T (1993) Phys Rev Lett 71(25):4162–4165
54. Olmsted PD et al (1998) Phys Rev Lett 81(2):373–376
55. Muthukumar M, Welch P (2000) Polymer 41(25):8833–8837
56. Ezquerra TA et al (1996) Phys Rev E 54(1):989–992
57. Strobl G, Cho TY (2007) Euro Phys J E 23(1):55–65
58. Rastogi S, Newman M, Keller A (1991) Nature 353(6339):55–57
59. Nogales A et al (2001) Polymer 42(12):5247–5256
60. Nogales A et al (2003) Macromolecules 36(13):4827–4832
61. Toki S et al (2003) Polymer 44(19):6003–6011
62. Carretero-Gonzalez J et al (2010) Soft Matter 6(15):3636–3642
63. Brydson JA (1988) Rubbery materials and their compounds. Elsevier Science Publishers Ltd., Essex
64. Hernandez M et al (2012) Macromolecules 45(2):1070–1075
65. Adachi K, Kotaka T (1988) Macromolecules 21(1):157–164
66. Boese D, Kremer F (1990) Macromolecules 23(3):829–835
67. Hernandez M et al (2010) Macromolecules 43(2):643–651
68. Magill JH (1995) Rubber Chem Technol 68(3):507–539
69. Wood LA, Bekkedahl N (1946) J Appl Phys 17(5):362–375
70. Poompradub S et al (2005) J Appl Phys 97(10)
71. Hernandez M et al (2011) Macromolecules 44(16):6574–6580
72. Hernández M (2012) Ph.D. thesis, University Compluense of Madrid
73. Hernández M et al (2013) Macromolecules 46(8):3176–3182
74. Ortiz-Serna P et al (2010) Macromolecules 43(11):5094–5102
75. Tosaka M et al (2004) Macromolecules 37(9):3299–3309
76. Toki S et al (2009) Polymer 50(9):2142–2148
77. Benedetti E, Corradini P, Pedone C (1975) Euro Polym J 11(8):585–587
78. Rajkumar G, Squire JM, Arnott S (2006) Macromolecules 39(20):7004–7014
79. Nogales A, Gutiérrez-Fernández E, García-Gutiérrez MC, Ezquerra TA, Rebollar E, Šics I, Malfois M, Gaidukovs S, Gēcis E, Celms K, Bakradze G (2019) Macromolecules 52(24):9715–9723
80. Schottelius A, Mambretti F, Kalinin A, Beyersdorff B, Rothkirch A, Goy C, Mueller J, Petridis N, Ritzer M, Trinter F, Fernandez JM, Ezquerra TA, Galli DE, Grisenti RE (2020) Nature Materials 19:512–516

Crystallization of Polymers Under 1D Confinement

Simone Napolitano

Abstract Crystallization of polymers becomes tremendously sluggish upon confinement at the nanoscale level, where a severe reduction in the overall crystallization rate is commonly observed. In extreme cases, below a critical thickness (usually on the order of few tens of nm) polymer chains do not crystallize. This phenomenon has attracted a considerable technological interest. Being able to suppress, or at least to reduce, the crystallization rate would yield, for example, a tremendous increase in safety of those amorphous drugs where the crystalline form has non-negligible toxicity, and a neat improvement the lifetime of polymer-based nanodevices where the presence of crystals affects materials properties. While most of the work on crystallization on confinement focused on the investigation of the formation of crystalline structures, less is known on the molecular origin of the confinement effects of the slower kinetics. Unveiling the nature of the changes in crystallization rate requires the use of experimental approaches, as broadband dielectric spectroscopy, permitting to achieve information also on molecular relaxation processes taking place in the noncrystalline component. In this chapter, we will summarize the outcome of the investigation of the cold crystallization of thin polymer films (1D confinement) via Broadband Dielectric Spectroscopy (BDS). After discussing the experimental protocol necessary to perform such measurements, we will show how BDS can be employed to disentangle the nucleation and the growth component of the kinetics. Finally, we will discuss on the interplay between chain adsorption and crystal growth in thin films and introduce a general picture of the competition between the two phenomena affecting mass transport at the nanoscale level.

Keywords Thin polymer films · 1D confinement · Dielectric spectroscopy · Segmental mobility · Crystallization · Irreversible adsorption

S. Napolitano (✉)
Polymer and Soft Matter Dynamics, Experimental Soft Matter and Thermal Physics (EST), Faculté des Sciences, Université Libre de Bruxelles (ULB), 1050 Ixelles, Brussels, Belgium
e-mail: snapolit@ulb.ac.be

Abbreviations

BDS   Broadband Dielectric Spectroscopy
C   Capacitance
G   Crystal growth rate
h   Film thickness
LN2   Liquid nitrogen
PEO   Polyethylene oxide
PEN   Poly(ethylene 2,6-naphthalate)
PET   Poly(ethylene terephthalate)
PHB   Poly(3-hydroxy butyrate)
PLLA   Poly(L-lactide acid)
t_{cry} Crystallization time
TFA   Trifluoroacetic acid
T_g Glass transition temperature
T_m Melting temperature
$\Delta\varepsilon$ Dielectric strength
ξ Stokes–Einstein exponent

1 Introduction

Nanoconfinement affects the crystallization of polymers [1]. For long chains, same as in the case of smaller molecules [2], the complex set of mechanisms leading to the formation of ordered structures is affected by both finite size [3] and interfacial effects [4]. The former case is related to a change occurring in a given property, e.g., the crystal growth rate, when reducing a size of the system from infinite to below a threshold value, related to a length scale of the system, e.g., a multiple of the lamellar thickness. Interfacial effects, instead, arise from a perturbation in material properties because of the presence of an interface with another medium. This is, for example, the case of density which might significantly vary in proximity of adsorbing walls or at the free surface with air.

The literature on the impact of nanoconfinement on the crystallization of polymers is impressively large [5–15]. Most of the work has, however, focused on the analysis of changes in crystalline morphology and perturbations in the crystal growth rate, by means of different optical and scanning probe microscopies. This type of investigation has brought to a tremendous advancement of our knowledge on crystallization: investigation of polymers confined at the nanoscale level permitted us to test the robustness of theories of crystal formation. Working with confined geometries has, in fact, allowed reaching regimes of undercooling, [16] and peculiar nucleation densities otherwise not achievable in bulk [3, 17].

Despite this progress, little is known on how molecular mobility affects crystallization in bulk and at the nanoscale. This is not related to lack of interest

towards the topics, but to the limited number of experimental techniques permitting to characterize the relaxation processes occurring in polymers during crystallization. In the case of confined geometries (thin films, nanorods, etc), at the state of the art, only broadband dielectric spectroscopy has been able to provide a microscopic information on mechanisms of crystallization [4, 14, 18–28].

In this chapter, focusing on 1D confinement (thin films), we will revise the results of the investigation of the kinetics of crystallization by means of broadband dielectric spectroscopy. After introducing the methodology to perform such measurements, we will discuss on a model of the thickness dependence of the crystallization rate and finally show the first experimental tests supporting its validity. We will conclude this chapter with a short perspective on future work which could further advance our understanding of the crystallization at molecular level.

2 Guidelines for Sample Preparation

Samples for the investigation of the crystallization in thin films are commonly prepared in the geometry of capped films, via a bottom-up approach permitting to fabricate nanocapacitors by alternating conductive and dielectric layers; see Fig. 1. Tough lacking a direct optical access, this geometry has several advantages. Its symmetry [29] (metal/polymer/metal) eases modeling with respect to the case of supported film (wall/polymer/gas) where the presence of two intrinsically different interfaces requires a larger number of hypotheses. Capped geometry is also a benchmark system for the investigation of nanocomposites, [30] and is relevant at industrial level, especially in the case of multilayers, for packaging applications.
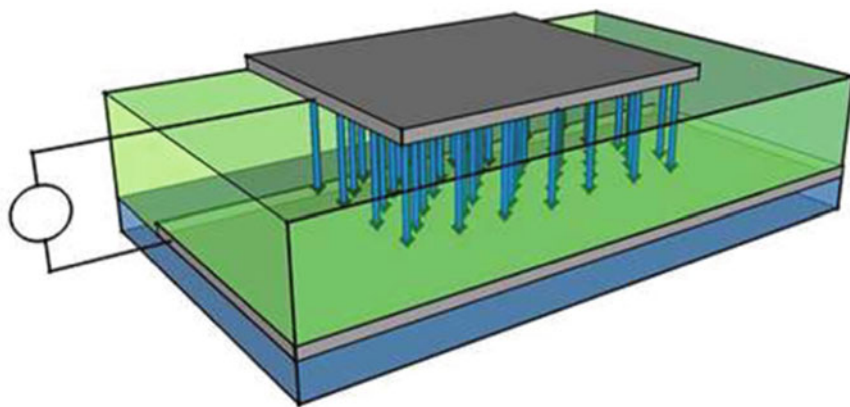
Fig. 1 Sketch of the approach currently used to perform crystallization experiments on ultrathin polymer films via dielectric spectroscopy. The polymer layer, a dielectric medium is capped between two conductive layers (e.g., thermally evaporated Al)

To ensure mechanical stability and to allow an easier manipulation of the whole sample, the first conductive layer is thermally evaporated onto a thick boronsilicate glass plate, that was previously cleaned in baths of commonly used solvents (e.g., acetone, isopropanol). The material usually chosen for the conductive layer is aluminum, which quickly oxides in contact with air (oxide layer thickness $\approx$3 nm). Aluminum is preferred to other metals with better electric properties, because it is cheaper, it can be directly evaporated onto glass and its roughness can be easily tuned [31], while Au having a lower wettability requires the previous deposition of Cr. Furthermore, Al forms sharper interfaces with polymers, while other metals, as Au and Ni, do diffuse inside the organic layer [32]. Regardless of the metal chosen for evaporation, high purity is required. The presence of contaminants, e.g., other metals, might increase the resistivity of the conductive layer, which results in a known electronic artifact affecting the high-frequency response of confined systems. Because of the reduced distance between electrodes, these samples are characterized by a high capacitance, which for thin films easily reach the nF range; combining the large capacity, C, values with a nonzero resistivity of the (non-pure) metallic layers gives rise to an RC circuit, with characteristic time up to few ms, which limits the investigation of dielectric properties at high frequencies. In the case of thin polymer films, as C decreases with the inverse of film thickness, a bad control of the metallic can evaporation can yield to a smaller and smaller frequency range where the measured dielectric function is not affected by this electronic artifact.

The dielectric medium, in this case, the thin polymer film, is deposited via spin-coating, a technique widely used to cover small to large flat surfaces. Solutions of the polymer in a good solvent are poured on a plate spinning at several thousand rotations per minute; within a short time (<1 min), the abrupt expulsion of solvent upon spinning yields vitrification of the polymer layer. Annealing above T_g allows evaporation of the solvent an eases reduction in mechanical stresses arising from film formation [33]. To allow application of an electric-field (E-field), a second metallic layer is deposited on top of the dielectric medium.

Depending on the polymer and solvent pair, the thin polymer film could contain a relevant crystalline volume fraction. To obtain noncrystalline samples, amorphization is possible by quenching the nanocapacitors from a temperature above the melting transition down to sufficiently low temperatures, ideally below the glass transition temperature, T_g. It should be noted that, despite the possibility of degradation upon processing of thin layers above the melting temperature, T_m, amorphizing thin films is easier than obtaining noncrystalline bulk melts, because of the most efficient heat transfer (reduced volume) and the drop in T_m upon confinement.

Dielectric measurements on thin films are performed as in the case of bulk samples, by applying a relatively small E-field (<10^6 V/m) to the (nano) capacitor and measuring the current flow as a function of the frequency of the field. Differently than in the case of micron-thick samples, the E-field is applied without a direct mechanical contact on the nanocondensator, because application of pressure would induce a shortcut. Peaks in the frequency domain are associated with molecular processes taking place at a timescale corresponding to the inverse of the frequency of the maximum [34].

Focusing on the structural process, the intensity of the polarization process is proportional to the number of dipole moments fluctuating at the time of the experiment [35]. Because of this link, the intensity of the structural peak, $\Delta\varepsilon$, is a probe of the volume fraction of the amorphous phase. The reduction in the solid angle over which dipole moments are allowed to fluctuate when they are incorporated into crystals allows monitor crystallization via BDS. The timescale of the reduction in $\Delta\varepsilon$ is thus associated with the conversion of the amorphous phase into the ordered structures, and to glass stability. Monitoring the changes in the dielectric response of a material while it crystallizes, hence, permits measuring the timescale of crystallization together with the changes in the structural relaxation time.

3   Slowing Down in the Crystallization Kinetics of 1D Confined Polymers

The crystallization kinetics in ultrathin polymer films has been investigated by several techniques in both isothermal and nonisothermal conditions [1]. The large experimental data set collected so far shows that the rate of crystallization strongly decreases upon reducing the thickness, leading to an increase of the crystallization time t_{cry} up to several orders of magnitude, compared to the value measured in bulk melts [4, 24, 36–39]. In some case, below a given thickness, crystallization seems suppressed, no detectable change is observed within timescales exceeding months [39, 40]. These extreme conditions have attracted a large number of studies. The inhibition of crystallization upon confinement has attracted a considerable technological interest. Being able to suppress, or at least reduce, the crystallization rate would yield, for example, a tremendous increase in safety of those amorphous drugs where the crystalline form has non-negligible toxicity [2], and a neat improvement in the lifetime of polymer-based nanodevices, as coatings for optics and display applications where the presence of crystals affects materials properties [1], e.g., opacity.

Understanding the reasons yielding these tremendous changes in crystallization rate upon confinement is thus of fundamental importance. One of the first hypotheses considered was an increase in glass transition temperature upon confinement [39]. Such change in T_g would imply an increase in segmental relaxation time in isothermal conditions and consequently lower self-diffusion coefficient. The latter reduction corresponds to a neat drop in mass transport towards the crystalline growth front, which would justify the observed confinement effect on crystallization. For example, in the case of poly(ethylene oxide), PEO, [41, 42] it was argued that a reduction in crystal growth factor by 2 orders of magnitude was imputable to an increase of 30 K in the glass transition temperature.

These hypotheses, however, were not supported by experimental evidence, because of the difficulties in monitoring crystallization kinetics and probing molecular mobility within the same experiment.

3.1 Is the Increase in Crystallization Time upon Confinement Straightforwardly Related to Slower Segmental Dynamics?

Measurements by Napolitano et al. in 2006 [36] could provide an answer to the question. By assembling nanocapacitors of poly(3-hydroxy butyrate), PHB, the authors showed that a reduction in crystallization rate does not imply an increase in relaxation time.

Bulk amorphous samples were produced by melting the polymer powder ($M_w = 170$ k, by Sigma) for 3 min at 175 °C ($T_m^{DSC} = 433$ K) and then cooling the melt onto a cold surface (metallic plate previously cooled at 268 K). Bulk samples were prepared between two brass circular electrodes, separated by glassy fibers (diameter $= 50$ μm), which fixed the sample thickness and allowed avoiding shortcuts. A clear peak, attributed to the α-relaxation, was present in the dielectric spectra in the temperature and the frequency range as previously reported for amorphous samples of this polymer; see Fig. 2. [43–45] Ultrathin films of poly(3-hydroxybutyrate) were obtained at room temperature, thus in the region of temperature above the glass transition temperature ($T_g^{DSC} = 275$ K). Samples as prepared were kept for 2 h at 318 K in order to remove solvent residuals. A second strip of Al was finally deposited onto the polymer surface, following the procedure described above. Film thicknesses were evaluated from the electrical capacity of the sample at high frequencies.

The applied annealing procedure brought the ultrathin samples in a semicrystalline state, as verified by dielectric spectroscopy; i.e., the α-relaxation was not detected. To obtain amorphous samples, the polymer layers were melted and quenched as reported
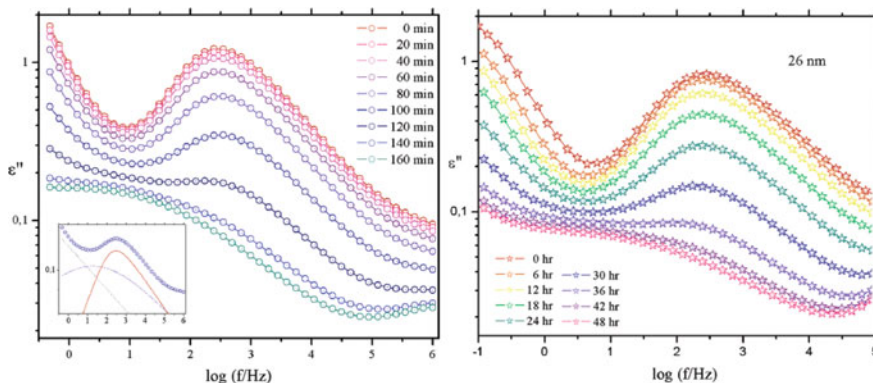
Fig. 2 Dielectric spectra of a 50 μm thick sample (left panel) and a 26-nm-thin film (right panel) during an isothermal crystallization at 291 K. The continuous lines are guides for the eye. In the inset, a fit for the spectrum recorded after 105 min of annealing. The spectrum was deconvolved as sum of a conductive contribute and two relaxation processes: the structural relaxation and the constrained amorphous phase at lower frequencies. Reproduced from Napolitano et al. [36] Copyright (2006) by the American Chemical Society

above for bulk samples. Successful amorphizations resulted in samples showing an α-relaxation peaked in the same frequency range and with a similar intensity as observed for bulk samples. Defining a general criterion to ensure reproducibility is, however, not straightforward. For the thinnest films analyzed, the dielectric strength was reduced by 10% compared to the bulk value, as discussed below. A priori it is not possible to know whether the starting value of $\Delta\varepsilon$ for a given thickness is correct, or if further material processing is necessary; we noticed that repeated essays of amorphization of the same sample resulted in degradation—easily detectable via a severe change in dielectric constant in the limit of high frequencies.

With respect to other more rigid polymers as poly(ethylene terephthalate), PET, poly(ethylene 2,6-naphthalate), PEN, and polyether ether ketone, PEEK, PHB has a serious advantage. Its structural relaxation time is not affected by the degree of crystallinity, which allows a more reliable determination of the absolute determination of the molecular mobility. Experiments were performed at 291 K, a temperature at which the intense peak attributed to the structural relaxation is present in the middle of the frequency window investigated, around 300 Hz. In bulk, the intensity of the segmental peak decreases upon annealing and in isothermal conditions within 3 h $\Delta\varepsilon$ drops to zero, indicating that crystallization is taking place.

For thin films, the same scenario is qualitative observed. No shift in segmental relaxation time is measured in a 26-nm-thin sample, and $\Delta\varepsilon$ decreases upon annealing. But, differently than in bulk, within 3 h no significant reduction in dielectric strength is detected. Based on further analysis of the results, the crystallization of the thin film appeared more than an order of magnitude slower than in bulk. Remarkably, the segmental mobility was invariant with confinement, which strongly confuted the original conjecture.

A more quantitative picture can be obtained considering the relation between crystallization and segmental times in bulk [46]. In its simplest formulation, the classical crystallization rate, $G(T) \sim t^{-1}_{\text{cry}}(T)$, can be written as the product of two exponential terms $n(T)$ and $D(T)$, respectively related to the nucleation/growth free energy term and molecular diffusion.

The latter component is related to the shear viscosity and to the main relaxation time via fractional Stokes–Einstein and Debye–Stokes–Einstein relations through a temperature-dependent parameter $\xi \leq 1$:

$$G(T) = n(T)D(T) = n(T)\tau(T)^{-\xi(T)} \tag{1}$$

In the temperature regime of cold crystallization, undercooling is elevated, which lowers the nucleation barrier, while mass transport is significantly reduced. This condition implies that $\partial n(T)/\partial T \ll \partial D(T)/\partial T$, which, coupled to the approximation $\partial \xi(T)/\partial T \approx 0$—valid over the relatively small T range were experiments are possible—yields an expression relating the timescales of crystallization and segmental mobility:

$$t_{\text{cry}}(T) \sim \tau(T)^{\xi} \tag{2}$$
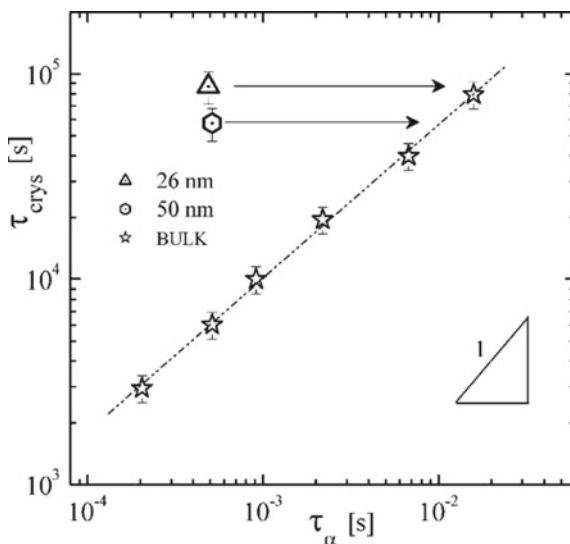
Fig. 3 Crystallization time as a function of the structural relaxation time for bulk and ultrathin films of poly(3-hydroxybutyrate). The dashed line is the best linear fit (R = 0.999) for the data reported. The arrows indicate the relaxation times of bulk samples that would correspond to the crystallization times of the confined systems, according to the best linear fit. Reproduced from Napolitano et al. [46] Copyright (2007) by the American Chemical Society

The experimental validity of Eq. 2 has been validated for PHB, with $\xi = 0.75\pm0.04$; see Fig. 3. Based on the correlation between t_{cry} and τ, the increase in crystallization time observed in 26-nm-thin films should have been accompanied by a segmental time 15 times larger than what measured. To fully agree with the prediction of Eq.2, the segmental peak should have shifted towards lowers frequencies by more than a decade, which corresponds to an increase in T_g by $\approx$5 K.

While the segmental relaxation time was thickness invariant over the whole temperature range investigated, the value of the dielectric strength at the onset of the crystallization process (i.e., in the amorphous state), dropped by 10% in the thinnest film; see Fig. 4. A reduction in $\Delta\varepsilon$ is, in fact, not only related to crystallization phenomena, but a common feature of immobilization processes [47]. The lower value of dielectric strength in the case of thinner amorphous samples was attributed to the presence of an immobilized layer, which at the time of publication (2006) was commonly indicated as "dead layer"; these layers are now considered as a part of the irreversibly adsorbed layer [48–53]. The correlation between the presence of a dead layer and the reduced crystallization is possible by considering that molecules in an immobilized layer cannot rearrange and thus inhibit or even just delay the formation of order structures in the core of the film [4, 37, 51]. Importantly, this hypothesis does not require a change in molecular mobility of the amorphous fraction.
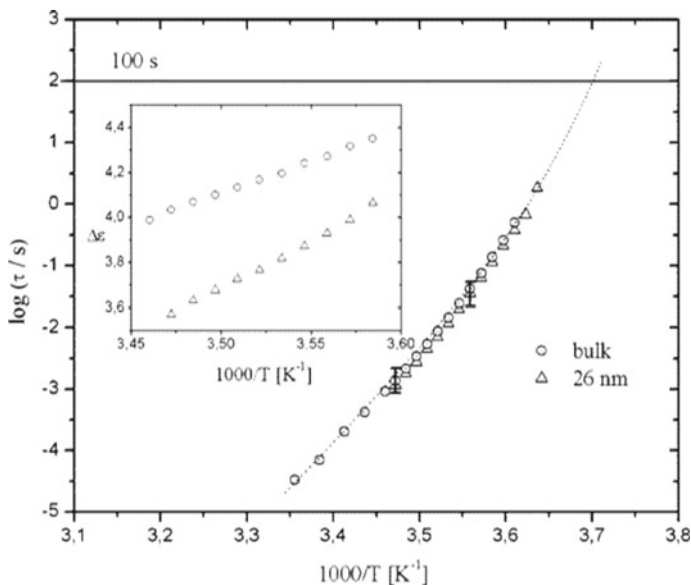
Fig. 4 Thermal evolution of the segmental relaxation time and of the dielectric strength (Inset) of a bulk sample and a 26 nm thin film. The same set of Vogel Fulcher Tammann parameters can be used to fit both series of data. Down to 26 nm, T_g, indicated in the figure as the temperature at which the structural relaxation lasts 100 s, shows no thickness dependence. Reproduced from Napolitano et al. [36] Copyright (2006) by the American Chemical Society

3.2 The Thickness Dependence of the Crystallization Rate

As the data set was limited to 3 samples, one of which thick enough to be considered as bulk (50 μm), this first investigation of the crystallization of thin polymer films could not provide further information on the origin of the increase in glass stability upon storing in isothermal conditions. Later work by Vanroy et al. [4] and by Martinez-Tong et al. [24] was able to shed more light on the interplay between interfacial immobilization and overall crystallization rate of confined polymers. Vanroy et al. investigated the thickness dependence of the conversion of the amorphous fraction of ultrathin films of poly(ethylene terephthalate) during isothermal cold crystallization at 373 K. Their work allowed to text the validity of an analytical method assessing the impact of irreversible chain adsorption and permitting to disentangle finite size and interfacial effects. Analyzing films ranging in thickness from 1 μm down to few tens of nm, they observed an increase in crystallization timescaling with the inverse of the film thickness, which was attributed to a mere effect of finite size effects. Even after prolonged annealing in the temperature range of the highest crystallization rate in bulk, samples thinner than ~20 nm did not crystallize. This result was explained in terms of the overruling role of adsorption on crystallization in the thinnest films.

Ultrathin films were prepared by spincoating solutions of PET in a mixture (5:2) of trifluoroacetic acid (TFA) and chloroform. Optimizing the relative concentration of the two liquids was possible by considering that TFA is a good solvent for PET, while chloroform increases the volatility of the mixture. Using solutions of PET in pure TFA for spincoating resulted in films with an undulated surface. This feature is usually attributed to a nonhomogenous distribution of solvent in the film during spinning, probably related to the low volatility of TFA. Adding chloroform permits to decrease the surface roughness of PET. Samples as prepared were kept for 4 h at 353 K in order to remove residual solvent and reduce stresses induced by the spin-coating preparation. No amorphization was necessary in this case, measurements via atomic force microscopy and X-rays proved that the used annealing conditions do not result in the formation of crystalline structures [54].

In the thickness range considered (7 nm–10 μm), the crystallization rate varies by more than five orders of magnitude. Investigating this enormous range of crystallization times requires a serious feasibility study before performing the dielectric experiments. Owing at investigating all the samples at the same experimental conditions, that is, the same annealing/crystallization temperature, the dielectric function was recorded at 373 K, where the characteristic crystallization time, t_{cry}, is ~7 min in bulk samples. Performing experiments at lower temperatures might have given a better control of the measuring conditions for bulk samples, but would have led to tremendously slower kinetics in the thinnest films; in addition to reducing the maximum number of samples to investigate within a given project time, measuring at lower temperatures is also prohibitive because of the larger consumptions in exchange gas used, and the finite volume of LN2 tanks, if employed. Working at higher temperatures, on the contrary is limited by the frequency window where the segmental relaxation is not affected by artifacts.

At 373 K, the structural relaxation process of PET appears as a strong peak in the imaginary component of the dielectric function, centered around 10 kHz (for bulk) (i.e., $\tau \sim 16\,\mu$s). As observed for PHB, $\Delta\varepsilon$ decreased during isothermal annealing; see Fig. 5. While for thick films this phenomenon could be directly explained in terms of crystallization, that is, via a drop in $\Delta\varepsilon$ following an Avami-like law of the type [23, 55]:

$$\Delta\varepsilon \ \sim \ -\exp\left(-t/t_{\text{cry}}\right)^{\beta} \tag{3}$$

with $1 < \beta < 4$. in the case of thinner films and extra term should be included. Prior to crystallization, a reduction in $\Delta\varepsilon$ not following Eq. (3) is observed for films thinner than $\approx$500 nm. This extra term is linear in a plot of $\Delta\varepsilon$ versus $\log t$ and increases in amplitude upon reduction of the thickness; see Fig. 5. Such further reduction in dielectric strength was associated with interfacial rearrangements increasing the monomer/surface density without affecting the number of chains adsorbed per unit surface [56]. Same as in the case of crystal perfection, this process yields an increase in the number of monomers directly adsorbed onto the substrate, without affecting the total adsorbed amount, that is. Under such conditions, the number of monomers
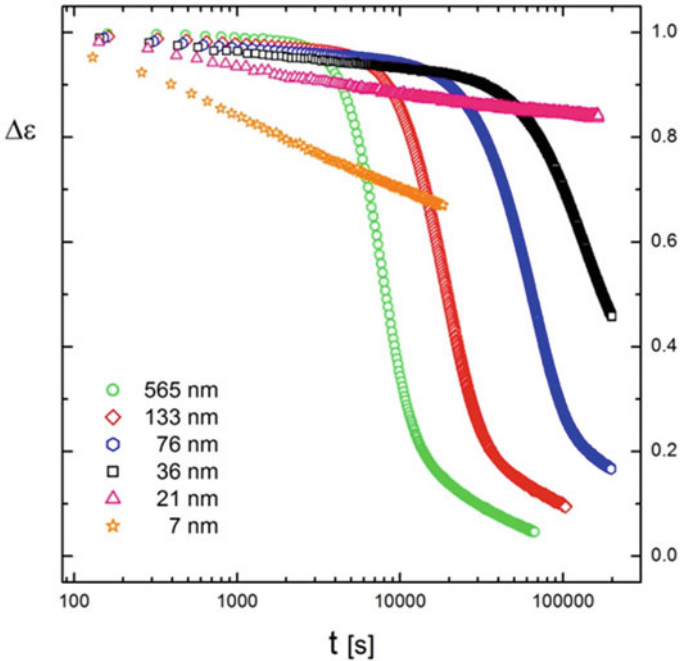
Fig. 5 Time evolution of the dielectric strength of films of PET of different thickness capped between aluminum layers. Reproduced from Vanroy et al. [4] Copyright (2013) by the American Chemical Society

adsorbed (immobilized dipole moments) per chain increases logarithmically as a function of time.

Taking into account the two phenomena, the time evolution of the dielectric strength could be modeled as:

$$\frac{\Delta\varepsilon(t)}{\Delta\varepsilon(t_0)} = 1 - \Gamma\left[\exp\left(-t/t_{cry}\right)^{\beta}\right] - \delta\,\log(t/t_0) \qquad (4)$$

where Γ indicates the final drop in dielectric strength (proportionally to the crystalline content of the sample), δ is a parameter proportional to the fraction of chains immobilized upon adsorption, and t_0 a conveniently short time, that we fixed for all samples at 1 s. The results of the analysis, not reporting Γ because of higher incertitude upon fitting data to Eq. (3), are given in Fig. 6.

We start commenting on the results by considering the upper and the lower panels, indicating the changes in the timescales involved, that is how τ and t_{cry} vary with thickness, h. From the microscale down to 20 nm, tcry increases with h^{-1}, while within the same thickness range set τ is confinement-invariant. This condition is the same as that observed for PHB. In the case of PET, having access to such a larger
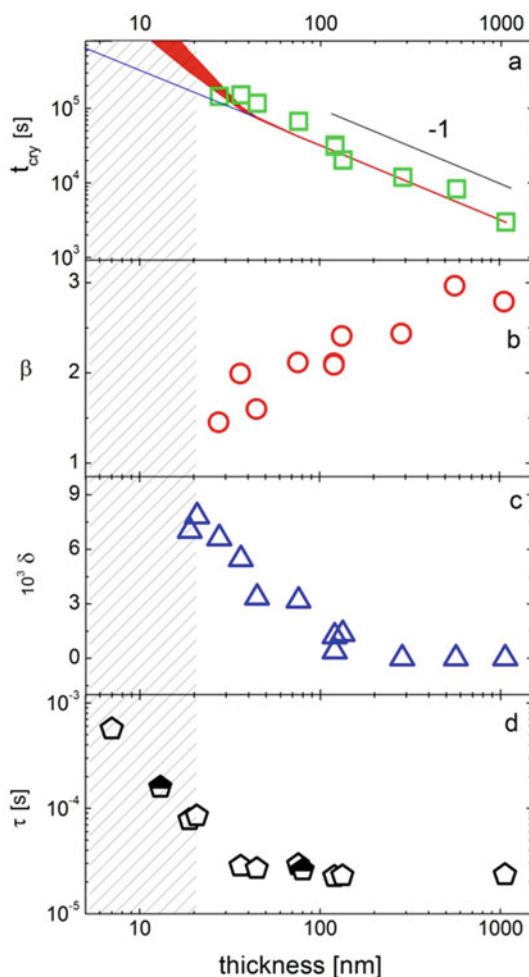
Fig. 6 Thickness dependence of the fitting parameters of crystallization time (a), Avrami exponent (b), adsorption coefficient (c) as obtained from the fit of the time evolution of the dielectric strength to Eq. (3). The values of the structural relaxation time of amorphous films at 373 K were also plotted (d). In panel a, the red area indicates the values of crystallization time as obtained via Eq. (5), where ξ was varied between the most probably values commonly shown in the literature for bulk samples, that is $0.5 \leq \xi \leq 1.0$; the blue line refers to the expected increase in tcry assuming only finite size effects. In panel d, data from ref [54]. were added for comparison (semiopen symbols). The shadow area below 20 nm indicates the thickness range where crystallization was not observed. Reproduced from Vanroy et al. [4] Copyright (2013) by the American Chemical Society

data set permitted us to build up the bases of a physical framework capable to explain the increase in crystallization time at molecular level.

Working at constant sample surface, the scaling $t_{cry} \sim h^{-1}$ implies that the crystal growth rate ($\sim t_{cry}^{-1}$) is directly proportional to the sample volume. This condition is in agreement with the trend observed in nanodroplets of PEO, where the nucleation time linearly scales with the volume of the drop [3, 17]. This implies that for films of PET down to 20 nm, the slowing down in the crystallization kinetics is merely related to nucleation issues. To understand how this reasoning implies the scaling $t_{cry} \sim h^{-1}$, let us consider a polymer melt with homogenous nuclei density. Reduction of the thickness, achievable by considering thinner and thinner slabs of the above-mentioned melt, yields lower and lower probabilities to find active nuclei within a given portion of the slab of constant surface. The scaling is finally obtained assuming that crystallization is limited by nucleation; that is, the timescale of the process is proportional to the probability of finding a nucleus in a slab of given surface and thickness h.

The continuous and unperturbed reduction of β, in line with the prediction of the finite size corrections proposed by Schultz to the Avrami model [57], further supports the reasoning. In the case of a finite volume, in fact, the presence of interfaces does not permit a full development of the crystals as in bulk and contribution of trunked crystals and lost nuclei (belonging to region outside the volume considered) results in a lower effective transformation rate and smaller values of β.

As observed for other systems, crystallization does not take place in the thinnest films. For films thinner than ~20–25 nm, no substantial reduction in dielectric strength imputable to crystallization was observed. In such films, only the logarithmic drop in $\Delta\varepsilon$ is present. Based on these results, we may conclude that either the crystallization rate decreased by more than three orders of magnitude or that crystallization was definitely inhibited. Because of the importance of this condition, further experiments were performed at higher temperatures, where the crystallization kinetics is sped up by the larger diffusion coefficients, and in repeated temperature scans up to $T_m + 20$ K. No crystallization was observed (Fig. 7).

Considering the increase in δ upon reduction of the thickness, it was proposed that adsorption could be responsible for the tremendous increase (eventually to an infinite value) in t_{cry} of films thinner than 20 nm. Adsorbed chains would have a lower (or zero) crystallization rate and thus act as a retarding agent on the formation of ordered structures. To test this hypothesis, it was necessary to verify that adsorption takes place before crystallization. In line with evidence from other polymers, thermal annealing in the liquid state promotes the adsorption of PET chains onto Al. Vanroy et al. monitored the irreversible adsorption kinetics by isolating irreversibly adsorbed layer from 40-nm-thick films held at 373 K for different annealing times. The thickness of such layer, h_{ads}, is an operational parameter to determine the amount of chains irreversibly adsorbed onto a unit surface [52, 58]. At 40 nm, the onset of crystallization is observed after 10 h of annealing at this temperature, while after already 10 min the adsorbed amount reached a constant value. Further tests at 363 K, where the kinetics of adsorption is much slower, permitted to better study the kinetics of adsorption and confirmed the same saturating value. These results clearly show
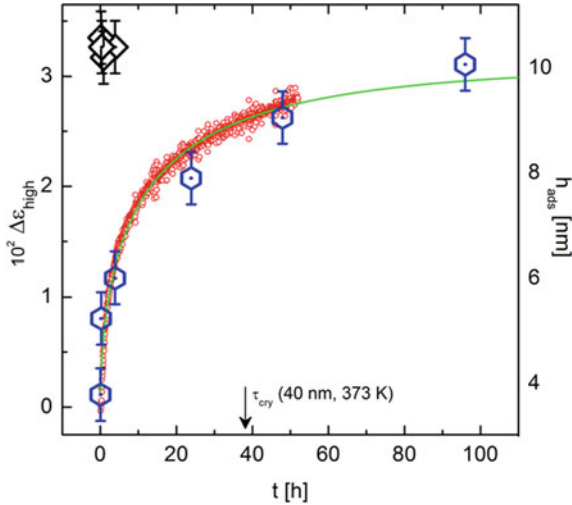
Fig. 7 Time evolution of the component of the dielectric strength scaling with the adsorbed amount, $\Delta\varepsilon_{high}$ (red circles, left axis), and the thickness of the irreversibly adsorbed layer, h_{ads}, obtained in the same annealing conditions (blue hexagons, right axis) at 363 K. Value of h_{ads} collected under the isothermal crystallization conditions, 373 K, are shown for comparison (black diamonds, right axis). Reproduced from Vanroy et al. [4] Copyright (2013) by the American Chemical Society

that in the temperature regime considered, adsorption takes place well before the onset of crystallization.

To crystallize, chains far from the interfaces need to pay the entropic loss required for the formation of stems, which then migrate towards the crystal growth front. On the contrary, interfacial chains—because of the different timescales involved—start to reduce their free energy via adsorption. Larger adsorption degrees, i.e., larger enthalpy gains per unit surface, however, correspond to an increase in the barrier to overcome before accessing the nearest available state of reduced free energy; the system gets thus trapped in a metastable non-crystalline state with an extremely long lifetime. Consequently, chains in the adsorbed layer are expected to have tremendously low growth rates, corresponding to the lack of crystallization within reasonable timescales, in line with the outcome of these experiments.

This condition implies $\xi > 1$; that is, diffusion would slow down way more than what expected from its correlation to segmental mobility.

With these considerations in mind, we can further shape our physical framework to describe the crystallization time of thin polymer films by explicitly considered the role of nucleation and that of sluggish mass transport:

$$t_{cry}(h, T) = \frac{\Lambda(T)}{h}\tau(h, T)^{\xi} \qquad (5)$$

where Λ is a fitting parameter, convoluted to the value of ξ, taking into account nucleation density. The results obtained for PET imply that $\xi \gg 1$. While the physics behind Eq. (5) is intuitive, the lack of experimental points below 20 nm, that is the region where a finite value of ξ could be determined, cannot grant validation of the framework.

To overcome this issue, we will consider the work by Martinez-Tong et al. [24] on thin films of poly(L-lactide acid) PLLA, a system forming less dense adsorbed layers, which should correspond to measurable ξ values. Before discussing on experiments on this biodegradable polymer, we remark that it is possible to reduce the adsorbed amount of thin films of PET by capping with a layer of another polymer [59]. The physics behind the reduction in adsorbed amount was discussed by Simavilla and coworkers [58].

PLLA nanocapacitors for dielectric measurements were prepared via a similar procedure to that described for PET and PHB. Here will consider the material-specific details. Thin films of thickness ranging between 300 and 8 nm of poly(L-lactide) (PLLA, $M_\mathrm{w} = 67,000$ g/mol, PDI < 1.4, Sigma-Aldrich) were spin-coated (3000 rpm, chloroform 99.9%) on top of the lower electrode. In order to guarantee the evaporation of the solvent, the spin-coated films were left on a hot plate at 333 K for one hour. Finally, a second aluminum layer ($\approx$50 nm) was evaporated on top of the polymer film. The annealing procedure resulted in semicrystalline samples. Amorphous films were obtained by heating the nanocapacitors at 453 K (liquidus temperature) for 30 s followed by cooling on a cold plate (278 K). Samples were stored at room temperature before measurements. Dielectric relaxation spectroscopy experiments were conducted isothermally at 343 K. Sweeping frequencies from 10 MHz to 0.1 Hz requires about 150 s, a measuring time that is much lower than the crystallization time of any sample studied in this work. Such a condition permits the investigation of the kinetics of crystallization in real time.

Same as in the case of PET, a preliminary study permitted to identify the most convenient crystallization temperature to follow within a reasonable time the whole thickness range. The data in Fig. 8 reveal a huge increase in glass stability upon reduction of the thickness. Figure shows the frequency dependence of the dielectric loss for two PLLA thin films of thicknesses h = 150–8 nm, respectively, representative of a bulk-like and an interfacial behavior. The top panels show the first dielectric sweep (t = 0 s), where the polymers are in the amorphous state, while the lower panels show the response after 25 min for the thick film and after 1600 min for the thinner film.

While the dielectric signal of the interfacial layer is almost unaltered by annealing for almost 3 h, the strength of the segmental peak of the thick film decreased by far. This system shows a lot of similarities to PET. The crystallization time increases upon reduction of the thickness, the segmental time is constant down to 30 nm and then sharply increases, the kinetics of reduction in $\Delta\varepsilon$; see Fig. 9, can be described by Eq. (5). In the case of thicker films, the drop in dielectric strength is mostly related to crystallization, while for the thinner samples the role of adsorption becomes predominant. Differently than PET, the crystallization time of thin films of PLLA does not reach values outside of the experimental time window in the case of the
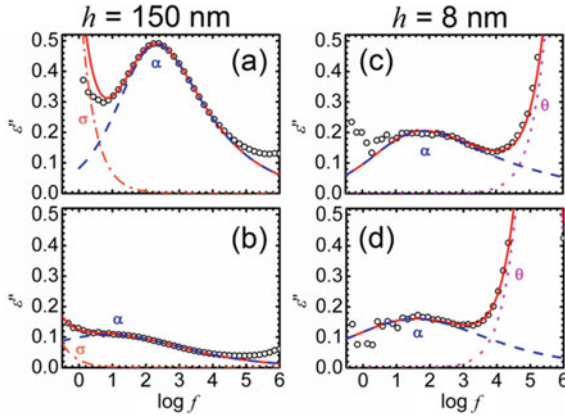
Fig. 8 Dielectric spectra for two PLLA thin films. (a) and (b) correspond to a film of thickness = 150 nm, amorphous and semicrystalline (t = 25 min) respectively. (c) and (d) correspond to a film of thickness = 8 nm, amorphous first sweep and amorphous last sweep (t = 1600 min) respectively. Reproduced from Martinez-Tong et al. [24] Copyright (2014) by the American Chemical Society
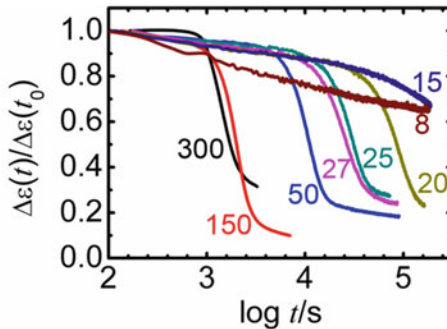
Fig. 9 Time evolution of $\Delta\varepsilon$ for films of PLLA of different thickness, whose value in nanometer is labeled next to each curve. Reproduced from Martinez-Tong et al. [24] Copyright (2014) by the American Physical Society

thinnest films. This system is thus optimal to fully test the validity of Eq. (4). Results are shown in Fig. 10, where the crystallization time is plotted as a function of the thickness.

For this system, we obtain a value of $\xi = 2.7\pm0.2$. For films of PET capped by thin layers of polystyrene [59], the value of ξ could be varied between approx 6 and 2. We remark that values of $\xi > 1$ are not experimentally observed when analyzing the temperature dependence of crystallization. The exotic condition $\xi > 1$ is a peculiar feature of spatial analysis, as the one proposed here as a function of the thickness. Based on recent work [60, 61], this intriguing condition hints at the presence of a gradient in tracer diffusivity (mass transport within the polymer matrix), with a
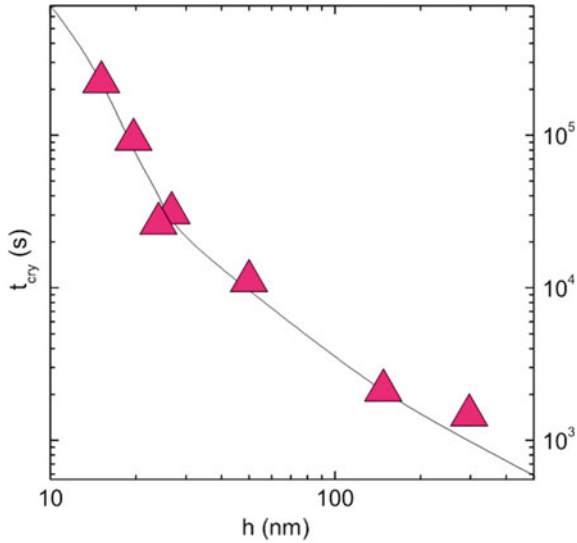
Fig. 10 Thickness dependence of the crystallization time of thin films of PLLA. Pink triangles indicate the experimental points of Martinez-Tong et al. [24], the continuous black line is a fit of the thickness dependence of the crystallization time to Eq. 5

larger sensitivity to the distance from the interface than the gradient in segmental mobility. While we expect values of $\xi < 1$ would be measured in each sublayer of the gradient, values of ξ larger than unity originate from a large drop in mass transport coupled to an almost constant value of τ all across the film; see sketch in Fig. 11. We expect that being able to modify this gradient would result in a change in ξ, or similarly by measuring ξ we would be able to provide information on the gradient. In particular, in the case of identical forms of the gradients in mass transport and mobility, the same value of ξ would be measured in temperature and spatial analysis. In the case of slower mobility in proximity of the interfaces, values of $\xi < 1$ would
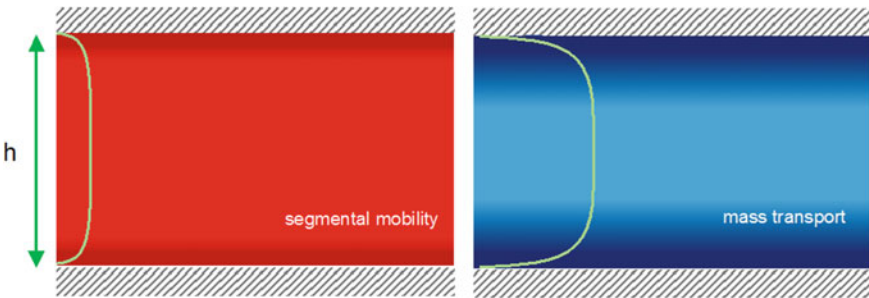
Fig. 11 Sketch of the gradients in segmental mobility and in mass transport in a thin slab of thickness h, leading to the exotic condition $\xi > 1$

be representative of gradients in mobility steeper than those in mass transport, and the condition $\xi > 1$ would originate from the opposite case.

4 Conclusion

In conclusion, in this chapter we have summarized the outcome of the experimental work on the crystallization of thin polymer films performed via broadband dielectric spectroscopy. We have discussed on the common issues related to sample preparation and showed that this technique was able to answer to a fundamental question of interest to the large and broad group of researchers working on the effects of nanoconfinement on the formation of polymer crystals. Differently that what previously speculated, the enormous reduction in crystallization rate cannot be associated with slower segmental mobility: The crystallization time can increase at constant dynamic glass transition temperature. We have shown that an analysis of the time evolution of the dielectric strength—an experimentally accessible parameter, sensitive to immobilization—can be used to determine the timescale of crystallization, and to estimate if adsorption of chains is concurrently taking place concurrently. In this regard, an analytical expression for the time dependence of the dielectric strength has been discussed. We have also discussed on the analysis of the thickness dependence of the crystallization time and indicated an expression capable to link the timescale of the formation of ordered structures to that of segmental mobility. The link between these two timescales was built up considering the role of finite size effects on nucleation and appropriately modified version of the Debye–Stokes–Einstein relation for bulk melts. Finally, we have shown that extending the latter equation, valid in the temperature domain, to nanoconfinement yield an exotic and intriguing condition, where mass transport along the film is more inhibited than what expected from a gradient in segmental mobility.

References

1. Liu YX, Chen EQ (2010) Polymer crystallization of ultrathin films on solid substrates. Coord Chem Rev 254(9–10):1011
2. Beiner M, Rengarajan GT, Pankaj S, Enke D, Steinhart M (2007) Manipulating the crystalline state of pharmaceuticals by nanoconfinement. Nano Lett 7:1381
3. Massa MV, Carvalho JL, Dalnoki-Veress K (2006) Confinement effects in polymer crystal nucleation from bulk to few-Chain systems. Phys Rev Lett 97:247802
4. Vanroy B, Wubbenhorst M, Napolitano S (2013) Crystallization of thin polymer layers confined between two adsorbing walls. Acs Macro Lett 2(2):168

5. Massa MV, Dalnoki-Veress K, Forrest JA (2003) Crystallization kinetics and crystal morphology in thin poly(ethylene oxide) films. Eur Phys J E 11(2):191

6. Reiter G (2003) Model experiments for a molecular understanding of polymer crystallization. J Polym Sci Part B-Polym Phys 41(16):1869

7. Sommer J-U, Reiter G (2003) Polymer crystallization observations, concepts and interpretations. Springer, Heidelberg

8. Mareau VH, Prud'homme RE (2005) In-situ hot stage atomic force microscopy study of poly(epsilon-caprolactone) crystal growth in ultrathin films. Macromolecules 38(2):398

9. Chen Y, Yang DC (2006) Crystallization and phase behavior of crystalline syndiotactic 1,2-polybutadiene/isotactic polypropylene blends in solution-cast thin films. Polymer 47(5):1667

10. Woo E, Huh J, Jeong YG, Shin K (2007) From homogeneous to heterogeneous nucleation of chain molecules under nanoscopic cylindrical confinement. Phys Rev Lett 98(13):4

11. Wang HP, Keum JK, Hiltner A, Baer E, Freeman B, Rozanski A, Galeski A (2009) Confined crystallization of polyethylene oxide in nanolayer Assemblies. Science 323(5915):757

12. Hu WB, Cai T, Ma Y, Hobbs JK, Farrance O, Reiter G (2009) Polymer crystallization under nano-confinement of droplets studied by molecular simulations. Faraday Discuss 143(129)

13. Flores A, Ania F, Arribas C, Ochoa A, Scholtyssek S, Balta-Calleja FJ, Baer E (2012) Confined crystallization of nanolayered poly(ethylene terephthalate) using X-ray diffraction methods. Polymer 53(18):3986

14. Martin J, Nogales A, Mijangos C (2013) Directional crystallization of 20 nm width polymer nanorods by the inducement of heterogeneous nuclei at their tips. Macromolecules 46(18):7415

15. Suzuki Y, Duran H, Steinhart M, Butt HJ, Floudas G (2013) Homogeneous crystallization and local dynamics of poly(ethylene oxide) (PEO) confined to nanoporous alumina. Soft Matter 9(9):2621

16. Weber CHM, Chiche A, Krausch G, Rosenfeldt S, Ballauff M, Harnaul L, Göttker-Schnetmann I, Tong Q, Mecking S (2007) Single lamella nanoparticles of polyethylene. Nano Lett 7(2024)

17. Massa MV, Dalnoki-Veress K (2004) Homogeneous crystallization of poly(ethylene oxide) confined to droplets: the dependence of the crystal nucleation rate on length scale and temperature. Phys Rev Lett 92(25)

18. Nogales A, Ezquerra TA, Denchev Z, Sics I, Calleja FJB, Hsiao BS (2001) Molecular dynamics and microstructure development during cold crystallization in poly(ether-ether-ketone) as revealed by real time dielectric and x-ray methods. J Chem Phys 115(8):3804

19. Sics I, Ezquerra TA, Nogales A, Denchev Z, Alvarez C, Funari SS (2003) Cold crystallization of poly(ethylene naphthalene-2,6-dicarboxylate) by simultaneous measurements of X-ray scattering and dielectric spectroscopy. Polymer 44(4):1045

20. Alvarez C, Nogales A, Garcia-Gutierrez MC, Sanz A, Denchev Z, Funari SS, Bruix M, Ezquerra TA (2005) Confined crystallization in phase-separated poly(ethylene terephthalate)/poly(ethylene naphthalene 2,6-dicarboxilate) blends. Eur Phys J E 18(4):459

21. Sanz A, Nogales A, Ezquerra TA, Lotti N, Munari A, Funari SS (2006) Order and segmental mobility during polymer crystallization: poly (butylene isophthalate). Polymer 47(4):1281

22. Sanz A, Nogales A, Ezquerra TA (2010) Influence of fragility on polymer cold crystallization. Macromolecules 43(29)

23. Napolitano S, Wubbenhorst M (2007a) Monitoring the cold crystallization of poly(3-hydroxy butyrate) via dielectric spectroscopy. J Non-Cryst Solids 353(47–51):4357

24. Martinez-Tong DE, Vanroy B, Wübbenhorst M, Nogales A, Napolitano S (2014) Crystallization of poly(l-lactide) confined in ultrathin films: competition between finite size effects and irreversible Chain adsorption. Macromolecules 47(2354)

25. Duran H, Steinhart M, Butt HJ, Floudas G (2011) From heterogeneous to homogeneous nucleation of isotactic poly(propylene) confined to nanoporous alumina. Nano Lett 11(4):1671

26. Suzuki Y, Duran H, Akram W, Steinhart M, Floudas G, Butt HJ (2013) Multiple nucleation events and local dynamics of poly(epsilon-caprolactone) (PCL) confined to nanoporous alumina. Soft Matter 9(38):9189

27. Suzuki Y, Duran H, Steinhart M, Butt HJ, Floudas G (2014) Suppression of poly(ethylene oxide) crystallization in diblock copolymers of poly(ethylene oxide)-b-poly(epsilon-caprolactone) confined to nanoporous alumina. Macromolecules 47(5):1793

28. Fukao K, Koyama A, Tahara D, Kozono Y, Miyamoto Y, Tsurutani N (2003) Structure formation from the oriented glassy states of poly(ethylene terephthalate). J Macromol Sci-Phys B42(3–4):717

29. Rotella C, Napolitano S, De Cremer L, Koeckelberghs G, Wubbenhorst M (2010) Distribution of segmental mobility in ultrathin polymer films. Macromolecules 43(20):8686

30. Rittigstein P, Priestley RD, Broadbelt LJ, Torkelson JM (2007) Model polymer nanocomposites provide an understanding of confinement effects in real nanocomposites. Nat Mater 6(4):278

31. Panagopoulou A, Rodríguez-Tinoco C, White RP, Lipson JEG, Napolitano S (2020) Substrate roughness speeds up segmental dynamics of thin polymer films. Phys Rev Lett 124(027802)

32. Bebin P, Prud'homme RE (2003) Comparative XPS study of copper, nickel, and aluminum coatings on polymer surfaces. Chem Mater 15(4):965

33. Reiter G, de Gennes PG (2001) Spin-cast, thin, glassy polymer films: highly metastable forms of matter. Eur Phys J E 6(1):25

34. Kremer F, Schoenhals A (2003) Broadband dielectric spectroscopy. Springer, Berlin

35. Bottcher C (1973) Theory of dielectric polarization. Elsevier Amsterdam

36. Napolitano S, Wubbenhorst M (2006) Slowing down of the crystallization kinetics in ultrathin polymer films: a size or an interface effect? Macromolecules 39(18):5967

37. Napolitano S, Sferrazza M (2017) How irreversible adsorption affects interfacial properties of polymers. Adv Colloid Int Sci 247(172)

38. Despotopoulou MM, Frank CW, Miller RD, Rabolt JF (1996) Kinetics of chain organization in ultrathin poly(di-n-hexylsilane) films. Macromolecules 29(18):5797

39. Frank CW, Rao V, Despotopoulou MM, Pease RFW, Hinsberg WD, Miller RD, Rabolt JF (1996) Structure in thin and ultrathin spin-cast polymer films. Science 273(5277):912

40. Capitan MJ, Rueda DR, Ezquerra TA (2004) Inhibition of the crystallization in nanofilms of poly(3-hydroxybutyrate). Macromolecules 37(15):5653

41. Schonherr H, Frank CW (2003a) Ultrathin films of poly(ethylene oxides) on oxidized silicon. 1. Spectroscopic characterization of film structure and crystallization kinetics. Macromolecules 36(4):1188

42. Schonherr H, Frank CW (2003b) Ultrathin films of poly(ethylene oxides) on oxidized silicon. 2. In situ study of crystallization and melting by hot stage AFM. Macromolecules 36(4):1199

43. Ahumada O, Ezquerra TA, Nogales A, BaltaCalleja FJ, Zachmann HG (1996) Influence of liquid crystalline order on the dielectric relaxation of random copolyesters of PET, PEN, and PHB. Macromolecules 29(14):5002

44. Bergmann A, Owen A (2004) Dielectric relaxation spectroscopy of poly (R)-3-hydroxybutyrate (PHB) during crystallization. Polym Int 53(7):863

45. El-Taweel SH, Hohne GWH, Mansour AA, Stoll B, Seliger H (2004) Glass transition and the rigid amorphous phase in semicrystalline blends of bacterial polyhydroxybutyrate PHB with low molecular mass atactic R. S-PHB-diol. Polymer 45(3):983

46. Napolitano S, Wubbenhorst M (2007b) Effect of a reduced mobility layer on the interplay between molecular relaxations and diffusion-limited crystallization rate in ultrathin polymer films. J Phys Chem B 111(21):5775

47. Napolitano S, Wubbenhorst M (2011) The lifetime of the deviations from bulk behaviour in polymers confined at the nanoscale. Nat Commun 2(260)

48. Gin P, Jiang N, Liang C, Taniguchi T, Akgun B, Satija SK, Endoh MK, Koga T (2012) Revealed architectures of adsorbed polymer chains at solid-polymer melt interfaces. Phys Rev Lett 109(26):265501

49. Asada M, Jiang N, Sendogdular L, Sokolov J, Endoh MK, Koga T, Fukuto M, Yang L, Akgun B, Dimitriou M, Satija S (2014) Melt crystallization/dewetting of ultrathin PEO films via carbon dioxide annealing: the effects of polymer adsorbed layers. Soft Matter 10(34):6392

50. Housmans C, Sferrazza M, Napolitano S (2014) Kinetics of irreversible chain adsorption. Macromolecules 47(10):3390

51. Jeong H, Napolitano S, Craig BA, Priestley RD (2017) Irreversible adsorption controls crystallization in vapor-deposited polymer thin films. J Phys Chem Lett 8(229)

52. Simavilla DN, Panagopoulou A, Napolitano S (2017) Characterization of adsorbed polymer layers: preparation, determination of the adsorbed amount and investigation of the kinetics of irreversible adsorption. Macromol Chem Phys 219(219):201700303
53. Napolitano S (2020) Irreversible adsorption of polymer melts and nanoconfinement effects. Soft Matter 16(23):5348–5365
54. Napolitano S, Prevosto D, Lucchesi M, Pingue P, D'Acunto M, Rolla P (2007) Influence of a reduced mobility layer on the structural relaxation dynamics of aluminum capped ultrathin films of poly(ethylene terephthalate). Langmuir 23(4):2103
55. Avrami M (1940) Kinetics of phase change. II transformation-time relations for random distribution of nuclei. J Chem Phys 8(212)
56. Rotella C, Napolitano S, Vandendriessche S, Valev VK, Verbiest T, Larkowska M, Kucharski S, Wubbenhorst M (2011) Adsorption Kinetics of ultrathin polymer films in the melt probed by dielectric spectroscopy and second-harmonic generation. Langmuir 27(22):13533
57. Schultz JM (1996) Effect of specimen thickness on crystallization rate. Macromolecules 29(8):3022
58. Simavilla DN, Huang W, Housmans C, Sferrazza M, Napolitano S (2018) Taming interfacial interactions via nanoconfinement. ACS Cent Sci 4(755)
59. Vanroy B, Wübbenhorst M, Napolitano S (2020) Remotely Controlling the Crystallization of Thin Polymer Coatings. Macromolecules 53(12):4882
60. Napolitano S, Rotella C, Wuebbenhorst M (2011) Is the reduction in tracer diffusivity under nanoscopic confinement related to a frustrated segmental mobility? Macromol Rapid Commun 32(11):844
61. Priestley RD, Cangialosi D, Napolitano S (2015) On the equivalence between the thermodynamic and dynamic measurements of the glass transition in confined polymers. J Non-Cryst Solids 407(288–295)
62. Napolitano S, Glynos E, Tito NB (2017) Glass transition of polymers in bulk, confined geometries, and near interfaces. Reports on Progress in Physics 80(3):036602

Dielectric Behavior of Nonpolar Polymers and Their Composites: The Case of Semicrystalline Polyolefins

Stavros X. Drakopoulos, Sara Ronca, and Ignacio Martin-Fabiani

Abstract Polyolefins are thermoplastic polymers used in a wide range of applications, including medical implants, insulating materials, fabrics, and packaging. The two most popular representatives, polyethylene (PE) and polypropylene (PP), present linear chemical structures that yield these materials semicrystalline (except for atactic PP). The versatility of their synthesis enables the fabrication of different grades, covering a wide range of crystallinities which can reach up to 90%. However, because of their symmetric aliphatic structure, they do not present a permanent dipole moment. Their nonpolar nature makes dielectric spectroscopy measurements challenging, as this technique relies on the relaxation of dipoles after the application of an external electric field. Here, we review different approaches that have been followed in order to introduce permanent dipoles and render polyolefins dielectrically active, including: (i) addition of probes with a permanent dipole moment, (ii) oxidation/chlorination to produce dielectrically active chains, or (iii) induced oxidation in the presence of metal oxide fillers. The introduction of dipoles, either intentionally or due to the presence of impurities, has enabled the characterization of the full relaxation spectra of polyethylene and polypropylene as well as the assignment of dielectric relaxations to their respective molecular mechanisms. We then turn our attention into PE and PP composites for electrical energy storage and insulation applications. We show how, in these materials, the effect of the polymer matrix and filler orientation has been proven key to enhance their dielectric breakdown strength.

Keywords Polyolefins · Nanocomposites · Crystallinity · Orientation · Dielectric probes · Entanglement · Dielectric breakdown strength · Treeing

S. X. Drakopoulos · S. Ronca · I. Martin-Fabiani (✉)
Department of Materials, Loughborough University, Loughborough, Leicestershire LE11 3TU, UK
e-mail: i.martin-fabiani@lboro.ac.uk

Abbreviations

PE	Polyethylene
LDPE	Low density polyethylene
HDPE	High density polyethylene
UHMWPE	Ultra-high molecular weight polyethylene
PP	Polypropylene
i-PP	Isotactic polypropylene
TiO_2	Titanium oxide
Al_2O_3	Aluminum oxide
DBANS	4,4′-(N,N-di- butylamino)-(E)-nitrostilbene
MMT	Montmorillonite
o-MMT	Organo-montmorillonite
CNF	Carbon nanofibers
MWCNT	Multi-wall carbon nanotubes
$CaCO_3$	Calcium carbonate
$BaTiO_3$	Barium titanate

1 Introduction

The global plastic production has increased exponentially since 1950, when 1.5 tonnes were produced, rising to almost 348 million tonnes in 2017. In Europe alone, over 1.5 million people are directly employed in the 60,000 companies related to the plastic industry [1]. Polyolefins, consisting of saturated aliphatic hydrocarbon macromolecules, account for more than 55% of the global plastics demand, with a market share of 34.4% for polyethylene (PE) and 24.2% for polypropylene (PP) [2]. PE and PP, whose chemical formulas are presented in Fig. 1, are produced mainly from oil and natural gas via a polymerisation process of ethylene or propylene, respectively. The versatility of their synthesis enables the fabrication of different grades, covering a wide range of beneficial properties. Low density polyethylene (LDPE) presents the most extensive degree of branching among polyolefins, and a degree of crystallinity which typically varies between 40–55%. As a result, it is easy to process
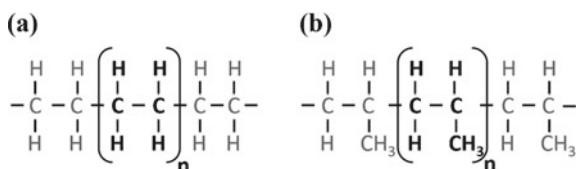
Fig. 1 Chemical structure of **a** polyethylene and **b** polypropylene. The structure presented for the latter represents its isotactic configuration, with the methyl group always on the same side of the main chain

and is not reactive at room temperature, making it suitable for use in reusable bags and food packaging films. Because of its very reduced amount of branching, crystallinity in high density polyethylene (HDPE) can reach 70–80%, resulting in higher tensile strength and thermal resistance than LDPE. HDPE is used in toys, milk, or shampoo bottles. Ultra-high molecular weight polyethylene (UHMWPE) is characterized by its extremely long chains, reaching molecular weights in the order of 10^6 g/mol. It embodies the advantages of HDPE and it has great chemical resistance, as well as having the best impact strength among thermoplastics. These properties make UHMWPE an excellent material for personal armor and medical implants. PP generally presents better mechanical properties and thermal resistance than PE, but its chemical resistance is lower. The most widely used is isotactic PP (i-PP), in which the methyl group is on the same side of the main chain (Fig. 1b), with a crystallinity in between that of LDPE and HDPE. PP is widely used in food packaging, bank notes, and sweet or snack wrappers.

In most of these products, the fundamental understanding of the relationship between the internal structure and dynamics of the polymer and the final properties are key to optimize performance. One of the most valuable techniques to obtain such understanding at a molecular and chain level is dielectric spectroscopy, which measures the relaxation of dipoles present in the material after the application of an external electric field of varying frequency [3]. This technique relies on the presence of polar molecules, whose orientation can be affected by the external field and their reorientation back to equilibrium can be detected. However, the chemical structure of polyolefins is nonpolar, resulting in a lack of dipoles which renders them dielectrically inactive in the absence of impurities. Different approaches have been studied to introduce dipoles in polyolefins, involving either chemical modifications to introduce polar groups such as direct oxidization, chlorination, or indirect oxidization through the introduction of inorganic fillers, as well as the addition of probes with a large permanent dipole moment. In this chapter, we will first discuss representative dielectric spectra of the most common variations of PE and PP, followed by a discussion on the different approaches used to render them dielectrically active. Then, we will present a summary of the studies on polyolefin composites for electrical energy storage and insulation applications.

2 Dielectric Spectra Overview

Dielectric relaxation dynamics of PE and i-PP have been extensively studied for decades, either relying on the presence of dipoles originated by impurities or sample preparation, or actively introducing dipoles in the polymer by different methods which will be reviewed in the following section. In this section, as a background for the rest of the chapter, we will give an overview of the different relaxations found in the different grades of PE and i-PP, as well as the current knowledge on their molecular origins.

Representative dielectric spectra for LDPE, HDPE, and i-PP are shown in Fig. 2. Both PE and i-PP (Fig. 2a-c) display three characteristic relaxations, traditionally named α, β, and γ, in order of decreasing temperature, with a fourth process at very low temperatures, δ, which is weak or absent in some cases. The α relaxation, associated to the crystalline phase, is attributed in PE to the longitudinal motion of polymer chains through the crystalline lamellae, in a helicoidal movement [4, 5]. As a result, the α relaxation is much more intense in HDPE when compared to LDPE, as the former has a higher degree of crystallinity and more chains in the crystalline phase to contribute to this process. The origin of the α process in i-PP is still a topic of debate, with evidence from mechanical experiments that it is due to a relaxation of defects in the crystalline phase with some additional contribution from the neighboring
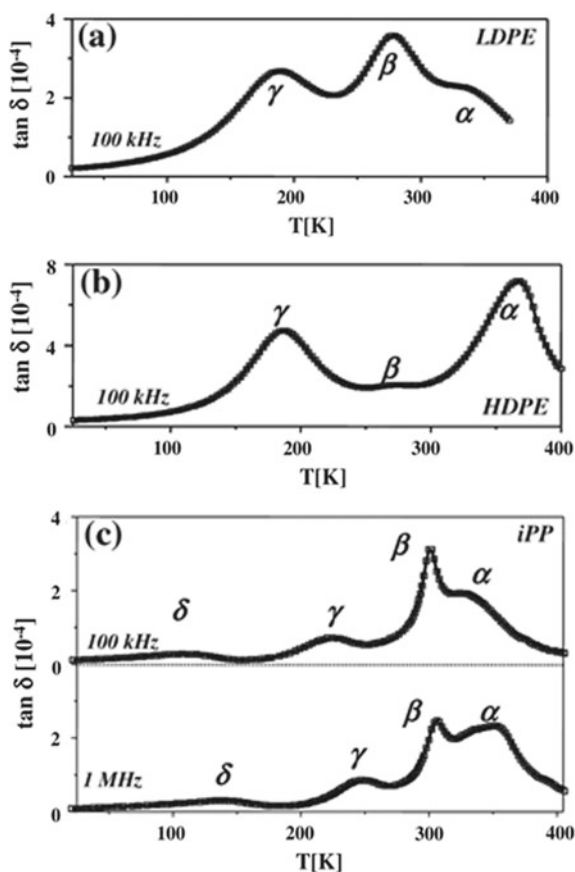
Fig. 2 Dielectric loss tangent for semicrystalline polyolefins as a function of temperature: **a** low density polyethylene (LDPE). **b** high density polyethylene (HDPE), and **c** isotactic polypropylene (iPP). Adapted with permission from Milicevic, D. Et al. Radiation-Induced Modification of Dielectric Relaxation Spectra of Polyolefins: Polyethylenes vs. Polypropylene. *Polym. Bull.* **2014**, *71*, 2317–2334

amorphous regions [6]. Dielectric [7] and mechanical [8] studies prove that the α process in i-PP is multicomponent, involving two or three subprocesses. The next process in order of increasing temperature is the β relaxation, which is related to the glass transition in both PE [9] and i-PP [6]. This process is more intense in LDPE than in HDPE, as the crystallinity is lower for LDPE and there are more amorphous chains available to contribute to the glass transition. Then we have the γ relaxation, which in PE is assigned to the movement of certain parts of chains in the amorphous regions in the vicinity of the crystalline lamellae. Several γ subprocesses have been reported, but their assignment to specific molecular dynamics is not fully clear yet [10–12]. In i-PP, the γ process has been related to the movement of chain ends or branches, in a crankshaft-type fashion, in mechanical and dielectric studies [8, 13, 14]. A fourth relaxation has been reported at very low temperatures in both PE and i-PP, the δ process. This relaxation has been correlated with hindered rotation of CH_3 groups [14, 15] and it is generally weak or absent. It is expected to be especially weak in the case of PE, where the CH_3 groups can only be found at the chain ends.

We believe it is of importance to mention that the matter of polyethylene's glass to rubber transition temperature has been an ongoing matter for decades and some researchers still do not fully agree on its assignment. Various works over the years have proposed that either the β-relaxation [16, 17] or the γ-relaxation [18, 19] correspond to the dynamic glass to rubber transition process. It has even been suggested that polyethylene has two glass transitions, γ-relaxation for linear polyethylene and β-relaxation for branched polyethylene [20, 21]. Generally, in semicrystalline polymers, the β-relaxation appears to be broadened when compared with amorphous samples and considerably less prominent than the β-relaxation, supporting the idea that the β-relaxation is the dynamic glass to rubber transition process [16]. On the other hand, the γ-relaxation has been found to increase in intensity with decreasing crystallinity, and has been assigned to mobile groups of amorphous chains in the vicinity of crystalline lamellae [22, 23]. For these reasons, and as described before, here we will follow the most widespread approach in the community of assigning the β relaxation to the glass transition of PE and the γ relaxation to a process associated to movement of localized amorphous chain segments.

3 Methods to Introduce Polar Groups

The unveiling of the dielectric spectra of polyolefins, whose nonpolar structures result in the absence of a permanent dipole moment, has only been possible thanks to the introduction of dipoles. For the polymer to be dielectrically active and enable the measurement of its relaxation spectra, such introduction of dipoles must have taken place, either unintentionally (e.g. oxidization due to impurities or sample preparation conditions) or intentionally. We will now review the different methods used to render PE and i-PP dielectrically active, as well as the influence these procedures have on their final dielectric spectra. Methods are classified into two types: (i) those that rely

on the chemical modification of the polymer chain to induce dipoles and (ii) the addition of probes with strong dipole moment into the polymer matrix.

3.1 Chemical Modifications

We will first report on methods that render polyolefins dielectrically active by means of chemical modifications, including oxidization and chlorination. The most common is oxidization, which introduces carbonyl groups into the polymer chain that serve as a dielectric probe. Thermally-initiated oxidization was one of the first methods to be used, which enabled the unveiling of the dielectric spectra of PE early on [24–26]. Boyd argued that the α relaxation observed in lightly oxidized PE must involve the screw rotation around the main chain axis of a perpendicular C=O dipole which is yielding the necessary dielectric activity to detect the process [4, 16]. Several studies have reported on the use of gamma radiation to oxidize PE and i-PP [12, 27–29]. As shown in Fig. 3, the dielectric losses of some relaxations increase with increasing doses, but after irradiation, some of the processes are not present anymore. For example, the disappearance of the β relaxation in HDPE and i-PP upon irradiation has been attributed to an increase in crystallinity due to chain scission and the occurrence of crosslinking, which reduces chain mobility [12, 27, 28]. The disappearance after irradiation of the γ process has been associated in mechanical measurements to the increase in carbonyl content and the decreased molecular weight of the highly oxidized PP due to chain scission [30, 31].

Artificial weathering has been proposed as an alternative to thermal oxidation, using UV radiation in a dry environment to induce photo oxidative chain scission
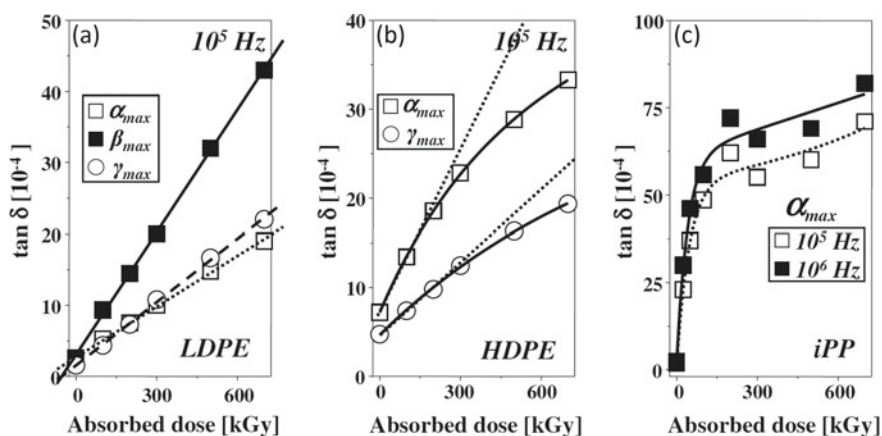
Fig. 3 Dielectric loss tangent versus absorbed dose for **a** LDPE, **b** HDPE, and **c** i-PP. Reproduced from Radiation-Induced Modification of Dielectric Relaxation Spectra of Polyolefins: Polyethylenes versus Polypropylene . *Polym. Bull.* **2014**, *71*, 2317–2334, reproduced with permission
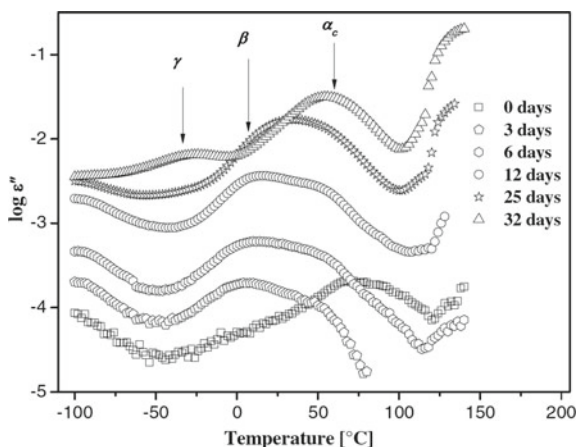
Fig. 4 Dielectric loss ε" versus. temperature of UV-weathered PE at a frequency of 1000 Hz for 0 (square), 3 (pentagon), 6 (hexagon), 12 (circle), 25 (star), and 32 (triangle) days of weathering. The three relaxation processes, namely α, β, and γ appear in order of decreasing temperature. The α relaxation is observed only for 25 (star) and 32 days (triangle) weathered LDPE in the given temperature range. Reproduced with permission from Ramanujam et al. [32]

in LDPE followed by cross-linking [32]. As weathering time increases, a balance is achieved between an increase of the glass transition temperature due to cross-linking and further crystallization of newly created shorter polymer chains, and a decrease of T_g related to the increase in free volume that the dangling chain ends provide. As shown in Fig. 4, the unirradiated sample presents a weak dielectric response, whereas the UV-weathered samples show an increasing dielectric strength as weathering time increases, until at 32 days all relaxations (α, β, and γ) are visible in the spectra. However, for these long weathering times, the polymer films were very brittle, leading to the complete loss of structural integrity.

Chlorination, consisting in the introduction of chlorine atoms as a side chain group, has been proven successful as well in rendering polyethylene dielectrically active. It has been reported that the dielectric strength of the α relaxation in chlorinated polyethylene is not proportional to its crystallinity, [24] as the chlorine atoms favor the amorphous phase [33].

In some cases, the introduction of inorganic fillers in a polymer matrix can result in chemical modifications that generate dipoles in the chain. Metal oxide nanomaterials can oxidize the polymer chains and generate the carbonyl groups needed to increase the number of dipoles present. Frübing et al. introduced different contents of titanium dioxide (TiO_2) nanoparticles (200 nm in diameter) in LDPE, enabling them to observe the α, β, and γ relaxations [9]. Figure 5 shows the relaxation map of LDPE with different TiO_2 contents. The relaxation map shows that with increasing TiO_2 content, the β process shifts to higher temperature values. This is because the TiO_2 particles tend to remain in the amorphous phase, rendering it more rigid and hindering chain movement. On the other hand, the position and slope of the Arrhenius plots of the
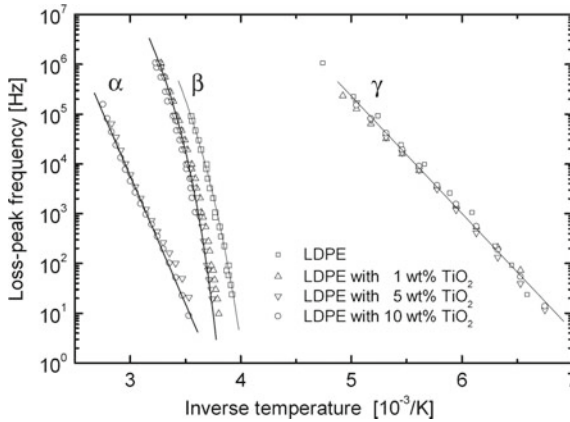
Fig. 5 Relaxation maps of LDPE with different titanium-dioxide content as indicated. The full curves are Arrhenius fits to the α and γ relaxations of LDPE with 10 wt% TiO$_2$ as well as VFT fits to the β relaxation of LDPE and LDPE with 5 wt% TiO$_2$. Reproduced with permission from Frübing et al. [9]

α and γ relaxation are hardly changed by the addition of TiO$_2$. In this case, if the filler remains in the amorphous phase, it is not expected to affect a crystalline phase process (α) and it will only influence a localized process (γ) if it is close to it, which for a low TiO$_2$ content it is unlikely. The authors reported that the dielectric strength of the α relaxation increases with increasing TiO$_2$ content and attributed this to the increased presence of carbonyl groups formed in the melt during sample preparation.

We recently studied the dielectric behavior of disentangled UHMWPE, [10] which contains a much lower fraction of entanglements than the commercial UHMWPE. The use of methylaluminoxane (MAO) as a catalyst in the polymerization reaction results in the presence of aluminum oxide (Al$_2$O$_3$) traces which oxidize the polymer chain and create carbonyl groups in the chain that renders the polymer dielectrically active [34, 35]. The disentangled character of our UHMWPE results into a non-equilibrium melt-state leading into an increase in elastic shear modulus G' in time due to the progressive formation of entanglements [36]. The plateau modulus at thermodynamic equilibrium, G_N^0, can be calculated as [37]:

$$G_N^0 = \frac{g_N \rho R T}{M_e} \tag{1}$$

where g_N is a numerical factor, r is the density of the material at the absolute temperature T, R is the gas constant. M_e is the molecular weight between entanglements, and it is inversely proportional to the entanglement density.

To follow the entanglement process in the melt state, dielectric spectra of UHMWPE during consecutive frequency sweeps were acquired at a constant temperature of 160 °C, considerably above the melting point of the material which is around
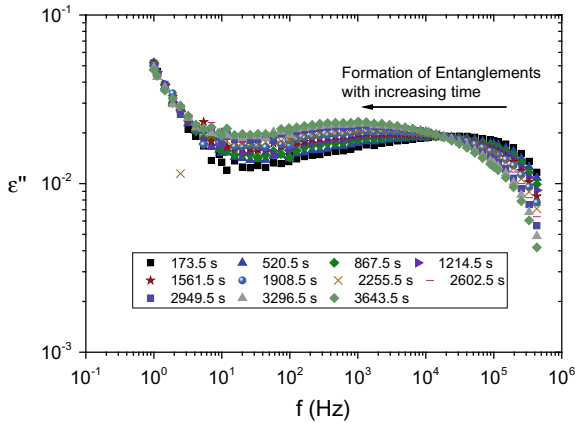
Fig. 6 Imaginary part of dielectric permittivity ε'' in disentangled UHMWPE during consecutive frequency sweeps at a constant temperature of 160 °C. The shift toward lower frequencies is indicative of entanglement formation and reduced chain mobility. Adapted (Creative commons license) from Drakopoulos et al. **150**, 35 [10]

140 °C. As presented in Fig. 6, the main dielectric signal shifts toward lower frequencies as entanglements form over time and the chain mobility is hindered [38]. In order to try to establish a correlation with the elastic shear modulus G from rheology, the complex electric modulus M^* was calculated as follows:

$$M^* = \frac{1}{\varepsilon^*} = \frac{1}{\varepsilon' - i\varepsilon''} = \frac{\varepsilon'}{\varepsilon'^2 + \varepsilon''^2} + i\frac{\varepsilon''}{\varepsilon'^2 + \varepsilon''^2} = M' + iM'' \tag{2}$$

where M', and M'' are the real and the imaginary parts of the electric modulus, respectively, ε^* is the complex permittivity and ε' and ε'' are the corresponding real and imaginary parts, in analogy to the complex modulus defined for other types of dynamic measurements. Figure 7 shows graphs for M' as a function of time at 160 °C, showing how the electric modulus, which is the inverse of permittivity, increases in time reaching a plateau. The same behavior can be observed for the elastic shear modulus obtained by rheology. The formed entanglements restrict the motion of filler-induced polar groups hindering their ability to align with the electric field. Consequently, polarization and permittivity diminish approaching a constant value as entanglements are formed.

3.2 Introduction of Dielectric Probes

As presented in the previous section, chemical modifications to introduce polar groups in the polymer chain can lead to undesired consequences such as changes
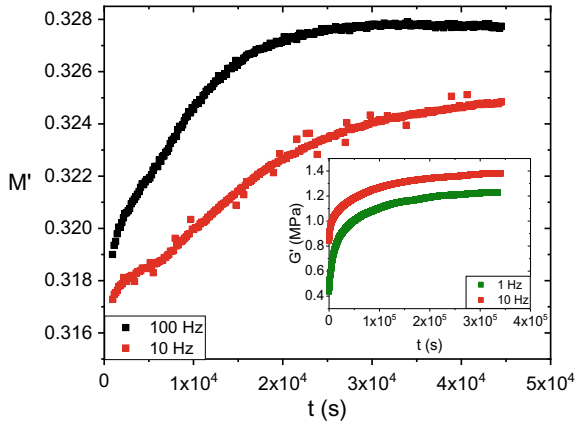
Fig. 7 The real part of electric modulus for disentangled UHMWPE at 160 °C as a function of time at 10–100 Hz. The inset shows elastic shear modulus as determined by rheology at 1–10 Hz. Adapted (Creative commons license) from Drakopoulos et al. **150**, 35 [10]

in crystallinity, [33] chain scission [31], and crosslinking [32]. Therefore, the introduction of small molecules that, rather than inducing dipoles in the polymer, carry their own permanent dipole moment, has been explored in recent years as a less invasive alternative.

Van den Berg et al. [39] introduced a 4,4-(N,N-di- butylamino)-(E)-nitrostilbene (DBANS), which has a large dipole moment (9D), in LDPE and i-PP at low concentrations (up to 1 wt%) to aid the measurement of their dielectric spectra. DBANS is a rigid rod-like molecule, eliminating possible signals coming from relaxations associated with intramolecular motions, and does not tend to crystallize due to its butyl tails. The dielectric loss ε" versus temperature graphs of LDPE and i-PP doped with different concentrations of DBANs are shown in Fig. 8. For undoped LDPE (Fig. 8a), the three main relaxation processes are observed, α, β, and γ. This is an indication of the occurrence of oxidation of the polymer possibly due to the presence of impurities. However, the dielectric losses are very low, in the range of 10^{-4}-10^{-3}. After the addition of DBANS, clear changes are observed in the dielectric spectra of LDPE, the most evident being a significant enhancement of the strength of the β relaxation. The probe does not seem to enhance the crystalline α relaxation, which is expected as the small molecules are more likely to dissolve in the amorphous phase. Moreover, the small concentrations of DBANS used minimizes the chances of influencing the strength of localized processes such as the γ relaxation, which remains fairly unaltered. The fact that the probe only enhances the β relaxation, attributed to the glass transition, implies that the DBANS molecules feel the changes in local viscosity associated with this process without the influence of other local phenomena. A similar effect is observed when DBANS is added to i-PP, as shown in Fig. 8b, where mainly a strengthening of the glass transition process (β) is observed. For both PE and i-PP, it was found that the dielectric enhancement of the dielectric
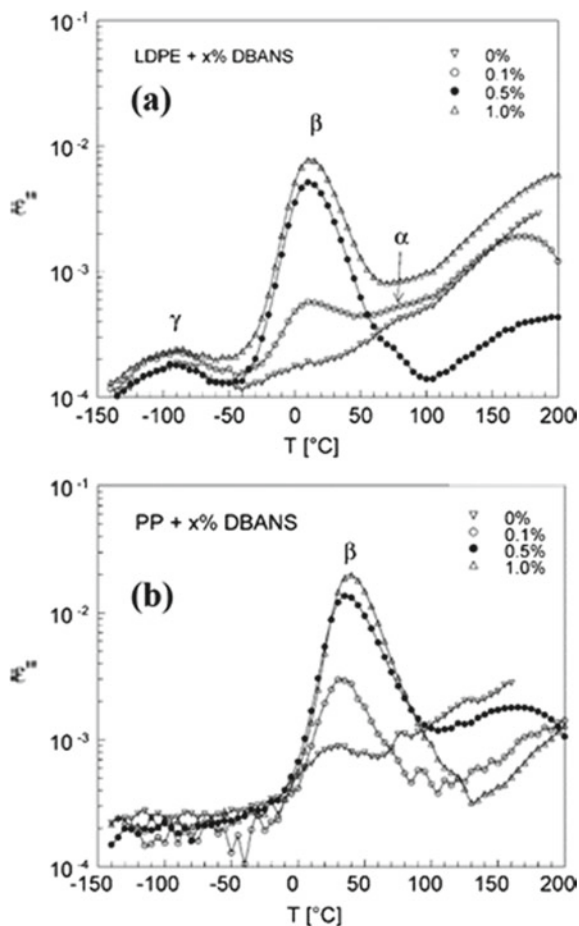
glass transition process is proportional to the probe concentration up to about 0.5 DBANS wt %, and that the relaxation time remained within one order of magnitude in frequency of that of the pristine polymer.

The same probe has been introduced in blends of PP and LDPE to study the glass transition dynamics [40]. PE-PP blends with different compositions and morphologies presented substantially the same glass transition dynamics, indicating a bulk behavior for both components. One of the main concerns when adding a dielectric probe to a polymer blend is the preference of the probe to migrate to one of the components or the blend or the interface between the different fractions, resulting in a dielectric signal which does not represent the blend system accurately. In this study, the relaxation strength normalized by the weight fraction of each polymer stayed constant for all compositions. Therefore, the distribution of the dielectric probe was homogeneous across the different phases of the sample.

4 Polyolefin Composites for Electrical Energy Storage and Insulation

4.1 Background

In recent years, renewed effort has been invested in the investigation of the storage, efficient recovery and distribution of electrical energy, affecting directly an interdisciplinary range of scientific fields, from fundamental and applied natural sciences to economics and sociology. The need for new advancements in the energy materials goes in parallel with the drawbacks of oil as a source of fuel, such as its impact on climate change and variable cost. In addition, other sources of electrochemical energy such as batteries are characterized by long recharging hours, thus limiting the applicability for future fast-responsive applications, [41] and technologies that are hazardous for the environment, generating a demand for more effective and safer storage materials.

Insulating materials used as dielectric mediums to store capacitive electrical energy find application in many modern electronic systems, ranging from electronic devices to hybrid electric cars [42]. For such applications, a specific combination of properties is required including [43–46]: (i) High values of dielectric permittivity, which is a measure of the ability of the material to store energy; (ii) low dielectric loss (tanδ) values, to maximize efficiency; (iii) low electrical conductivity, in order to reduce leakage currents; and (iv) high dielectric breakdown strength so higher electrical fields can be physically endured by the dielectric medium. Polymers, and especially non-polar ones such as polyolefins, are characterized by low values of dielectric permittivity and high breakdown strengths. In contrast, ceramic materials exhibit the exact reciprocal behavior, presenting high permittivity and low breakdown strength. Therefore, composite materials composed of a polymer matrix and ceramic nanofillers are a priori great candidates for electrical energy storage materials [47].

In heterogeneous dielectric nanomaterials, understanding the role of interface/interphase properties and the possibility to tailor them at will is of great scientific and technological importance [48, 49]. In this respect, semicrystalline polymers often are considered as heterogeneous materials, with the amorphous regions of the polymer chains forming the continuous matrix phase and the rigid crystallites in the role of the filler [50]. The crystallinity and crystal morphology also affect the dielectric properties by enhancing interfacial polarization phenomena [51], and increase the dielectric breakdown strength due to higher resistance to electrical treeing (current propagation to failure) [52]. Toward this direction, biaxial orientation of semicrystalline polymers, like polypropylene, has found use as thin dielectric membranes for electrical energy storage applications [53]. In addition, fillers of various shapes, electrical characteristics and orientation, have been employed to enhance the dielectric behavior of such polymers [43].

The addition of electrically conducting fillers within an insulating polymer matrix can enhance their electrical and electromagnetic properties for applications in electromagnetic interference shielding and conductive adhesives in circuit elements in the

microelectronics industry [54]. Due to the vastly different electrical conductivities between the constituents of such system, the direct-current conductivity is strongly dependent on the conducting filler concentration, thus leading to two basic charge transport mechanisms:

(i) At low filler concentrations, the mean distance between conducting fillers is sufficiently high and so the electrical properties of the composite are dominated by the insulating matrix. In such cases, the charge carriers (in most cases electrons, ions, and holes) hop to a nearby state that can be quantum-mechanically described with higher or lower energetic jumps of the potential barrier, the latter achieved through quantum tunnelling [55].

(ii) At concentrations equal or higher than the percolation threshold, the conducting fillers are in contact and the charge carriers can move with low resistance (current flow), exhibiting the behavior of a conductor [56]. This can also be determined by the temperature dependence of electrical conductivity. In dielectric materials, conductivity increases with temperature due to higher mobility of charge carriers, whereas in conductors conductivity decreases with temperature due to polaron scattering effects [57].

The movement of the charge carriers from the conductive fillers can cause a dipolar response from the insulating polymer matrix and the corresponding interphase as well, leading to a Maxwell–Wagner–Sillars interfacial polarization and increasing the capacitive storage ability of the resulting composite [58]. Surface modification processes to customize the interfaces between the matrix and the filler have been extensively studied in the past decade to enhance dielectric performance. These modifications affect the polarizability of the polyolefin matrix by introducing polar groups and enhancing the hydrophobicity, resulting into better-performing insulating materials [59].

4.2   Polyethylene Composites

Polyethylene is traditionally employed as an insulating material for cable manufacturing, due to its extremely weak conductivity and high dielectric breakdown strength. The two are interconnected, as the dielectric breakdown strength is dependent on electrical conductivity; the addition of high permittivity or high conductivity particles will enhance or decrease the dielectric breakdown strength, respectively. Moreover, the presence of agglomerates forming a percolating network can highly improve the thermal conductivity of the nanocomposite but decrease the dielectric breakdown strength [60]. In polyethylene/montmorillonite composites, Li et al. observed that the inclusion of aligned fillers results in an enhancement of the dielectric breakdown response that adds up to that provided by the oriented polymer crystals [61]. This effect could be exploited in materials that already present a drastic improvement of thermal conductivity when stretched, such as UHMWPE, [62] to provide a suitable material for electrical energy storage.

Another very important factor for cable insulation applications is the desired hydrophobic character of the dielectrics in use; the unwanted water molecules induce charge transport resulting into poor dielectric breakdown strengths and failure. Studies of hydrophilic/hydrophobic nanofillers at different humidity environments have shown that the drawbacks from the moisture sorption can be greater than the benefit of having the ceramic nanofiller in some cases [63]. As it can be observed in Table 1, composites with oxide fillers perform much worse in ambient and wet environments when compared with dry conditions, whereas composites using nitride fillers had a much more consistent response under ambient humidity. *Ayoob* et al. introduced hexagonal boron nitride in polyethylene to impart good great thermal conductivity and hydrophobicity to the polymer matrix, resulting in minimal charge transport at even very high filler concentrations (30% w/w) [60]. To reduce the drawbacks from the diffusion and adsorption of water molecules intended for such applications, chemical modification of the surface between the fillers and the polymer matrix can be implemented [64].

Other key features to consider when designing new composite insulators are the geometry and orientation of the fillers. Montmorillonite (MMT) nanosheets characterized by a high aspect ratio, have been proved to diminish the electrical treeing, through the encapsulation of mobile charge carriers in the interfaces between the matrix and the nanosheets [43, 49]. Further enhancement on the dielectric properties was observed by inducing filler orientation, which yields higher dielectric breakdown strength and higher energy efficiency when compared to an isotropic system of the same composition [43]. The anisotropic character can be enhanced further by orienting the crystalline and amorphous domains of the polymer matrix

Table 1 DC breakdown values for polyethylene composites with oxide and nitride fillers in different humidity environments [63]. Adapted from Hosier et al. The effects of hydration on the DC breakdown strength of polyethylene composites employing oxide and nitride fillers. IEEE Transactions on Dielectrics and Electrical Insulation 2017, 24, 3073–3082

Nominal filler content and type	Ambient conditioning (MV/m)	Dry conditioning (MV/m)	Wet conditioning MV/m
–	416 ± 30	425 ± 32	408 ± 32
5 wt. % Si_3N_4	409 ± 30	431 ± 34	172 ± 14
10 wt. % Si_3N_4	389 ± 30	450 ± 27	150 ± 12
5 wt. % SiO_2	228 ± 14	431 ± 30	135 ± 12
10 wt. % SiO_2	194 ± 12	414 ± 30	102 ± 7
5 wt. % AlN	366 ± 19	362 ± 18	241 ± 14
10 wt. % AlN	362 ± 18	373 ± 15	350 ± 26
5 wt. % Al_2O_3	349 ± 17	393 ± 24	241 ± 14
10 wt. % Al_2O_3	259 ± 15	360 ± 25	154 ± 12
5 wt. % SiO_2©	425 ± 42	442 ± 34	295 ± 26
10 wt. % SiO_2©	463 ± 29	436 ± 20	207 ± 23

by melt-state or solid-state processing, resulting in an improvement of the electrical breakdown properties. As it can be observed in Fig. 9, the breakdown strength of polyethylene/organo-montmorillonite (o-MMT) composites increases as they are stretched further [65]. A percolative behavior of normalized breakdown strength with crystalline orientation (strain) can be seen in Fig. 9b for PE composites with 9 wt% of o-MMT. The observed increase in breakdown strength was correlated with crystal orientation, as the crystallites provide higher potential barriers for electrical treeing [66].

The introduction of conducting fillers can impart to highly insulating polyethylene semiconducting electrical behavior even at low filler concentrations. The effect of such fillers in polyethylene in DC (s_{dc}) and AC (s_{ac}) conductivities can be appreciated in Figs. 10 and 11 where carbon nanofibers (CNF) or multi-wall carbon nanotubes
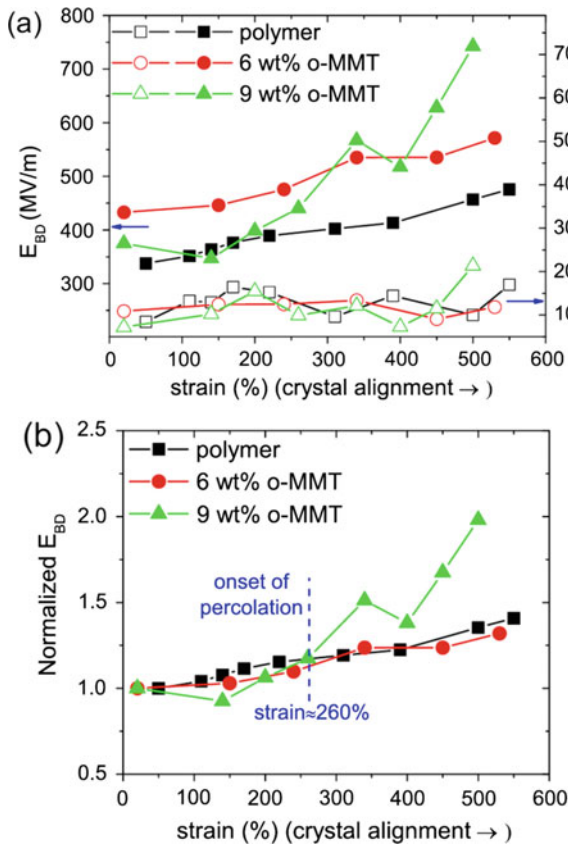
Fig. 9 Electric breakdown properties of polyethylene nanocomposites with different contents of organo-montmorillonite as a function of strain: **a** Weibull breakdown strength (E_{BD}) and Weibull modulus (b_w) and **b** normalized E_{BD} with respect to the first low-strain breakdown point in each film [65]. Reproduced with permission from Li et al. Appl. Phys. Lett. 111, 082,906 (2017)
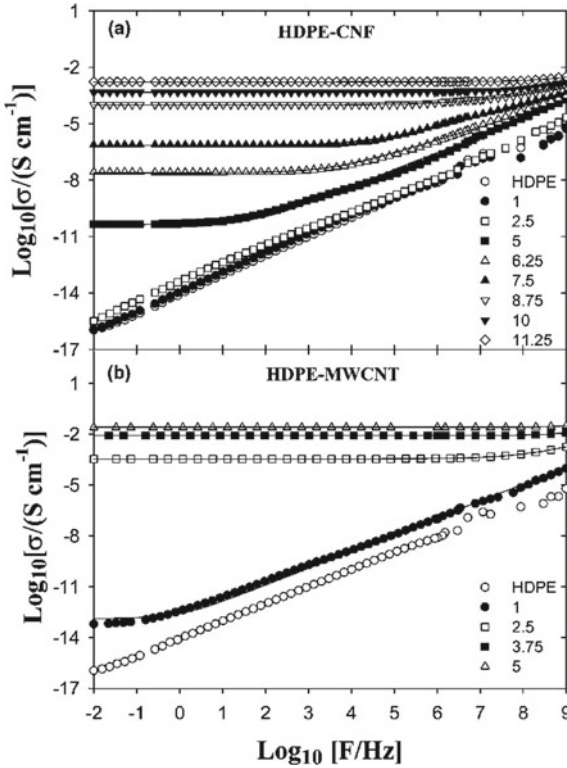
Fig. 10 AC conductivity as a function of frequency for HDPE composites with **a** carbon nanofibers (CNFs) and **b** Multi-wall carbon nanotubes (MWCNTs) for different filler concentrations [67]. Reproduced with permission from Linares et al. Macromolecules 2008, 41, 7090–7097

(MWCNT) are added to high density polyethylene (HDPE). In Fig. 10, it can also be appreciated that with the increase of fillers concentration, the AC conductivity becomes increasingly less dependent on frequency [67]. Since there is a contribution of DC conductivity to the imaginary part of dielectric permittivity $\left(\frac{\sigma_{dc}}{\omega \varepsilon_0}\right)$ when the s_{dc} becomes sufficiently high, it shadows the molecular dipolar response originating from the dielectric material resulting into $s_{ac}(f,T) \approx s_{dc}(T)$. This effect is considerably more intense in polyolefins such as polyethylene due to their very weak relaxation strengths ($\Delta \varepsilon = \varepsilon_s - \varepsilon_\infty$).

As it can be appreciated from Fig. 11, the percolation threshold of CNF and MWCNT in DC current is found to be at 3 and 1% v/v, respectively, which according to percolation theory, is the concentration where a continuous network of conductive fillers is formed. It is significant to note that the electrical conductivity of the nanocomposites at the percolation threshold is around 14 orders of magnitude the one of plain polyethylene, highlighting the enhancement of the electrical properties.
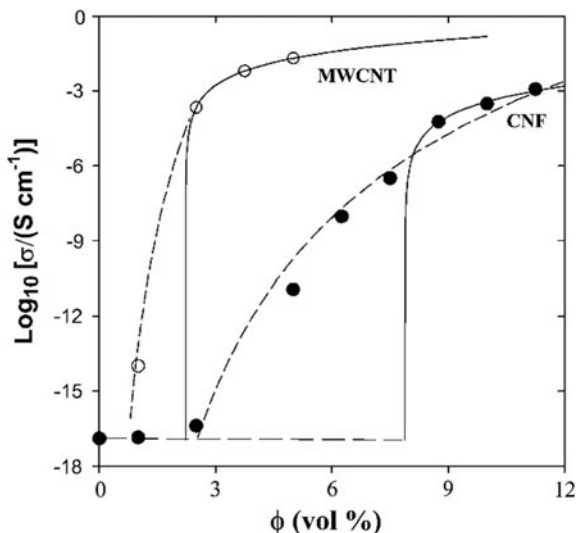
Fig. 11 DC conductivity as a function of filler volume concentration of polyethylene nanocomposites with carbon nanofibers (CNF, solid symbols) or multi-wall carbon nanotubes (MWCNTs, empty symbols) [67]. Reproduced with permission from Linares et al. Macromolecules 2008, 41, 7090–7097

4.3 Polypropylene Composites

Polypropylene is currently the material of choice for capacitor applications over several other polymers (e.g., polystyrene, polyethylene terephthalate) due to its very low dissipation factor (*tanδ* < 0.001), superior dielectric strength (~700 MV/m), thermal stability (130 °C < T_m < 170 °C), and its easier melt processing [53, 68]. Advancements in the chemistry of polyolefins has resulted into isotactic polypropylene (iPP) exhibiting an isotacticity of 97–99% and very low impurity concentration (30 ppm), facilitating processing and bringing its melting point of around 165 °C [69]. In industrial settings, the financial aspects related to the manufacturing conditions play a significant role on the choice of material. For the aforementioned reasons, polypropylene has remained the best option for over half a century. Since 1963 and the MAGVAR invention from General Electric, biaxially oriented polypropylene films have been employed in capacitor applications, as they provide a thin and efficient energy solution for the storage and recovery of electrical energy [68]. The orientation in these films can be achieved through several methods, including simultaneous stretching in two perpendicular directions utilizing an apparatus such as the one presented in Fig. 12. However, in industry, the prevalent approach is the tubular process, which enables continuous production of BOPP [70].

During the earliest tests on unoriented polypropylene, it became clear that orientation is paramount to achieve time endurance, as an increase in dielectric breakdown strength by at least a factor of 2 is achieved with the orientation process. Nash
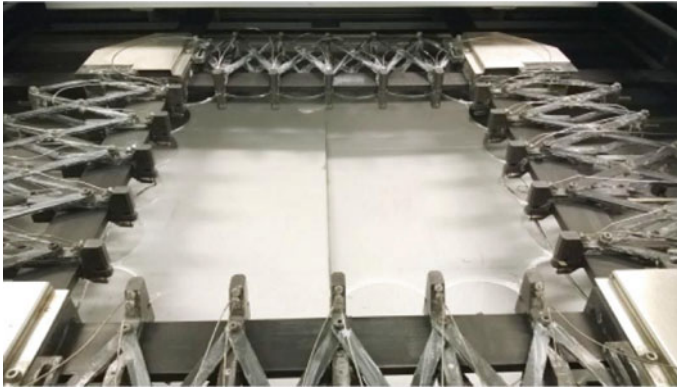
Fig. 12 A biaxial stretching machine [53]. Reproduced with permission from Ryroluoto et al. European Polymer Journal, 2017, 95, 606–624

performed a thorough comparison (averaging 70 production samples) between the dielectric breakdown strength values of oriented and unoriented polypropylene films [68]. The enhancement in the dielectric breakdown strength upon orientation, shown in Fig. 13, is attributed to the transformation of the spherulitic crystalline morphology to a highly ordered fibrillar network, consisting of oriented crystallites [53]. As in the case of polyethylene composites, the improvement of the dielectric breakdown
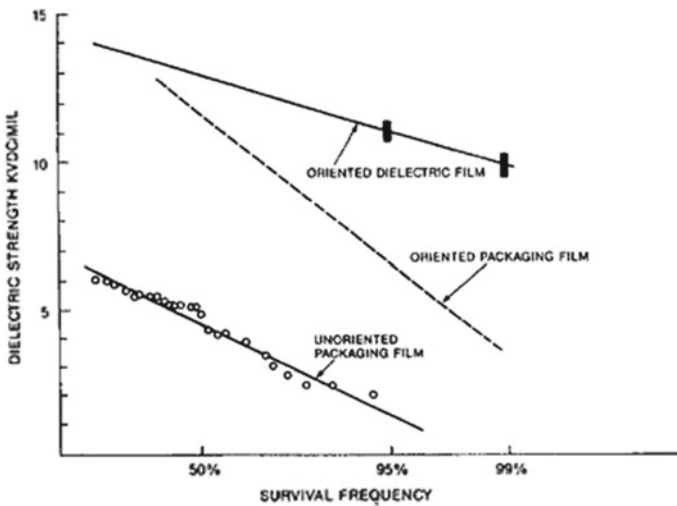
Fig. 13 Dielectric breakdown strength of unoriented and biaxially oriented polypropylene packaging films [68]. J.L Nash, Polymer Engineering and Science, 1988, 28, 862–870. Reproduced with permission

strength due to orientation can be attributed to the crystallites acting as a barrier against treeing [66].

Two more parameters have been found to play a significant role on the dielectric properties of biaxially oriented polypropylene. The first factor is that with orientation, the porosity decreases enhancing thus the dielectric breakdown strength. This is explained on the basis that the density of the material increases through the alignment of the amorphous segments and crystallites [53]. Therefore, orientation reduces the topological electric field enhancement generated around microcavities that induces dielectric failure and breakdown. The second factor relies on the crystal transformation of polypropylene from the β to the α crystal phase that takes place upon stretching. An inversely proportional relationship has been found between the amount of β-phase and the dielectric breakdown strength which also connects with the presence of microvoids within the sample [53]. As shown in Fig. 14, the dielectric breakdown strength is reduced when the β-phase content is increased, thus predicting a better dielectric stability for oriented samples.

Different nanosized inorganic fillers have been used to dope polypropylene and enhance its dielectric properties, resulting in the development of the so-called nanodielectric materials. Calcium carbonate ($CaCO_3$) particles, which are highly polar, are often employed as fillers due to their low commercial price and good thermal resistance. When their size is in the nanoscale (1–100 nm), their inclusion in a propylene matrix increases the dielectric direct-current breakdown, which reaches a maximum at 1.8 wt.% concentration [71]. However, they tend to agglomerate and are hydrophilic, which can be detrimental for electrical energy storage applications [72]. These drawbacks can be avoided through surface modification and chemical functionalization, which can reduce hydrophilicity of the particles and improve the
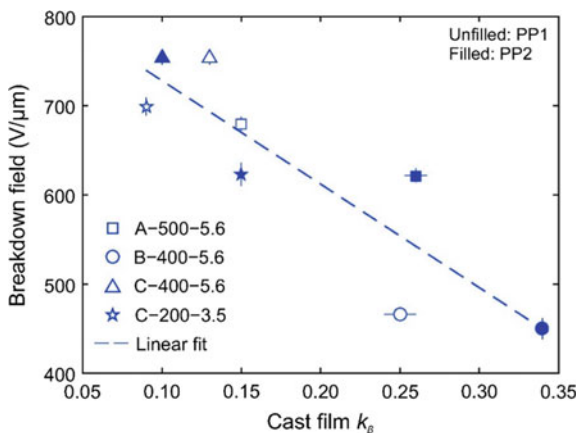
Fig. 14 Breakdown field as a function of the β crystal phase content in two isotactic polypropylenes PP1 and PP2, with Mw, PDI, Tm to be equal to 400 kg/mol, 6.0, 161 °C, and 300 kg/mol, 8.0, 163 °C, respectively [53]. Reproduced with permission from Ryroluoto et al. European Polymer Journal, 2017, 95, 606–624

Table 2 Dielectric properties of metal-isotactic polypropylene nano-composites having different volume fractions of Al nanoparticles in the polymer matrix [75]. Adapted from Fredin et al. Substantial recoverable energy storage in percolative metallic aluminum-polypropylene nanocomposites. Advanced Functional Materials 2013, 23, 3560–3569

Al particle vol%	Permittivity	Interparticle distance (nm)	Dielectric breakdown strength (MV/m)	Al particle vol%
0.7	2.4 ± 0.4	321.3	123.7	0.7
2.0	2.8 ± 0.9	196.9	–	2.0
2.9	3.0 ± 0.4	162.3	85.2	2.9
10.4	10.5 ± 0.3	71.4	119.3	10.4
12.4	15.4 ± 0.1	61.6	75.8	12.4
25.4	conductive	27.3	–	25.4
38.2	conductive	11.1	–	38.2
40.8	conductive	8.7	–	40.8

adhesion/compatibility. The latter effect can enhance the mechanical properties, such as the case when stearic acid is used as a functionalization agent [73]. Another range of ceramic nanoparticles that improve the dielectric behavior of polypropylene are those of very high dielectric constants, like barium titanate (BaTiO3, $\varepsilon_r \sim 2{,}000$). It has been proven that the addition of the $BaTiO_3$ nanoparticles combined with uniaxial orientation can indeed result in high energy densities [74].

Besides ceramic nanofillers, metallic nano-inclusions can be added to enhance the interfacial polarization and hence the dielectric constant of the resulting composite. Table 2 and Fig. 15 show the permittivity and dielectric breakdown strength values for polypropylene composites with metallic aluminum nanoparticles. The composite's permittivity increases up to $\varepsilon_r = 15.4$ for a volume fraction of nanoparticles of 12.4%. This maximum permittivity is reached just before the percolation volume fraction, 16%.

5   Conclusions

In this chapter, we have elaborated on the importance of understanding the correlations between structure, molecular dynamics, and properties in polyolefins and their composites, and how to overcome the difficulties of obtaining insights from dielectric spectroscopy in such nonpolar polymers. We can draw three main conclusions:

1. Different approaches have been successfully implemented to render polyolefins dielectrically active through the introduction of permanent dipoles in the system. These methods might take place either inadvertently during sample preparation/synthesis or deliberately, and include the following: Direct oxidization through thermal treatments, UV-weathering, or gamma radiation exposure, to introduce carbonyl groups in the polymer chain; indirect oxidization, induced by
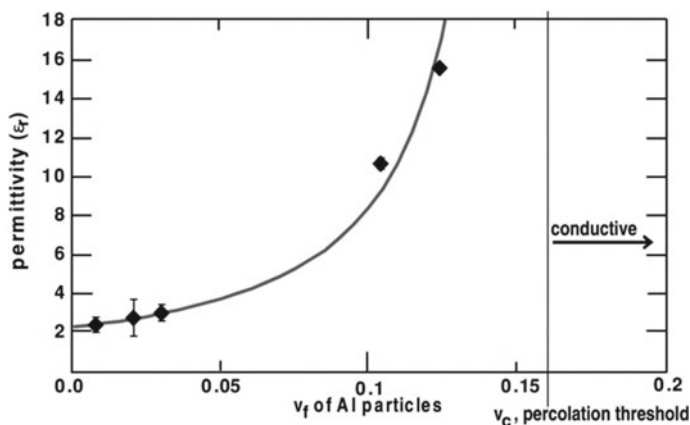
Fig. 15 Experimental permittivity for Al– iso PP nanocomposites as a function of Al nanoparticle volume fraction. Each permittivity is calculated from average capacitance measurements on at least five devices on at least two different thin films; error bars are included for each point, and the solid line is the percolation theory fit for the composites below the critical threshold [75]. Reproduced with permission from Fredin et al. Advanced Functional Materials 2013, 23, 3560–3569

the inclusion of inorganic fillers (e.g., metal oxides); and the addition of small molecules with a large permanent dipole moment that act as dielectric probes.

2. These approaches have enabled a wide range of dielectric studies on polyethylene and polypropylene and provided insights on the molecular origins of the main dielectric relaxations ($\alpha, \beta, \gamma, \delta$), in some cases aided by complimentary mechanical experiments. Moreover, the introduction of dipoles has allowed the monitoring of additional molecular processes, such as the entanglement formation dynamics in ultra-high molecular weight polyethylene (UHMWPE).

3. Polyolefin composites are of great relevance in electrical energy storage and insulation applications, as it is possible to tune their properties by combining the high permittivity and low dielectric losses of the polymer with the right choice of filler properties. The orientations of the polymer crystals, as well as filler orientation and hydrophilicity, have a strong influence on the final dielectric properties, for example, the higher orientation the larger the dielectric breakdown strength.

References

1. Plastics Europe (2018) Plastics—the Facts
2. Plastics Europe (2015) Plastics—the Facts
3. Schönhals A, Kremer F (2003) Broadband dielectr. Spectrosc 59
4. Boyd RH (1985a) Polymer 26:1123
5. Boyd RH, Gee RH, Han J, Jin Y (1994) J Chem Phys 101:788
6. Jourdan C, Cavaille JY, Perez J (1989) J Polym Sci Part B Polym Phys 27:2361

7. Suljovrujic E, Trifunovic S, Milicevic D (2010) Polym Degrad Stab 95:164
8. Tiemblo P, Gómez-Elvira JM, García Beltrán S, Matisova-Rychla L, Rychly J (2002) Macromol. 35:5922
9. Frübing P, Blischke D, Gerhard-Multhaupt R, Khalil MS (2001) J Phys D Appl Phys 34:3051
10. Drakopoulos SX, Psarras GC, Forte G, Martin-Fabiani I, Ronca S (2018) Polymer 150:35
11. Kakizaki M, Kakudate T, Hideshima T (1985) J Polym Sci Polym Phys Ed 23:809
12. Stamboliev G, Suljovrujic E (2010) Polym Degrad Stab 95:593
13. Quijada-Garrido I, Barrales-Rienda JM, Pereña JM, Frutos G (1997) J Polym Sci Part B Polym Phys 35:1473
14. Suljovrujic E (2012) Polym Bull 6:2033
15. Starkweather HW, Avakian P, Matheson RR, Fontanella JJ, Wintersgill MC (1992) Macromolecules 25:6871
16. Boyd RH (1985b) Polymer 26:323
17. Wunderlich B (2003) Prog Polym Sci 2:383
18. Stehling FC, Mandelkern L (1970) Macromolecules 3:242
19. Lee H, Cho K, Ahn T, Choe S, Kim I, Park I, Lee BH (1997) J Polym Sci Part B Polym Phys 3:1633
20. Vlassopoulos D (2006) Eur Phys J E 19:113
21. Alberola N, Cavaille JY, Perez J (1992) Eur Polym J 2:949
22. Cooper JW, Mccrum NG (1972) J Mater Sci 7:1221
23. McCrum NG, Read BE, Williams G (1967) Anelastic and dielectric effects in polymer solids. Wiley, London
24. Ashcraft CR, Boyd RH (1976) J Polym Sci Polym Phys Ed 1:2153
25. Gilchrist JLG (1978) J Polym Sci Polym Phys Ed 16:1773
26. Phillips WA (1970) Proc R Soc A Math Phys Eng Sci 319:565
27. Milicevic D, Micic M, Suljovrujic E (2014) Polym Bull 7:2317
28. Suljovrujic E (2009) Polym Degrad Stab 9:521
29. Ribes-greus A, Calleja RD (1989) 38:1127
30. Olivares N, Tiemblo P, Gómez-Elvira JM (1999) Polym Degrad Stab 6:297
31. Livanova NM, Zaikov GE (1997) Oxid Commun 2:443
32. Ramanujam M, Wachtendorf V, Purohit PJ, Mix R, Schönhals A, Friedrich JF (2012) Thermochim Acta 530:73
33. Roe RJ, Gieniewski C (1973) Macromolecules 6:212
34. Rastogi S, Lippits DR, Peters GWM, Graf R, Yao Y, Spiess HW (2005) Nat Mater 4:635
35. Romano D, Andablo-Reyes E, Ronca S, Rastogi S (2015) Polymer 74:76
36. Ferry JD (1980) Viscoelastic properties of polymers, 3rd edn. Wiley, New York
37. Liu K, de Boer EL, Yao Y, Romano D, Ronca S, Rastogi S (2016) Macromolecules 49:7497
38. Adachi K, Kotaka T (1987) J Mol Liq 3:75
39. Van Den Berg O, Sengers WGF, Jager WF, Picken SJ, Wübbenhorst M (2004) Macromolecules 37:2460
40. Sengers WGF, Van Den Berg O, Wübbenhorst M, Gotsis AD, Picken SJ (2005) Polymer 46:6064
41. Simon P, Gogotsi Y, Dunn B (2014) Science (80–) 343:1210
42. Presser V, Dennison CR, Campos J, Knehr KW, Kumbur EC, Gogotsi Y (2012) Adv Energy Mater 2:895
43. Tomer V, Polizos G, Randall CA, Manias E (2011) J Appl Phys 1:074113
44. Jiang J, Zhang X, Dan Z, Ma J, Lin Y, Li M, Nan C-W, Shen Y, Appl ACS (2017) Mater Interfaces 9:29717
45. Hao X (2013) J Adv Dielectr 0:1330001
46. Chen Q, Shen Y, Zhang S, Zhang QM (2015) Annu Rev Mater Res 4:433
47. Yao Z, Song Z, Hao H, Yu Z, Cao M, Zhang S, Lanagan MT, Liu H (2017) Adv Mater 29s
48. Roy M, Nelson JK, MacCrone RK, Schadler LS, Reed CW, Keefe R, Zenger W (2005) IEEE Trans Dielectr Electr Insul 1:629
49. Tanaka T, Kozako M, Fuse N, Ohki Y (2005) IEEE Trans Dielectr Electr Insul 1:669

50. Ezquerra TA, Majszczyk J, Baltà-Calleja FJ, López-Cabarcos E, Gardner KH, Hsiao BS (1994) Phys Rev B 50:6023
51. Arous M, Ben Amor I, Kallel A, Fakhfakh Z, Perrier G (2007) J Phys Chem Solids 68:1405
52. Hozumi N, Ishida M, Okamoto T, Fukagawa H (1990) IEEE Trans Electr Insul 2:707
53. Rytöluoto I, Gitsas A, Pasanen S, Lahti K (2017) Eur Polym J 9:606
54. Luo X, Chung DD (1999) Compos Part B Eng 3:227
55. Psarras GC (2006) Compos Part a Appl Sci Manuf 3:1545
56. Lux F (1993) J Mater Sci 2:285
57. Connor MT, Roy S, Ezquerra TA, Baltá Calleja FJ (1998) Phys Rev B 57:2286
58. Tsangaris GM, Psarras GC, Kouloumbi N (1998) J Mater Sci 3:2027
59. Pourrahimi AM, Olsson RT, Hedenqvist MS (2018) Adv Mater 3:1
60. Ayoob R, Alhabill F, Andritsch T, Vaughan A (2018) J Mater Sci 5:3427
61. Li B, Xidas PI, Manias E (2018) ACS Appl Nano Mater acsanm.8b00671
62. Ronca S, Igarashi T, Forte G, Rastogi S (2017) Polymer 123:203
63. Hosier IL, Praeger M, Vaughan AS, Swingler SG (2017) IEEE Trans Dielectr Electr Insul 2:3073
64. Wang W, Min D, Li S (2016) IEEE Trans Dielectr Electr Insul 2:564
65. Li B, Xidas PI, Triantafyllidis KS, Manias E (2017) Appl Phys Lett 1:082906
66. Yahagi K (1980) IEEE Trans Electr Insul EI-15 241
67. Linares A, Canalda JC, Cagiao ME, Garcia-Gutiérrez MC, Nogales A, Martín-Gullón I, Vera J, Ezquerra TA (2008) Macromolecules 41:7090
68. Nash JL (1988) Polym Eng Sci 2:862
69. Rabuffi M, Picci G (2002) IEEE Trans Plasma Sci 3:1939
70. Ajji A, Dumoulin MM, In Karger-Kocsis J ed (1999) Springer Netherlands, Dordrecht, pp 60–67
71. Virtanen S, Ranta H, Ahonen S, Karttunen M, Pelto J, Kannus K, Pettersson M (2014) J Appl Polym Sci 1:1
72. Bánhegyi G, Karasz FE (1987) Colloid Polym Sci 2:394
73. Etelaaho PJP, Haveri S (2011) Polym Compos 3:464
74. Zheng MS, Zheng YT, Zha JW, Yang Y, Han P, Wen YQ, Dang ZM (2018) Nano Energy 48:144
75. Fredin LA, Li Z, Lanagan MT, Ratner MA, Marks TJ (2013) Adv Funct Mater 2:3560

Confined Glassy Dynamics in a Star-Shaped Polymer Induced by Crystallization: Case Study of Polyhedral Oligomeric Polysilesquioxane—Isotactic Polystyrene (POSS-iPS)

Martin Tress, Arthur Markus Anton, Maximilian Vielhauer, Pierre Lutz, Rolf Mülhaupt, and Friedrich Kremer

Abstract The crystallites in semi-crystalline polymers typically constrain the segmental motion of the protruding chains in close proximity. While segments far away from the crystallites have the same (unperturbed) dynamics as the purely amorphous state (mobile amorphous fraction), the segments in the transition regions around the crystallites relax significantly slower (rigid amorphous fraction). Here, we present a study combining broadband dielectric spectroscopy (BDS) and Fourier transform infrared spectroscopy (FTIR) which reveals a further type of perturbation of contrary impact on the dynamics. In a star-shaped polymer—based on a polyhedral oligomeric silesquioxane (POSS) molecule as center and isotactic polystyrene arms—we demonstrate for the first time that in the semi-crystalline state remaining amorphous segments can exhibit a faster mean relaxation rate than in the purely

M. Tress (✉) · A. M. Anton · F. Kremer
Leipzig University, Leipzig, Germany
e-mail: martin.tress@uni-leipzig.de

A. M. Anton
e-mail: arthur.anton@sheffield.ac.uk

F. Kremer
e-mail: friedrich.kremer@physik.uni-leipzig.de

A. M. Anton
The University of Sheffield, Sheffield, UK

M. Vielhauer · R. Mülhaupt
University Freiburg, Freiburg, Germany
e-mail: maximilian.vielhauer@fmf.uni-freiburg.de

R. Mülhaupt
e-mail: rolf.muelhaupt@makro.uni-freiburg.de

P. Lutz
University Strasbourg, Strasbourg, France
e-mail: lutz@ics.u-strasbg.fr

267

amorphous state. This signature is typical for spatial confinement and a decomposition of the respective relaxation time distribution yields three fractions of different dynamics. These are assigned to a rigid amorphous fraction around the crystallites, a mobile amorphous fraction, and a confined amorphous fraction of enhanced dynamics presumably located around the POSS centers. In complementary FTIR measurements, crystalline and amorphous moieties can be addressed individually and their evolution upon crystallization can be traced. The better time resolution of the FTIR data reveals a multi-step process with a particular lag time; firstly, a fast mechanism initializes the crystallization, secondly, a tenfold slower process is present, which matches the BDS results. This suggests a complex interplay between the crystallization of the iPS arms and conformational changes due to the complex architecture and structural constraints.

Keywords Star-polymer · Confinement · Enhanced dynamics · POSS

Abbreviations

BDS   Broadband Dielectric Spectroscopy
CAF   Confined Amorphous Fraction
DSC   Differential Scanning Calorimetry
FTIR   Fourier Transform Infrared Spectroscopy
HN   Havriliak-Negami
iPS   Isotactic Polystyrene
MAF   Mobile Amorphous Fraction
RAF   Rigid Amorphous Fraction
POSS   Polyhedral Oligomeric Silsesquioxane
RTD   Relaxation Time Distribution

1   Introduction

Crystallization in polymers can tremendously alter their material properties and is therefore of great interest in fundamental and applied research [1, 2]. Thereby, not only the properties of the crystalline structure itself are relevant. Due to the fact that polymers basically never crystallize entirely, the implications for the remaining amorphous fraction are of similar or even bigger importance. In most cases, the material becomes macroscopically more rigid while its toughness is reduced after (partial) crystallization [3, 4]. On the molecular scale this can be comprehended by the smaller number of chains which can relax and dissipate mechanical stress. In the crystalline domains the chains are arranged in lamellar structures which do not allow for stress release (except for mobility along the chain axis in certain polymers [5]).

Additionally, several chains can become connected if parts of them are joined in the same crystallite. This connection acts as crosslink which further inhibits mechanical stress relaxation.

A more subtle effect is the impact on the polymer segments of the chains protruding from the crystallites. Due to the immobilization of chain segments in the crystallite, the adjacent segments which are not part of the crystalline order are still limited in their mobility. While structural aspects of crystallization are typically addressed with scattering techniques [6–8] and thermodynamic methods [9, 10], such mobility implications require dynamical methods that directly probe molecular quantities [11, 12]. The development of the so-called rigid amorphous fraction (RAF), i.e. a transition zone from the normal amorphous domain to the crystallite, with a reduced mobility has been demonstrated by dielectric spectroscopy investigations in several polymers [2, 11]. To some extent, the RAF corresponds to the interfacial layer in polymer-nanocomposites where attractive interactions between nanoparticles and polymer segments generate a layer of segments with reduced mobility at the interface of the particles [13, 14]. This effect is fundamental to the property enhancement of nanocomposites.

Here we present a case where the dynamics in the amorphous fraction of the polymer becomes faster after partial crystallization of a star-shaped polymer. The reason for this unexpected and counterintuitive response is the complex architecture of the chains and its interplay with constraints arising from the crystallization process. Further we will demonstrate how dielectric spectroscopy can be used to resolve regions of different dynamics; in fact, the signature of a RAF is found as well as normal amorphous behavior and a considerable fraction which exhibits characteristics of dynamics in confinement [15, 16]. Finally, complimentary measurements by means of infrared spectroscopy reveal a lag time of about 30 min in-between the temperature jump initializing the crystallization process and first impacts on structure-specific molecular vibrations become detectable. After this lag time, a fast mechanism with a time constant around $2–3 \times 10^3$ s primes the crystallization and a second process follows which is about 10 times slower and matches to the BDS results. This suggests a multi-step process which is probably a result of the interplay of constraints imposed by the crystallization and the complex architecture of the molecules.

2 Sample Preparation and Measurements

2.1 Synthesis

Vinyl-terminated isotactic polystyrene (iPS) was synthesized by polymerization of styrene on post-metallocene titanium catalysts using 1,9-decadiene as chain transfer agent in toluene under dry argon atmosphere. Octakis (dimethylsilyloxy) silesquioxane was obtained from Hybrid Plastics and used as received. It was

dissolved in toluene together with the vinyl-terminated iPS. Under dry argon atmosphere the hydrosilylation reaction to connect the iPS to the edges of the octakis (dimethylsilyloxy) silesquioxane was initiated by adding a xylene solution with Karstedt catalyst. After 2 h reaction time the solvent was removed by drying, and then, the product was purified in a chloroform solution and fractionation by methanol. The resulting star-polymers have 6–8 iPS arms attached to a polyhedral oligomeric silsesquioxane (POSS) molecule. Details on the synthesis were published elsewhere [17].

2.2 Crystallization Procedure

In order to remove any thermal history before each experiment, the sample is heated above its melting temperature of $T_m = 206$ °C (~480 K). The amorphous state is prepared by annealing at 210 °C for about 1 h in the case of dielectric and calorimetric experiments and 4 h before the infrared measurements. The sample was crystallized at $T_c = 460$ K for up to 20 h. In the case of the dielectric experiments, the sample dynamics was probed at certain times during and after the crystallization whereby the sample had to be cooled rapidly from T_c to $T_g + 25$ K (335 K) and below for each measurement. In the case of the infrared measurements spectra are collected continuously at T_c and molecular vibrations are monitored.

2.3 Broadband Dielectric Spectroscopy (BDS)

The broadband dielectric spectroscopy (BDS) measurements were performed with an Alpha-A Analyzer (Novocontrol) connected to a Quatro cryo-system (Novocontrol) in a frequency and temperature range from 0.1 Hz to 1 MHz and 350 to 480 K, respectively.

The sample was prepared by spin-coating from a toluene solution onto a piece of highly conductive and ultra-flat silicon as lower electrode after a thorough cleaning by acetone rinse, plasma treatment (100 W for 5 min) and expurgation with supercritical CO_2 [12]. The film of several hundred nm thickness was then covered by a top electrode also made of highly conductive silicon which had silica nano-structures as spacers with a height of 550 nm. These spacers prevent an electrical short circuit between the electrodes and establish a free upper interface of the film which allows for relaxation of mechanical stresses and structural rearrangements during potential phase transitions.

2.4 Fourier-Transform Infrared Spectroscopy (FTIR)

Fourier transform infrared spectroscopy (FTIR) measurements were performed with a Bio–Rad FTS 6000 FTIR spectrometer equipped with a UMA 500 IR microscope and a liquid nitrogen-cooled mercury-cadmium telluride (MCT) detector (Kolmar Technologies, Inc., USA). To control the sample temperature, a THMS 350 V stage (Linkam Scientific Instruments, UK) has been used and continuously flushed with dry nitrogen during the measurement. To monitor the sample during crystallization, spectra were recorded with an initial time resolution of approximately 2 min which was increased to about 5 min after 2 h of crystallization.

The sample material has been deposited by drop-casting from toluene solution (20 mg/ml) onto an IR-transparent substrate (BaF2, Korth Kristalle GmbH, Germany) until the desired sample thickness and, thus, absorption was reached. Then, the sample was dried under ultra-high vacuum (10^{-5} mbar) at 423 K for 20 h before the actual measurement.

2.5 Differential Scanning Calorimetry (DSC)

The differential scanning calorimetry (DSC) measurements were conducted with a Q2000 differential scanning calorimeter (TA Instruments) in a temperature range from 335 to 515 K. Sample masses of 5–10 mg were put into standard aluminum pans and studied at a heating rate of 10 K/min. From the area underneath the melting peak the specific heat of fusion ΔH_f was extracted to calculate the degree of crystallinity f_c according to [18]:

$$f_c = \frac{\Delta H_f}{\Delta H_{f,c}} \tag{1}$$

where $\Delta H_{f,c} = 86.5864$ J/g [18, 19] denotes the specific heat of fusion of iPS with 100% crystallinity.

3 Experimental Results

3.1 Crystallite Dimensionality

Classically, crystallization is monitored by calorimetric techniques. Also, the heat capacity of POSS-iPS as determined by means of DSC exhibits a sharp melting peak if the material was crystalized before (Fig. 1a). The area under this peak is used to
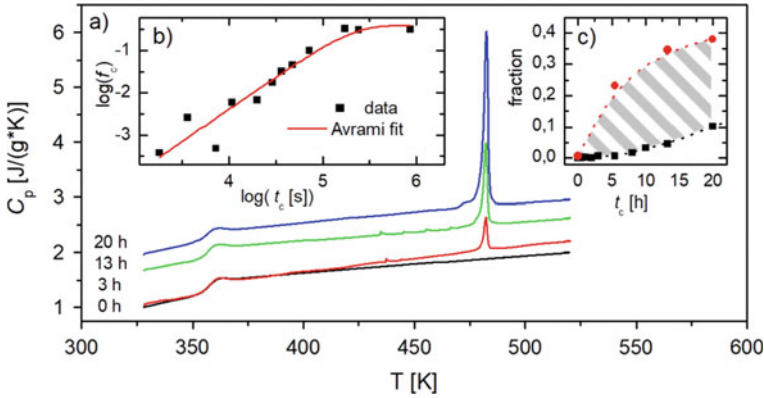
Fig. 1 a Specific heat capacity of POSS-iPS after different times of crystallization at 460 K as indicated; for clarity the curves are shifted vertically. **b** Double-logarithmic plot of the degree of crystallinity f_c versus the crystallization time t_c at 460 K as well as a fit to the Avrami equation. **c** Proportion of crystallinity f_c as determined by DSC (black squares) and fraction of the immobilized segments $1 - \Delta\varepsilon(t_c)/\Delta\varepsilon(t_c = 0)$ (red circles) as measured by BDS as function of crystallization time t_c at 460 K. The dotted lines are a guide to the eye and the gray-shaded areas indicate the number of segments which are immobilized but not crystalized. Taken with permission from [12]

calculate the degree of crystallinity according to Eq. 1. Its time dependence $f_c(t)$ can be described by the Avrami equation [20] (Fig. 1b):

$$f_c(t) = f_{c,\max}\big[1 - \exp\big(-Kt^n\big)\big] \qquad (2)$$

where $f_{c,\max}$ is the maximum degree of crystallinity that can be achieved in the experiment, K is a constant which depends on the rates of nucleation and growth, and n is the so-called Avrami exponent. The latter is interpreted as an indicator for the dimensionality of the growth of the crystallites [21]. For the 2-dimensional lamellar crystallite structure in linear iPS, which is verified by X-ray scattering [11], Avrami exponents of ~1.7 have been deduced from the crystallization kinetics [22]. For the POSS-iPS we find a value of 1.6 (± 0.6) which is close and suggests a similar crystallite dimensionality.

3.2 Dynamical Changes After Crystallization

The dielectric loss spectra $\varepsilon''(\omega)$ of purely amorphous POSS-iPS exhibit a clear relaxation process in the investigated frequency range at temperatures from 355 to 375 K (Fig. 2a). To analyze its characteristic parameters, a Havriliak Negami (HN) function is fitted to the data [23]:
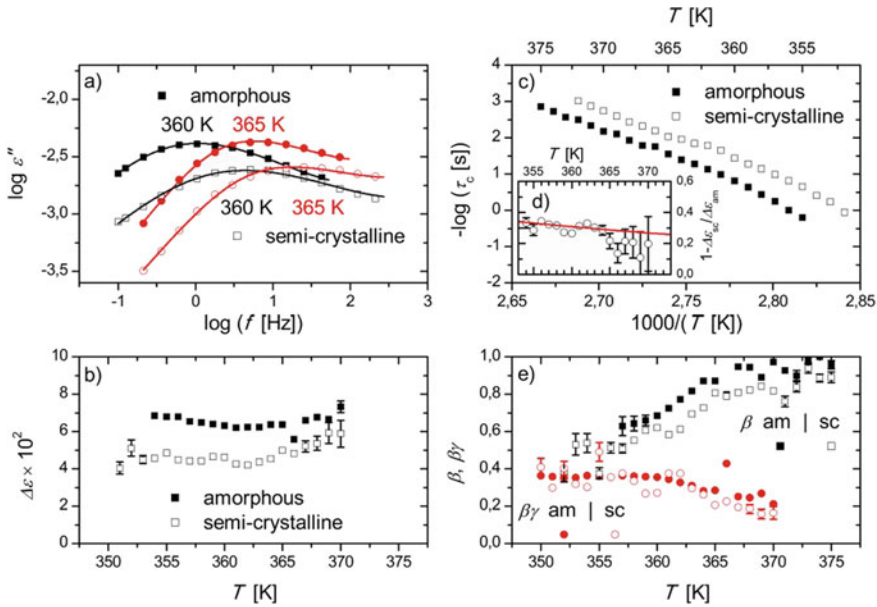
Fig. 2 **a** Dielectric loss spectra $\varepsilon''(f)$ in the amorphous and semi-crystalline state at different temperatures as indicated. A high frequency contribution from the silicon electrodes[25] has been cropped for clarity. The solid lines are fits to an equivalent circuit equation including the Havriliak-Negami function. From these fits, the following parameters were extracted: **b** relaxation strength $\Delta\varepsilon$ versus temperature, **c** mean relaxation time τ_c versus inverse temperature, **d** fraction of immobilized segments $1 - \Delta\varepsilon_{sc}/\Delta\varepsilon_{am}$ and **e** slopes of the low and high frequency wing of the relaxation peak β and $\beta\gamma$, respectively. The experimental error is smaller than the symbol size unless indicated otherwise. Taken with permission from [12]

$$\varepsilon''(\omega) = -\text{Im}\left[\frac{\Delta\varepsilon}{\left(1 + (i\omega\tau_{HN})^\beta\right)^\gamma}\right] \tag{3}$$

Here Im denotes the imaginary part, $\Delta\varepsilon$ the relaxation strength, τ_{HN} the relaxation time while β and γ are the symmetric and asymmetric shape parameter, respectively. The characteristic relaxation time τ_c reflecting the peak position can be calculated according to [15]:

$$\tau_c = \tau_{HN}\left[\frac{\sin\left(\frac{\pi\beta\gamma}{2+2\gamma}\right)}{\sin\left(\frac{\pi\beta}{2+2\gamma}\right)}\right]^{1/\beta} \tag{4}$$

It corresponds to the invesre mean relaxation rate and follows a non-Arrhenius temperature dependence (Fig. 2c) which can be described by the empirical Vogel-Fulcher-Tammann equation [24–26]:

$$\tau_c = \tau_0 \exp\left(\frac{B T_0}{T - T_0}\right) \tag{5}$$

where τ_0 is the limiting relaxation time, B a constant and T_0 the Vogel temperature. This type of thermal activation is characteristic for segmental fluctuations which resemble the dielectric α-relaxation.

In the semi-crystalline state, the α-relaxation peak is still clearly visible, but its relaxation strength is diminished (Fig. 2b) which reflects the reduced number of mobile segments. Compared with the relaxation strength in the purely amorphous state, a reduction of about 20–35% is found; whereby the lower end of this range is observed at higher temperatures with a continuous increase toward lower temperatures (Fig. 2c). This implies that a considerable fraction of the immobilized segments is not part of the crystallites since they can be thermally activated. That is also corroborated by the fact that the crystallinity deduced from the DSC measurements is considerably lower than the reduction in relaxation strength (Fig. 1c).

Moreover, the peak is shifted to higher frequencies in the semi-crystalline state which resembles a faster mean relaxation rate of the mobile segments. It still exhibits a VFT-type thermal activation, but it is about half to one decade faster than in the purely amorphous state (Fig. 2c). Additionally, the shape of the relaxation process changes after crystallization; especially the high frequency wing and to a smaller extent also the low frequency wing exhibit less pronounced slopes as quantified by the reduced values of the parameters β and $\beta\gamma$, respectively (Fig. 2e).

3.3 Dissecting Dynamics in the Semi-crystalline State

To examine the implication of the crystallite formation on the dynamics in greater detail, the relaxation time distributions (RTD) $G(\tau)$ were calculated from the HN fit parameters according to [15]:

$$G(\tau) = \frac{\sin\left(\gamma\left[\frac{\pi}{2} - \arctan\left(\frac{\left(\frac{\tau}{\tau_{HN}}\right)^\beta + \cos(\pi\beta)}{\sin(\pi\beta)}\right)\right]\right)}{\pi\left(1 + 2\cos(\pi\beta)\left(\frac{\tau_{HN}}{\tau}\right)^\beta + \left(\frac{\tau_{HN}}{\tau}\right)^{2\beta}\right)^{\gamma/2}} \tag{6}$$

Since the quality of the calculated $G(\tau)$ relies strongly on the accurate determination of the shape parameters, the values obtained at a temperature of 360 K were used for this analysis. At this temperature, the relaxation peak is located centrally in the accessible frequency range which guarantees optimal conditions to determine the slopes of both the low and high frequency wings of the relaxation. By scaling the relaxation time distribution functions with the ratio of the actual relaxation strength of the respective process and the relaxation strength in the purely amorphous state as pre-factor, the area under the curve directly reflects the number of mobile segments
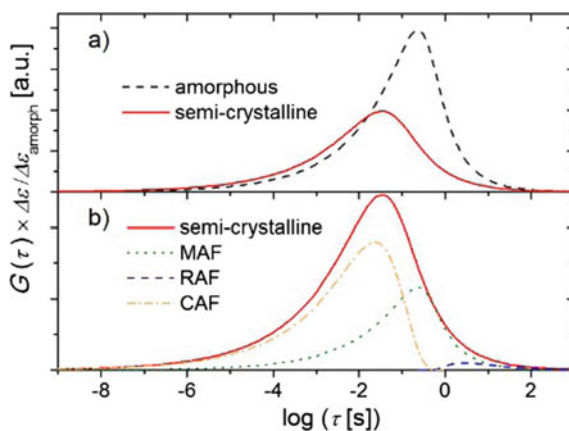
Fig. 3 **a** Scaled relaxation time distributions $G(\tau)\Delta\varepsilon/\Delta\varepsilon_{am}$ of the purely amorphous state and the semi-crystalline sample after 20 h of crystallization. **b** $G(\tau)\Delta\varepsilon/\Delta\varepsilon_{am}$ of semi-crystalline sample and its decomposition into the contributions of the CAF and the RAF by subtracting a downscaled $G(\tau)$ of the amorphous state which resembles the MAF. Modified with permission after [12]

in the corresponding state. This enables a quantitative comparison of the RTD taken before and after the crystallization (Fig. 3a). In addition to the shift in the mean relaxation time which has been found also from the loss peaks, this presentation reveals the emergence of new relaxation modes at shorter times during the crystallization. This may be interpreted in the sense that different spatial regions are formed which exhibit different dynamics; some regions may retain the unperturbed dynamics known from the purely amorphous state while in other regions the dynamics are altered.

To disentangle these, the purely amorphous RTD is downscaled so that its maximum just fits into the RTD of the semi-crystalline state (Fig. 3b). The ratio of the areas of these two curves is then an estimate for the fraction of mobile segments which show unperturbed dynamics. Subtracting the former from the latter curve yields the RTD of the perturbed segments which is a bimodal distribution; one large peak at shorter times and a small peak at longer times. The latter resembles a small fraction of segments with slower dynamics which can easily be attributed to the RAF known from the literature. It is plausible that such a fraction is present around the crystallites also in this special case but only due to the detailed analysis it can be resolved. The faster fraction is even larger than the fraction of unperturbed segments, and apparently the dominant moiety for the overall dynamical response. This indicates that a considerable number of segments exhibits altered dynamics as known from systems in geometrical confinement where molecular packing is frustrated [16]. In relation to this we will call this proportion of segments the confined amorphous fraction (CAF). Since this observation opposes previous knowledge of the impact of crystallites on the dynamics of the surrounding amorphous chains in linear polymers, we concur that the interplay of the crystallization with the complex architecture of the presented molecules leads to altered conformations and, thus, to a qualitatively different change in dynamics.

3.4   Spatial Distribution of Regions with Different Dynamics

Following the picture that the RAF is not only dynamically distinct but also spatially separated, namely in a layer surrounding each crystallite, we assume that also the segments belonging to the CAF are concentrated in a particular region. Hence, CAF does not only refer to a certain proportion of the segments but also to particular spatial regions. The architecture of the chains then allows more detailed conjectures about the distribution of these regions.

It is known that in the presence of POSS molecules the crystallization of polymer chains is suppressed [27–30]. Since in the studied star-polymer the arms are relatively short, the chains are likely to resemble soft spherical shapes with only limited interpenetration of arms of adjacent chains. Consequently, the POSS which connects the arms of each molecule will be located roughly in the centers of these sphere-like molecules and their arrangement may be approximated by some spherical packing. For reasons of simplicity we will assume close packing of spheres to estimate the average center-to-center distance of adjacent molecules of volume V which is then given by:

$$2r = \left(\sqrt{2}V\right)^{1/3} \tag{7}$$

The volume of a single POSS-iPS molecule is calculated from its molecular weight per arm $M_{n,a} = 5500$ g/mol and the number of arms n_a (6–8) as well as the bulk density of amorphous iPS $\rho_{am} = 1.06$ g/cm^3 and Avogadro's number N_A:

$$V_m = n_a \frac{M_{n,a}}{\rho_{am}N_A} \tag{8}$$

which yields center-to-center distances of 4.2–4.6 nm. This is exceeded by the combined size of the one amorphous and one crystalline domain thickness in linear iPS by a factor of 3 (12.5–14.5 nm) [11]. This strongly indicates that at least in its final stages the crystallization is likely to be constrained. Furthermore, it appears favorable for crystallites to start growth as far away as possible from the POSS kernels, i.e. in the regions where arms of adjacent molecules join. As a result, each star-polymer may become connected to its neighbors via joint crystallization of the tips of the arms.

The density increase upon crystallization requires a concentration of segments in the outer region of the sphere-like molecules. Since, due to the star architecture, this process can happen in all directions from the POSS kernel, the chains are stretched from the center to provide a higher density at the crystallites. This stretching may also decrease the density especially in the vicinity of the POSS kernel. Both effects the stretching of chains [31] and the reduction of density [16] are known to enhance the dynamics. For reasons of continuity we can infer that the RAF forms a layer around the crystallites which is then followed by a region of segments which exhibit

the same dynamics as in the purely amorphous state, the so-called mobile amorphous fraction (MAF), before the fastest dynamics is present most likely around the POSS (CAF).

If we understand the different dynamical fractions to reflect a spatial heterogeneity, the areas of the scaled RTD also resemble the relative size of the corresponding regions. To introduce an absolute length scale, we may infer that crystallites typically grow in lamellar structures which in the present case must fit in-between the planes defined by the arrangement of the POSS kernels of the star-shaped polymer chains. Consequently, the separation between these planes defines a maximum distance. We assume that the POSS kernels are in the center of the CAF which means that the distance $h = (2/3)^{1/2} 2r = 3.6 \ (\pm 0.2)$ nm (considering a close packing pattern) between two adjacent planes of POSS kernels contains two times half the thickness of the CAF $2d_{\mathrm{CAF}}/2$, two times the thickness of each the MAF d_{MAF} and the RAF d_{RAF} (we consider $d_{\mathrm{MAF}}/2$ to reflect the thickness of a single MAF layer; the same applies to $d_{\mathrm{RAF}}/2$), and the thickness of the crystalline lamella d_c:

$$h = d_c + d_{\mathrm{RAF}} + d_{\mathrm{MAF}} + d_{\mathrm{CAF}} \tag{9}$$

In a lamellar geometry, the ratio of any of these thicknesses to h is equivalent to the volume fraction of the corresponding dynamical fraction. From the degree of crystallinity f_c as determined by DSC it can be determined directly that $d_c = f_c h = 0.11 \ (\pm 0.02)$ nm. The thicknesses of the other dynamical fractions can be estimated from the area ratio A_i/A_{total} of the scaled RTD where A_i is the area under the RTD of the separated component (the index i denotes CAF, MAF or RAF) and A_{total} the area under the corresponding total RTD. Since A_{total} reflects only the number of mobile segments, a scaling by the factor $\Delta\varepsilon_{\mathrm{sc}}/\Delta\varepsilon_{\mathrm{am}}$ is required to normalize to the whole volume; here $\Delta\varepsilon_{\mathrm{sc}}$ and $\Delta\varepsilon_{\mathrm{am}}$ denote the relaxation strengths in the semi-crystalline state under study and the purely amorphous state, respectively. This yields for the volume fractions of the CAF:

$$f_{\mathrm{CAF}} = \frac{A_{\mathrm{CAF}}}{A_{\mathrm{total}}} \frac{\Delta\varepsilon_{\mathrm{sc}}}{\Delta\varepsilon_{\mathrm{am}}} \tag{10}$$

and the MAF

$$f_{\mathrm{MAF}} = \frac{A_{\mathrm{MAF}}}{A_{\mathrm{total}}} \frac{\Delta\varepsilon_{\mathrm{sc}}}{\Delta\varepsilon_{\mathrm{am}}} \tag{11}$$

For the RAF, however, it must be considered that only a certain proportion of it is mobile while a considerable part is immobilized and does not contribute to the relaxation data. Therefore, two terms are required for its description; that of the former is equivalent to the terms describing the CAF and the MAF whereas the latter basically denotes the difference between the proportion of immobile segments $(1 - \Delta\varepsilon_{\mathrm{sc}}/\Delta\varepsilon_{\mathrm{am}})$ and the crystalline fraction f_c:

$$f_{RAF} = \frac{A_{RAF}}{A_{total}} \frac{\Delta\varepsilon_{sc}}{\Delta\varepsilon_{am}} + 1 - \frac{\Delta\varepsilon_{sc}}{\Delta\varepsilon_{am}} - f_c \qquad (12)$$

Based on these considerations, domain thicknesses of $d_{RAF}/2 = 0.46\ (\pm 0.09)$ nm, $d_{MAF}/2 = 0.45\ (\pm 0.09)$ nm and $d_{CAF} = 1.66\ (\pm 0.23)$ nm are obtained for the rigid amorphous, mobile amorphous and confined amorphous fraction, respectively [the corresponding volume fractions are $f_{RAF} = 0.26\ (\pm 0.04)$, $f_{MAF} = 0.25\ (\pm 0.04)$ and $f_{CAF} = 0.46\ (\pm 0.04)$].

Although one can expect to find smaller domain thicknesses than in linear iPS, particularly the calculated thickness of the crystalline domain is unphysically small (about half of a typical repeat unit length of polystyrene). Consequently, we presume that the crystallites actually grow thicker, but instead of expanding through the entire plane they are rather limited to small islands (Fig. 4b). This suggested limitation in growth may also be plausible in view of the reduced values of the Avrami exponents compared to the linear iPS.

Fig. 4 Sketches of **a** extended lamellae of crystalline domains and **b** small crystalline domains. Each large hexagon approximates the extension of one POSS-iPS star-molecule. Taken with permission and modified after [12]
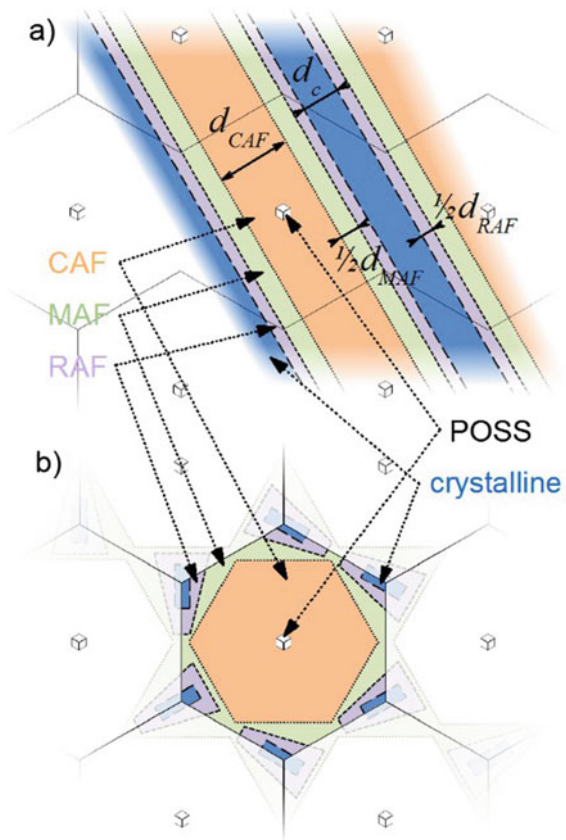
3.5 Kinetics of the Crystallization and Coevolution of the Dynamical Changes

In order to trace the development of the changes in the amorphous regions during the formation and growth of the crystallites, the dynamics at a temperature of 360 K were recorded after different times of crystallization at 460 K. The reduction of the relaxation strength as well as the relaxation time both follow the law of an exponential decay. The corresponding time constants are 2.3×10^4 s in the former and 1.2×10^4 s in the latter, which is merely comparable. This indicates that both changes are related which agrees with the conjecture that the crystallization (which reduces $\Delta\varepsilon$) causes conformational changes which in turn yields faster relaxation times (Figs. 5 and 6).

To obtain deeper insight into the individual evolution of the different dynamical regions, the separation procedure described in the previous section is applied to the RTD at different crystallization times. In the case of the RAF, the mean relaxation time is almost constant which is plausible since the mobility constraint is just caused by the presence of crystallites. Only their size and quantity determine the number of segments in the RAF because the latter scales with the combined surface area of

Fig. 5 **a** Characteristic relaxation time τ_c and **b** dielectric relaxation strength $\Delta\varepsilon$ of segmental relaxation at 360 K as function of the crystallization time. The experimental uncertainty is smaller than the symbol size if not stated otherwise; the red line represents a fit to an exponential function
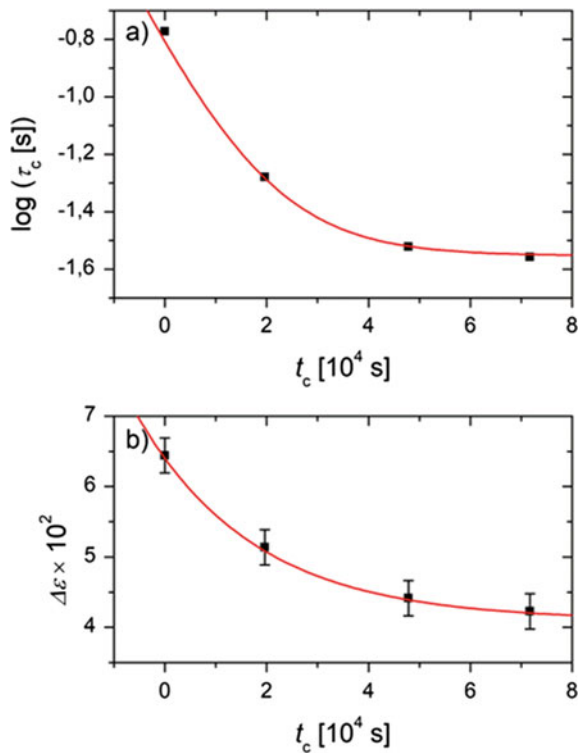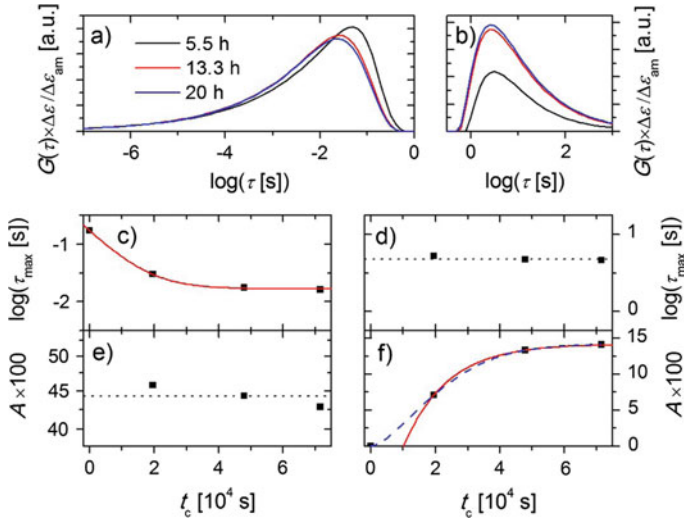
Fig. 6 Development of the scaled relaxation time distributions $G(\tau)\Delta\varepsilon/\Delta\varepsilon_{am}$ of **a** the CAF and **b** the RAF depending on the crystallization time as indicated in panel **a** (vertical axes in (**a**) and (**b**) not to scale). From the peak positions of the $G(\tau)\Delta\varepsilon/\Delta\varepsilon_{am}$, the corresponding mean relaxation times τ_{max} are extracted for **c** the CAF and **d** the RAF. Similarly, the integrated areas of the $G(\tau)\Delta\varepsilon/\Delta\varepsilon_{am}$ are depicted for **e** the CAF and **f** the RAF. In panels **c–f**, solid red lines represent exponential functions and the dashed blue line is an Avrami equation fitted to the data; the dotted black lines are constants and serve as a guide to the eye. The experimental uncertainty is smaller than the symbol size. Taken an modified with permission after [12]

the crystallites. This is reflected by the increase of the area of the extracted RTD of the RAF; considering that at $t_c = 0$ no RAF is present, an exponential growth with a time constant for of 1.2×10^4 s describes the process.

The CAF on the other hand exhibits only a minimal reduction in the area of the separated RTD (most likely because the overall fraction of mobile segments decreases) while its mean relaxation time becomes much smaller than the initial value of the purely amorphous state; the time constant of the latter is, based also on an exponential decay, 8.4×10^3 s which is on the same order of magnitude as the other changes. The similarity of the time constants also in the separated contributions suggests a strong interrelation of these phenomena which supports the hypothesized mechanism.

3.6 Structural Details in the Crystallization Kinetics

In order to address the dynamical changes with chemical specificity, the BDS experiments were complemented by FTIR measurements which enable tracing the evolution of both crystalline and amorphous moieties of the sample. In detail, we analyze

the IR absorption bands at $\nu = 840$, 906, 1155, and 980 cm^{-1} (Fig. 7) whereby the former three are assigned to the amorphous state while the latter is present in the crystalline state [32, 33]. To quantitatively examine the oscillator strength of these bands Voigt functions are fitted to the spectra and the integrated absorbance (area under the curve) as a measure of the oscillator strength is extracted (Fig. 7).

The oscillator strengths of all analyzed bands exhibit a lag time t_0 of about 2 $\times$ 10^3 s (approx. 30 min) between the temperature decrease from 210 °C to T_c initializing the crystallization and the appearance of first effects of crystallization on molecular vibrations. This delayed crystallization is known for iPS from previous studies [32]. Its duration depends on the crystallization temperature; for $T_c = 190$ °C a value of 12 min was reported which is in the range of the ~30 min determined here. This lag time was not observed in the BDS measurements reported here since such short crystallization times were not investigated. As expected, the oscillator strength of the three amorphous bands (at 840, 906, and 1155 cm^{-1}) drops upon crystallization after the lag time indicating a reduction of the number density of amorphous segments. For the two bands at 840 and 1155 cm^{-1} a reduction by about 10% is observed which is in accord with the degree of crystallinity deduced from the DSC measurements. However, while the reduction of these amorphous IR absorption bands has a characteristic time of 2–3 $\times$ 10^3 s, the crystallization traced via DSC happens much slower (Figs. 1 and 8).

The absorption band at 906 cm^{-1} exhibits a much larger drop in oscillator strength of about 37% which is comparable to the reduction of $\Delta\varepsilon$ in the BDS measurements. When fitted to a single exponential, the extracted time constant is 3 $\times$ 10^3 s which corresponds to those found for the other two analyzed amorphous IR bands, but is almost 10 times shorter than the time constant extracted from the BDS results. However, in contrast to the two bands at 840 and 1155 cm^{-1}, the integrated absorbance of the band at 906 cm^{-1} can be determined with better accuracy which reveals a mismatch of the single exponential fit with the data (Fig. 7f). Using a double exponential, the evolution of the oscillator strength and thus reduction of amorphous moieties due to crystallization can be described much better, the respective time constants are 2.2 $\times$ 10^3 s and 2.6 $\times$ 10^4 s. While the former is similar to that one from the single exponential fit (and those of the other two amorphous bands), the latter corresponds well with the time constant of the reduction in $\Delta\varepsilon$. This suggests a multi-step process in the course of crystallization whereby only the slower step is resolved in the case of BDS measurements.

In addition, the absorption band at 980 cm^{-1} is assigned to an out-of-plane ring deformation sensitive to the crystalline moiety [32, 34]. Thus, this band grows significantly upon crystallization (at times longer than the lag time t_0). The single exponential fit yields a characteristic time of 2.8 $\times$ 10^3 s which is very similar to those of the amorphous bands. Like in the case of the band at 906 cm^{-1} a deviation from the single exponential fit is evident, consequently, a double exponential is fitted to the spectra, as well. The resulting time constants are 2.3 $\times$ 10^3 and 2.3 $\times$ 10^4 s which agrees well with the values obtained from the band at 906 cm^{-1}. Thus, on the basis of a second band distinct from that at 906 cm^{-1}, another strong indication for a multi-step process in the course of crystallization has been derived independently.
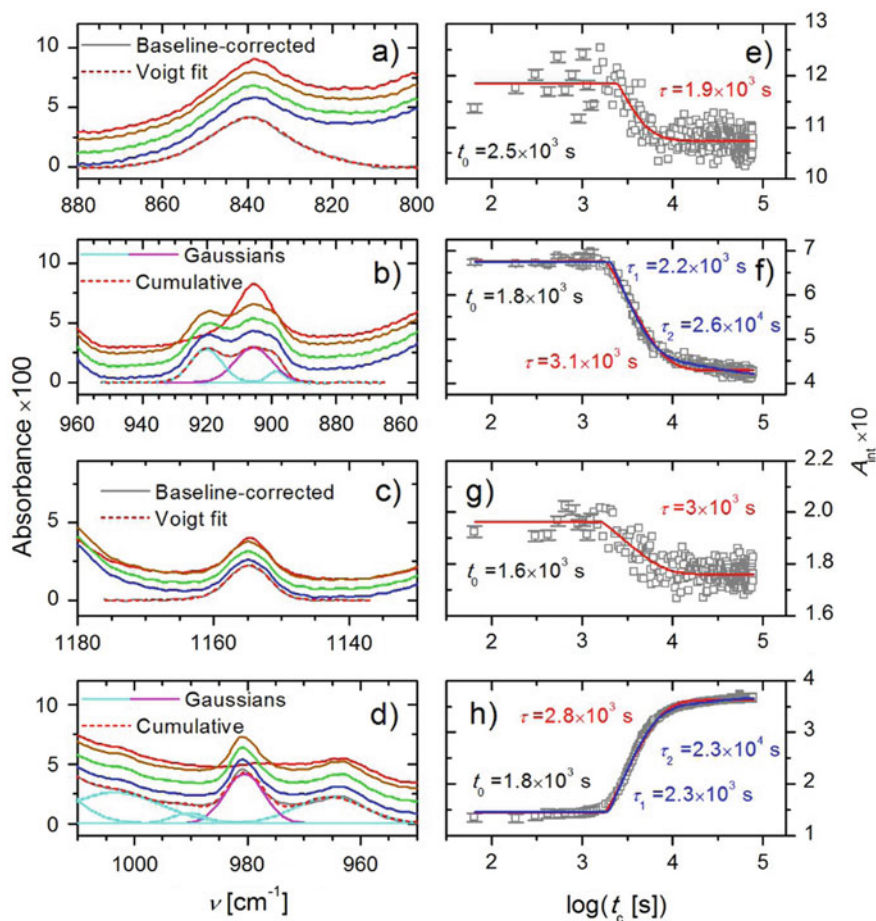
Fig. 7 Infrared absorbance spectra of POSS-iPS for different spectral regions targeting absorption bands assigned to **a** and **b** out-of-plane ring deformations (840 and 906 cm^{-1}), **c** in-plane C–H bending deformation at the benzene rings (1155 cm^{-1}), and **d** out-of-plane ring deformation (980 cm^{-1}) [32, 34]. Solid lines depict absorbance spectra after crystallization at 460 K for 60 s (red), 4820 s (brown), 43,410 s (green), and 71,880 s (blue). For the final state (71,880 s), the baseline-corrected spectrum is shown (gray line) as well as the fit (dashed red line); where applicable, the single fit contributions of adjacent bands are depicted (cyan lines) in addition to the fit of the target band (magenta line). For each target band in **a**–**d**, the respective integrated absorbance A_{int} is presented as function of crystallization time t_c in panels **e**–**h**. The experimental uncertainty is indicated in the initial data points; fits to single (red lines) and double (blue lines) exponential functions are shown together with the respective time constants (τ for the single exponentials and τ_1 and τ_2 for the double exponentials, respectively) and the lag time t_0 until the crystallization process starts
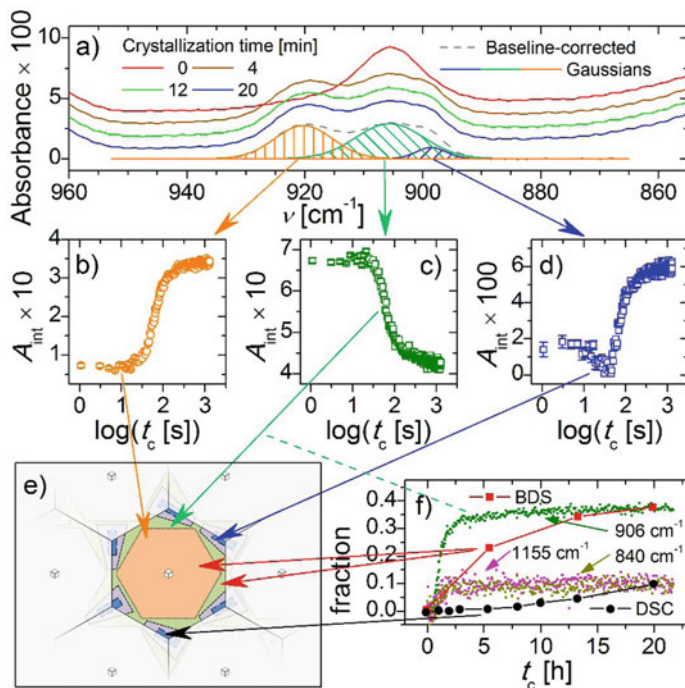
Fig. 8 **a** Infrared absorbance spectra of POSS-iPS for the spectral region around 900 cm^{-1} which exhibit up to three absorption bands. Their integrated absorbances are traced during the crystallization and, based on their spectral position and changed intensity, each peak is assigned to a vibrational mode specific for **b** the CAF, **c** the MAF, and **d** the crystalline fraction. **e** Assignment of the IR bands to the proposed spatial distribution of the different dynamic regions. **f** Temporal evolution of the degree of crystallinity as probed by different IR bands, BDS and DSC

Further insight is gained through the analysis of the absorption around 900 cm^{-1} which contains a single peak at 906 cm^{-1} in the purely amorphous state [35]. During crystallization, however, two new contributions arise (Fig. 8a), whereas the integrated absorbance of the amorphous peak at 906 cm^{-1} decreases by 37% (Fig. 8c), which corresponds to the reduction of $\Delta\varepsilon$ in the BDS measurements. Thus, we conclude that this vibration marks one mode of the purely amorphous system and is sensitive to changes arising from crystallization but also from constraints. In the literature, the two other peaks emerging at 899 and 920 cm^{-1} are assigned to intramolecular conformational changes and the formation of a 3_1 helix structure of the iPS chains. However, since crystallization introduces geometrical confinements, typically giving rise to a red shift of the bands in a slightly distorted system, we ascribe the peak at 899 cm^{-1} to the crystalline phase. On the other hand, since chain "stretching" and a reduced density (increased free volume) typically lead to a blue shift, we ascribe the third peak (920 cm^{-1}) to the CAF. Further support for this conclusion is provided by the fact that the ratio of the integrated absorbance A_{int} of the bands assigned to the

crystalline fraction and the CAF corresponds to the ratio of crystallinities extracted from DSC and BDS (1:4). Apparently, different peaks can reflect distinct moieties with rather subtle differences. E.g. the peak at 840 is assigned to iPS segments in an amorphous structure, i.e. its integrated absorbance drops only, when the segments are incorporated into the crystalline phase (the CAF still contributes to this peak). In contrast, the peak at 906 cm^{-1}, is sensitive to mobility of the segments, i.e. its integrated absorbance drops already when the iPS segments experience the constrains in the CAF (only the MAF contributes).

4 Conclusion

BDS measurements of a star-shaped polymer based on a polyhedral oligomeric silesquioxane (POSS) molecule as center and isotactic polystyrene arms reveal a faster mean relaxation time of about 1 decade in the amorphous fraction in the semi-crystalline state compared to the purely amorphous state. Such a signature is typical for spatial confinement and suggests tremendous constraints within the material. A decomposition of the respective relaxation time distributions yields three fractions of different dynamics: a rigid amorphous fraction (RAF) around the crystallites which is well known from the literature, a mobile amorphous fraction (MAF) which was considered identical to the purely amorphous state, and a confined amorphous fraction (CAF) of enhanced dynamics presumably located around the POSS centers. The latter is assigned to chain stretching of the arms due to the volume reduction upon crystallization. This is promoted by the POSS centers which suppress crystallization in their surrounding as well as the star-shape which connects arms from all directions and, thus, prevents a relaxation by contraction. Investigation of the kinetics reveals an exponential decay of both relaxation strength and mean relaxation time with time constants of about $1–2 \times 10^4$ s.

Complementary FTIR measurements of crystalline and amorphous moieties with a better time resolution reveal a multi-step process with a lag time of about 30 min before actual changes can be observed. Then, a fast mechanism initializes the crystallization with time constants of about $2–3 \times 10^3$ s before a second transition follows with a 10 times slower rate corresponding to the BDS results. This suggests an intricate interplay between the crystallization of iPS arms giving rise to conformational changes and structural constraints in the sample's complex chain architecture.

References

1. Strobl G (2006) Prog Polym Sci 31:398
2. Strobl G (2007) The physics of polymers. Springer, Berlin, Heidelberg
3. Bai H, Xiu H, Gao J, Deng H, Zhang Q, Yang M, Fu Q, Appl ACS (2012) Mater Interfaces 4:897
4. Galeski A (2003) Prog Polym Sci 28:1643
5. Schulz M, Seidlitz A, Kurz R, Bärenwald R, Petzold A, Saalwächter K, Thurn-Albrecht T (2018) Macromolecules 51:8377
6. Cebe P, Hsiao BS, Lohse DJ (1999) Scattering from polymers. Characterization by X-rays, neutrons, and light. American Chemical Society, Washington, DC
7. Agarwal PK, Somani RH, Weng W, Mehta A, Yang L, Ran S, Liu L, Hsiao BS (2003) Macromolecules 36:5226
8. Portale G, Cavallo D, Alfonso GC, Hermida-Merino D, van Drongelen M, Balzano L, Peters GWM, Goossens JGP, Bras W (2013) J Appl Cryst 46:1681
9. Hay JN, Fitzgerald PA, Wiles M (1976) Polymer 17:1015
10. Toda A, Androsch R, Schick C (2016) Polymer 91:239
11. Natesan B, Xu H, Ince BS, Cebe P (2004) J Polym Sci Part B: Polym Phys 42:777
12. Tress M, Vielhauer M, Lutz PJ, Mülhaupt R, Kremer F (2018) Macromolecules 51:501
13. Holt AP, Griffin PJ, Bocharova V, Agapov AL, Imel AE, Dadmun MD, Sangoro JR, Sokolov AP (2014) Macromolecules 47:1837
14. Cheng S, Carroll B, Bocharova V, Carrillo J-M, Sumpter BG, Sokolov AP (2017) J Chem Phys 146:203201
15. Kremer F, Schönhals A (eds) (2003) Broadband dielectric spectroscopy. Springer, Berlin, Heidelberg
16. Kipnusu WK, Elsayed M, Kossack W, Pawlus S, Adrjanowicz K, Tress M, Mapesa EU, Krause-Rehberg R, Kaminski K, Kremer F (2015) J Phys Chem Lett 6:3708
17. Vielhauer M, Lutz PJ, Reiter G, Mülhaupt R (2013) J Polym Sci Part A: Polym Chem 51:947 (Wiley Subscription Services, Inc., A Wiley Company)
18. Xu H, Ince BS, Cebe P (2003) J Polym Sci Part B: Polym Phys 41:3026
19. Brandrup J, Immergut EH (1989) Polymer handbook. Wiley Interscience, New York, Chichester, Brisbane, Toronto, Singapore
20. Harnisch K, Muschik H (1983) Colloid Polym Sci 261:908
21. Jeziorny A (1978) Polymer 19:1142
22. Wang C, Lin CC, Tseng LC (2006) Polymer 47:390
23. Havriliak S, Negami S (1967) Polymer 8:161
24. Vogel H (1921) Physikalische Zeitschrift 22:645
25. Fulcher GS (1925) J Am Chem Soc 8:339
26. Tammann G, Hesse W (1926) Zeitschrift für anorganische und allgemeine Chemie 156:245
27. Zheng Z, Kuang F, Zhao J (2010) Macromolecules 43:3165
28. Maitra P, Wunder SL (2002) Chem Mater 14:4494
29. Núñez E, Ferrando C, Malmström E, Claesson H, Gedde UW (2004) J Macromol Sci Part B Phys 43:1143
30. Kuo S-W, Chang F-C (2011) Prog Polym Sci 36:1649
31. Lee H-N, Ediger MD (2010) Macromolecules 43:5863
32. Kimura T, Ezure H, Tanaka S, Ito E (1998) J Polym Sci B 36:1227
33. Olmos D, Martín EV, González-Benito J (2014) Phys Chem Chem Phys 16:24339
34. Liang CY, Krimm S (1958) J Polym Sci 27:241
35. Zhang J, Duan Y, Sato H, Shen D, Yan S, Noda I, Ozaki Y (2005) Initial crystallization mechanism of isotactic polystyrene from different states. J Phys Chem B 109:5586

Index